LA-13037-T
Thesis

UC-700
Issued: November 1995

The Dynamics of Variable-Density Turbulence

Donald L. Sandoval

Los Alamos
NATIONAL LABORATORY
Los Alamos, New Mexico 87545

DISCLAIMER

Portions of this document may be illegible in electronic image products. Images are produced from the best available original document.

DISCLAIMER

ACKNOWLEDGMENTS

I wish to express my sincerest thanks to Professor James J. Riley, committee chairman, for all his assistance, support, and friendship during the course of this research project. Without his guidance I could not have conducted this research. I'd also like to especially thank Professors George Kosály and Bob Briedenthal at the University of Washington for enlightening conversations regarding my work. I'd also like to thank Dr. Ruddy Mell for the use of his numerical data for this study.

I'd also like to express my gratitude to Dr. Timothy T. Clark at the Los Alamos National Laboratory for all the useful conversations regarding this work and useful interpretations of some of the results and for his friendship and encouragement during this project. I also want to thank Dr. Francis H. Harlow for his help in this project and his friendship over all these years. Without Frank's encouragement I could not have made it.

I also want to express thanks to Dr. Charles Zemach, Dr. Rick Rauenzahn, and the members of Group T-3 and the Los Alamos National Laboratory for all the help and support they have given me during the course of this work.

Finally, this work was supported in part by the Ford Foundation Predoctoral Minority Fellowship, The Seafirst Bank Minority Fellowship, a National Science Foundation computer grant at the Pittsburgh Supercomputing Center and the Los Alamos National Laboratory.

TABLE OF CONTENTS

LIST OF FIGURES

LIST OF TABLES

THE DYNAMICS OF VARIABLE-DENSITY TURBULENCE

by

Donald L. Sandoval

ABSTRACT

The dynamics of variable-density turbulent fluids are studied by direct numerical simulation. The flow is incompressible so that acoustic waves are decoupled from the problem, and implying that density is not a thermodynamic variable. Changes in density occur due to molecular mixing. The velocity field is, in general, divergent. A pseudo-spectral numerical technique is used to solve the equations of motion. Three-dimensional simulations are performed using a grid size of 128^3 grid points. Two types of problems are studied: (1) the decay of isotropic, variable-density turbulence, and (2) buoyancy-generated turbulence in a fluid with large density fluctuations (such that the Boussinesq approximation is not valid).

In the case of isotropic, variable-density turbulence, the overall statistical decay behavior, for the cases studied, is relatively unaffected by the presence of density variations when the initial density and velocity fields are statistically *independent*. The results for this case are in quantitative agreement with previous numerical and laboratory results. In this case, the initial density field has a bimodal probability density function (pdf) which evolves in time towards a Gaussian distribution. The pdf of the density field is symmetric about its mean value throughout its evolution. If the initial velocity and density fields are statistically *dependent*, however, the decay process is significantly affected by the density fluctuations. For this case, the pdf of the density becomes asymmetric about its mean value during the early stages of its evolution. It is argued that these asymmetries in the pdf of the density field are due to different entrainment rates, into the mixing region, that favor the high speed fluid.

For the case of buoyancy-generated turbulence, variable-density departures from the Boussinesq approximation are studied. Also, Reynolds number effects are investigated using initial density fields with moderately large initial density variations. An important parameter that characterizes buoyancy driven flow is the initial value of

the ratio of the rms density fluctuations to the mean density. If this quantity is less than approximately 0.1 than the resulting buoyancy-driven flow is within the Boussinesq approximation. It is shown that the mean pressure gradient, which is constant in the Boussinesq limit, varies with time and is a function of magnitude of the density fluctuations and the acceleration. Vorticity dynamics for this flow are also studied.

The results of the buoyancy-generated turbulence are compared with variable-density model predictions. Both a one-point (engineering) model and a two-point (spectral) model are tested against the numerical data. Some deficiencies in these variable-density models are discussed and modifications are suggested.

Chapter 1

INTRODUCTION

1.1 Motivation

A large body of work exists on the topic of turbulence in constant-density fluids [38]. Theoretical, experimental and numerical methods have been used to gain an understanding of such flows. The study of turbulence with large density variations is still in its infancy, however, and the understanding of such flows is far from complete. Many industrial and engineering applications involve variable-density fluids. Most chemical reactions, e.g., in engine combustion, involve the turbulent mixing of two or more fluids of different densities. In nuclear reactors one can find fluids of different densities (e.g., water and steam) that are mixing due to turbulence. Natural phenomenon involving variable-density flows are quite diverse, ranging from turbulent mixing driven by buoyant convection in the oceans, the atmosphere, and the Earth's mantle, to turbulence found on Jupiter or the turbulent mixing of gases from an exploding nova. Turbulence affects the environment in many ways, from the natural phenomenon of the turbulent mixing of plumes of smoke and ash rising from a volcano, to the man-made phenomenon of the turbulent transport and mixing of pollutants from a power plant into the atmosphere.

Because of the importance of turbulence mixing in industrial applications, a number of turbulence mixing models (with and without chemical reactions) have been proposed for variable-density flows. One approach that describes the transport of two fluids consists of the so-called multi-phase (field) models [41]. Stewart and Wendroff [83] give a good review of such models. In these models there are two or more distinct fluids (or phases) separated by a discontinuous interface. Each fluid has a smoothly varying composition with steep gradients of properties close to the interface [29]. The continuum field equations of motion are employed for each fluid with appropriate boundary conditions between the fluids. Kataoka [46] has developed local,

instantaneous field conservation equations for density, velocity, and energy that account for discontinuous changes at the interface between the two fluids. In his model, if the interfacial force and energy discontinuity are neglected, the two-field model reduces to that of a single-fluid. From this two-field model, Kataoka and Serizawa [47] develop a transport equation for turbulent energy using averaging techniques (for a discussion of averaging techniques see Appendix A). An attribute of two-field models of this nature is that they do not take into account molecular mixing [83] across the interface. The mixing that occurs is at a macroscopic level and obtained through averaging procedures. The advantage, here, is that this approach can account for de-mixing when the two fluids are set to an acceleration.

There is a great deal of interest in modeling variable-density turbulent mixing, which accounts for molecular mixing (e.g., in Britain, France, Russia and the United States). Therefore, several single-field turbulence transport models for variable-density compressible flow have been developed (see, e.g., Andronov et al. (1982) [1], Besnard et al. (1987) [8], Cranfill (1992) [27]). These engineering models (one-point statistical models) typically include the transport of the turbulent kinetic energy and the turbulent energy dissipation rate (i.e., k-ϵ models). The model presented by Besnard, Harlow, Rauenzhan and Zemach (1992) [10] (herein referred to as the BHR model) is a one-point model that describes variable-density turbulent flows. Transport equations for the Reynolds stress tensor and the turbulent energy dissipation rate are derived, as well as transport equations for the density-velocity correlation and the density-density correlation. This model was developed employing techniques and concepts from incompressible, constant-density turbulence modeling and incorporates ideas from two-phase flow models.

In order to aid in the closure of such models, multi-point models are also developed. For example, two-point models for constant-density incompressible turbulence are of interest because they account for the spectral character of turbulence and predict nonequilibrum flows more accurately [33]. Clark and Spitz (1994) [23] present a two-point model (herein referred as the CS model) for variable-density turbulence. Their derivation is based on the two-point generalization of the Reynolds stress tensor, and the derived equations are Fourier transformed with respect to the separation distance between the two points. Transport equations are derived for the generalized Reynolds stress tensor, the fluctuating density-velocity-specific volume

correlation, and the density-specific volume correlation. These models contain many terms, ad-hoc assumptions and unknown model constants that need to be determined by comparison with experimental and numerical data.

1.2 Previous work

Knowledge of constant-density turbulence has increased throughout the years due to much theoretical, numerical and experimental research [38]. The extension of this work to include variable-density effects is experimentally (and theoretically) more difficult. This is partially due to the fundamental problems associated with how the density and velocity fields are dynamically coupled. Some research has been carried out to address this issue. The experiment of Brown and Roshko [15] was one of the first designed to isolate the importance of the density fluctuations on turbulent flow. They were interested in examining the effects of the density ratio between two streams of different gases on the growth of a plane mixing layer. Their interest in this problem was due to observations in a supersonic jet that, as the Mach number increased, the growth of the mixing layer between the jet and the external gas decreased. This inhibition was originally attributed to the increasing density ratio between the jet and the external gas. If this was the case, then the trends seen in the growth rate of a subsonic mixing layer would be similar to that of a supersonic layer for the same density ratio. To isolate the question of whether the growth rate suppression was due to increasing density rations or compressibility effects, Brown and Roshko performed experiments of a plane turbulent mixing layer between two different gases. The Mach number of both fluids was low enough that the flow was effectively incompressible. They controlled the walls of their experimental apparatus to obtain near zero pressure gradients, and examined density ratios of 1/7, 1 and 7. Their results showed that, even though there was an effect of a change in the density ratio on the growth rate of the mixing layer in this subsonic flow, these changes were small when compared to previous supersonic results. Using Reynolds-averaged equations for incompressible and for supersonic flow, Brown and Roshko showed that the pressure-velocity correlations accounted for the observed differences in growth rates, and not density ratio changes. Spark shadow photographs of the flow also showed that, for all ratios of density difference between the two streams, the mixing layer is dominated by large, coherent quasi-two-dimensional structures. It has also

been observed (see, e.g., Dimotakis (1986) [28]) in these spatially growing shear layers that the flow entrains an unequal amount of fluid from each of the freestreams, which results in a mixed fluid that favors the high-speed fluid.

In many other experiments to investigate the effects of scalar mixing in turbulence, the scalar field was effectively passive (see, e.g., Lesieur (1990) [52]), i.e., not affecting the velocity field. From an experimental viewpoint the simplest case of a scalar in a turbulent flow is that of decaying passive scalar (e.g., temperature) fluctuations in approximately isotropic, grid-generated turbulence. For example, Warhaft and Lumley (1978) [88] reported on the decay of temperature fluctuations in grid-generated turbulence. In their experiments the flow was incompressible with a Prandtl number of order unity, since the fluid was air. Temperature fluctuations were small enough that the corresponding density fluctuations did not affect the flow field, i.e., temperature fluctuations were acting as a passive scalar. Warhaft and Lumley also reported that the velocity characteristics for a heated grid remained the same as for an unheated grid, again an indication of the scalar being passive. This work was followed up by the experiments of Jayesh and Warhaft [42, 43], who studied the probability density distributions of the scalar and velocity in grid-generated turbulence. More recently, Jayesh et al., (1994) [44] report on passive temperature spectra from wind tunnel, grid-generated turbulence. Robey (1990) [73] presented results on the spectral density of passive temperature fluctuations in a turbulent channel flow. Some new, remarkable experimental techniques have recently been developed by Dahm et al., (1991) [89]. In an axisymmetric, incompressible turbulent jet with a Schmidt number much greater than 1, using laser-induced fluorescence, they were able to capture highly resolved, four-dimensional measurements of the fine-scale structure of a conserved scalar and showed that mixing occurs in sheet-like layers.

Another large area of research where variable-density effects are being studied is mixing in stratified flows, both stable and unstable, e.g., in oceanic and atmospheric turbulence. Hopfinger (1987) [39] gives a good review of the experimental, numerical and theoretical developments in turbulence in stably-stratified flows. Stratified turbulent shear flows have been studied in the laboratory and the results demonstrate that stable stratification inhibits the turbulence mechanisms, thus decreasing mixing. Shy and Breidenthal (1991) [80] studied the effects of buoyancy reversal in a stratified interface between two fluids. Their experimental observations suggest that the

entrainment rate at the stratified interface depends on the Schmidt, Reynolds and Richardson numbers. A number of laboratory experiments have been performed to quantify the effect of buoyancy forces on mixing (see, e.g., Lienhard and Van Atta (1988) [54], Yoon and Warhaft (1990) [90], and Itsweire, et al (1986) [40]). Barrett and Van Atta (1991) [2] studied the decay of velocity and density fluctuations in buoyancy influenced turbulence generated by a grid, towed horizontally through a stably stratified fluid. They showed that immediately behind the grid (i.e., at an early time in the flow), the turbulence was unaffected by buoyancy forces. At late times, buoyancy forces have significant effects on the decay of the turbulent flow.

Other experiments have been reported involving the mixing across an interface between two fluids induced by Rayleigh-Taylor instability due to an acceleration of the interface (see e.g., Sharp (1984) [78]; Smeeton and Youngs (1987) [81]; Linden and Redondo (1991) [55]; and Sturtevant (1987) [84]). In these experiments large-scale structures grow from instabilities on the interface between the two fluids and these structures account for most of the mixing seen in these experiments.

In addition to experiments, numerical methods have been extensively employed to further our understanding of variable-density flow. The advantages and disadvantages of using numerical approaches instead of experiments are given in Section 1.3. Direct numerical simulations (DNS) and large-eddy simulations[1] (LES) have been used for these investigations. DNS has been employed in the study of passive scalar mixing in forced isotropic turbulence (e.g., Chasnov, Canuto and Rogallo (1988) [19]; Eswaran and Pope (1988) [30]; Ruetsch and Maxey (1991) [76]), and decaying isotropic turbulence (e.g., Herring and Kerr (1982) [37]; Mell, (1994) [60]). Of particular interest are the results of Eswaran and Pope and of Mell who show the evolution of the probability density function (pdf) of the passive scalar. In both forced and decaying turbulence the pdf, which initially is of double-delta function form, evolves towards a Gaussian. LES have also been used to study passive scalar mixing in decaying isotropic turbulence (see, e.g., Lesieur and Rogallo (1989) [53]). DNS and LES have also been used to investigate turbulence in stably stratified flows (see, e.g., Riley et al. (1981) [72]; Métais and Lesieur (1992) [61]). Finite difference techniques are often used in the study of mixing due to Rayleigh-Taylor instability (see, e.g., Glimm et al. (1990)

[1] Large-eddy simulations are like direct numerical simulations, but the sub-grid scale effects not resolved by the mesh are accounted for using a sub-grid scale model

[35]; Youngs (1991) [91]). Batchelor, Canuto and Chasnov (1991) [7] presented DNS and LES results of homogeneous, buoyancy-generated turbulence. This type of flow is generated by an 'active' scalar since it is through the density field, which represents a source of potential energy, being accelerated by a body force (e.g., gravity) that kinetic energy is created. As the scalar field decays so does the source of potential energy; what remains is a decaying turbulent flow. Using the Boussinesq approximation (assuming small density fluctuations) in their numerical scheme, Batchelor et al. present (along with analytical results) a description of the birth, life and "lingering death" of buoyancy-generated turbulence.

1.3 Current work

We are interested in understanding the turbulent interactions of two miscible, incompressible fluids of different densities. By the terminology *incompressible fluid* we mean a fluid whose compressibility coefficient and thermal expansion coefficient are both zero (see, e.g., Panton [67], Chapter 2). This decouples acoustic waves from the problem, implying an infinite sound speed and that density is no longer a thermodynamic variable and therefore not a function of the pressure. For a flow to be incompressible, the main criterion is that the Mach number be low ($M \rightarrow 0$). In our study, the Mach number is assumed to be zero. Note that this definition of incompressible flow is slightly different than that sometimes given in the literature. For example, Panton (chapter 10, page 237) defines "incompressible flow" as a flow where changes in the density are negligible, leading to a non-divergent velocity field, i.e., $\nabla \cdot \vec{u} = 0$. However, it has been shown [45] that the velocity field for the mixing of two miscible, incompressible fluids is not in general divergence free, i.e.,$\nabla \cdot \vec{u} \neq 0$. Herein, we refer to the flow in our study as being incompressible due to the low Mach number criterion and this reference does not imply that the divergence of the velocity field is zero.

With this in mind, we are interested in the effects of variable-density on turbulence at a fundamental level. That is, we are interested in the nonlinear processes of turbulence and the influence of variable density on this process. Therefore, we restrict our fluids and flow to be incompressible (as described above) such that compressibility effects do not complicate the flow. To further isolate the effects of variable-density on the turbulence we restrict our flow to be statistically homogeneous and initially

isotropic. This requirement eliminates the study of flows with large-scale coherent structures (e.g., plane mixing layers and flows generated by Rayleigh-Taylor instabilities). With these requirements we investigate the effects of variable density on turbulence by studying two types of flows: (1) isotropic decay of variable-density turbulence and (2) homogeneous buoyancy-generated turbulence. The study of such flows using experimental techniques is difficult. To avoid these difficulties, and following our desire to obtain a complete description of the flow, we resort to numerical techniques, using direct numerical simulations to investigate these two types of flows. The simulation procedure is analogous to an experiment and is sometimes referred to as a 'numerical experiment'. The main advantages of using a numerical simulation over laboratory experiments are that (a) since the entire flow field is known at every step in time and every point in space, much more (statistical) information of interest can be obtained, (b) the parameters can be easily varied and (c) the external conditions are more controllable so that we can simulate the conditions of the two problems of interest more easily. The disadvantage of a numerical simulation is that the temporal and spatial resolution is limited. The spatial resolution limits the range of scales that can be computed, and, thus, the maximum Reynolds numbers that can be treated. A review of the literature suggests that the state-of-the-art resolution for DNS of a passive scalar in isotropic turbulence is with a mesh size of about 128^3 grid points having a maximum initial Taylor Reynolds number around 65 for $S_c \leq 1$. In Chapter 2 of this dissertation is discussed the formulation of the equations of motion that are used in the research presented. In Chapter 3 is discussed the numerical solution procedure used to solve the equations of motion.

For the case of isotropic turbulence, only small, passive density variations have been treated. It is our intention to investigate how variable-density affects the decay of isotropic turbulence (presented in Chapters 4 and 5). It is known that in isotropic turbulence a single-point scalar-velocity correlation is zero (see, e.g., Lesieur (1991) [52]). Intuitively, as density fluctuations change there must be some effect of this change on the turbulence. With the lack of correlation between the density and velocity field, the question that arises is: Where and how do density changes affect the turbulence?

Previous work for the case of turbulence that includes buoyancy effects has been for cases of (a) stably stratified flows or (b) flows within the Boussinesq approximation

(or both). We are interested in the generation of turbulence due to buoyancy effects in an unstably stratified field not within the Boussinesq approximation. To our knowledge there has not been any research reported for this problem. The results of Batchelor et al. [7], using the Boussinesq approximation, will provide a basis to study the limits of this approximation for buoyancy-generated turbulence. This is addressed in Chapter 6.

It is our hope that the knowledge gained from this numerical study will be invaluable in the development of variable-density models, such as the BHR and CS variable-density turbulence models. In Chapter 7 are described some comparisons between the predictions of the BHR and CS models with the results of direct numerical simulation taken from this study. Some deficiencies in the models are identified and modifications to these models are suggested.

Chapter 2

FORMULATION

In this numerical study of variable-density turbulence, the most general approach is to use the single-field representation of variable-density flow and to perform a direct numerical solution of the Navier-Stokes equations [67] for variable-density flows. This is what is done for the research presented in this dissertation. In this chapter are described the equations of motion used in this study. A constraint equation is developed for the velocity divergence using the conservation equations for two miscible fluids and assuming mixing according to Fick's law. The equations of motion are also rewritten in nondimensional form in preparation for their numerical solution.

2.1 Equations of Motion

In this study consider the flow of a viscous, Newtonian fluid at zero Mach number. The conservation of mass is

$$\frac{\partial \rho}{\partial t} + \frac{\partial \rho u_j}{\partial x_j} = 0. \tag{2.1}$$

The equations for the conservation of momentum are the Navier-Stokes equations [67], here given as

$$\frac{\partial \rho u_i}{\partial t} + \frac{\partial \rho u_i u_j}{\partial x_j} = -\frac{\partial p}{\partial x_i} + \frac{\partial \tau_{ij}}{\partial x_j} + \rho g_i \tag{2.2}$$

with the viscous stress tensor defined by

$$\tau_{ij} = \mu \left\{ \frac{\partial u_i}{\partial x_j} + \frac{\partial u_j}{\partial x_i} - \frac{2}{3}\delta_{ij}\frac{\partial u_n}{\partial x_n} \right\}.$$

Here $\rho(x_i, t)$, $p(x_i, t)$ and $u_i(x_i, t)$ are the density, pressure and velocity fields, respectively, dependent on the spatial coordinate x_i and on time t, g_i is an acceleration (e.g., gravity), and μ the fluid viscosity.

These equations require specified boundary and initial conditions. A condition for a mean pressure gradient is also required to correctly specify the problem of

a variable-density fluid subjected to an acceleration. The most common approach to study variable-density flows is to use the Boussinesq approximation [69]. This approximation is valid when the actual density and pressure fluctuations vary only slightly from their respective means, the vertical scale of motion is small compared with the scale height, and the Mach number of the flow is low.

In this work we consider a low Mach number flow with large density variations. The Boussinesq approximation is not valid as the density and pressure vary significantly from their mean. Because the Mach number is low acoustic waves are suppressed, making the flow incompressible [52] and decoupling the energy equation from the problem. Variations of the density field are due to the mixing of two fluids with different reference densities. The densities of these two fluids are assumed to be constant and not equal to each other. Fluctuations in the temperatures of the two fluids are assumed to be small, however the temperatures of the two fluids are not necessarily equal. For a single fluid, incompressibility usually implies that $\nabla \cdot \vec{u} = 0$. It has been shown [45] that this equation is inexact for the diffusion of two miscible, incompressible liquids. To account for this, equations for the concentration of mass for each species are employed.

2.2 *Description of Mass Diffusion*

To study variable-density flows we consider flow consisting of two miscible fluids of different microscopic densities. The conservation of mass for species α, assuming Fick's law [12, 10] with with a constant diffusion coefficient, $\mathcal{D}$, is

$$\frac{\partial \rho C_\alpha}{\partial t} + \frac{\partial \rho u_n C_\alpha}{\partial x_n} = \frac{\partial}{\partial x_n}\left(\rho \mathcal{D} \frac{\partial C_\alpha}{\partial x_n}\right), \tag{2.3}$$

where $C_\alpha(x,t)$ is the local mass fraction, i.e., the local mass of species α (= 1 or 2) divided by the local total mass. Using the conservation of mass [eq. (2.1)], equation (2.3) can be rearranged giving

$$\rho \frac{DC_\alpha}{Dt} = \frac{\partial}{\partial x_n}\left\{\rho \mathcal{D} \frac{\partial C_\alpha}{\partial x_n}\right\}. \tag{2.4}$$

Here

$$\frac{D}{Dt} = \frac{\partial}{\partial t} + u_j \frac{\partial}{\partial x_j}$$

is the substantial (material) derivative.

The local mass fractions and the specific volume satisfy [12]

$$C_1 + C_2 = 1 \tag{2.5}$$

and

$$\frac{1}{\rho} = \frac{C_1}{\rho_1} + \frac{C_2}{\rho_2}. \tag{2.6}$$

Here, ρ_α ($\alpha = 1$ or 2) is the local microscopic density, i.e., the local mass of each species divided by the local volume occupied by that mass. It follows directly that ρ can be uniquely described in terms of C_1 or C_2:

$$\frac{1}{\rho} = \frac{C_1}{\rho_1} + \frac{C_2}{\rho_2} = \left(\frac{1}{\rho_1} - \frac{1}{\rho_2}\right) C_1 + \frac{1}{\rho_2}. \tag{2.7}$$

The microscopic densities, ρ_α ($\alpha = 1$ or 2), are assumed constant and not equal to one another. This assumption implies both small temperature fluctuations and that the Mach number is low, and we conclude that the density is only a function of the mass fraction, i.e., $\rho = \rho(C_1)$. With the relationship between C_1 and ρ, the conservation of mass for a specie, eq. (2.4), can be written in terms of the density, ρ. If the constant F is defined as

$$F = \frac{1}{\rho_1} - \frac{1}{\rho_2},$$

then, using eq. (2.7),

$$\frac{DC_1}{Dt} = -\frac{1}{\rho^2 F}\frac{D\rho}{Dt}. \tag{2.8}$$

Likewise

$$\frac{\partial C_1}{\partial x_n} = -\frac{1}{\rho^2 F}\frac{\partial \rho}{\partial x_n}. \tag{2.9}$$

Substituting (2.9) and (2.8) into eq. (2.4) for $\alpha = 1$ gives

$$\frac{D\rho}{Dt} = \frac{\partial \rho}{\partial t} + u_j \frac{\partial \rho}{\partial x_j} = \rho \frac{\partial}{\partial x_n}\left\{\frac{\mathcal{D}}{\rho}\frac{\partial \rho}{\partial x_n}\right\} \tag{2.10}$$

Equation (2.10) can be used instead of eq. (2.4) for incompressible mixing. This equation, along with (2.1) and (2.2), comprise the complete system of equations which,

given the appropriate initial and boundary conditions, describe the time evolution of variable-density, zero Mach number flows.

Comparison of eq. (2.10) with (2.1) leads to the following result for incompressible mixing flows:

$$\frac{\partial u_n}{\partial x_n} = -\frac{\partial}{\partial x_n}\left\{\frac{\mathcal{D}}{\rho}\frac{\partial \rho}{\partial x_n}\right\}. \tag{2.11}$$

Thus, the incompressible velocity field is divergent.

2.3 Nondimensionalization of the equations of motion

The principle of dynamical similarity can be expressed in our equations of motion by considering the following nondimensionalization:

$$\begin{aligned} \hat{u_i} &= \frac{u_i}{U}, \\ \hat{x_n} &= \frac{x_n}{L}, \\ \hat{t} &= \frac{t}{L/U}, \\ \hat{p} &= \frac{p}{\rho_o U^2}, \\ \hat{\rho} &= \frac{\rho}{\rho_o} \\ \hat{g}_i F_r^{-2} &= \frac{g_i}{F_r^2 U^2/L}. \end{aligned} \tag{2.12}$$

Here U is a characteristic velocity, L a characteristic length, ρ_o a characteristic density, L/U^2 a characteristic time and $\rho_o U^2$ is twice the characteristic dynamic pressure head. Substituting the nondimensionalizations into eqs. (2.10) and (2.2) gives the nondimensional equations of motion (dropping the hat notation and assuming μ is constant). The density equation becomes

$$\frac{\partial \rho}{\partial t} + u_j \frac{\partial \rho}{\partial x_j} = \frac{\rho}{R_e S_c}\frac{\partial}{\partial x_j}\left(\frac{1}{\rho}\frac{\partial \rho}{\partial x_j}\right),$$

or

$$\frac{\partial \ln \rho}{\partial t} + u_j \frac{\partial \ln \rho}{\partial x_j} = \frac{1}{R_e S_c}\frac{\partial^2 \ln \rho}{\partial x_j^2}. \tag{2.13}$$

and the momentum equation becomes

$$\frac{\partial \rho u_i}{\partial t} + \frac{\partial \rho u_i u_j}{\partial x_j} = -\frac{\partial p}{\partial x_i} + \frac{1}{R_e}\frac{\partial \tau_{ij}}{\partial x_j} + \rho g_i F_r^{-2}, \tag{2.14}$$

with

$$\tau_{ij} = \left\{ \frac{\partial u_i}{\partial x_j} + \frac{\partial u_j}{\partial x_i} - \frac{2}{3}\delta_{ij}\frac{\partial u_n}{\partial x_n} \right\}.$$

Substituting the nondimensionalizations into the equation for velocity divergence, eq. (2.11), gives

$$\frac{\partial u_n}{\partial x_n} = -\frac{1}{R_e S_c}\frac{\partial}{\partial x_n}\left\{ \frac{1}{\rho}\frac{\partial \rho}{\partial x_n} \right\}. \tag{2.15}$$

The solutions of these equations, (2.13), (2.14) and (2.15), depend on the following dimensionless groups:

$$R_e = \frac{UL}{\nu}$$

$$S_c = \frac{\nu}{\mathcal{D}},$$

and

$$F_r^2 = \frac{U^2}{gL}.$$

R_e is a Reynolds number formed from characteristic length and velocity scales, and represents the ratio of inertial forces to viscous forces. S_c is the Schmidt number which depends on the properties of the fluids, ν and $\mathcal{D}$, and is the ratio of momentum diffusion to mass diffusion. F_r is the Froude number and is the ratio of inertial to buoyancy forces.

Chapter 3

NUMERICAL SOLUTION METHOD

In this chapter is described the solution method for the equations of motion used in this study. A numerical algorithm is developed to study the decay of isotropic turbulence experienced by two miscible fluids as well as the mixing of two fluids subjected to a constant acceleration. Spectral methods are used to approximate the spatial gradients; for temporal discretization an Adams-Bashforth method is employed. The solution procedure consists of first solving for the density at the next time step; then the half-step momentum (the momentum not including pressure effects) is solved for and finally the next time step density is used in a projection step to solve a Poisson equation for the pressure and thus the next time step momentum.

3.1 Temporal Discretization

A numerical algorithm for solving eqs. (2.13), (2.14), and (2.15) is developed here. It is based on the algorithm of McMurtry [58] for low Mach number, variable-density reacting flows. Here it is modified for the incompressible mixing of two miscible fluids subject to a constant acceleration. This method is related to the projection method [68] but takes into account the fact that the velocity field is divergent. The equations are temporally discretized using an Adams-Bashforth scheme, except for the initial time step in which is a forward Euler scheme is used.

3.1.1 Density Equation

A useful simplification to the nondimensional equation for the density ρ [eq. (2.10)] is to rewrite it in terms of $\ln \rho$, i.e., eq. (2.13), repeated here

$$\frac{D \ln \rho}{Dt} = \frac{1}{R_e S_c} \frac{\partial^2 \ln \rho}{\partial x_i^2}. \tag{3.1}$$

It is useful to rearrange this into the form

$$\frac{\partial \ln \rho}{\partial t} - \frac{1}{R_e S_c}\frac{\partial^2 \ln \rho}{\partial x_i^2} = u_i \frac{\partial \ln \rho}{\partial x_i}.$$

In order to time-step this equation a 3rd-order Adams-Bashforth scheme is used. The integral on the right side is approximated as

$$\int_{t_n}^{t_{n+1}} u_i \frac{\partial \ln \rho}{\partial x_i} dt = \frac{1}{2}\left(3\left\{u_i \frac{\partial \ln \rho}{\partial x_i}\right\}^n - \left\{u_i \frac{\partial \ln \rho}{\partial x_i}\right\}^{n-1}\right)\Delta t + O(\Delta t^3). \qquad (3.2)$$

As will be shown below in discussing the approximation of spatial derivatives using spectral methods (section 3.2), that the time-derivative and the diffusion terms can be combined together using an integrating factor.

3.1.2 Momentum Equation

The momentum equation, eq. (2.14), is rewritten as

$$\frac{\partial \rho u_i}{\partial t} = -\frac{\partial p}{\partial x_i} + \frac{1}{R_e}\frac{\partial \tau_{ij}}{\partial x_j} - \frac{\partial \rho u_i u_j}{\partial x_j} + F_r^{-2}\rho g_i \equiv -\frac{\partial p}{\partial x_i} + A_i + F_r^{-2}\rho g_i, \qquad (3.3)$$

Using the Adams-Bashforth philosophy, we integrate eq. (3.3) from t_n to $t_{n+1} = t_n + \Delta t$ to give:

$$\int_{t_n}^{t_{n+1}} \frac{\partial \rho u_i}{\partial t} dt = -\int_{t_n}^{t_{n+1}} \frac{\partial p}{\partial x_i} dt + \int_{t_n}^{t_{n+1}} A_i dt + \int_{t_n}^{t_{n+1}} F_r^{-2}\rho g_i dt$$

The term on the left side immediately integrates to give:

$$\int_{t_n}^{t_{n+1}} \frac{\partial \rho u_i}{\partial t} dt = (\rho u_i)_{n+1} - (\rho u_i)_n.$$

In the first term on the right side, the gradient operator commutes with the integration to give

$$-\int_{t_n}^{t_{n+1}} \frac{\partial p}{\partial x_i} dt = -\frac{\partial}{\partial x_i}\int_{t_n}^{t_{n+1}} p dt = -\frac{\partial \tilde{p}}{\partial x_i}\Delta t$$

where

$$\tilde{p} = \frac{1}{\Delta t}\int_t^{t+\Delta t} p dt$$

is the average pressure over the integral t to $t+\Delta t$. Using the trapezoid rule,

$$\tilde{\rho} = \frac{1}{\Delta t}\int_t^{t+\Delta t} \rho dt \cong \frac{1}{\Delta t}\frac{[\rho(t)+\rho(t+\Delta t)]\,\Delta t}{2} = \frac{\rho^{n+1}+\rho^n}{2} \tag{3.4}$$

is the density averaged over the same interval. Finally, the second term on the right side is evaluated with a second-order accurate expression

$$\int_{t_n}^{t_{n+1}} A_i dt = \frac{1}{2}\left(3A_i^n - A_i^{n-1}\right)\Delta t + O(\Delta t^3).$$

Putting these all together gives a time approximation to eq. (3.3):

$$\frac{(\rho u_i)^{n+1} - (\rho u_i)^n}{\Delta t} = -\left(\frac{\partial \tilde{p}}{\partial x_i} - F_r^{-2}\tilde{\rho} g_i\right) + \frac{1}{2}\left(3A_i^n - A_i^{n-1}\right) + O(\Delta t^2). \tag{3.5}$$

The solution procedure for this equation is related to the projection method [68]. This momentum equation is solved in two steps, the first step taking account of the viscous and nonlinear effects and the second step including the pressure and acceleration effects. The first step is

$$(\rho u_i)^* = (\rho u_i)^n + \frac{\Delta t}{2}\left[3A_i^n - A_i^{n-1}\right] \tag{3.6}$$

and the second step is

$$(\rho u_i)^{n+1} = (\rho u_i)^* - \Delta t\left(\frac{\partial \tilde{p}}{\partial x_i} - F_r^{-2}\tilde{\rho} g_i\right). \tag{3.7}$$

Equations (3.6) and (3.7) sum to give (3.5). Equation (3.6) is solved to obtain the half-step momentum field $(\rho u_i)^*$. This is then used to find the pressure using a Poisson equation for $\tilde{p}$, which is obtained by taking the divergence of (3.7), i.e.,

$$\frac{\partial^2 \tilde{p}}{\partial x_i^2} = -\frac{1}{\Delta t}\left\{\frac{\partial}{\partial x_i}(\rho u_i)^{n+1} - \frac{\partial}{\partial x_i}(\rho u_i)^*\right\} + \frac{\partial}{\partial x_i}\left(F_r^{-2}\tilde{\rho} g_i\right). \tag{3.8}$$

An estimation for

$$\frac{\partial}{\partial x_i}(\rho u_i)^{n+1} \tag{3.9}$$

is needed in order to solve for $\tilde{p}$ since $(\rho u_i)^{n+1}$ has not yet been calculated. One method, developed by McMurtry [58], for determining this is to employ the conservation of mass at time-step $n+1$, i.e.,

$$\frac{\partial}{\partial x_i}(\rho u_i)^{n+1} = -\left(\frac{\partial \rho}{\partial t}\right)^{n+1}. \tag{3.10}$$

At this point in the numerical solution ρ^{n+1} has been obtained using the mass equation. Thus a backward difference of (3.10) can be used to estimate (3.9),

$$\left(\frac{\partial \rho}{\partial t}\right)^{n+1} = \frac{3\rho^{n+1} - 4\rho^n + \rho^{n-1}}{2\Delta t}. \tag{3.11}$$

Equation (3.11) is substituted into (3.10) and an estimation for (3.9) is obtained. This estimation has been found to work well if the fluctuations in density are not too large. If the fluctuations are large (i.e., $|\rho'|/\overline{\rho} < 0.4$), however, we have found that this approximation can cause the numerical scheme to breakdown. A more robust estimation is

$$\frac{\partial(\rho u_i)^{n+1}}{\partial x_i} = u_i^{n+1}\frac{\partial \rho^{n+1}}{\partial x_i} + \rho^{n+1}\frac{\partial u_j^{n+1}}{\partial x_j} = u_i^{n+1}\frac{\partial \rho^{n+1}}{\partial x_i} - \mathcal{D}\rho^{n+1}\frac{\partial^2}{\partial x_j^2}(\ln \rho)^{n+1}, \tag{3.12}$$

obtained by expanding (3.9). Here, ρ^{n+1} is known and an estimation for u_i^{n+1} is needed and is derived below. Consider the Taylor series representation of u_i^{n+1} based on u_i^n

$$u_i^{n+1} = u_i^n + \left(\frac{\partial u_i^n}{\partial t}\right)(\Delta t) + \left(\frac{\partial^2 u_i^n}{\partial t^2}\right)\frac{(\Delta t)^2}{2} + O(\Delta t^3) \tag{3.13}$$

along with the Taylor series representation of u_i^{n-1} based on u_i^n

$$u_i^{n-1} = u_i^n + \left(\frac{\partial u_i^n}{\partial t}\right)(-\Delta t) + \left(\frac{\partial^2 u_i^n}{\partial t^2}\right)\frac{(-\Delta t)^2}{2} - O(\Delta t^3) \tag{3.14}$$

Equation (3.14) and (3.13) are used to solve for u_i^{n+1}:

$$u_i^{n+1} = 2u_i^n - u_i^{n-1} + O(\Delta t^2) \tag{3.15}$$

where u_i^n and u_i^{n-1} are known from previous time-steps. Equation (3.15) is substituted into (3.12), then eq. (3.12) is substituted into the Poisson equation, eq. (3.8).

Recently, Najm [63] has proposed a predictor-corrector projection method which increases the stability of the projection method of McMurtry [58]. The use of this predictor-corrector method may be helpful in the numerical scheme presented in this study. However, we have not investigated this.

The solution procedure for the momentum consists of first solving for the half-step momentum using (3.6). Then the next-step momentum is solved using (3.7). The pressure $\tilde{p}$ is solved using (3.8) , (3.12) and (3.15) and $\tilde{\rho}$ is found using eq. (3.4). This projection method ensures that the pressure is computed so as to "project" the velocity vector into the space of $u_i's$ satisfying

$$\frac{\partial u_n}{\partial x_n} = -\frac{\partial}{\partial x_n}\left\{\frac{\mathcal{D}}{\rho}\frac{\partial \rho}{\partial x_n}\right\}.$$

3.1.3 Mean Pressure Gradient in Accelerated Case

The case of a statistically homogeneous turbulence [7, 23] subjected to a constant acceleration (e.g. gravity) will also be examined in this dissertation. The flow is generated by an acceleration acting on a fluctuating density field, which represents a source of potential energy. The kinetic energy, initially near zero, is created as the heavy and light fluids are set into motion. The mean pressure gradient in the direction of acceleration (i.e., the z-direction) is not periodic. As discussed below, the use of Fourier transforms in the spatial discretization of the equations of motion restrict the computational mesh to be periodic. To take this periodicity into account we start by considering the momentum equation

$$\frac{\partial \rho u_i}{\partial t} + \frac{\partial \rho u_i u_n}{\partial x_n} = -\frac{\partial p}{\partial x_i} + \frac{\partial \tau_{in}}{\partial x_n} + \rho g_i.$$

Letting a tilde denote a mass-weighted (or Favre) average and an overbar denote a volume-weighted (or Reynolds) average (see Appendix A), we have

$$u_i = \overline{u}_i + u_i' = \tilde{u}_i + u_i''.$$

As a consequence, $u_i'' = a_i + u_i'$ where $a_i = \overline{u''}_i$. We shall choose the frame of motion to be one in which the volumetric mean (Reynolds-averaged) velocity is zero, so $\overline{u}_i = 0 = \tilde{u}_i + a_i$. A useful analogy for the use of this reference frame is the case of a gravitational acceleration. The effects of gravity and acceleration can be interchanged

using a change of reference frames following the well-known "Elevator" principle [85] (see for example, G. Birkhoff [11] or Synge and Griffith [85]). From Birkhoff [11]: "The effect of an acceleration $G(t)$ relative to the laboratory frame is the same as an apparent gravity $g(t) = -G(t)$, relative to an accelerated frame moving with the fluid." An advantage of this reference frame is that, for an incompressible fluid, there is no net volumetric flux of fluid, i.e., $\overline{u}_i = 0$. Using the momentum equation above, and exploiting homogeneity, the averaged equation for the turbulence mass flux a_i (see Appendix B) is

$$\frac{\partial a_i}{\partial t} + \overline{u_n' \frac{\partial u_i'}{\partial x_n}} = -\frac{b}{\overline{\rho}} \frac{\partial \overline{p}}{\partial x_i} + \overline{v' \frac{\partial \tau_{ni}'}{\partial x_n}} - \overline{v' \frac{\partial p'}{\partial x_n}}. \tag{3.16}$$

where

$$\frac{b}{\overline{\rho}} = \left(\overline{v} - \frac{1}{\overline{\rho}} \right) = \frac{(\overline{\rho}\,\overline{v} - 1)}{\overline{\rho}} = -\frac{\overline{\rho' v'}}{\overline{\rho}}.$$

Again, exploiting homogeneity, the mass-weighted mean velocity is given (see eq. (B.20) in Appendix B) by

$$\frac{\partial \tilde{u}_i}{\partial t} = -\frac{1}{\overline{\rho}} \frac{\partial \overline{p}}{\partial x_i} + g_i. \tag{3.17}$$

We have chosen the frame of motion to be one which the mean (Reynolds-averaged) velocity is zero, so $\overline{u}_i = 0 = \tilde{u}_i + a_i$. As a consequence,

$$\frac{\partial}{\partial t} (\tilde{u}_i + a_i) = 0. \tag{3.18}$$

Then from eqs. (3.16) and (3.17) we have

$$\overline{u_n' \frac{\partial u_i'}{\partial x_n}} - \left(-\frac{b}{\overline{\rho}} \frac{\partial \overline{p}}{\partial x_i} + \overline{v' \frac{\partial \tau_{ni}'}{\partial x_n}} - \overline{v' \frac{\partial p'}{\partial x_i}} \right) + \frac{1}{\overline{\rho}} \frac{\partial \overline{p}}{\partial x_i} - g_i = 0.$$

Solving for the pressure gradient and rearranging the velocity-velocity gradient correlation and exploiting homogeneity gives

$$\frac{\partial \overline{p}}{\partial x_i} = \frac{1}{\overline{v}} \left\{ g_i + \overline{v' \frac{\partial \tau_{ni}'}{\partial x_n}} + \overline{u_i' \frac{\partial u_n'}{\partial x_n}} - \overline{v' \frac{\partial p'}{\partial x_i}} \right\}. \tag{3.19}$$

In the limit of vanishing density fluctuations the last three terms on the right side of eq. (3.19) vanish and the mean-pressure gradient is $\bar{\rho}g$, which is the hydrostatic mean pressure gradient.

This condition is implemented into the numerical scheme as follows. Consider the momentum equation

$$\frac{\partial \rho u_i}{\partial t} + \frac{\partial \rho u_i u_n}{\partial x_n} = -\frac{\partial p}{\partial x_i} + \frac{\partial \tau_{in}}{\partial x_n} + \rho g_i.$$

Splitting the right side into mean and fluctuating parts gives

$$\frac{\partial \rho u_i}{\partial t} + \frac{\partial \rho u_i u_n}{\partial x_n} = -\frac{\partial \bar{P}}{\partial x_i} - \frac{\partial p'}{\partial x_i} + \frac{\partial \tau'_{in}}{\partial x_n} + \bar{\rho} g_i + \rho' g_i \tag{3.20}$$

Substituting eq. (3.19) into (3.20) gives

$$\frac{\partial \rho u_i}{\partial t} + \frac{\partial \rho u_i u_n}{\partial x_n} = \frac{1}{\bar{v}} \left\{ b g_i - \overline{u'_i \frac{\partial u'_n}{\partial x_n}} - \overline{v' \frac{\partial \sigma'_{in}}{\partial x_n}} \right\} - \frac{\partial p'}{\partial x_i} + \frac{\partial \tau'_{in}}{\partial x_n} + \rho' g_i \tag{3.21}$$

where b is defined as $b = \bar{\rho}\bar{v} - 1$ (see Appendix A). It can be shown by averaging eq. (3.21) and exploiting homogeneity, that the term in brackets on the right side is the mean momentum ($\overline{\rho' u'_i}$) contribution from the mean pressure gradient. The remaining terms are the contribution to the fluctuating momentum, $\rho' u'_i$. In the numerical scheme, the mean momentum equation is computed separately from the fluctuating momentum equation. Defining the mean pressure gradient contribution to the mean momentum as

$$B_i = \frac{1}{\bar{v}} \left\{ b g_i - \overline{u'_i \frac{\partial u'_n}{\partial x_n}} - \overline{v' \frac{\partial \sigma'_{in}}{\partial x_n}} \right\}, \tag{3.22}$$

then the equation for $\overline{\rho' u'_i}$ is

$$\frac{\partial \overline{\rho' u'_i}}{\partial t} = B_i.$$

Therefore, the mean momentum is computed using the Adams-Bashforth scheme as

$$\left(\overline{\rho' u'_i}\right)^{n+1} = \left(\overline{\rho' u'_i}\right)^{n} - \frac{\Delta t}{2}\left(3B_i^n - B_i^{n-1}\right). \tag{3.23}$$

This scheme ensures that the momentum flux evolves properly due to the mean pressure gradient and ensures that the mean (Reynolds-averaged) velocity remains zero.

3.1.4 Simplification for Isotropic Turbulence

For the case of the decay of isotropic turbulence without a gravitational acceleration, the numerical scheme presented here can be simplified. The gravity terms in eqs. (3.7) and (3.8) are set to zero since $g = 0$. Also, the mean momentum, $\overline{\rho' u_i'}$ is always zero since the density and velocity fields are uncorrelated in isotropic turbulence. Thus, eqs. (3.22) and (3.23) do not need to be computed.

3.2 Spatial Discretization

The spatial discretization utilized is a spectral technique [17] in which the equations of motion are represented as a truncated series of orthogonal functions. The three main types of expansion functions that are usually used in numerical simulations are trigonometric polynomials (Fourier series), Chebyshev polynomials, and Legendre polynomials. The choice of expansion functions used in the solution procedure is dependent on the boundary conditions of the physical problem being studied. Chebyshev and Legendre polynomials are typically used for problems where the boundaries are rigid with no-slip. Fourier series expansions are used for problems where the boundaries are periodic or free-slip.

In this study we consider flows that are periodic with, say, period L. Thus, our equations of motions are transformed to wave number space using the following discrete Fourier transform (see, e.g., Bracewell [13])

$$\hat{F}(k_n, t) = \frac{1}{N} \sum_{j=1}^{N} f(x_j, t) e^{-ik_n x_j}.$$

and the inverse discrete transform:

$$f(x_j, t) = \sum_{n=1}^{N} \hat{F}(k_n, t) e^{ik_n x_j}.$$

Here, $\hat{F}(k_n, t)$ are the expansion coefficients, $k_n = \frac{2\pi n}{L}$, and $e^{\pm ik_n x_j}$ are the linearly independent expansion functions. $f(x_j, t)$ is the representation of f at the discrete points x_j. In our use of the discrete Fourier transform f represents a continuous property of the flow, say e.g., velocity or density. N is the number of collocation points used to discretely represent the continuous function $f(x, t)$. The expansion

coefficients are the quantities that are time-advanced in this numerical scheme. By expanding the individual terms in the equations of motion, the spatial derivatives are easily computed by multiplying each of the expansion coefficients in the finite series by ik (where $i = \sqrt{-1}$). It can be shown that the error in the approximation of the spatial derivatives decreases to zero faster than any finite power of N as N gets large [17]. Thus the accuracy of the spatial derivative is increased as the number of modes, N, of the expansion is increased.

As a result of expanding the equations of motion using discrete Fourier transforms, the nonlinear terms of the equation become convolution sums over all possible wavenumbers, k_i. The direct summation operation of the convolution sum takes $O(N^6)$ operations for a quadratic term in three dimensions. This is computationally expensive considering that, for finite-difference algorithms, the nonlinear term takes $O(N^3)$ operations. To avoid this computationally expensive operation the variables in the nonlinear term are individually transformed to physical (real) space using highly efficient Fast Fourier Transforms (FFT's). The variables are then multiplied in physical space and the product is transformed back to Fourier space. This is known as a pseudo-spectral method and enables the nonlinear product to be computed in $O(N^3 \log_2 N)$ operations. This solution procedure for the nonlinear products introduces aliasing errors (see, e.g., Rogallo, 1981) [74] into the computational results. Aliasing errors occur when the product of two (or more) data points (with wave numbers, say, n and m) that have a given wave number span, k (where $1 - N/2 < k < N/2$), produces a wave number span greater than N (say $n + m = M > N$) so that the affected wave, M, is aliased to wave $M - N$. The aliasing is partially removed using spherical truncation where the upper part of the wave number spectrum is set to zero. For a quadratic product, alias free results are produced in the lowest $2N/3$ modes [65]. For the product of three terms this cutoff is more severe, a truncation [93] is needed at $N/2$ to produce alias free results. In the simulations described here a $9N/10$ truncation is used, allowing some aliasing to occur. This aliasing effect will be small, however, as long as the various fields are well resolved.

3.2.1 *Solution of the Density Equation*

The density equation, eq. (2.13), is Fourier transformed and evolved in Fourier space. Introducing an integrating factor the transformed density equation can be written as

$$\frac{\partial}{\partial t}\left\{(\widehat{\ln\rho})\exp\left(\tfrac{k^2 t}{Re\,Sc}\right)\right\} = -e^{\left(\frac{k^2 t}{Re\,Sc}\right)}T_1.$$

where

$$T_1 = F.T.\left\{u_n\frac{\partial \ln\rho}{\partial x_n}\right\},$$

and $F.T.()$ is a Fourier transform of ().

As mentioned previously, this is solved using an Adams-Bashforth discretization, written as

$$(\widehat{\ln\rho})^{n+1} = e^{\frac{-k^2}{Re\,Sc}\Delta t}(\widehat{\ln\rho})^n - \frac{\Delta t}{2}\left\{3e^{\frac{-k^2}{Re\,Sc}\Delta t}T_1^n - e^{\frac{-2k^2}{Re\,Sc}\Delta t}T_1^{n-1}\right\}. \tag{3.24}$$

During the first time step , T_1^{n-1} is not known, so that the Adams-Bashforth scheme is not adequate for the solution of $(\hat{\ln\rho})^{n+1}$. For the initial time-step a forward Euler time discretization is used,

$$(\widehat{\ln\rho})^{n+1} = e^{\frac{-k^2}{Re\,Sc}\Delta t}\left\{(\widehat{\ln\rho})^n - (\Delta t)T_1^n\right\}.$$

3.2.2 *Solution of the Momentum Equation*

In the solution procedure, eqs. (3.6)-(3.8) are Fourier transformed and the equations of motion are time advanced in Fourier space using an Adams-Bashforth scheme (a forward Euler is used for the first time step). The procedure is as follows: eq. (3.6) becomes, upon transformation

$$\hat{m_i}^* = \hat{m_i}^n + \frac{\Delta t}{2}\left[3\hat{A_i}^n - \hat{A_i}^{n-1}\right] \tag{3.25}$$

where $\hat{m_i}$ is $(\widehat{\rho u_i})$. The pressure is solved from the Poisson equation, eq. (3.8), transformed to Fourier space, i.e.,

$$\hat{\tilde{P}} = \frac{T_2 - ik_i\hat{m}_i^*(k_i)}{k^2(\Delta t)} - \frac{\left(ik_i\hat{\tilde{\rho}}\right)g_i F_r^{-2}}{k^2}.$$

Here

$$T_2 = F.T.\left\{\nabla \cdot m^{n+1}(\vec{x})\right\}.$$

Next $\nabla \cdot m^{n+1}(\vec{x})$ is found from the transform of (3.12) and (3.15). $\hat{\tilde{P}}$ is then substituted into the transform of eq. (3.7) to obtain the momentum at $n+1$:

$$\hat{m}_i^{n+1}(k_i) = \hat{m}_i^*(k_i) - \frac{ik_i}{k^2}\left\{T_2 - ik_i\hat{m}_i^*(k_i) - \Delta t\left(ik_i\hat{\tilde{\rho}}\right)g_i F_r^{-2}\right\} + \Delta t\hat{\tilde{\rho}}g_i F_r^{-2}. \quad (3.26)$$

The numerical solution procedure consists of solving for the density $\hat{\rho}^{n+1}(k_i)$ using the discretized diffusion equation, eq. (3.24). Then the momentum equation is solved, neglecting pressure effects using eq. (3.25). Knowing $\hat{\rho}^{n+1}(k_i)$ and the two previous step values of $\hat{\rho}(k_i)$, T_2 can be found using the transform of eqs. (3.12) and (3.15). Knowing this and the half-step momentum, the momentum at n+1 is found using eq. (3.26). The mean momentum is time advanced using (3.23).

For the computation of isotropic decay of turbulence without acceleration, g_i is zero in eq. (3.26) and the mean momentum time-advancement using eq. (3.23) is not needed.

3.3 Initial Conditions

There are two types of flows of interest in this study: the mixing of two miscible fluids due to the isotropic decay of turbulence and the mixing due to a constant acceleration of a variable-density fluid. The initial velocity and density fields used in this study are described in the chapters 4 and 6. Appendices C and D describe the initialization procedures for the velocity and density fields respectively.

3.3.1 Initialization of the Velocity Field

In the study of isotropic turbulence using direct numerical simulations, since the mean velocity $\overline{u}_i$ is constant in time, it is common to use a Galilean transformation to choose a coordinate system such that it is zero, i.e., $\overline{u}_i = 0$. In the work presented in this thesis, the initial fluctuating velocity field is initialized using two methods depending on the problem: (a) the method of Orszag [64] suitably modified to account for the divergent aspect of the velocity [eq. (2.11)], and (b) the method of Mell [60]. These

methods are described in Appendix C. The choice of method depends on the problem under study and is discussed in conjunction with the results of the problem. For the isotropic decay case, the mean momentum, $\overline{\rho' u_i'}$ is zero initially and remains zero throughout the simulation.

In the study of a variable-density fluid subjected to a constant acceleration, a reference frame is chosen such that the mean velocity, $\overline{u}_i$ is zero. In this case the initial velocity is nearly zero (as the initial density fluctuations are increased, so to does the velocity that accounts for the divergent aspect of the velocity field). Here, the correlation between the initial velocity field and the initial density field is initially nearly zero. This correlation will quickly grow as the high density field is set into motion in the direction of the acceleration and the low-density fluid is set into motion in the opposite direction. Thus there is a strong correlation between density and velocity fields in the accelerated case.

3.3.2 Initialization of the Density Field

In this study, there are two type of initial density fields utilized. The first (and most frequently used in this study) is the bimodal density field initialized using the method of Eswaran and Pope [30]. This method creates an initial density field that conforms approximately to a double-delta function probability density function (pdf), where the initial fluid consists of regions of either high or low density fluid typified by an integral length scale of $l_\rho = 0.53$ (see Section 4.3) which is roughly half the velocity integral scale (see Section 4.2). In order for the field to be well resolved they are smoothed to avoid sharp gradients. Following Eswaran and Pope, the initial scalar field is initialized such that the two scalar values of the initial double-delta function pdf are $+1$ and -1. A linear transformation from this scalar field to a density field, ρ, is made such that the two density values of the initial double-delta function correspond to positive values of the density with a nonzero mean. The details of this initialization scheme can be found in Eswaran and Pope [30] and are presented in Appendix D. This density field represents the early stages in the mixing of two fluids of different densities.

The second type of initialization used is an initialization which creates a random density field that has Gaussian statistics. The details of this initialization scheme are also presented in Appendix D. In this case the most probable value is the mean

density. This initial density field represents the late stages of the mixing of two fluid of different densities.

3.4 Implementation of Numerical Scheme

Computer programs to solve the system of equations described above have been developed for both the Cray (Y-MP and C90) and the Connection Machine (CM-2, CM-200). These codes have been tested, developed and used at the Los Alamos National Laboratory's Cray Y-MP, Cray M-98 and CM-200 as well as on the Pittsburgh Supercomputer Center's Cray C90 and CM-2 (no longer active). Comparative testing of this algorithm amongst the different machines and CPU time availability has led us to exclusively use the Cray computers. A great deal of effort was put into the CM version of our numerical scheme, however; thus it will be described briefly.

To solve the system of equations a pseudo-spectral technique is employed, whereby spatial derivatives are computed in Fourier space and nonlinear products in physical space. The transformation of the real physical data field into Fourier amplitudes is accomplished with Fast Fourier Transforms (FFT). The numerical solution involves numerous transformations per time-step. These transformations are the most costly part of the simulation, comprising roughly 80 percent of the total CPU time of the simulation. Thus it is essential that the FFT algorithm used has been optimized for the specific machine on which the computations are being made.

The three-dimensional nature of the physical problem we are studying coupled with the parallel nature of the spectral scheme makes the massively parallel architecture of the Connection Machines (CM-2, CM-200, or CM-5) highly attractive for these types of problems. Currently, state-of-the-art simulations of constant-density turbulent flow using spectral techniques are computed on Connection Machines [79]. A version of our code has been developed using the CM Scientific Software Library (CMSSL) FFT complex-to-complex algorithm. An efficient FFT driver has been written [20] and optimized to ensure that all of the cyclic operations are executed in parallel. The code was written in CM FORTRAN, a derivative of FORTRAN 90.

A version of the code written in FORTRAN 77 is employed on the Cray Y-MP, M-98 and the C90. The code utilizes the Cray scientific library FFT package. This is a highly optimized FFT algorithm written in assembly language specifically for the Cray computers. Comparisons between the Cray results and the CM results revealed

disagreements which have not been resolved. The results of a test problem using the algorithm on the CM-200 agreed with those of the Cray Y-MP for the identical test problem. However, results for the same test problem using the CM-2 did not agree with the results of the CM-200. The initial conditions of the test problem and the numerical code were identical in the CM comparisons, yet the numerical solution on the CM-2 became unstable while the solutions on the CM-200 did not.

This discrepancy of CM-2 and CM-200 results, coupled with the vanishing of our CM-2 resources directed us to dedicate our efforts towards the well established Cray architecture. A numerical code was developed in FORTRAN 77 to solve the equations of motion. This code requires approximately 120 Mwords of memory to execute a 128^3 simulation, and a typical simulation takes 10 to 30 hours depending on whether the problem being solved is an isotropic decay or a constant acceleration problem. The main cycle routines (excluding the FFT package) run at about 300 Mflops, while the FFT package runs at about 306 Mflops on a Cray C90. 80 percent of the CPU time is spent in the FFT package; thus it is crucial to have an optimized FFT package for this type of problem.

3.4.1 Computational Mesh

Using pseudo-spectral techniques to solve the equations of motion limits the type of boundary conditions considered. As mentioned in section (3.2), the use of Fourier series in the numerical scheme implies that the computational domain is periodic.

The numerical scheme takes advantage of the complex-conjugate symmetry of the data field in spectral space. The arrays in the computational code are defined such that the Fourier amplitudes, which are complex, are loaded as follows: in the k_x (corresponding to the physical space x direction) the complex data is loaded from $k_x = -(k_{max} - 1)$ to $k_x = 0$, while in the k_y and k_z direction the data is loaded from $-(k_{max} - 1) \leq k \leq k_{max}$. In physical space this data corresponds to a three-dimensional box that has periodic boundaries. The smallest nonzero wavenumber in the simulation is 1 and the wavenumber spacing, Δk, is also 1. Therefore the nondimensional box length is $L = 2\pi/\Delta k = 2\pi$.

For direct numerical simulations of isotropic constant-density turbulence, the limitations of the initial Taylor microscale Reynolds number due to mesh size are well known. Mell [59] has given the relationship between the mesh resolution requirements

and the initial Taylor microscale Reynolds number in order that the passive scalars are well-resolved. For variable-density simulations of turbulence the relationship between the mesh resolution requirements and the initial Taylor scale Reynolds number is not well established. It is expected, however, that the Taylor scale Reynolds number that can be achieved in simulations that are well resolved should be similar to that reported in the literature for constant-density and passive scalar simulations.

Chapter 4

ISOTROPIC DECAY OF STATISTICALLY INDEPENDENT INITIAL TURBULENT VELOCITY AND DENSITY FIELDS

4.1 Introduction

In our study of isotropic, decaying, variable-density turbulence the density and velocity fields approximately satisfy the conditions of statistical isotropy; the various fluctuating quantities can be considered as random functions that are statistically invariant under translations, rotations and reflections. Therefore, a property of this isotropic turbulence is that there is no net momentum, i.e., the correlations between a scalar and velocity field are zero [52], or $\overline{\rho' u_i'}$ is zero.

There are many ways to characterize the initial conditions of the flow fields used in the study of isotropic, decaying turbulence. One characterization is that the initial velocity field is statistically independent on the initial density field. This characterization implies that we impose on a velocity field a density field that is *independent* of this velocity field. This characterization is one that is analogous to that typically used in the numerical study of passive scalars. This chapter examines the behavior of isotropic, decaying, variable-density turbulence using initial velocity and density fields that are statistically independent.

An alternative characterization is that the initial velocity field is statistically *dependent* on the initial density field. This characterization is studied in the following chapter. There are two types of statistical dependence studied. One type is where the high velocities are associated with the positive density fluctuations and the other is where the high velocities are associated with the negative density fluctuations.

There has been considerable work reported on the isotropic mixing of passive scalars (scalars that have no influence on the velocity field) [30, 52, 53, 60]. To date there has been no work reported on the isotropic mixing of scalars that are not passive. The numerical scheme presented here allows for scalars (the density) to effect the time development of the velocity field and thus permits the study of the

effect of "active" scalars on the velocity field. Of course, in the limit as the density fluctuations go to zero the behavior should be like that of a passive scalar.

Below are described the initialization of the statistically *independent* velocity and density fields used in this numerical study of isotropically decaying variable-density turbulence and the results of simulations using these initial fields.

4.2 Initialization of the Velocity Field

The initial velocity field used for this study of isotropically decaying variable-density turbulence is the velocity field "3u" used by Mell [60] in his study of passive scalars. This velocity field is in "full spectrum decay" at an initial Taylor-scale Reynolds number of 55. [The term "full spectrum decay" means that the velocity spectrum is decaying at all wavenumbers in an approximately self-similar fashion.] This initial velocity field is statistically independent of the initial density field and is a "Navier-Stokes" velocity field. This means that the initial velocity field does not have random Fourier amplitudes and phasing. The procedure for establishing this velocity field is as follows. First, a random velocity field is computed using the method of Orszag and Patterson [65], which gives random Fourier amplitudes and phasing. Then this random field is evolved using a numerical Navier-Stokes solver until the initial random velocity field has reached full spectrum decay. The resulting velocity field is rescaled to give a desired initial Taylor-scale Reynolds number and then used as the initial velocity field in this study. The main advantage of this procedure is that it avoids the early time adjustment period of the spectral evolution that occurs using only the method of Orszag and Patterson. This velocity field initialization method was developed by Mell [60] and is described in more detail in Appendix C. The use of velocity field "3u" in this study will thus also provide a comparison with the numerical results of Mell. This comparison is made to validate the numerical method used in our study of variable-density turbulence.

Table 4.1 lists the simulations and the initial velocity statistics for the variable-density isotropic decay simulations reported here. N^3 is the number of computational grid points, Re_λ is the Reynolds number based on the Taylor microscale, ν is the kinematic viscosity, l, λ and η_k are the integral, Taylor and Kolmogorov velocity length scales, respectively. From Tennekes and Lumley [87] the integral velocity scale

is

$$l \equiv (3\pi/4)\ \frac{\int_o^\infty E(k,t)/k\ dk}{\int_o^\infty E(k,t)\ dk},$$

the Taylor microscale is

$$\lambda = \mathcal{U}(15\nu/\epsilon)^{1/2},$$

where

$$\mathcal{U} = \left(\frac{\overline{u_i' u_i'}}{3}\right)^{1/2}$$

is the root-mean-square velocity. The Kolmogorov velocity length scale is

$$\eta_k = (\nu^3/\epsilon)^{1/4},$$

and a characteristic strain rate of the largest eddies is

$$\mathcal{S} = \mathcal{U}/l.$$

The initial energy per unit mass is $\frac{1}{2}\overline{u_i' u_i'}$ and the initial total energy (Favre energy) is $\frac{1}{2}\overline{\rho u_i' u_i'}$.

Runs 55 and 55a use the initial velocity field "3u" created by Mell for his study and which is statistically independent of the initial density field.

Runs Iso3, Iso4, Iso5, Iso6, Iso7 and Iso8 have initial velocity fields that are statistically dependent on the initial density field. The initialization processes and results for these cases are discussed in Chapter 5.

4.3 Initialization of the Density Field

The density field is initialized using the method of Eswaran and Pope [30]. This method creates an initial density field that conforms approximately to a double-delta function probability density function (pdf), where the density values of the initial field corresponds closely to either the high density or low density value. The pdf is not an exact double-delta function because the density field is smoothed to avoid sharp

Table 4.1: List of initial velocity statistics for isotropic decay simulations

Run No.	N^3	Re_λ	ν	l	λ	η_k	$\mathcal{S}$	$\frac{1}{2}\overline{u_i'u_i'}$	$\frac{1}{2}\overline{\rho u_i'u_i'}$
55	128^3	55.0	.005	1.12	.30	.0207	0.81	1.245	1.245
55a	128^3	55.0	.005	1.12	.30	.0207	0.81	1.245	1.245
Iso3	128^3	54.9	.005	1.07	.29	.0201	0.87	1.245	1.32
Iso4	128^3	58.2	.005	1.13	.29	.0195	0.87	1.480	1.32
Iso5	128^3	52.4	.005	1.02	.29	.0204	0.87	1.205	1.32
Iso6	128^3	58.2	.005	1.13	.29	.0195	0.87	1.480	1.32
Iso7	128^3	54.9	.005	1.07	.29	.0201	0.87	1.245	1.32
Iso8	128^3	52.4	.005	1.02	.29	.0204	0.87	1.205	1.32

gradients so that it is well resolved in the simulation. Following Eswaran and Pope, the initial scalar field is created such that the two scalar values of the initial double-delta function pdf are $+1$ and -1. A linear transformation from this scalar field to a density field is made such that the two density values of the initial double-delta function correspond to desired values.

The details of this initialization scheme can be found in Eswaran and Pope [30] and are presented in Appendix D. Briefly, the Fourier amplitudes of the scalar field are assigned random values corresponding to an initial spectral shape. This random field represented by Fourier amplitudes is inverse transformed to physical space and the positive values in this random field are given the value of ρ_{max} and the negative values are given a value of ρ_{min}. This adjusted field is then transformed into spectral space and the Fourier amplitudes are multiplied by a filter function that "smoothes" the physical-space density field, thus producing a physical density field that is well-resolved in the simulation.

This initialization procedure creates a fluid with regions of high and low density typified by an integral length scale

$$l_\rho = (\pi/2) \left[\int_o^\infty E_\rho(k,t)/k \; dk\right] / \int_o^\infty E_\rho(k,t) \; dk.$$

Here, E_ρ is the spectra of the variance of the isotropic density field. For all the simulations presented in this study $l_\rho = 0.53$, which is roughly half the initial velocity

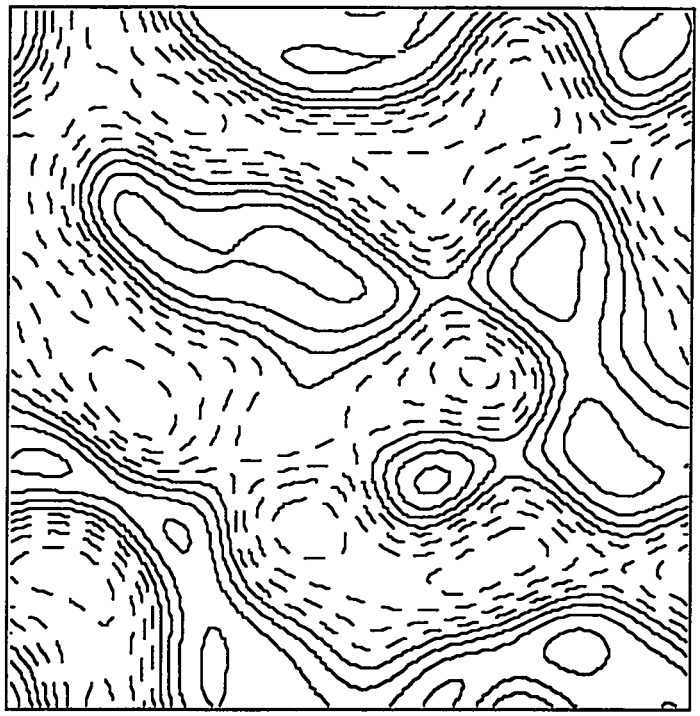

Figure 4.1: Typical 2-D slice of the 3-D initial density field

integral scale. Figure 4.1 shows a typical two-dimensional slice of the three dimensional density field. The solid contours represent density values that are larger than the mean density, while the dashed contours represent values smaller than the mean. Visible are regions of high density, ρ_{max}, surrounded by regions of low density, ρ_{min}, which can represent the two fluids. In between the high and low density regions are smooth gradients of the density field which represents a "premixed" interface between the two fluids. Figure 4.2 shows the corresponding initial probability density function of the 3-D density field. This shows high probability for the density to be either ρ_{max} or ρ_{min}, and also the "U-shaped" lower probability region in between the two peaks representing the premixed interface.

Table 4.2 lists the initial density field statistics for the variable-density isotropic decay simulations reported in this study. The cases with the density ratio of 1.02 are nearly constant-density cases performed to provide comparisons with the variable-density cases, which have a density ratio of either 2.33 or 4.0. The quantity $B(t) = \overline{\rho'\rho'}/\overline{\rho}^2$ is the mean-square-fluctuating density (i.e., the variance) divided by the mean

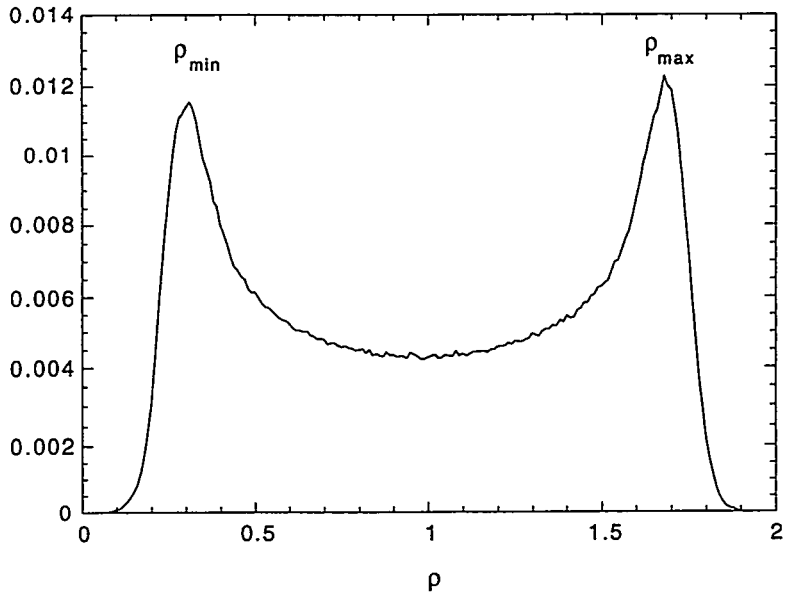

Figure 4.2: The initial PDF of the 3-D density field

density squared, and the quantity

$$b(t) = -\overline{\rho' \left(\frac{1}{\rho}\right)'} \tag{4.1}$$

is the negative of the correlation between the fluctuating density and fluctuating specific volume. Both of these quantities are a nondimensional measure of the density variations in the flow. In the limit as the density fluctuations tend to zero $b(t) \approx B(t)$.

4.4 Isotropically decaying turbulence with small *density variations*

Consider first the case of a freely-decaying, isotropic, variable-density flow. The initial statistically independent velocity field is field "3u" described in the previous sections. The bimodal density field is setup using the scheme of Eswaran and Pope. The pdf of the initial density field is symmetric about its mean ($\bar{\rho} = 1.0$). A result of the condition of isotropy is that any vector correlation between a scalar field and the velocity field will be zero [38, 52]. In these isotropic problems it is anticipated that the effect of the density field (the active scalar) on the evolution of the total energy will be small. It will be shown in Section 4.4.1 that the total turbulent kinetic energy density is made up of three terms: $\overline{\rho}\ \overline{u_i' u_i'}$, $\overline{\rho' u_i' u_i'}$ and $\overline{\rho} a_i a_i$ where $a_i = -\overline{\rho' u_i'}/\overline{\rho}$. In

Table 4.2: List of initial density field statistics for isotropic decay simulations

Run No.	ρ_{max}	ρ_{min}	ρ_{max}/ρ_{min}	$\overline{\rho'\rho'}/\overline{\rho}^2$	$-\overline{\rho'\,(1/\rho)'}$
55a	1.01	0.99	1.02	7.53e-5	7.53e-5
55	1.60	0.40	4.00	0.4530	.498
Iso3	1.01	0.99	1.02	7.55e-5	7.55e-5
Iso4	1.40	0.60	2.33	0.1209	.149
Iso5	1.40	0.60	2.33	0.1209	.149
Iso6	1.01	0.99	1.02	7.55e-5	7.55e-5
Iso7	1.01	0.99	1.02	7.55e-5	7.55e-5
Iso8	1.01	0.99	1.02	7.55e-5	7.55e-5

isotropic turbulence, $\overline{\rho' u_i'}$ is zero for all times. It will also be shown that because of the lack of statistical dependence of the initial velocity and density fields $\overline{\rho' u_i' u_i'} \approx 0$ for all times. So the velocity self-correlation is the dominant term in the energy evolution. Also, because the Taylor-scale Reynolds number and $|\rho'|/\overline{\rho}$ are low, the statistical dependence between the velocity and density fields will not develop in a manner such that $\overline{\rho' u_i' u_i'}$ will effect the energy decay behavior.

The first velocity field (Mell's field "3u") used in this study of isotropic decay of variable-density turbulence has an initial Taylor-scale Reynolds number of 55. This is fairly low compared to laboratory flows and implies that almost all the scales of motion are significantly influenced by viscous forces. This initial velocity field is statistically isotropic and undergoing full spectrum decay. The first simulation using this velocity field is Run 55a. The initial density field has a density ratio (ρ_{max}/ρ_{min}) of 1.02, nearly constant density ($\rho_{max} = 1.01$ and $\rho_{min} = 0.99$). The initial energy spectrum for this simulation (and Run 55) is shown in Fig. 4.3. Here, $< () >$ refers to the spectrum of (). An explanation of how the energy spectra is computed is given in Appendix E. The initial velocity integral scale is 1.19. The domain size is $L = 2\pi/\Delta k = 2\pi$ ($\Delta k = 1$) so that $l/L \approx 1/5$. This suggests that there are initially approximately 5 large eddies in one direction and thus 5^3 large eddies in the computational box.

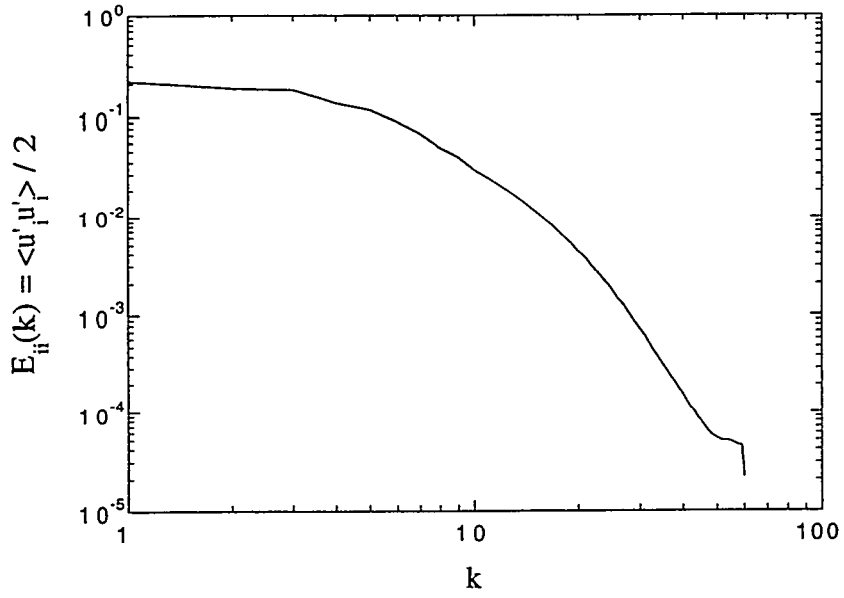

Figure 4.3: The initial velocity spectra for Runs 55 and 55a

There are two reasons for using this initial velocity field with an initial density field that is nearly constant. The first is to provide a direct comparison with the numerical results of Mell [60]. In the limit as the initial density variations goes to zero the numerical scheme used in this study should reproduce constant-density turbulence results. An agreement with Mell's results will give us confidence that, within the limit as the density fluctuations go to zero, the numerical scheme is reproducing known results. Second, this simulation will provide results for comparison with a simulation with large density variations (Run 55, discussed below).

This section describes the results of the numerical simulation, Run 55a, with the initial conditions described above. A direct comparisons will be made with the results of Mell. Also, results will be presented that demonstrate consistency (i.e., in quantitative agreement) with constant-density results and expectations.

4.4.1 Decay of turbulent kinetic energy

The total turbulent kinetic energy density, which is half of the trace of the Favre-averaged Reynolds stress tensor for variable-density flow, eq. (A.6), is given as

$$\frac{1}{2}R_{ii}(t) = \frac{1}{2}\overline{\rho u_i'' u_i''} = \frac{1}{2}\overline{\rho}\ \overline{u_i' u_i'} + \frac{1}{2}\overline{\rho' u_i' u_i'} - \frac{1}{2}\overline{\rho} a_i a_i \tag{4.2}$$

where

$$a_i = -\frac{\overline{\rho u_i}}{\overline{\rho}} = -\frac{\overline{\rho' u_i'}}{\overline{\rho}} \tag{4.3}$$

is the turbulent mass flux divided by the mean density. Here the $\overline{()}$ represents a volume average over the entire computational domain. For this case a_n should be identically zero since there is no scalar-velocity correlation in isotropic decay. Figure 4.4 shows the evolution of R_{ii} as a function of t for this nearly constant-density case (Run 55a). The time, t, used in plotting the DNS data is the actual time nondimensionalized by the initial large eddy turnover time, l_o/u_o. The $\overline{\rho} a_i a_i$ term is zero due to isotropy. The triple correlation term, $\overline{\rho' u_i' u_i'}$, is initially zero since the initial velocity and density fields are statistically independent, and it remains small since the density fluctuations are very small. Thus the total turbulent kinetic energy density is approximately the mean density multiplied by the mean squared velocity, i.e.,

$$\frac{1}{2} R_{ii}(t) = \frac{1}{2} \overline{\rho}\, \overline{u_i' u_i'}.$$

This figure also shows the result of Mell's simulation for the term $\overline{u_i' u_i'}$ (note that Mell's simulation was carried out to a time of 5). This can be directly compared to the $\overline{\rho}\, \overline{u_i' u_i'}$ term of Run 55a since in this case (as with all the cases in this study) $\overline{\rho} = 1.0$. This figure shows that the two numerical schemes give the same mean-velocity-squared decay for the same initial velocity field.

To gain insight into the flow energetics, we can write the decay of the total turbulent kinetic energy, eq. (B.14), for an isotropic, decaying turbulence field (without body forces), employing homogeneity, as

$$\frac{\partial}{\partial t}\left\{\frac{1}{2}\overline{\rho u_i' u_i'}\right\} = \overline{p \frac{\partial u_i'}{\partial x_i}} + \overline{u_i' \frac{\partial \tau_{ij}'}{\partial x_j}}. \tag{4.4}$$

For a complete derivation of this equation see Appendix B. The first term on the right side of eq. (4.4) is the pressure-work term and represents a production/destruction of energy due to dilatation effects. For the immiscible problem and constant-density flows this term is zero. The second term on the right side is the viscous dissipation rate term and represents the rate of decrease in kinetic energy due to viscous dissipation.

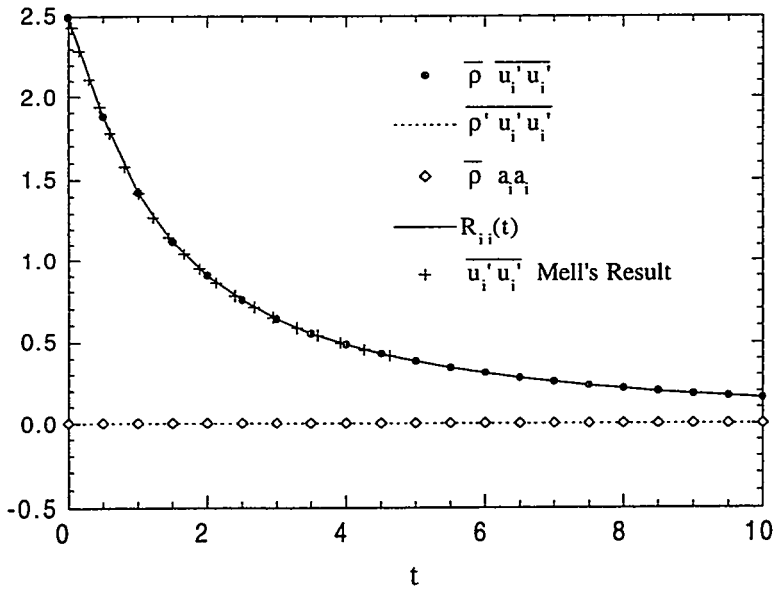

Figure 4.4: Evolution of R_{ii} for Run 55a

Figure 4.5 shows the evolution of each term of eq. (4.4). This clearly demonstrates that kinetic energy decay follows the viscous dissipation rate term. Evolution equations for each term of the total turbulent kinetic energy density, given by eq. (4.2), are derived in Appendix B. Since the behavior of $\overline{\rho}\ \overline{u_i' u_i'}$ is the same as the behavior as $R_{ii}(t)$, its decay is solely due to viscous dissipation.

As previously mentioned, the decay of isotropic turbulence has been extensively studied using laboratory experiments and direct numerical simulations. In all these studies a common characteristic is a power-law decay of the mean-square of the fluctuating velocities,

$$K_{ii}(t) = \frac{\overline{u_i' u_i'}}{2} = K_o \left[1 + \frac{t}{t_o}\right]^{-\gamma}, \tag{4.5}$$

where K_o, t_o and γ are constants and t_o is called the virtual origin. K_o is the energy at time $t = 0$ and γ is the power-law exponent. (Note that $K_{ii} = R_{ii}/2\overline{\rho}$). The power law exponent has been determined from many experimental and numerical studies [24]. These studies have been inconclusive in this regard. The numerical studies are limited by the turbulence Reynolds number that can be obtained. Thus the flows studied are at least moderately viscous dominated, and the study of the dynamics of flows that are primarily due to nonlinear interactions cannot be made using direct

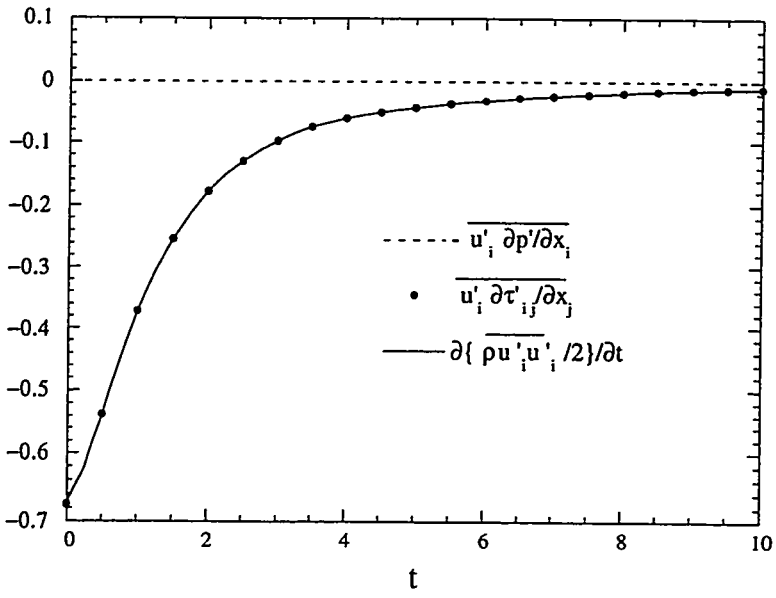

Figure 4.5: Terms in the evolution equation [eq. (4.4)] for the total kinetic energy density for Run 55a

numerical simulations. In the simulations here, the power law decay of the turbulence is found to be consistent with previous laboratory experiments.

A characteristic time scale for the decay of isotropic turbulence is

$$\tau_K = -\frac{K_{ii}(t)}{\{\partial K_{ii}(t)/\partial t\}} = \frac{1}{\gamma}(t + t_o). \tag{4.6}$$

Following Mell [60], substituting eq. (4.5) into (4.6) and solving for the power-law exponent gives

$$\gamma(t) = -(t + t_o)\frac{\{\partial K_{ii}(t)/\partial t\}}{K_{ii}(t)}. \tag{4.7}$$

In order to use this equation to determine the $\gamma(t)$, the virtual origin, t_o, must be found using curve-fitting. The virtual origin was found to be $t_o = 1.82$. In Mell's results, the virtual origin was found to be 2.074. This difference is probably due to the fact that the DNS simulations in this study were carried out twice as far in time as that of Mell's. If we curve-fit over the time range used by Mell the virtual origin is found to agree with that found by Mell. Thus the power-law exponent can be

evaluated from

$$\overline{\gamma(t)} = -(t + 1.82)\frac{\{\partial K_{ii}(t)/\partial t\}}{K_{ii}(t)}. \tag{4.8}$$

Here, $\overline{\gamma(t)}$ is referred to as the "average" value (not volumetric average as previously defined) of the power-law exponent computed from the DNS. The term "average" (adopted by Mell) is used because of the curve fitting involved in obtaining t_o.

Another determination of the power-law exponent can be made by taking the time derivative of eq. (4.6) to get

$$\gamma(t) = -\left\{\frac{d}{dt}\left\{\frac{K_{ii}(t)}{\partial K_{ii}(t)/\partial t}\right\}\right\}^{-1}. \tag{4.9}$$

Here, $\gamma(t)$ is referred to as the "instantaneous" value of γ. This method has the advantage of not having to compute a virtual origin.

Figure 4.6 shows τ_K (+ curves), $\overline{\gamma(t)}$ (• curve) and $\gamma(t)$ (× curve) as functions of time for this nearly constant-density case. The solid lines are the results of Mell and this figure again shows good agreement between Mell's results and this nearly constant-density case. The value of $\gamma(t)$ varies quite a bit at early times but at late times this "instantaneous" power-law exponent is very nearly the same value as the "average" power-law exponent $\overline{\gamma(t)}$. It is also seen that $\overline{\gamma(t)}$ grows slightly at early times but then remains nearly constant at a value of about 1.65 at late times.

This value is larger than the bulk of the experimental data from grid experiments. In the initial period of decay, γ is found to range from 1.2 to 1.35 [38]. However, Mohamed and LaRue [62], surveying experimental data, argue that this variation in γ is due to the selection of the virtual origin, t_o. Their analysis shows that if t_o is selected in a consistent manner then $\gamma = 1.3$. For a more detailed discussion of this see, for example, Clark [22]. For a discussion on the relationship between the power-law exponent and the low wavenumber exponent see Section 4.4.5.

4.4.2 Velocity-derivative skewness

The velocity-derivative skewness is defined as (see, e.g., Tavoularis et al. [86])

$$S_i(t) = -\frac{\overline{\left(\frac{\partial u_i}{\partial x_i}\right)^3}}{\overline{\left(\frac{\partial u_i}{\partial x_i}\right)^2}^{\frac{3}{2}}}\ , \text{ no summation on } i \tag{4.10}$$

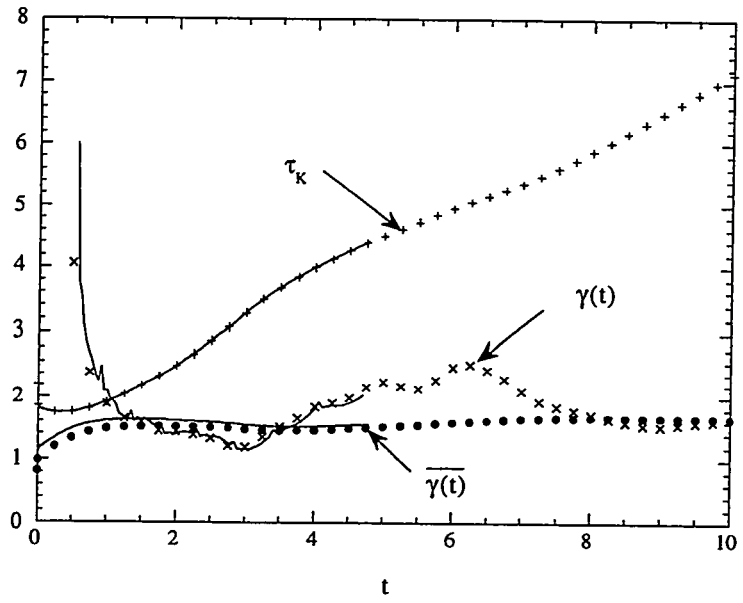

Figure 4.6: Time scale and power law exponents for Run 55a and comparison to Mell's results (solid lines)

where u_i is any component of the velocity ($i = 1, 2$ or 3). The velocity-derivative skewness would be zero if the velocity derivative were Gaussian. The velocity-derivative skewness represents the average rate of production of the mean-square vorticity (enstrophy) by vortex stretching [86]. If the velocity-derivative skewness is positive there is an increase in enstrophy due to vortex stretching [52]. Figure 4.7 shows the velocity-derivative skewness as a function of time for all three components of the velocity. For this case, $S_i(t) \approx 0.5$, which agrees with Orszag and Patterson [66], and falls within the range of nearly-isotropic grid experiments, $S_i(t) \approx 0.32 - 0.6$ reported in Tavoularis et al. [86].

4.4.3 Length scales and Taylor Reynolds number

There are three characteristic length scales that are often used in turbulence. The largest is the velocity integral scale, l, and is a measure of the size of the most energetic eddies in the flow. The Taylor microscale, λ, is the second characteristic length and is smaller than the integral scale, but does not typify the smallest scales in turbulence. The smallest scales are typified by the Kolmogorov scale, η_k, which is a measure of the smallest eddy that can be expected in a turbulent flow. It is at this

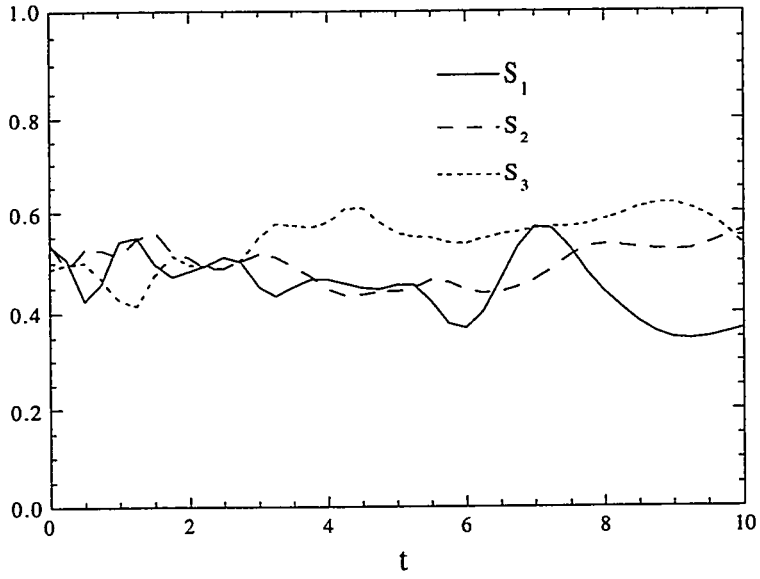

Figure 4.7: Velocity-derivative skewness for the three components of velocity for Run 55a

scale that viscous and convective forces are in balance, so that the local Reynolds number is unity. Figure 4.8 show these length scales as functions of time for this nearly constant-density case. Comparisons of the integral length scale, the Taylor length scale and the Kolmogorov length scale are made with the results of Mell (dots, diamonds and triangles) and are in good agreement. This figure also shows that for $t > 0.5$ all the length scales are growing in time.

The Taylor Reynolds number, R_λ, is a Reynolds number based on the Taylor microscale. Figure 4.9 shows the evolution of this quantity as a function of time for the nearly constant-density case (Run 55a) and also shows the results of Mell. Again, there is good agreement between the two simulations. Mell [60] compared the behavior of the Taylor Reynolds number found in his simulations with grid turbulence experiments of Comte-Bellot and Corrsin [25] and Sreenivasan et al. [82], and found that the results of his numerical simulations are in qualitative agreement with the grid turbulence experiments.

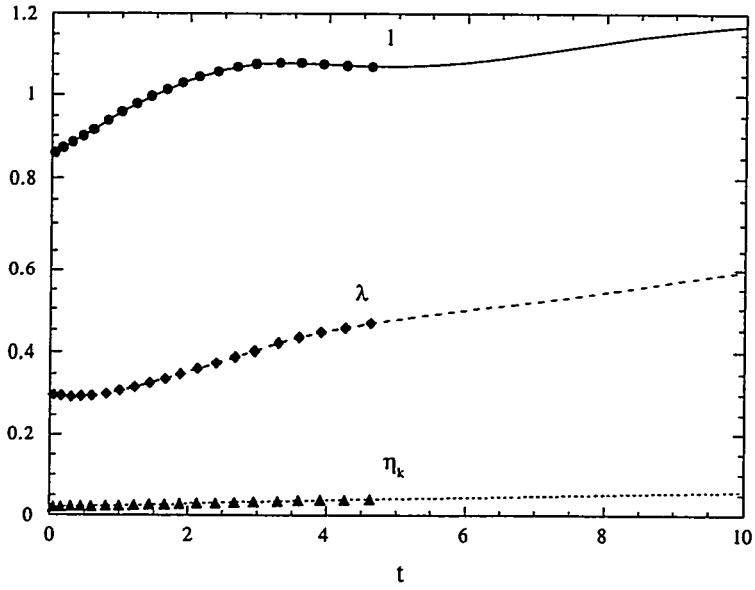

Figure 4.8: Length as a function of time comparison with Mell's result and Run 55a

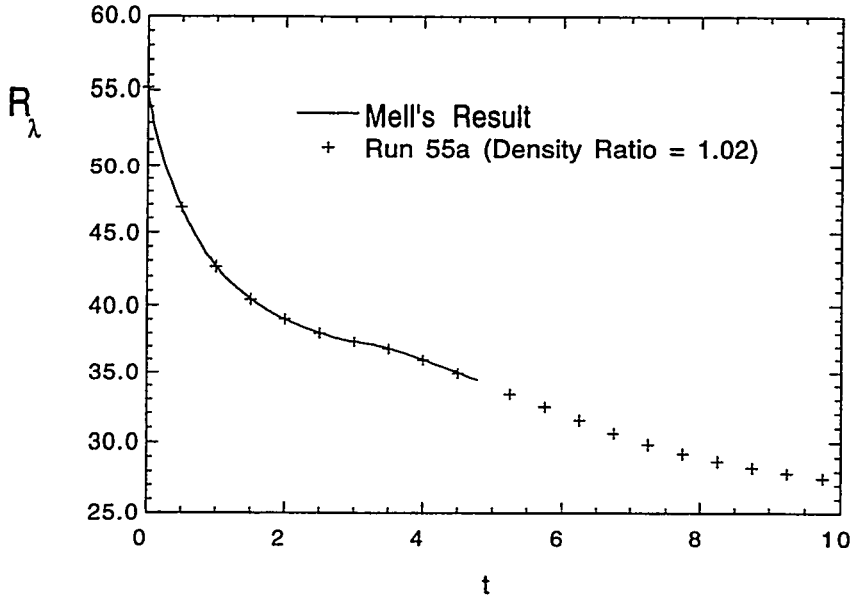

Figure 4.9: Evolution of R_λ comparison with Mell's result and Run 55a

4.4.4 Energy spectrum

The spectral data are obtained in Fourier space by averaging the dependent variables of interest over spherical shells creating a spectrum over the entire wavenumber range. The usefulness of this data is that it gives an understanding of the length scales of the computed quantity. The energy spectrum is a decomposition of the energy into fluctuations at different wavelengths, and the value at a given wavelength is the energy associated with that wavelength.

Previous researchers have studied the energy spectrum in detail using laboratory experiments, numerical simulations and theory. Analyzing the spectrum from the DNS is a good way to determine (a) if the simulation is well resolved and (b) how well the simulation represents "real world" turbulence by qualitative comparison with experimental data. Appendix E describes the binning procedure used to compute the velocity spectra.

As mentioned before, the initial velocity field used in this study is in full spectrum decay. This means that the velocity spectrum is decaying at all values of the wavenumber, k. Figure 4.10 shows the energy spectrum for a sequence of times for this simulation of nearly constant-density flow. As time proceeds the spectrum is decaying at all wavenumbers. The values of the spectrum of energy are largest at the low wavenumbers, so that the large eddies in the flow contain the majority of the energy. Only integer wave vectors are resolved in our numerical simulations. The energy spectrum values decrease nearly 4 decades from the low wavenumbers to the high wavenumbers at the initial time. This decrease gets larger with time, so it is observed that in this simulation the energy is well resolved since high wavenumber contributions are small compared with the low wavenumber contributions.

4.4.5 Wavenumber ranges of the energy spectrum

There are several characteristic ranges in the one-dimensional energy spectrum of turbulence. The first range, called the "energy containing range", is in the low wavenumber part of the spectrum, and contains the large-scale energetic eddies of turbulence. At these scales the turbulence receives energy from the mean-flow reservoir of kinetic energy through coupling to the mean-flow shear, and from the reservoir of potential energy, through differential acceleration from an externally applied pressure gradient. At these scales the effect of viscosity is small if the Reynolds number is high enough.

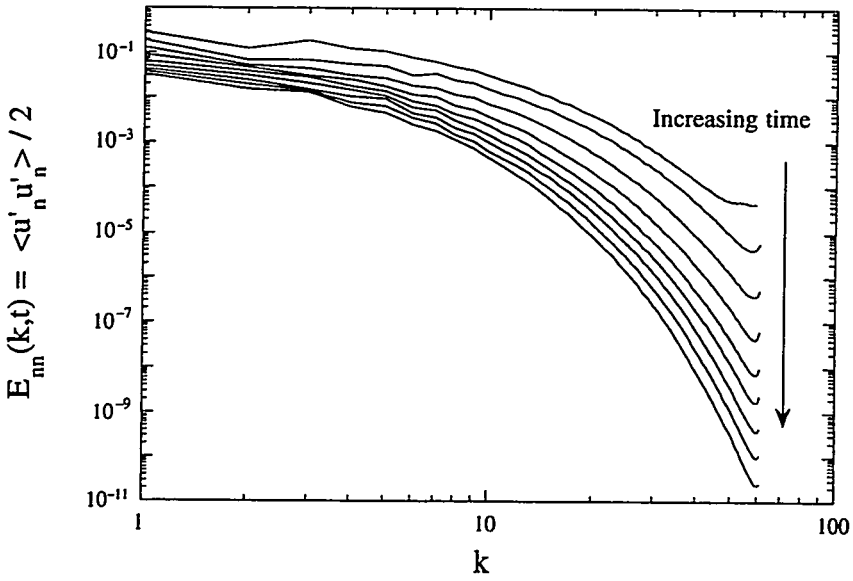

Figure 4.10: Energy spectrum for a sequence of times for Run 55a

In a second range of the energy spectrum (the so-called "inertial range"), energy cascades from the energy-containing range to the third range (the so-called "dissipation range"). Using turbulent length scales we can propose self-similar expressions for the energy spectrum as (see, e.g., Lesieur [52])

$$E(k,t) = KL\ F(kL). \tag{4.11}$$

Here K is typical kinetic energy, L a typical length scale and F is a dimensionless form function that characterizes the spectral shape.

In the energy containing range where the effects of viscosity is small, a typical kinetic energy may the mean-squared velocity, *i.e.*, $K = \mathcal{U}^2$ and a typical length scale may be the integral length scale, i.e., $L = l$. Then the self-similar expression [eq. (4.11)] becomes (see, e.g., Tennekes and Lumley [87])

$$\frac{E(k,t)}{\mathcal{U}^2 l} = F(kl).$$

Using this normalization for scales of motion where viscosity is not important, the energy spectra should collapse onto a self-similar curve.

To emphasize self-similarity of the energy containing range, Fig. 4.11 shows the entire energy spectrum normalized by $\mathcal{U}^2 l$ plotted as a function of kl. The scales of

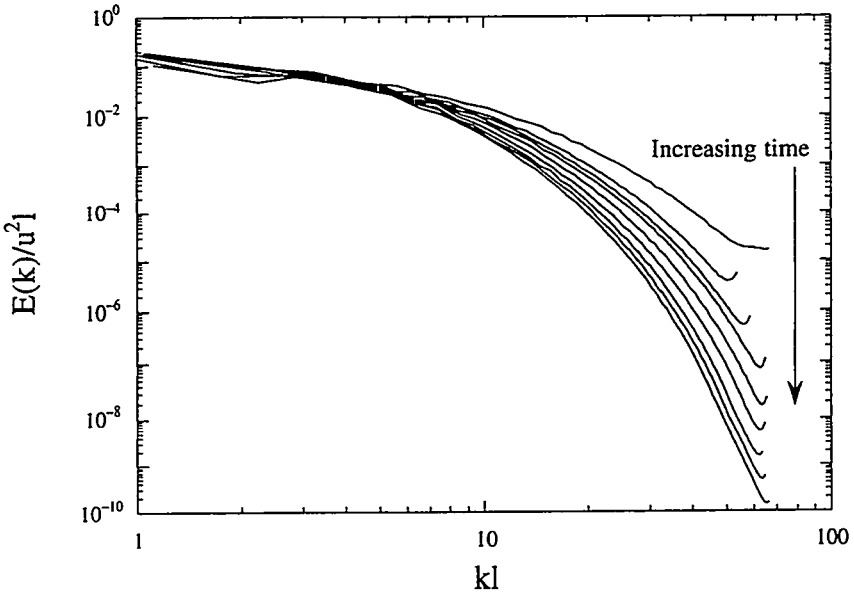

Figure 4.11: Large-scale normalization of the energy spectrum evolution for Run 55a

motion for $kl < 6$ are developing in a self-similar manner.

There has been considerable work with the goal of understanding the low wavenumber power-law exponent, n, and its relationship to the energy decay exponent, γ, (see, e.g., Saffman [77] and Clark and Zemach [24]) i.e.,

$$\lim_{k \to 0} E(k,t) = C(t)k^n,$$

and

$$K(t) = K_o \left[1 + \frac{t}{t_o}\right]^{-\gamma}.$$

The simulations of this study are inconclusive regarding the relationship between n and γ. The reason for this is two-fold. First, the Reynolds number is low and, second, there is inadequate resolution of the low wavenumber portion of the flow. There do exist two limits for the relationship between the low wavenumber power-law exponent, n, and the decay exponent, γ. In the limit of infinite Reynolds number this relationship is [24]

$$\gamma = \frac{2(n+1)}{n+3}, \tag{4.12}$$

and in the limit of the "final period of decay" [6], where the turbulent motions are of an entirely viscous nature,

$$\gamma = \frac{n+1}{2}. \tag{4.13}$$

At late times in the simulation, the energy decay exponent, γ, is 1.65. Assuming the flow is in the final stages of decay then the low wavenumber power-law exponent is found from eq. (4.12) to be 2.3. However, due to insufficient low wavenumber resolution in the simulation, the low wavenumber exponent cannot be determined accurately as it appears in Fig. 4.10 that there is no region where $E(k,t) \approx C(t)k^n$.

It is hypothesized that, in the limit of infinite Reynolds number, there exists a subrange (the "inertial" range) in which the energy spectrum is independent of viscosity and also independent of the energy-containing range. This inertial range is in the "equilibrium" range at scales between the "energy-containing" range and the "dissipation" range. Dimensional analysis applied to this hypothesis gives the $k^{-5/3}$ law of Kolmogorov [38, 50]. Due to an inadequate resolution in this simulation the Reynolds number is low, and therefore, there is an absence of this inertial range.

The third range, the "dissipation" range, which characterizes the smallest scales of motion is also in the "equilibrium" range. Kolmogorov [48] hypothesized the existence of this "dissipation" range where, for a sufficiently high Reynolds number, there exists statistical equilibrium such that the energy flux into this range is balanced by viscous dissipation. Therefore the energy spectra can be uniquely determined by the energy dissipation rate, ϵ, and viscosity, ν. In this range the time scales of motion are so short that the mean flow coupling to turbulence (i.e., energy transfer from the mean flow to turbulence) is not important. Thus, the strain rate of the mean flow is not relevant and energy cascades from large scale to small scale at the energy dissipation rate. At the smallest scales, kinetic energy is finally dissipated into heat by viscosity. At these small scales the kinetic energy is typified by the Kolmogorov velocity squared, *i.e.*, $K = v^2 = (\nu\epsilon)^{1/2}$ and a typical length scale is the Kolmogorov microscale, i.e., $L = \eta_k$. Then the self similar expression [eq. (4.11)] becomes (see, e.g., Tennekes and Lumley [87])

$$\frac{E(k,t)}{v^2\eta_k} = G(k\eta_k).$$

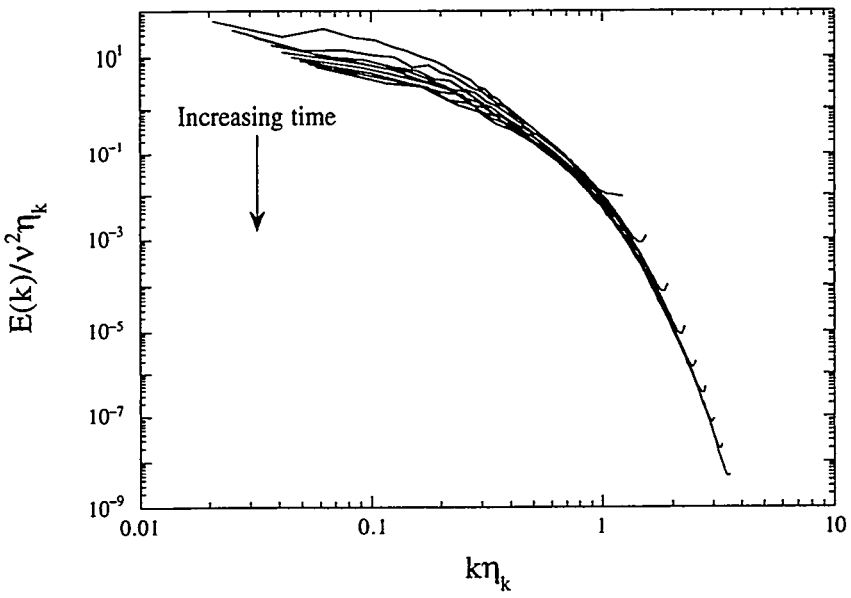

Figure 4.12: Small-scale normalization of the energy spectrum evolution for Run 55a

To address self similarity of the dissipation range, Fig. 4.12 shows the energy spectrum normalized by $v^2\eta_k$ plotted as a function of $k\eta_k$. At high wavenumbers there is self-similar collapse, consistent with the assumption that, at these small scales, the energy transfer is dominated by the dissipation rate and viscosity (note that $v^2\eta_k = \nu^{5/4}\epsilon^{1/4}$).

4.4.6 Discussion

The results presented above for the nearly constant-density simulation, Run 55a, shows quantitative agreement with constant-density results of Mell [60]. Thus, when the initial density fluctuations are small the results of the numerical scheme used in our study approach the constant-density limit. The comparison with Mell's results, and the fact that the results of Mell qualitatively agree with actual grid turbulence experiments gives us confidence in the numerical scheme used in our study.

4.5 Decaying, isotropic turbulence with large *density variations*

Consider now the case where the initial density variations of the flow are somewhat large. The initial density field used in this case has the same spatial distribution as that for the nearly constant-density field used in Run 55a; here the fluctuations

are scaled by a factor of 60 so that $\rho_{max} = 1.6$ and $\rho_{min} = 0.4$ and the density ratio, ρ_{max}/ρ_{min}, is 4. The initial velocity field used here is similar to that used in the nearly constant-density case, the difference being the adjustment to the velocity field due to condition (2.11). The initial Taylor Reynolds number is 55. The initial velocity spectrum is shown in Fig. 4.3. This section describes the isotropic decay of this variable-density flow simulation, Run 55.

4.5.1 Decay of turbulent kinetic energy

For isotropic decay the total turbulent kinetic energy per unit mass is given as (see eq. (A.7) in Appendix A)

$$K(t) = \frac{\overline{\rho u_i' u_i'}}{2\overline{\rho}} = \frac{\overline{u_i' u_i'}}{2} + \frac{\overline{\rho' u_i' u_i'}}{2\overline{\rho}}. \tag{4.14}$$

Initially, this variable-density case has nearly the same total energy as the nearly constant-density case for two reasons. The mean density, $\overline{\rho}$, is the same for both, and, there is a lack of statistical correlation between the initial density and velocity fields, i.e., $\overline{\rho' u_i' u_i'} = 0$. Figure 4.13 shows $K(t)$ as a function of time for the case with the density ratio of 1.02 (nearly constant-density) and the case with the density ratio of 4 (variable-density). From this plot it is seen that the total kinetic energy per unit mass decay is nearly unaffected by the large density variations. Figure 4.14 shows the evolution of R_{ii} as a function of t for this variable-density case. Due to isotropy, the $\overline{\rho} a_i a_i$ term is zero. The triple correlation term, $\overline{\rho' u_i' u_i'}$, is initially zero since the initial velocity and density fields are statistically independent. As the flow develops this triple correlation term becomes slightly negative (discussed in more detail below) then decays to a negligibly small positive value. Therefore the behavior of the total turbulent kinetic energy for this variable-density case is governed by the evolution of $\overline{u_i' u_i'}$, which decays with time in the same manner as the total energy for the constant-density case.

To gain insight on the behavior of various terms of importance to the process of energy decay, we plot the various terms in the total kinetic energy evolution equation [eq. (4.4)] for the present case. Figure 4.15 shows the evolution of each term in eq. (4.4). This shows that the energy decay follows the behavior of the viscous dissipation term, as the pressure-work term has little effect. Since the triple correlation, $\overline{\rho' u_i' u_i'}$,

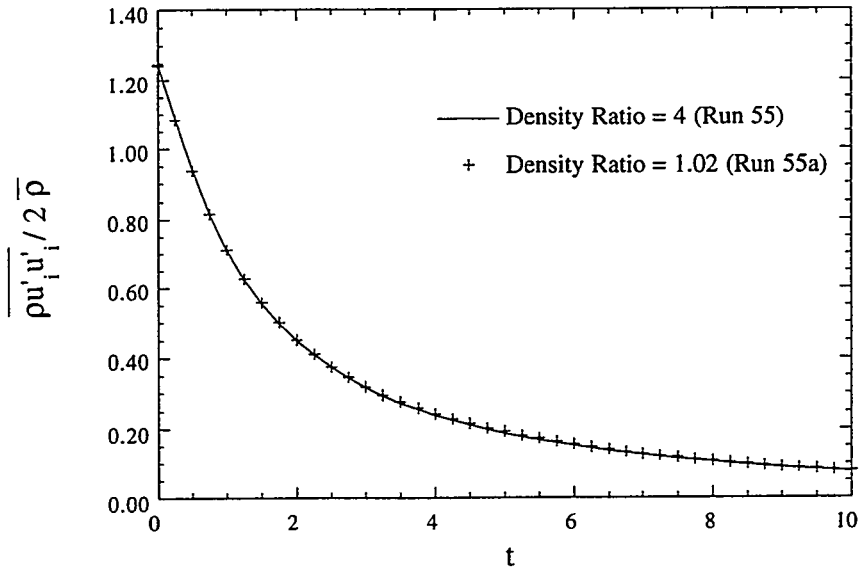

Figure 4.13: Decay comparison of the total kinetic energy per unit mass for the nearly constant-density case and the variable-density case

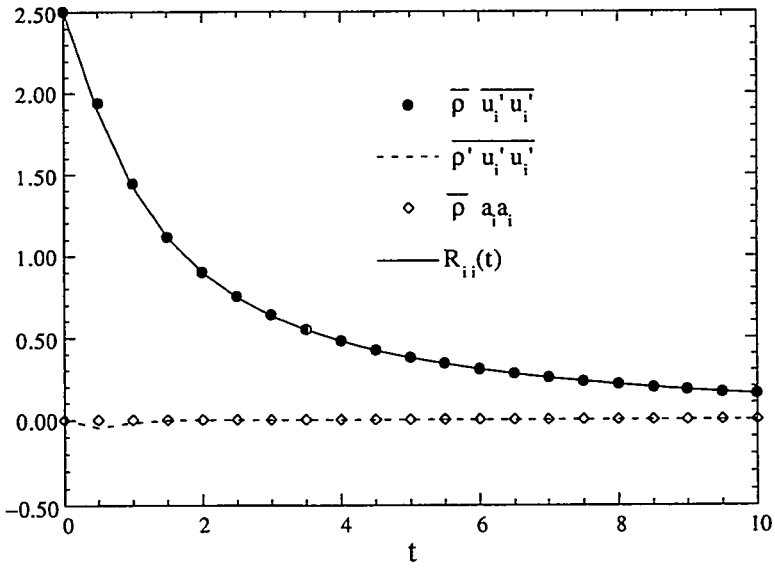

Figure 4.14: Evolution of R_{ii} for Run 55

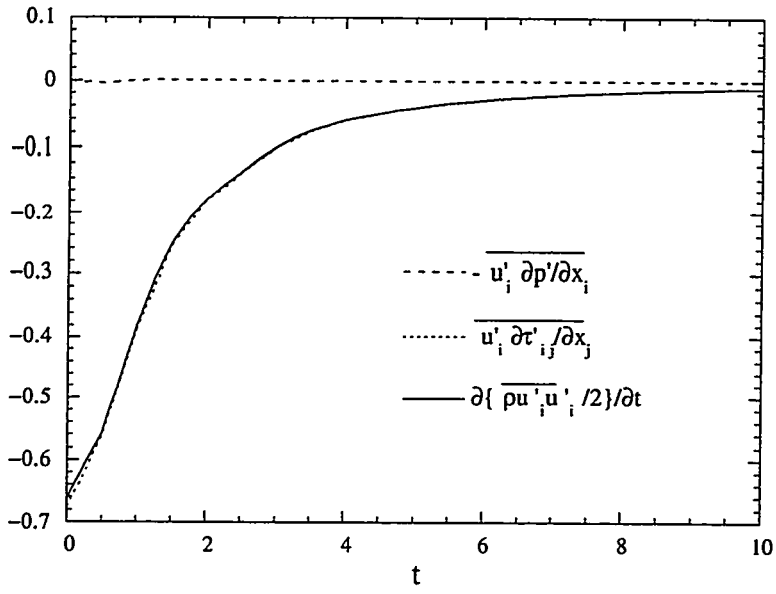

Figure 4.15: Contributing terms in the evolution equation for total fluid kinetic energy density [eq. (4.4)] for Run 55

does not grow to an appreciable amount, the decay of $\overline{\rho}\ \overline{u_i'u_i'}$ is nearly the same as that of $R_{ii}(t)/2$.

It is seen in Fig. 4.14 that the triple correlation term, $\overline{\rho' u_i'u_i'}$, is initially zero, grows to a small nonzero value and then decays to a negligibly small value. This behavior can be understood by observing the spectral distributions for $\rho u_i'u_i'/2$, $\overline{\rho}\ u_i'u_i'/2$ and $\rho' u_i'u_i'/2$. Figure 4.16 shows the initial spectrum for $\rho u_i'u_i'/2$ and $\overline{\rho} u_i'u_i'/2$. Initially these two spectrum are slightly different. The small difference is due to a nonzero initial spectral distribution of $\rho' u_i'u_i'/2$, which is shown in Fig. 4.17. The initial spectrum of $\rho' u_i'u_i'/2$ is small compared to the spectra given in Fig. 4.14 and integrates over all wavenumbers to a zero value for $\overline{\rho' u_i'u_i'}/2$. Figure 4.17 also shows the spectra of $\rho' u_i'u_i'/2$ for a sequence of early times. As this spectrum evolves in time, the values within the spectrum are redistributed such that its spectrally integrated value becomes nonzero. Also, as time evolves the spectrum is decaying so that its spectrally integrated value also decays.

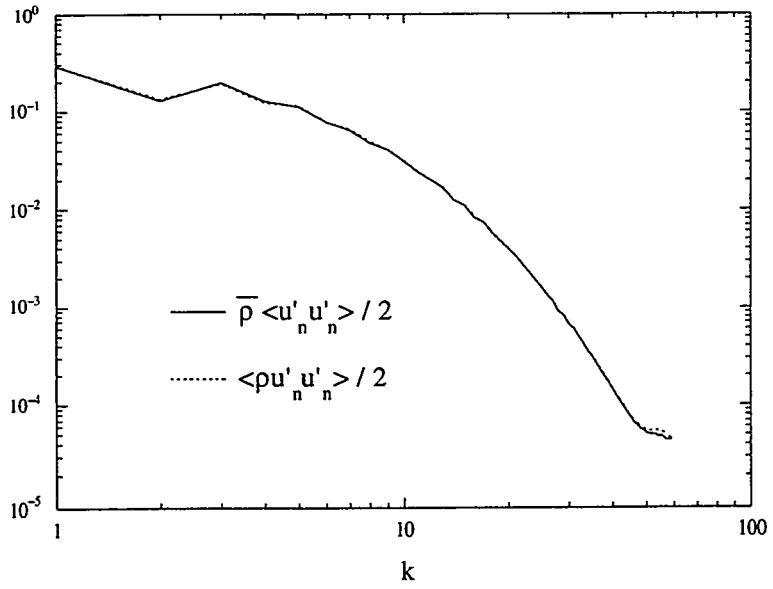

Figure 4.16: Initial spectrum for $\overline{\rho} < u_i' u_i' > /2$ and $< \rho u_i' u_i' > /2$ for Run 55

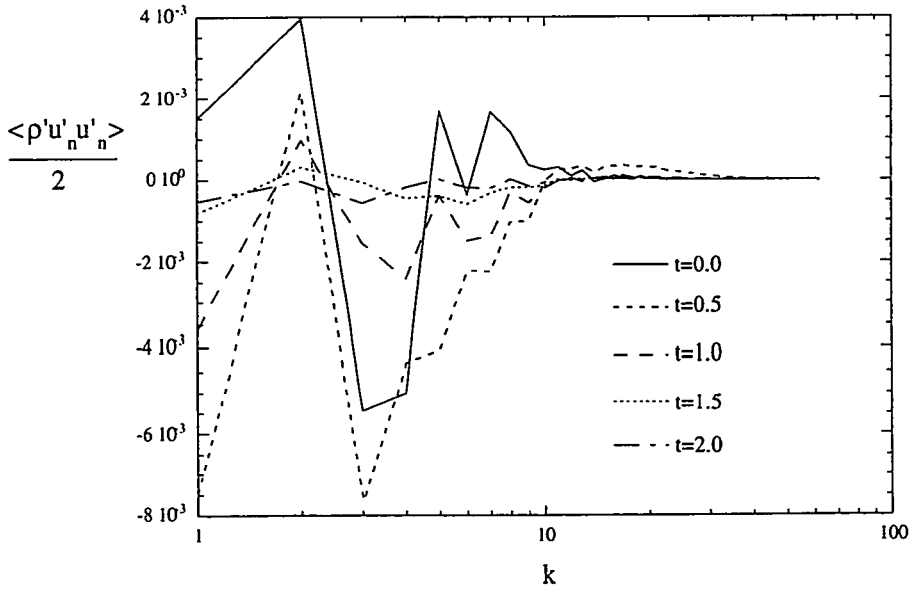

Figure 4.17: Spectral evolution of $< \rho' u_i' u_i' > /2$ for Run 55

4.5.2 *Decay of density field*

In section 4.3 the negative of the correlation between fluctuations of density and those of specific volume is defined as

$$b(t) = -\overline{\rho' \left(\frac{1}{\rho}\right)'} = -\overline{\rho' v'},$$

where $v = 1/\rho$ is the specific volume. This can be written as (see Appendix B)

$$b(t) = \overline{\rho v} - 1.$$

This can also be written [10] as

$$b(t) = \overline{\rho' \left(\frac{1}{\overline{\rho} + \rho'} - \frac{1}{\overline{\rho}}\right)} = \overline{\left(\frac{\rho' \rho'}{\rho \overline{\rho}}\right)}.$$

From this latter result, it can be seen that $b(t)$ is nonnegative, and in the limit as the density fluctuations tend to zero, $b(t) \approx \overline{\rho' \rho'}/\overline{\rho}^2$. This quantity is important since it arises in the modeling of variable-density flow [10, 23]; thus its behavior is described here. Figure 4.18 shows $b(t)$ as a function of t for the nearly constant-density case, Run 55a (dashed curve), and this variable-density case, Run 55 (solid curve), plotted to different scales. The left axis is for the nearly constant-density case, while the right axis is for the variable-density case. Note that the large difference in values is due to the difference in the initial density fluctuations. For both cases this quantity decays rapidly for $t < 1.5$ and more slowly thereafter. Also note that $b(t)$ decays slightly differently for the two cases.

Another measure of the decay of the density fluctuations is the *variance*, or the *second* (central) *moment* [56]. The variance is the mean-square departure from the mean value, and is defined as

$$\sigma_{\rho'}^2 = \int_{-\infty}^{\infty} (\rho')^2 P(\rho') d\rho' \equiv \overline{\rho' \rho'} \approx \frac{1}{N} \sum_{n=1}^{N} (\rho - \overline{\rho})^2,$$

where $P(\rho')$ the probability density of the fluctuating density and the summation is over all mesh points. The square root of the variance is the *standard deviation* (rms amplitude), $\sigma_{\rho'}$. Figure 4.19 shows the evolution of the variance for the fluctuating

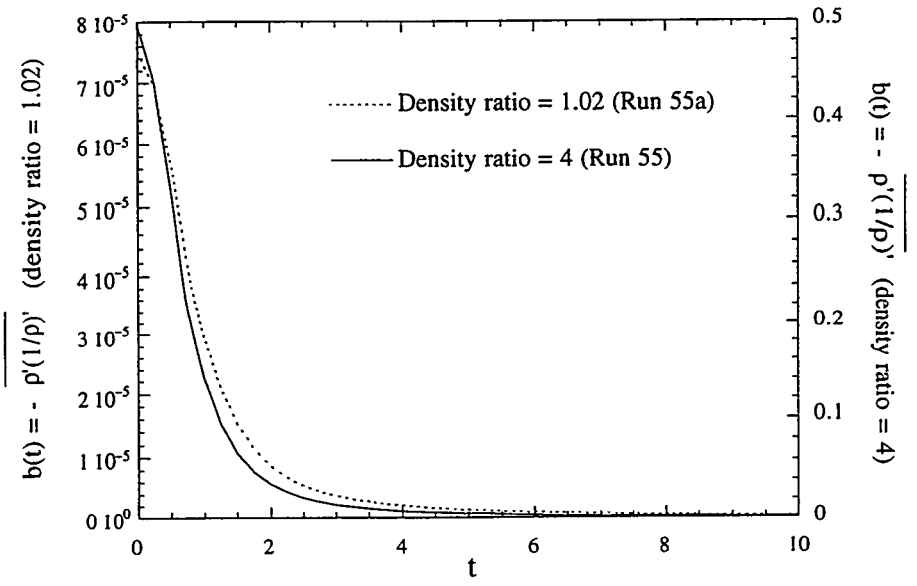

Figure 4.18: Comparison of the evolution of $b(t)$ for Run 55 and Run 55a

density field for both the nearly constant-density and variable-density case to different scales. The decay of the two density fields are quite similar, indicating that the density field in the case with the large density fluctuations is behaving approximately as a passive scalar.

As previously mentioned, in the limit as the density variations tends to zero, $b(t)$ should tend to $\overline{\rho'\rho'}/\overline{\rho}^2$. It is convenient to employ the same nomenclature used in Besnard, et el. [10], i.e.,

$$B(t) = \overline{\rho'\rho'}/\overline{\rho}^2.$$

Figure 4.20 shows a comparison of the decay of $b(t)$ and $B(t)$ for Run 55. Initially $b(t)$ is almost twice as large as $B(t)$. For $t < 2$, when the density fluctuations are large, $b(t)$ decays faster than $B(t)$. For $t > 2$, as the density fluctuations become smaller, $b(t)$ tends towards $B(t)$. Figure 4.21 shows the same results on a log-log plot. For $t < 0.5$, convective mixing occurs and the decay rate is small; thereafter, molecular mixing occurs and the decay rate is larger. For $t > 2$, the curves decay as a power law. Curve fitting gives a power law exponent of about 2.29. The "average" value of the power law exponent can be computed for the decay of $b(t)$ and $B(t)$ using an

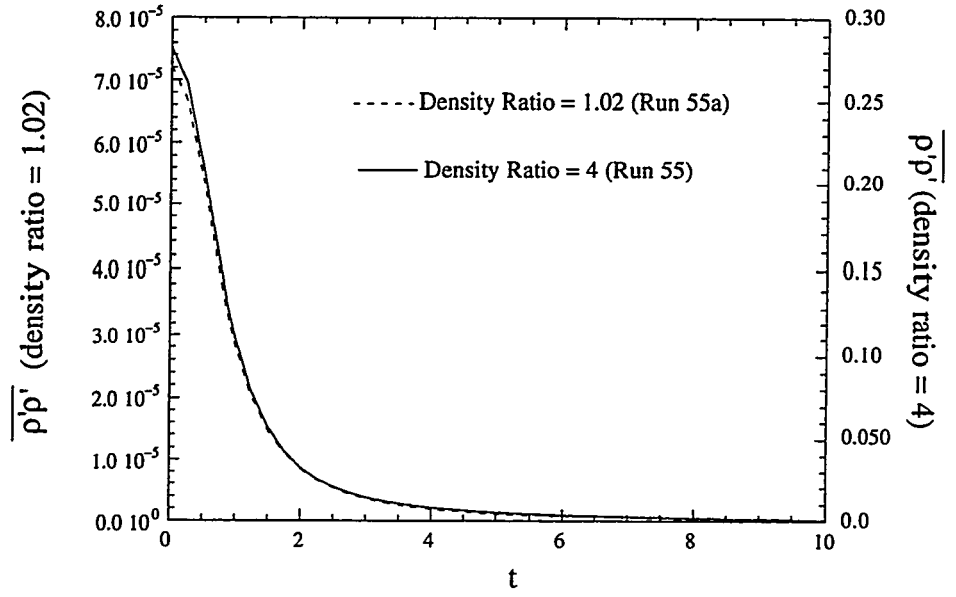

Figure 4.19: Evolution of $\overline{\rho'\rho'}$ for Run 55 and Run55a

equation similar to eq. (4.8), written here as

$$\overline{\gamma_\xi(t)} = -(t+t_o)\frac{\{\partial\xi(t)/\partial t\}}{\xi(t)}.$$

Here ξ is either $b(t)$ or $B(t)$ and t_o is the virtual origin. Another estimate of the power-law exponent is the "instantaneous" value. An equation similar to eq. (4.9) is used, i.e.,

$$\gamma_\xi(t) = -\left\{\frac{d}{dt}\left\{\frac{\xi(t)}{\partial\xi(t)/\partial t}\right\}\right\}^{-1}.$$

Figure 4.22 shows the "instantaneous" and "average" values for the power law exponent of $b(t)$ and $B(t)$ for Run 55. At early times when $b(t)$ and $B(t)$ are different the "average" value of the power law exponent is different. At late times, when $b(t)$ tends towards $B(t)$, the power law exponents become nearly the same value of about 2.3.

The characteristic time scales of decay for $K(t)$ and $b(t)$ are written as

$$\tau_K = -\frac{K(t)}{\partial K(t)/\partial t} \tag{4.15}$$

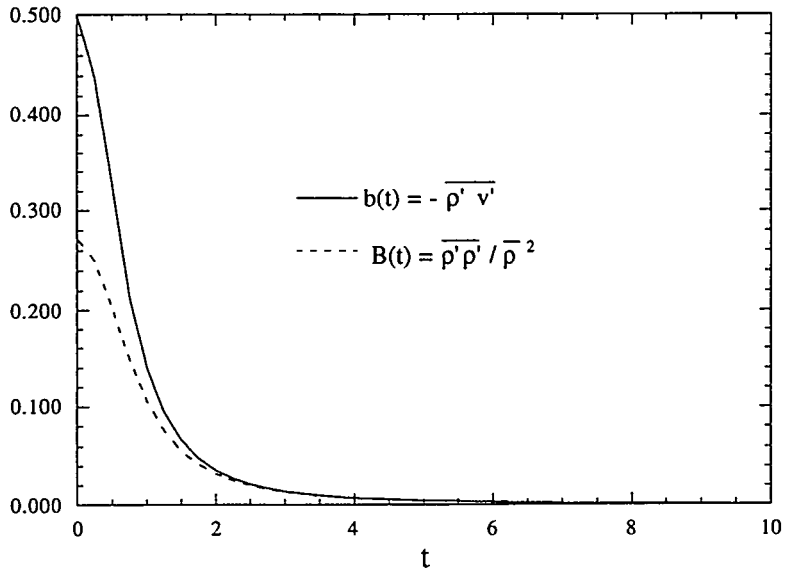

Figure 4.20: Evolution of $b(t)$ and $B(t)$ for Run 55

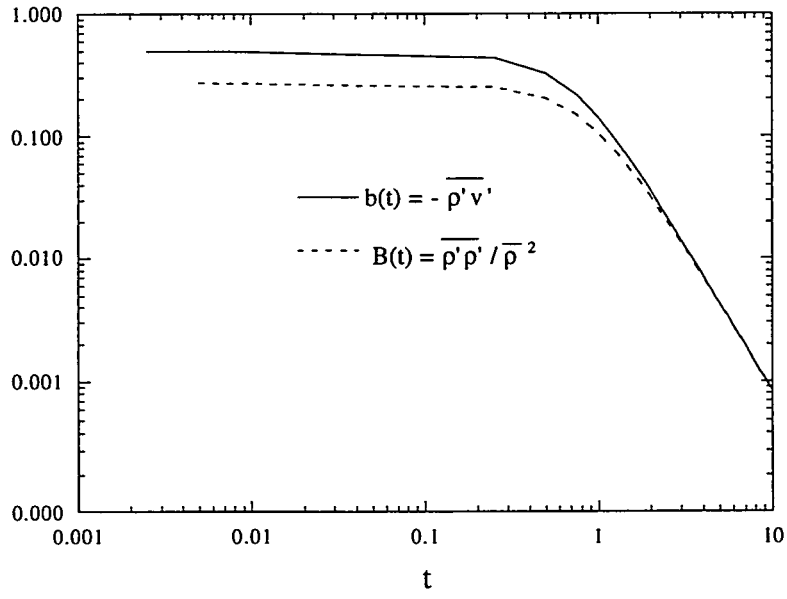

Figure 4.21: Evolution of $b(t)$ and $B(t)$ for Run 55

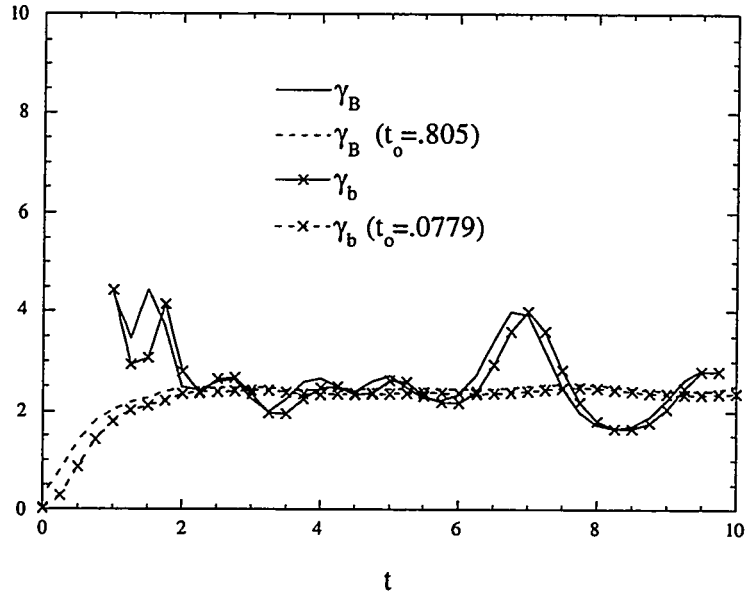

Figure 4.22: Power law exponents for the decay of $b(t)$ and $B(t)$ for Run 55

and

$$\tau_b = -\frac{b(t)}{\partial b(t)/\partial t} \tag{4.16}$$

Figure 4.23 shows the time evolution of the time scales for $K(t)$ and $b(t)$ for this variable-density case. After a time greater than 1 the curves are approximately straight lines with positive slopes, characteristic of power law decay behavior. Assuming power law decay,

$$K(t) = K_o \left[1 + \frac{t}{t_o}\right]^{-\gamma},$$

the characteristic time scale for the decay can be written as

$$\tau_K = -\frac{K(t)}{\{\partial K(t)/\partial t\}} = \frac{1}{\gamma}(t + t_o).$$

Thus if the characteristic time scale is growing linearly, then the power law coefficient is the slope of this curve. Another interesting feature seen in Fig. 4.23 is that the time scale for the decay of the total turbulent kinetic energy density is larger than that for b(t), implying that $K(t)$ is decaying slower than $b(t)$. This can also be seen by

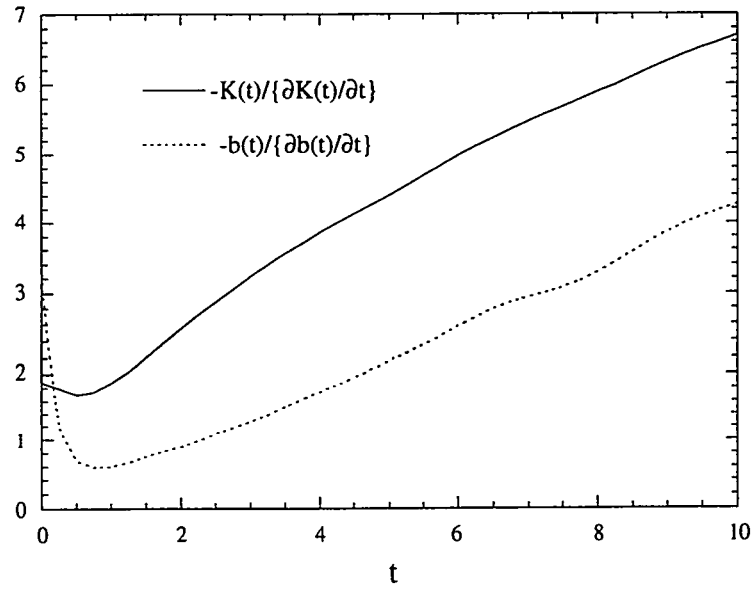

Figure 4.23: Time scale evolution of $K(t)$ and $b(t)$ for Run 55

comparing Fig. 4.18 with Fig. 4.13. For laboratory experiments with decaying grid turbulence the scalar (usually a temperature field) and velocity fields decay according to power laws [88]. Here the velocity and density decay (at late times) nearly as power laws, with a corresponding mechanical-to-density time-scale ratio

$$r = \frac{\tau_K}{\tau_b}$$

that varies slowly [30]. Figure 4.24 shows r for Runs 55 and 55a. In both cases this ratio becomes nearly constant with a value of almost 2 for t greater than 2. Warhaft and Lumley [88] and Sreenivasan et al. [82] have shown that this time-scale ratio in grid turbulence has values that range from $0.6 - 2.4$ depending on the initial conditions. In our study the time-scale ratio is near the upper limits of their range.

An evolution equation for $b(t)$ can be derived (see Appendix B), assuming statistical homogeneity and isotropy, and is

$$\frac{\partial b(t)}{\partial t} = 2\overline{\rho}\ \overline{v' \frac{\partial u_n'}{\partial x_n}}. \tag{4.17}$$

Note that if the divergent velocity field condition, eq. (2.11), is substituted into eq.

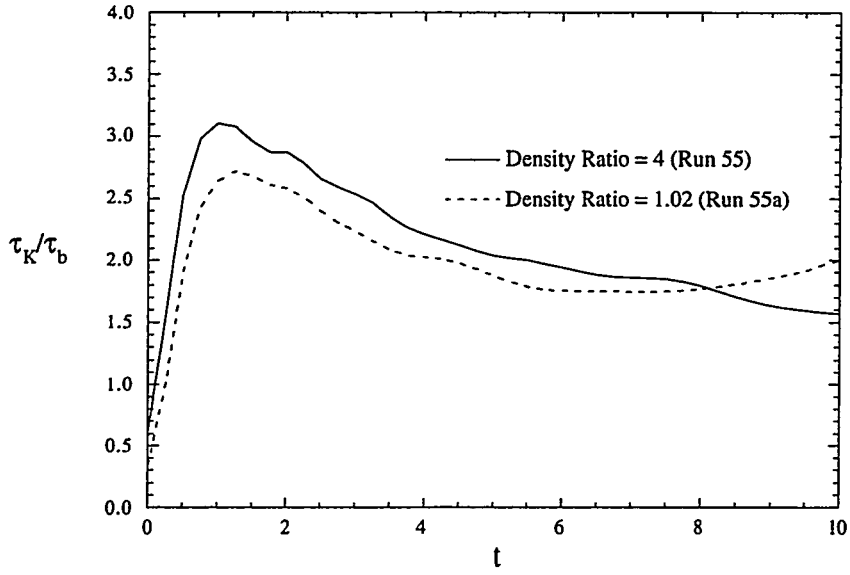

Figure 4.24: Mechanical-to-density time-scale ratio for Run 55 and 55a

(4.17) this leads to (assuming $\mathcal{D}$ is constant)

$$\frac{\partial b(t)}{\partial t} = -2\mathcal{D}\overline{\rho}\,\overline{v'\frac{\partial}{\partial x_n}\left\{\frac{1}{\rho}\frac{\partial \rho}{\partial x_n}\right\}}.$$

For a fixed Schmidt number $S_c = \nu/\mathcal{D}$, as the Reynolds number increases the molecular diffusion of $b(t)$ decreases. Therefore, $b(t)$ will decay slower at higher Reynolds numbers because the length scales at which diffusion is relevant decrease. The decay rate for $b(t)$,

$$\epsilon_b = -2\overline{\rho}\,\overline{v'\frac{\partial u_n'}{\partial n_n}},$$

is plotted in Fig. 4.25 as a function of t, showing behavior similar to what Mell [60] reported in his study of passive scalars. The increase in ϵ_b is due to convective mixing which increases the density gradients, while the decay of ϵ_b is due to molecular mixing. The time at which convective mixing occurs corresponds to the time that $b(t)$ decays rapidly (see Fig. 4.18) . During this time period, the time scales for the decay of $K(t)$ and $b(t)$ are also decreasing (see Fig. 4.23).

The right side and the left side of eq. (4.17) can be computed individually and compared. This is a useful numerical check to determine whether the decay of $b(t)$

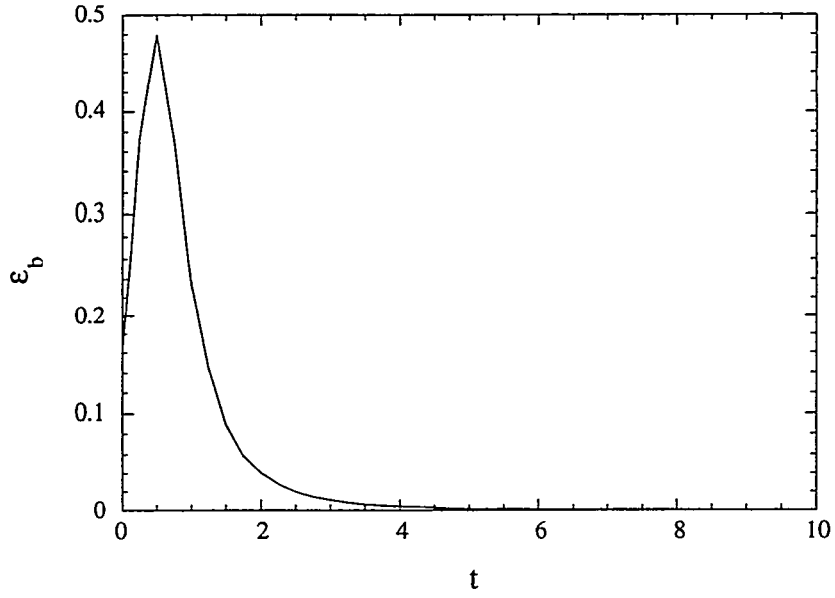

Figure 4.25: Dissipation rate of $b(t)$ as a function of t for Run 55

is being accurately computed in the simulation. Figure 4.26 shows each term of eq. (4.17) plotted as a function of time, indicating that indeed the simulation is accurately computing the decay of $b(t)$.

4.5.3 PDF evolution

In this section, the evolution of the pdf of density and of velocity are presented. Comparison between the nearly constant-density case (density ratio = 1.02) and the variable-density case (density ratio = 4) will be made. Again, the initial velocity fields used for both cases are nearly the same with modifications to take into account the divergent velocity condition.

Evolution of the density PDF

Knowledge of the pdf of the density field is important in helping to understand the mixing behavior of the density field. It has been observed that, in the mixing of passive scalars which have been initialized with a bimodal distribution [60, 30], the scalar pdf's evolve toward a Gaussian distribution. As the fluids continue to mix the final state of the scalar field should be a delta function at the mean of the initial scalar field, representing a completely mixed fluid.

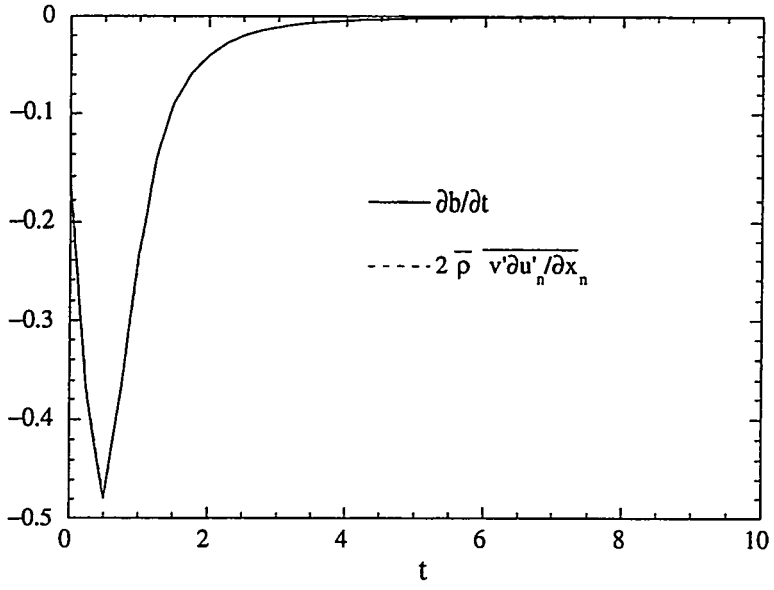

Figure 4.26: $\partial b(t)/\partial t$ evolution equations terms as a function of t for Run 55

Figure 4.27 shows the evolution of the density field pdf for both the variable-density (solid curves) and nearly constant-density (dashed curves) cases. The plot show the probability of a given pdf as a function of the fluid density. The horizontal axis is labeled with two density values, one for the variable-density case and the other for the nearly constant-density case. The initial pdf's for both cases have the same shape because the two initial density fields are similar, the difference being that the fluctuations have been scaled to give a variable-density field in one case, and a nearly constant-density field in the other. As a result, axes of the plot for the nearly constant-density field can be scaled and compared with the variable-density case. Initially the two pdf's are the same. As time evolves the bimodal distribution approaches a Gaussian distribution as the initially separated fluids become more thoroughly mixed. The time increment between curves is 0.5. By $t = 1.0$ the density field has lost its bimodal distribution, and the pdf has a nearly semi-circle distribution. From this plot it is seen that the evolution of both density fields are nearly identical, the only noticeable difference being that the pdf for the variable-density is slightly skewed positive to the mean density value of 1.

Defined in section 4.5.2 is the *variance* of the density field. The square-root of the variance is the standard deviation and is a measure of the width of the probability

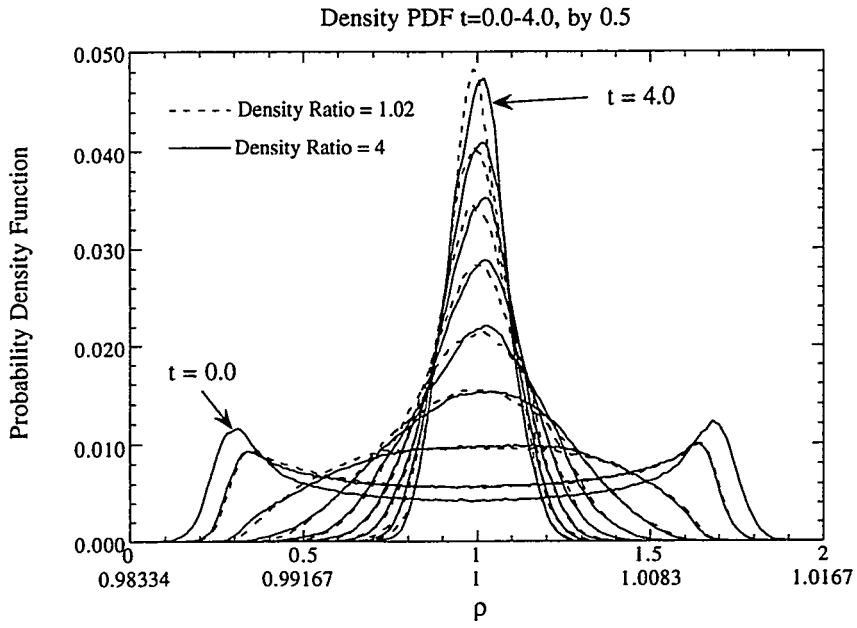

Figure 4.27: Density pdf evolution for Run 55 and Run 55a

density. Figure 4.19 shows that the variance for these density fields decays rapidly for $t < 2$. Thus, the standard deviation also decays rapidly during this time. This is seen in the pdf as it is during this time the bimodal distribution approaches a Gaussian shape.

A measure of whether or not the pdf is Gaussian is the *third* and *fourth moments* of the fluctuating density field. The *third moment* nondimensionalized by the standard deviation is known as the *skewness*, and is a measure of the lack of symmetry of the pdf. The skewness is defined as

$$S_{\rho'} = \frac{1}{\sigma_{\rho'}^3} \int_{-\infty}^{\infty} (\rho')^3 P(\rho') d\rho' \approx \frac{1}{\sigma_{\rho'}^3} \left\{ \frac{1}{N} \sum_{n=1}^{N} (\rho - \overline{\rho})^3 \right\}.$$

For a probability density function that is Gaussian, the skewness is zero. The *fourth moment* nondimensionalized by the standard deviation is known as the *kurtosis*, sometimes referred to as the *flatness factor*, and is a measure of the broadness of the probability density. The kurtosis of the fluctuating density field is defined as

$$K_{\rho'} = \frac{1}{\sigma_{\rho'}^4} \int_{-\infty}^{\infty} (\rho')^4 P(\rho') d\rho' \approx \frac{1}{\sigma_{\rho'}^4} \left\{ \frac{1}{N} \sum_{n=1}^{N} (\rho - \overline{\rho})^4 \right\}.$$

For a probability density function that is Gaussian, the kurtosis is three. Figure 4.28 shows the skewness and kurtosis of the fluctuating density field as functions of

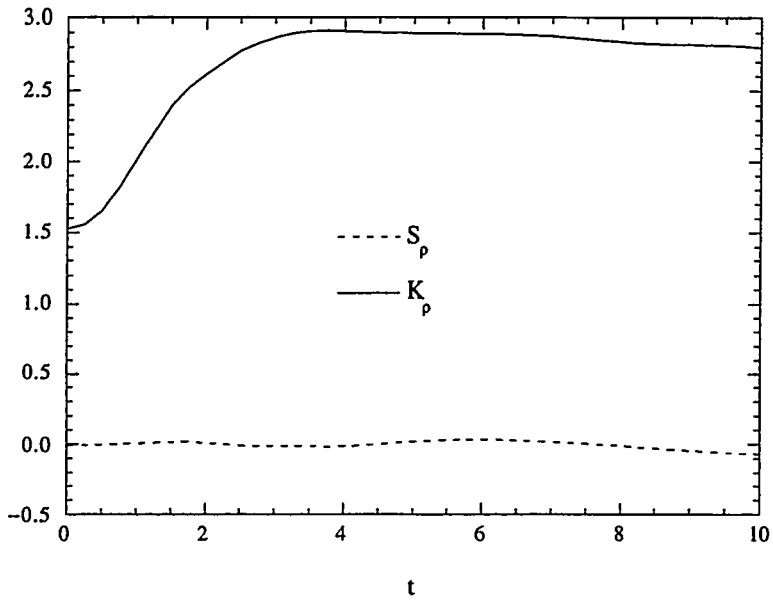

Figure 4.28: Evolution of the skewness and kurtosis of the density field for Run 55a

time for the nearly constant-density case. The density field has very little skewness and the kurtosis is very nearly three at late times, indicating that the fluctuating density field is indeed nearly Gaussian. Figure 4.29 shows the skewness and kurtosis of the fluctuating density field as a function of time for the variable-density case. The density field indeed has some skewness to it, though it is small. Also, the kurtosis is very nearly three for late times, again indicating that the fluctuating density field is approaching a Gaussian form.

Evolution of the Velocity PDF

In this case where the initial velocity and density fields are statistically independent the statistical behavior of the flow is nearly the same for the nearly constant-density field and the variable-density field. Figure 4.30 shows the evolution of the pdf of the velocity magnitude at three times, where the velocity magnitude is defined as $|u| = (u'^2 + v'^2 + w'^2)^{1/2}$. At $t = 0$ the pdf is the same for the two cases. At $t = 3$ (the last time shown), the velocity field pdf is still essentially the same. The case with the density ratio = 4 is slightly skewed to the positive side of the mean. This skewness is so small, however, that it is not clear whether it is due to statistical error or whether it is a true effect of variable density.

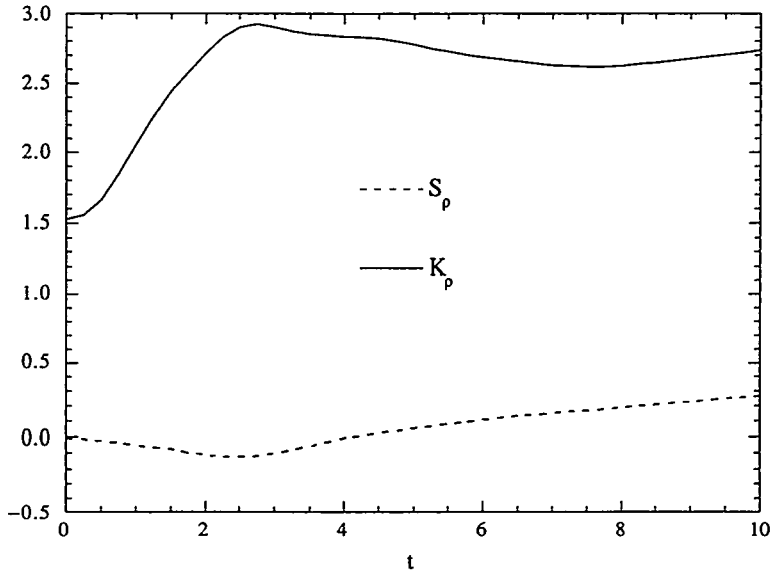

Figure 4.29: Evolution of the skewness and kurtosis of the density field for Run 55

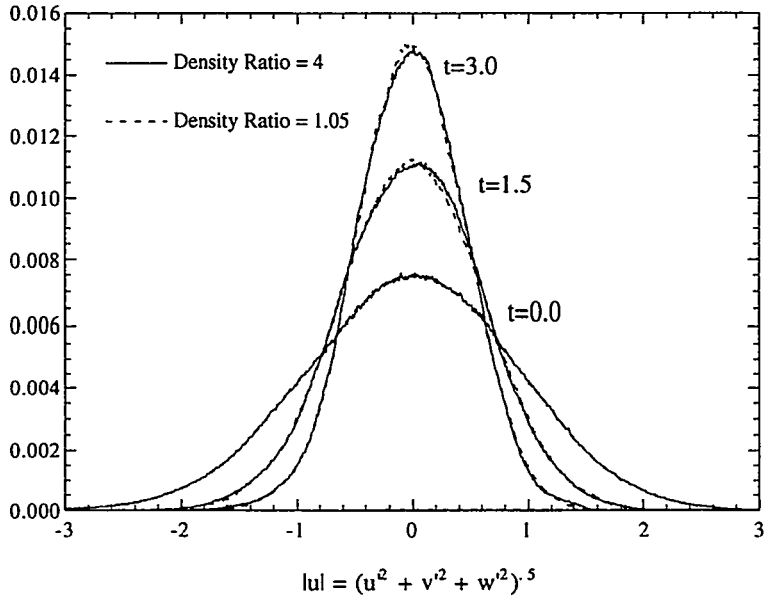

Figure 4.30: Velocity pdf evolution for Run 55 and Run 55a

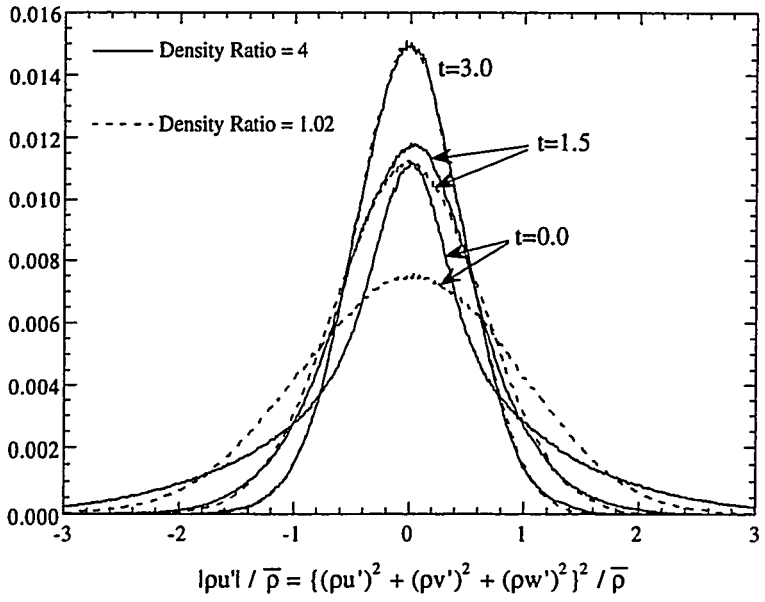

Figure 4.31: Momentum pdf evolution for Run 55 and Run 55a

Because there is a difference in the momentum fields between the nearly constant-density case and the variable-density case, it is anticipated that the pdf of the momentum magnitude divided by $\overline{\rho}$ for the two cases will be quite different. Figure 4.31 shows the evolution of the pdf of the momentum magnitude divided by $\overline{\rho}$ for the same three times that are given for the velocity field. The momentum magnitude divided by $\overline{\rho}$, $|\rho u|/\overline{\rho}$, is defined as $|\rho u|/\overline{\rho} = \{(\rho u')^2 + (\rho v')^2 + (\rho w')^2\}^{1/2}/\overline{\rho}$. Clearly, at $t = 0$ there is a difference for the two cases. For the nearly constant-density case (dashed curve) the initial momentum divided by $\overline{\rho}$ pdf is very nearly Gaussian and in fact is the same as the initial pdf for the velocity field for that case. For the variable-density case there is a larger peak about the mean momentum, and "tails" that are of larger value than that of the nearly constant-density case. As time evolves the pdf's become nearly the same as the density variations tend to zero. At $t = 3$ (an early time in the simulation) the pdf's are essentially identical.

4.5.4 Spectral Statistics

In this section are discussed spectra of $B(t) = \overline{\rho'\rho'}/\overline{\rho}^2$, $b(t) = -\overline{\rho' v'}$ and of the square of the velocity divergence, i.e., $(\partial u_n'/\partial x_n)^2$. For the nearly constant-density case the spectra of $B(t)$ and $b(t)$ should be the nearly same as the density fluctuations are

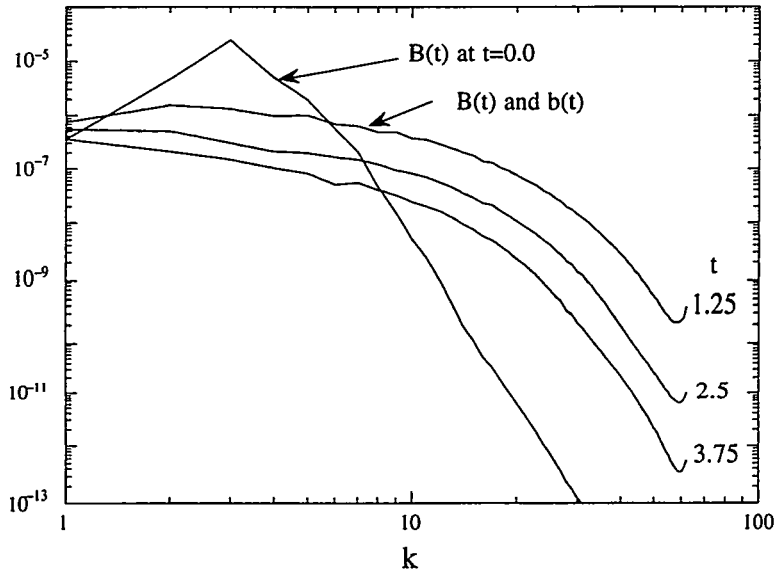

Figure 4.32: Density self-correlation and negative density-specific volume correlation spectra for Run 55a

small about the mean density. Figure 4.32 shows the spectral evolution of $B(t)$ and $b(t)$ at four different times for Run 55a. The initial spectrum for $b(t)$ is not shown as it is negative at some wavenumbers. At all the other times shown, the spectra for these two quantities are essentially the same.

It has already been shown the $b(t)$ and $B(t)$ for the variable-density case start out different, but, as the density fluctuations decay, these two terms become nearly the same. This may also be seen in the spectra of these quantities because, as the density fluctuations tend to zero, $b(t)$ can be approximated by $B(t)$. Figure 4.33 shows the spectral evolution of $B(t)$ and $b(t)$ for the variable-density case for the same times as for the nearly constant-density case. Again the initial spectrum for $b(t)$ is not shown. However, at $t = 1.25$ and $t = 2.5$ there are clearly differences in the spectra. These differences are small by $t = 3.75$ as the density fluctuations are becoming small about their mean.

Figures 4.34 and 4.35 show the spectral evolution of $(\partial u_n'/\partial x_n)^2$ for the nearly constant-density case and the variable-density case, respectively. From these two figures it is seen that the velocity field divergence is largest at the small scales (high wavenumbers) as the spectra have a maximum at a wavenumber of about 23 for

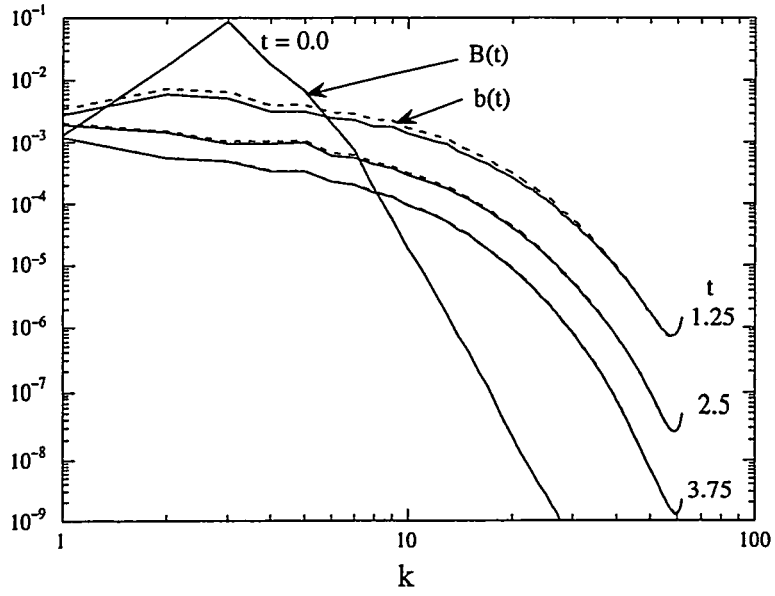

Figure 4.33: Density self-correlation and negative density-specific volume correlation spectra for Run 55

$t \geq 1.25$. Between $t = 0.0$ and $t = 1.25$ there is a build up at the higher wavenumbers. After this time there is full spectrum decay at all wavenumbers. From Figs. 4.34 and 4.35, it appears that the spectral evolution of $(\partial u_n'/\partial x_n)^2$ for the two cases are nearly the same within a constant factor. This may be expected as the velocity field divergence is related to the density field through the compressibility condition given by eq. (2.11). As the initial density fluctuations are larger, so also is the velocity field divergence. Figure 4.36 shows the spectra for the two cases, with the nearly constant-density case scaled by the ratio of the spectrum of $b(t)$ (defined here as $< b >$) for the two cases. With this scaling the spectra for the two cases are almost identical.

4.6 Summary

Presented in this chapter are the results of the isotropic decay of a nearly constant-density (Run 55a) turbulent flow and a variable-density (Run 55) turbulent flow. For each case the initial velocity and density field are statistically independent. Comparisons are made between the results for the nearly constant-density case and the results of Mell, who used the same initial velocity field to study closure models for nonpremixed turbulent reacting flows. This comparison shows that, in the limit as

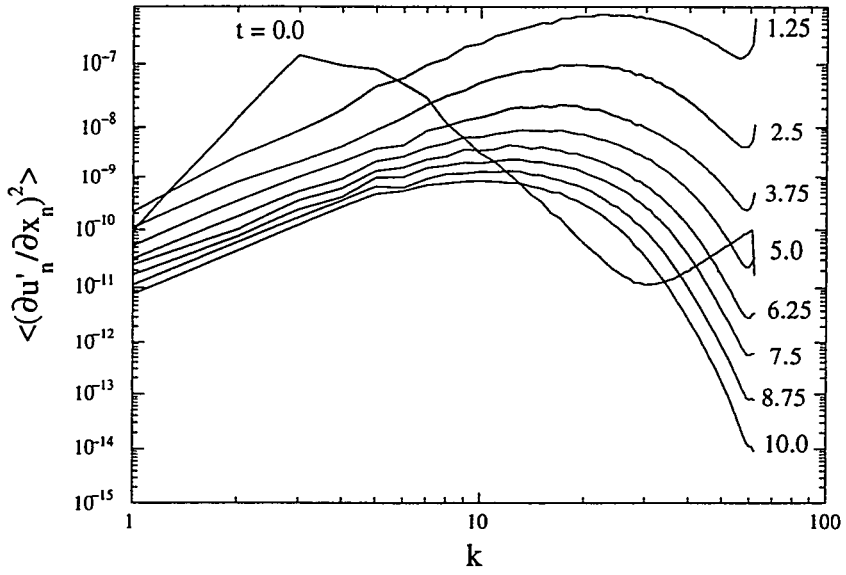

Figure 4.34: Spectra of the square-divergent velocity field condition for Run 55a

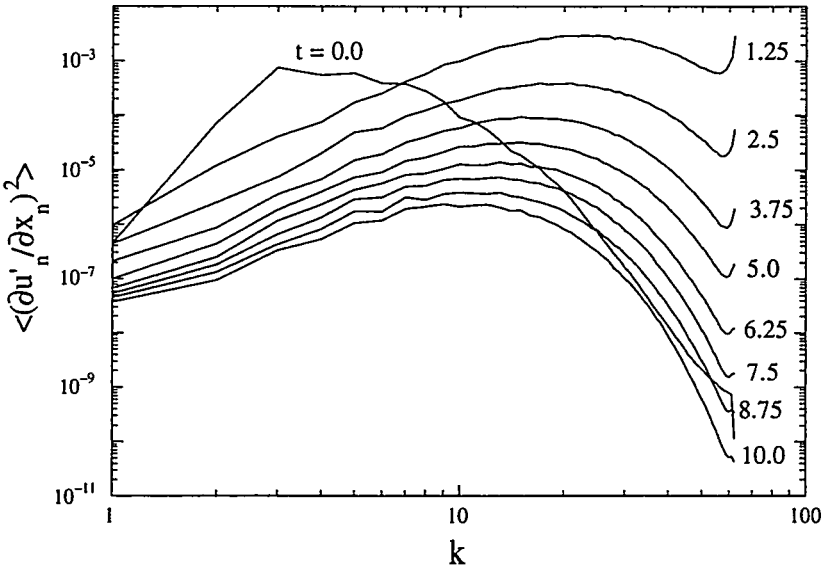

Figure 4.35: Spectra of the square-divergent velocity field condition for Run 55

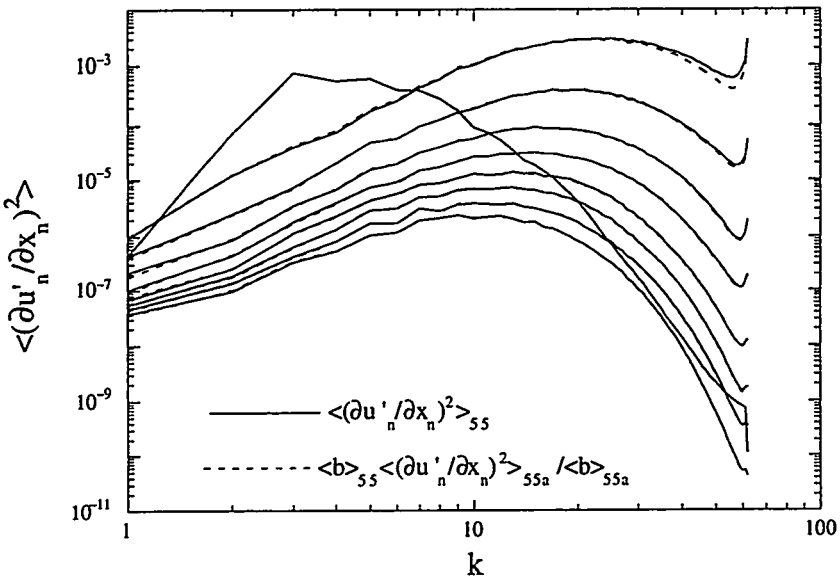

Figure 4.36: Spectra of the square of velocity divergent field for Run 55 and scaled for Run 55a

the density fluctuations tend to zero, the numerical scheme used in this study is able to produce results that are consistent with known results. It was also shown by Mell [60] that his results are consistent with laboratory isotropic grid-turbulence. This comparison gives us confidence in our numerical scheme.

Comparisons are also then made between the nearly constant-density results and the variable-density results. This comparison shows that, for this case in which the initial velocity and density field are statistically independent, the presence of variations of density has little effect on the overall statistical decay behavior of the flow. For the case with large initial density fluctuations, the decay of the total turbulent kinetic energy density closely follows the decay of the mean-square velocity. This is due to the fact that $\overline{\rho' u_i' u_i'}$ is initially zero and, for the conditions of the flow, remains small such that it has little effect on the decay processes. It is seen that, in the variable-density case, the triple correlation term does grow to a small amount. However, because the flow is at low Reynolds number and dominated by viscous effects this triple correlation remains small. It has been seen in the course of this study (described in the following chapter) that, if this triple correlation is nonzero, the decay of the turbulent velocity and density fields are affected by the fluctuations in density. The statistics presented are all averaged quantities of second

order moments or higher. And though the results showed that the decay processes are almost unaffected by the presence of variable-density , this does not prove that on a pointwise basis the turbulent field showed no effect of the variations in density. To test differences on a pointwise basis we computed correlation coefficients between the two turbulent flows for the three components of the velocity, the density and the pressure. The correlation coefficient for a given quantity is given as

$$C_\alpha = \frac{\overline{\alpha'_{55}\alpha'_{55a}}}{\overline{\alpha'^2_{55}}^{.5}\,\overline{\alpha'^2_{55a}}^{.5}} ,$$

where 55 is the quantity α from Run 55 (variable-density case) and 55a is the quantity α from Run 55a (constant-density case). Figure 4.37 shows the correlation coefficients of three components of the velocity field (solid line curves), the density field (dashed curve), the fluctuating density field (solid line with x's), and the pressure field (solid line with •'s). At $t = 0$ the correlation coefficient for the velocity and fluctuating density fields are equal to one. For early times, $t < 3$, the correlation coefficients rapidly change. During this time the velocity and fluctuating density fields for the two cases quickly become uncorrelated. The correlation coefficient for the initial density field is 0.9, and as the fluctuating density field rapidly decays, the two density fields become highly correlated.

For times $t > 3$, the correlation coefficients vary more slowly. This corresponds to the times when the density fields of the two cases are highly correlated. The decorrelation of the velocity field must be due to density differences as the initial density is the only difference between the two cases. These coefficients show that the flow behavior, on a pointwise basis, is affected by the density changes. The question is then: how can variable-density effects be felt on the averaged statistics of the flow? It will be shown in the next chapter that if $\overline{\rho' u'_i u'_i}$ is allowed to develop, statistical differences occur. The next chapter describes an initialization scheme that imparts a statistical dependence between the initial density field and the initial velocity field, producing fields that have $\overline{\rho' u'_i u'_i}$ initially nonzero. The effects of $\overline{\rho' u'_i u'_i}$ initially nonzero on the decay behavior of variable-density turbulence is studied.

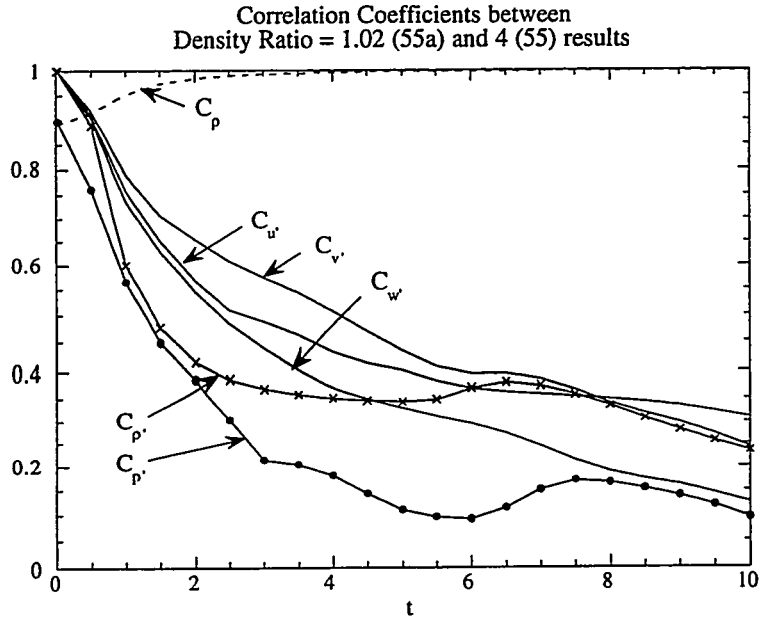

Figure 4.37: Correlation coefficients for the velocity, density and pressure fields between Run 55 and Run 55a

Chapter 5

ISOTROPIC DECAY OF STATISTICALLY DEPENDENT INITIAL VELOCITY AND DENSITY FIELDS

5.1 Introduction

Two characterizations of the initial velocity and density fields were discussed in Chapter 4. In the first, the initial velocity and density fields are statistically *independent.* Results from simulations of decaying, isotropic, variable-density turbulence using this characterization were presented. In particular, it was shown that, when the initial fields are statistically independent, so that the triple correlation, $\overline{\rho' u_i' u_i'}$, is initially zero, this triple correlation remained small. It was observed that the behavior of statistical quantities of the flow were relatively unaffected by the density variations.

In the second characterization, the initial velocity and density fields are statistically *dependent.* This statistical dependence is discussed in this chapter. Also, results of several simulations of decaying, isotropic, variable-density turbulence using the second characterization are presented and discussed. By initializing the flow simulations with an initial velocity field that is statistically dependent on the density field, it will be shown that this triple correlation is initially nonzero and, as a result, may have an important effect on the behavior of variable-density turbulent flows.

Presented in this chapter are the results of two types of initial variable-density fields. The first set of results are obtained using the initial bimodal pdf density field; these are runs Iso3 to Iso8 computed on a 128^3 computational grid. The second set of results are obtained using an initial variable-density field having density fluctuations which have a Gaussian distribution about the mean density, and are computed on a 64^3 grid.

5.2 Initialization of the Velocity and Density Fields

It is not possible to use velocity field "3u" (which was created and used by Mell [60] and used in our study presented in Chapter 4) for this study of statistically

dependent fields because this velocity field is statistically independent of the density fields we are studying. We use, however, the initial energy spectrum from velocity field "3u" to create, using the method of Orszag and Patterson [65], an initial random velocity field. This random velocity field is created such that the fluctuations have a normal, Gaussian distribution about the its mean and are statistically dependent on the initial density field (discussed briefly below in Section 5.3). By using the method of Orszag and Patterson, the initial velocity field has random initial Fourier amplitudes and phasing. A description of the procedure that initializes a velocity field that is statistically dependent on the density field is described briefly below in Section 5.3 and in more detail in Appendix C.

There are two type of statistical dependence utilized in the study presented in this chapter. In the first case the large velocity magnitudes are associated with positive density fluctuations (and, correspondingly, small velocity magnitudes are associated with negative density fluctuations). Therefore, on the average the heavier fluid has larger velocity magnitudes and the lighter fluid has smaller ones. In this case the triple correlation, $\overline{\rho' u_i' u_i'}$, will be initially positive since positive fluctuations in density are associated with a larger value of $u_i' u_i'$. In the second case, large velocity magnitudes are associated with negative density fluctuations (and, correspondingly, small velocity magnitudes are associated with positive density fluctuations). Here, the triple correlation, $\overline{\rho' u_i' u_i'}$, will be initially negative because on the average negative fluctuations in density are associated with larger values of $u_i' u_i'$. Table 4.1 lists the initial velocity statistics for the statistically-dependent, initial variable-density fields used in the simulations reported here.

For the first set of results presented in this chapter, the density field is initialized using the method of Eswaran and Pope [30]. This method creates an initial density field that conforms approximately to a double-delta pdf, where the initial fluid consists of regions of either high or low density typified by an integral length scale of $l_\rho = 0.53$ (see section 4.3), which is roughly half the velocity integral scale. This method was describe briefly in Chapter 4 and in detail in Appendix D, so it will not be repeated here. The second set of results presented in this chapter uses a random initial density field created such that the density fluctuations have a Gaussian distribution about the its mean value of one. The details of this initialization scheme can be found in Appendix D. Table 4.2 lists the initial density field statistics for the statistically-

dependent, initial variable-density fields used in the simulations reported here.

Qualitative comparison between the results of the two types of initial density fields will be discussed. The case of the bimodal density distribution represents approximately two unmixed fluids, whereas the Gaussian distribution could represent the late stages of flow development of the bimodal (unmixed) pdf case. It will be shown that, due to the statistical dependence of the initial velocity on the initial density field, for the bimodal case the pdf becomes asymmetric. As the density fluctuations become smaller the asymmetry is reduced and the pdf's evolve to a nearly Gaussian form. It will be found for the case with initial Gaussian distribution that, due to the Gaussian statistical nature, the effects of the fluctuating density are not strongly felt (at least for the cases presented in this study).

5.3 Creating statistically dependent initial velocity and density fields

This section describes briefly how a velocity field is created that is statistically dependent on the initial density field. For more detail the reader is referred to Section C.3 in the appendix. The first step in the initialization procedure is to use the method of Orszag and Patterson [65] to create a vector field, $\hat{\vec{A}}$, that has random Fourier amplitudes and phases. The initial energy spectrum from velocity field "3u" [60] is used with the method of Orszag and Patterson in order to determine $\vec{A}$. This random vector field is then multiplied in real space by some function of the density, $f(\rho)$, to give $\vec{A}' = f(\rho)\vec{A}$. $\vec{A}'$ represents the non-divergent part of the initial velocity field and is now directly dependent on the initial density field. To obtain an initial velocity field with large velocity magnitudes associated with low densities, the function $f(\rho)$ is defined to be $f(\rho) = c_A/\rho$, where c_A is a constant (chosen to be 1 in this study). This is referred to as Method A. To obtain an initial velocity field with large velocity magnitudes associated with high densities, the function $f(\rho)$ is defined to be $f(\rho) = c_B\rho$, where c_B is a constant (chosen to be 1 in this study). This is referred to as Method B. As the initial density fluctuations increase, so also does the initial statistical dependence. The next step in this procedure is to rescale the velocity field such that it has the desired energy spectrum. Finally, the velocity field is modified to account for the non-divergent condition given by eq. (2.11).

5.4 Results for the case with the initial bimodal pdf

5.4.1 Introduction

We now consider the case of a freely decaying, isotropic, variable-density flow where the initial velocity field is statistically dependent on the initial bimodal density field. As mentioned in a previous section (Section 5.2) there are two types of dependence studied, one where large velocity magnitudes are associated with low densities (Run Iso4) and the other where large velocity magnitudes are associated with the high densities (Run Iso5). Because of this dependence, there will be nonzero values for the triple correlation, $\overline{\rho' u_i' u_i'}$. The two variable-density problems (Iso4 and Iso5) each are examined with an initial density ratio of 2.33.

To compare these cases (Iso4 and Iso5) to nearly constant-density results, a third case (Run Iso3) is simulated with a density ratio = 1.02. In all of these cases, the initial total turbulent kinetic energy, $\overline{\rho u_i' u_i'}/2$, will have the same value of 1.32, which is achieved by rescaling each initial velocity field by a constant value. This is discussed in more detail in Section 5.4.3 below. Studied will be the decay processes and the density pdf evolution. For these three cases the grid resolution is 128^3.

Finally, two other cases are presented in order to examine the effect of statistical dependence when the initial density fluctuations are very small. In both cases, the density ratio is 1.02. In one case (Run Iso6), the high velocity magnitudes are associated with negative density fluctuations, while in the other (Iso8), high velocity magnitudes are associated with positive density fluctuations. For these two cases the grid resolution is 128^3.

5.4.2 Nearly constant-density case

To provide a result for which the variable-density cases can be compared, a nearly-constant density case (Run Iso3) is simulated using an initial density ratio of 1.02. By using Method A for this case, the initial density fluctuations and kinetic energy (per unit mass) are positively correlated. Because the initial density fluctuations are small, the triple correlation $\overline{\rho' u_i' u_i'}$ is initially nearly zero. In this case the density field should act as a passive scalar.

Because the initial energy spectrum and viscosity used in this study are the same as for the statistically independent fields reported in Chapter 4, the initial Taylor

Reynolds number is $R_\lambda = 54.9$. The initial velocity field is nearly in full spectrum decay, although there is a small build-up phase where there is growth of energy at the high wave numbers prior to decay at these wave numbers.

Decay of the turbulent kinetic energy

In this section the decay behavior of the total turbulent kinetic energy density is investigated. The terms of the total kinetic energy density is described by eq. (4.2). For isotropic decay the $\overline{\rho} a_n a_n/2$ term is zero since scalar-velocity correlations are zero. Figure 5.1 is a plot of the components of the generalized Reynolds stress tensor, R_{nn}, (twice the total kinetic energy density) as a function of time, t. Here t is the computational time divided by the initial large eddy turnover time, u_o/l_o (where $u_o = (\overline{u_i' u_i'}/3)^{1/2}$ at $t = 0$ and l_o is the initial velocity integral scale). For this nearly constant density case, $\overline{\rho' u_i' u_i'}$ is initially small compared to $\overline{\rho}\ \overline{u_i' u_i'}$ and remains nearly zero throughout the evolution of the flow. Thus, as seen in the results of Chapter 4 for nearly constant-density flows, the total turbulent kinetic energy density is approximately equal to $\overline{\rho}\ \overline{u_i' u_i'}/2$ as the $\overline{\rho' u_i' u_i'}/2$ is nearly zero. The decay of the total turbulent kinetic energy density is given by eq. (4.4) written here for homogeneous flow as

$$\frac{\partial}{\partial t}\left\{\frac{1}{2}\overline{\rho u_i' u_i'}\right\} = \overline{p\frac{\partial u_i'}{\partial x_i}} + \overline{u_i' \frac{\partial \tau_{ij}'}{\partial x_j}}.$$

The first term on the right side is the pressure-work term due to dilatational effects. The second term represents changes in the total turbulent kinetic energy due to the viscous dissipation rate. Figure 5.2 shows the evolution of each term of this equation. The pressure-work term is small for this case so that the decay of total kinetic energy density is due to viscous dissipation.

Figure 5.3 shows the time scale for the decay of the total kinetic energy density, given by eq. (4.6), as a function of time. For times later than 1, the time scale is growing nearly linearly, indicating that the decay of the energy is following a near power-law behavior. Curve fitting suggests that the power-law exponent in this case is 1.7.

Figure 5.4 shows the velocity-derivative skewness [given by eq. (4.10)] for all three directions as a function of time. Initially it is zero, reflecting the fact that the spectral

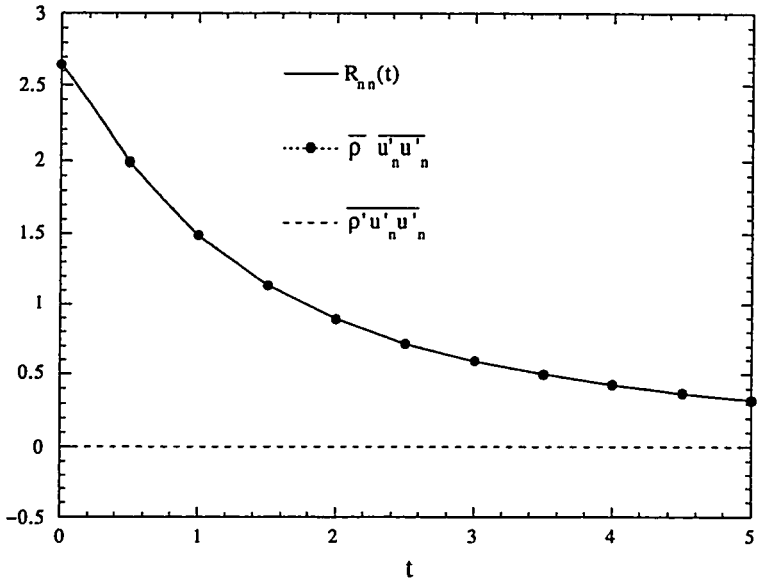

Figure 5.1: The evolution of R_{nn} for Run Iso3

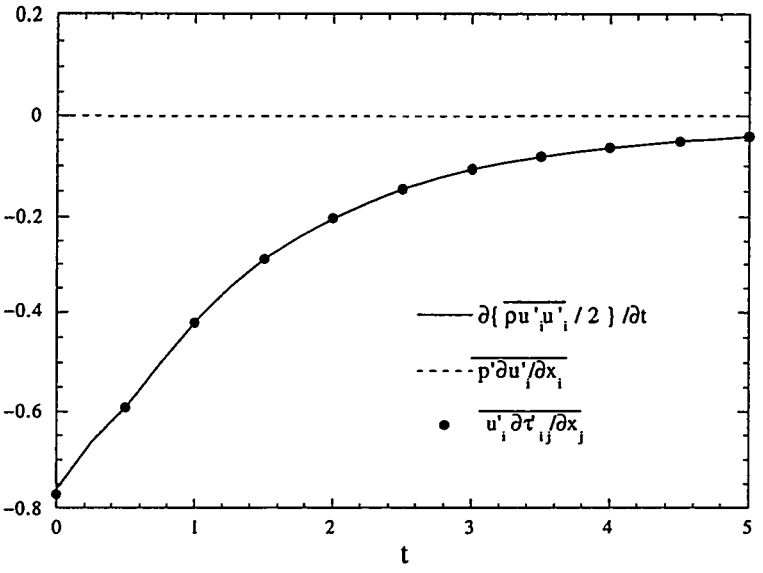

Figure 5.2: Terms in the evolution equation [eq. (4.4)] for the total kinetic energy density for Run Iso3

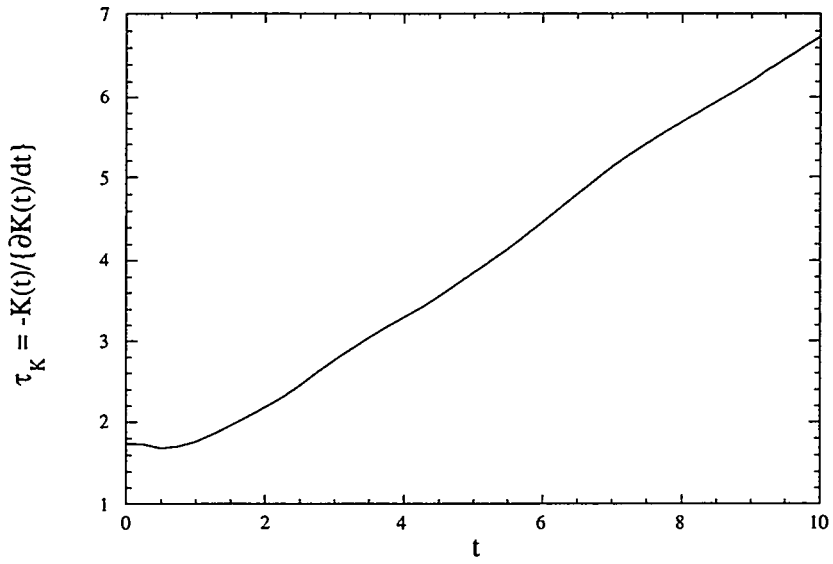

Figure 5.3: Time scale of decay for the total kinetic energy density for Run Iso3

energy transfer is initially zero [72], due to the initialization method, which forces the wave number amplitudes to be statistically independent. The transfer spectrum quickly builds up as the initial velocity field properly adjusts, and hence the velocity-derivative skewness builds up to values typical of laboratory grid turbulence, and are consistent with the results reported in Chapter 4.

Decay of the density fluctuations

In this section is described the decay of the density fluctuations for this nearly constant-density case. For this case, the evolution of $b(t) = -\overline{\rho' v'}$ should be nearly the same as the evolution of $B(t) = \overline{\rho'\rho'}/\overline{\rho}^2$. Figure 5.5 shows the evolution of these quantities as a function of time, demonstrating that these two quantities evolve nearly identically. As in the results shown in Chapter 4, the decay of the density field is fast for early time, and by $t = 2$ the variance of the density field is about 10 percent of its initial value. Figure 5.6 shows the dissipation rate for $b(t)$. The increase in ϵ_b for time less than 0.5 is due to convective mixing, which increases the density gradients. For times larger than 0.5 the decay of ϵ_b is due to molecular mixing.

Figure 5.7 shows the skewness and kurtosis for the density field. The density field is not skewed at early times and becomes slightly skewed at late times. The kurtosis

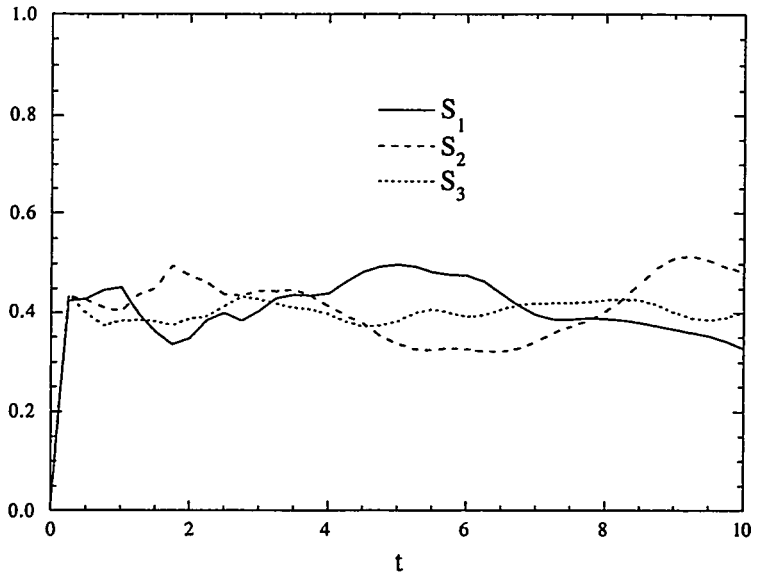

Figure 5.4: The velocity derivative skewness for the three components of velocity for Run Iso3

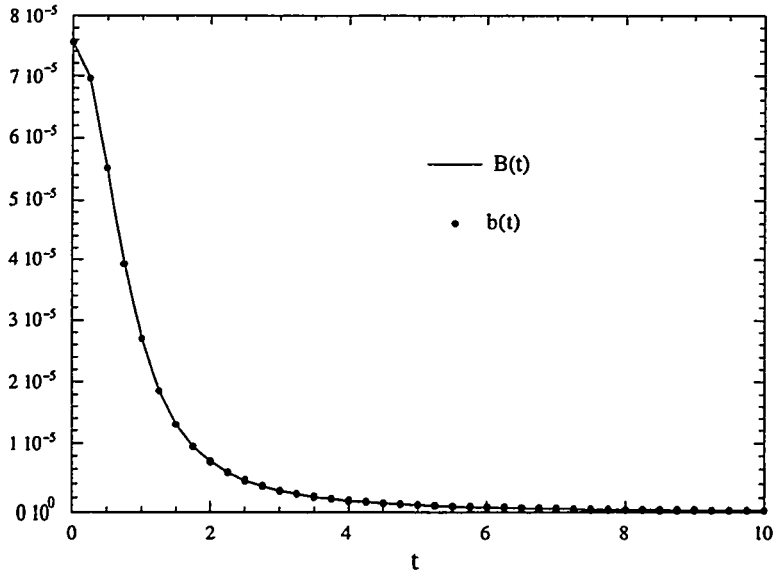

Figure 5.5: Evolution of $b(t) = -\overline{\rho' v'}$ and $B(t) = \overline{\rho' \rho'}/\overline{\rho}^2$ for Run Iso3

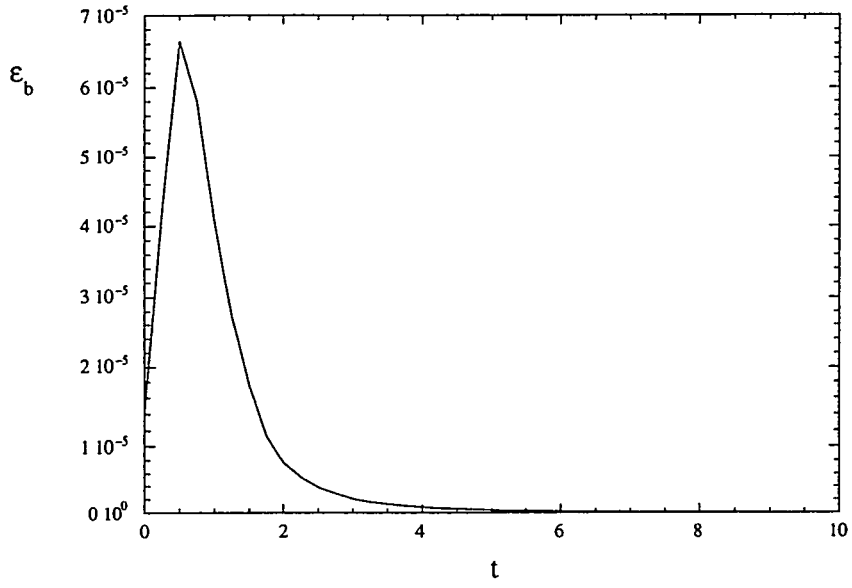

Figure 5.6: Dissipation rate evolution for $b(t) = -\overline{\rho' v'}$ for Run Iso3

starts out at 1.5 and grows to a nearly constant value of 3.5. With the density field slightly skewed and its kurtosis not equal to 3, the field is not quite Gaussian. Figure 5.8 shows the evolution of the pdf of the density field from $t = 0$ to $t = 4$ in steps of 0.5. The pdf evolves in a nearly symmetric manner towards a nearly Gaussian form. The evolution is very similar with the results presented in Chapter 4 for the statistically independent initial fields, which also show the evolution of the pdf of the density field towards a nearly Gaussian distribution.

Energy Spectrum evolution

Figure 5.9 shows the evolution of the energy spectrum (i.e., energy per unit mass, $u'_n u'_n/2$) in time increments of 1 from the initial time to $t = 10$. The initial spectrum is the same as for the simulations presented in Chapter 4. The evolution of the spectra for this nearly constant-density case is very similar to the energy spectrum evolution for the statistically independent case. This is expected since the initial energy spectra for the two cases are the same.

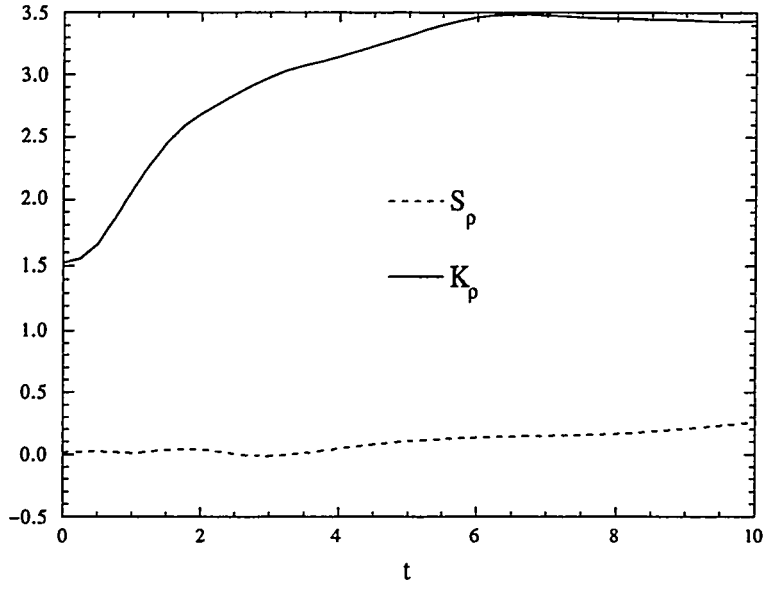

Figure 5.7: Skewness and Kurtosis of the density field for Run Iso3

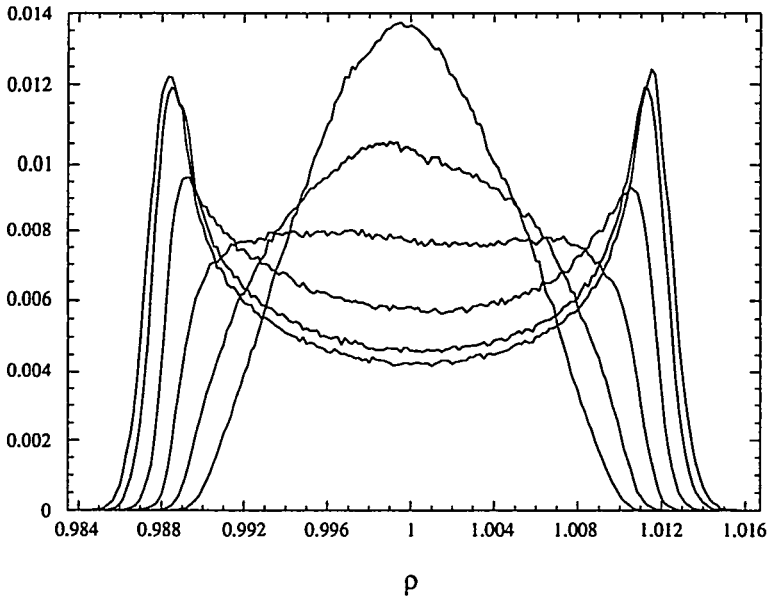

Figure 5.8: PDF evolution, $t = 0.0$ to 1.5 by 0.25, for Run Iso3

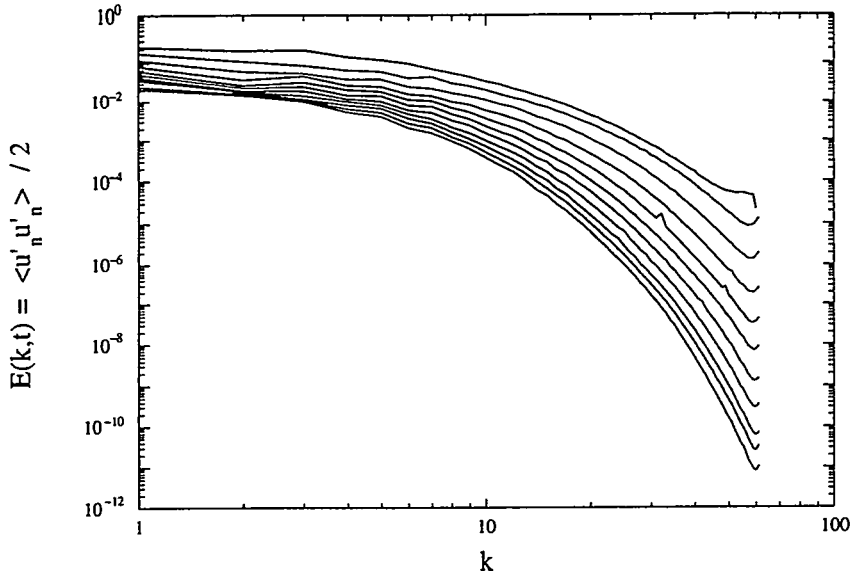

Figure 5.9: Energy spectrum evolution, $t = 0.0$ to 10.0 by 1.0, for Run Iso3

Conclusions of this nearly constant-density case

It has been seen that the decay process of this nearly constant-density case, where the initial velocity and density are statistically dependent, are similar to the results for the statistically independent initial fields. The reason for this is two-fold; first, these simulations have the same spectral shape for the initial velocity and density fields, and second, the initial density fluctuations are small. By using of the initial spectral shape of Mell's velocity field, "3u", we are able to create an initial velocity field that is dependent on the density field, and with initial statistics similar to the initial velocity fields used in the study of Chapter 4. The nearly constant-density case presented here provides a comparison for the variable-density, statistically-dependent cases studied in the following sections.

5.4.3 Cases with large initial density fluctuations

In this section, two decaying, isotropic, variable-density turbulence cases will be presented. Both have initial density ratios of 2.33. In the first case, Run Iso4, the velocity field has large magnitudes where the density is low (i.e., where the density fluctuations are negative) and in the second case, Run Iso5, the velocity magnitude is large where the density is high (i.e., where the density fluctuations are positive). The

initial total turbulent kinetic energy density for these two cases is the same as for the nearly constant-density case presented in the previous section, which is achieved by rescaling the initial energy per unit mass for each case. The effects of this rescaling can be seen in the initial spectrum of $u_n' u_n'/2$ for Runs Iso3, Iso4 and Iso5, shown in Fig. 5.10. For Run Iso4, the initial spectrum has slightly higher values than for the other two cases, while for Run Iso5, the initial spectrum has slightly lower values than for the other two cases. Figure 5.11 shows the initial total kinetic energy spectrum, $< \rho u_n' u_n' > /2$, for these three cases. All three of these initial spectra integrate to give the same initial value for $\overline{\rho u_n' u_n'}/2$. For Run Iso4 the initial spectrum is slightly larger than for the other two cases at the small wavenumbers and slightly smaller than the other two cases at the higher wavenumbers. For Run Iso5 the initial spectrum is slightly smaller than for the other two cases at the small wavenumbers and slightly larger than the other two cases at the higher wavenumbers. Figure 5.12 shows the initial spectrum of $\rho' u_n' u_n'/2$ for all three cases. For the nearly constant-density case, Run Isom3, the initial spectrum is small compared to the other two cases. For the case with large initial density fluctuations, where the large velocity magnitudes are associated with the negative density fluctuations, Run Iso4, the initial spectrum is negative. For the case with large initial density fluctuations, where the large velocity magnitudes are associated with the positive density fluctuations, Run Iso5, the initial spectrum is positive.

The results for these simulations will be presented first as a comparison between all three cases, and then each of the variable-density cases will be studied individually.

Decay of the turbulent kinetic energy for the three cases

The total turbulent kinetic energy density for the two variable-density cases and the nearly constant-density case, given by eq. (4.2), is plotted as a function of time in Fig. 5.13. The nearly constant-density case is shown by the solid line curve, the variable-density case Iso5 is shown by the "small" dashed curve, and cases Iso4 is shown by the "large" dashed curve. Initially all three of these cases start with the same turbulent kinetic energy density. At very early times, the turbulent kinetic energy decays fastest for case Iso4 and slowest for case Iso5 (i.e., for $t < 0.2$). The reason for this observed behavior is due to the difference in the initial dissipation rates for the three cases. To ensure that the initial total turbulent kinetic energy

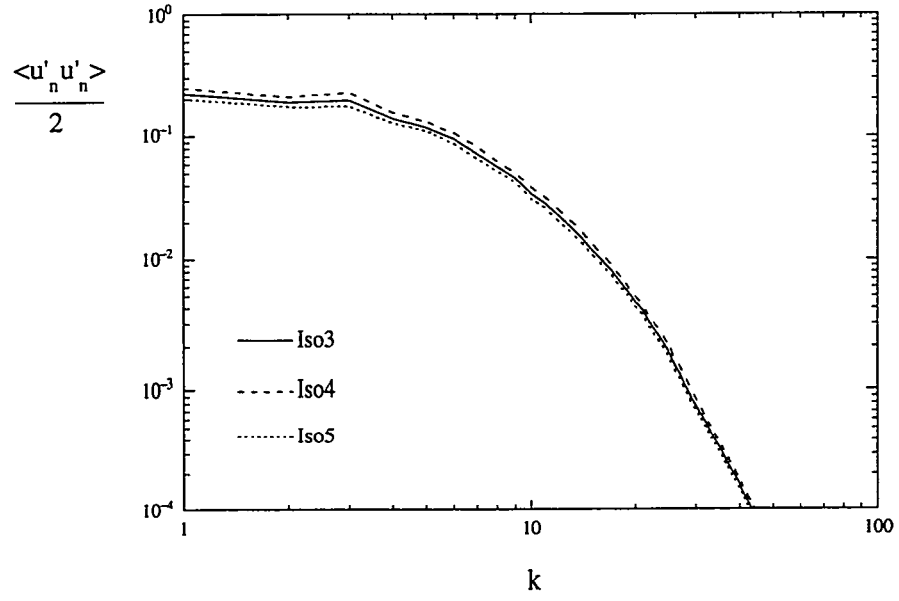

Figure 5.10: Initial spectrum of $u'_n u'_n/2$ for Run Iso3, Iso4 and Iso5

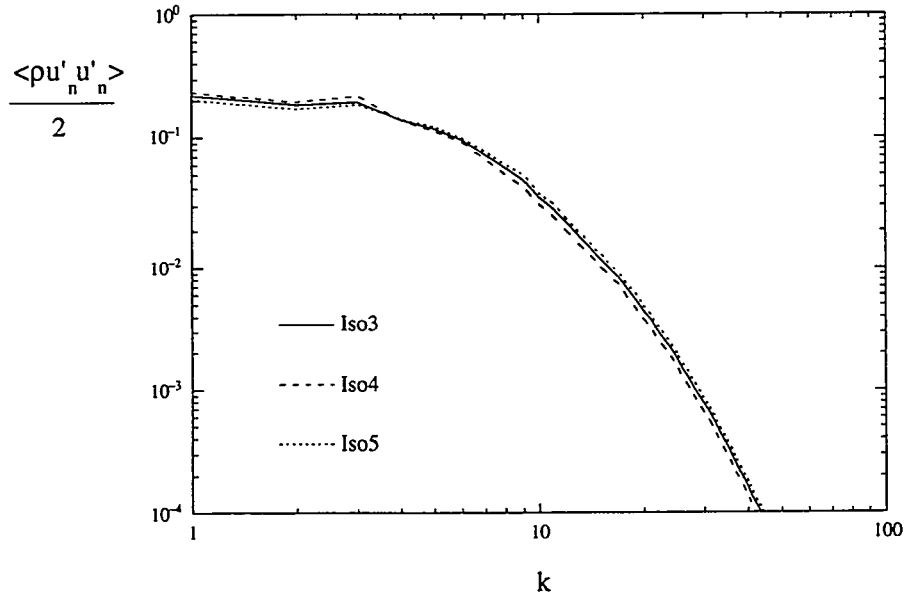

Figure 5.11: Initial spectrum of $\rho u'_n u'_n/2$ for Run Iso3, Iso4 and Iso5

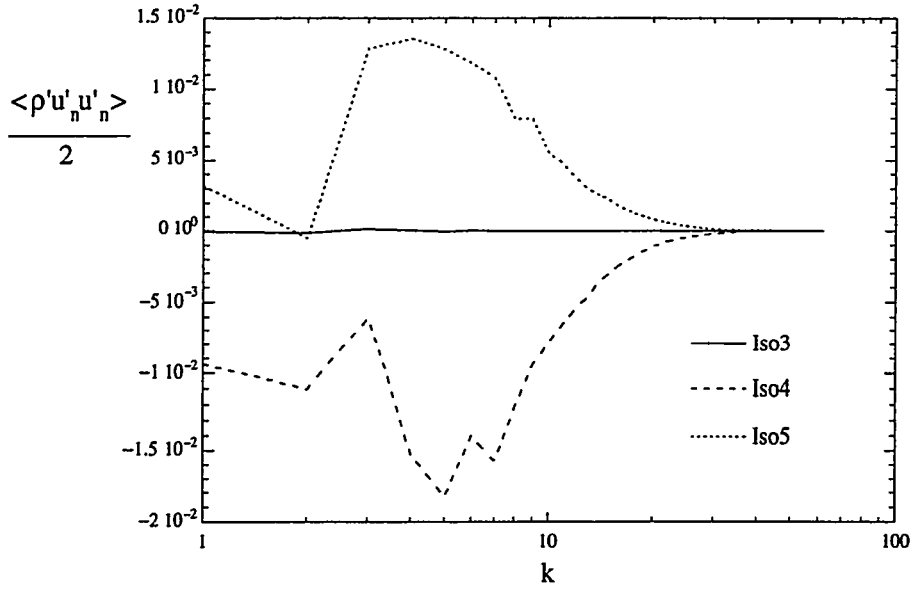

Figure 5.12: Initial spectrum of $\rho' u_n' u_n'/2$ for Run Iso3, Iso4 and Iso5

for all three cases is the same, the initial velocity fields need proper re-scaling. For case Iso5, the initial velocity field needs to be re-scaled downwards to a lower mean-squared velocity, $\overline{\rho}\ \overline{u_i' u_i'}/2$, value so that the total turbulent kinetic energy density, $\overline{\rho u_i' u_i'}/2$, is initially the same as that of the nearly constant-density case. For case Iso4, the initial velocity field needs to be re-scaled upwards. This can be seen in Fig. 5.14 which shows $\overline{\rho}\ \overline{u_n' u_n'}/2$ as a function of time for all three cases. Initially, $\overline{\rho}\ \overline{u_i' u_i'}/2$ is the largest for case Iso4 and smallest for case Iso5. As the result of this re-scaling of the initial velocity field, the initial dissipation rates for these three cases are different.

Figure 5.15 shows the dissipation rate for the turbulent kinetic energy per unit mass for variable-density flows, defined for homogeneous flows [87] as [10]

$$\epsilon = 2\nu\ \overline{s_{ij} s_{ij}}$$

where ν is assumed constant, and s_{ij} is the fluctuating rate of strain, defined by,

$$s_{ij} \equiv \frac{1}{2}\left(\frac{\partial u_i'}{\partial x_j} + \frac{\partial u_j'}{\partial x_i}\right).$$

This figure shows that the initial dissipation rates of the turbulent kinetic energy per unit mass are different for the three cases. The dissipation rate for Iso4 is the largest

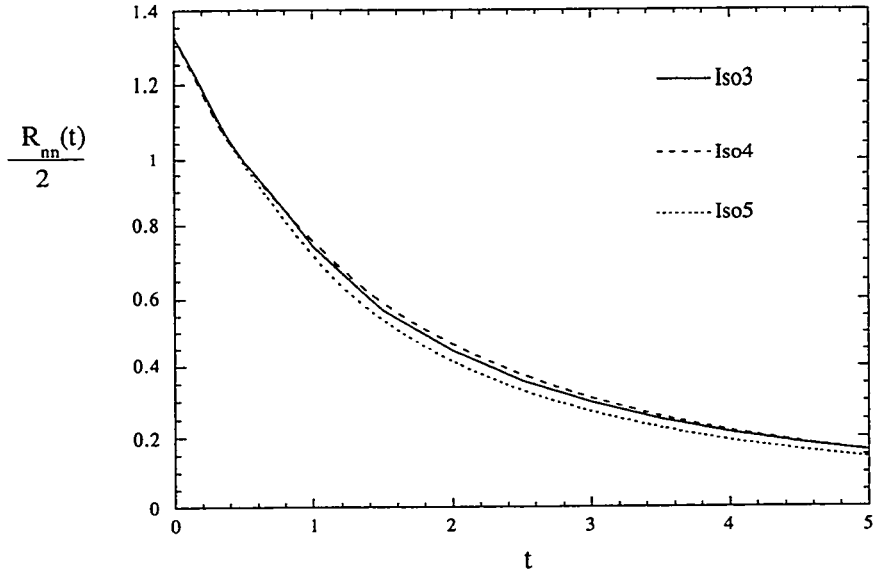

Figure 5.13: Total turbulent kinetic energy density evolution for Runs Iso3 (nearly constant-density), Iso4 (light fluid moving fast) and Iso5 (heavy fluid moving fast)

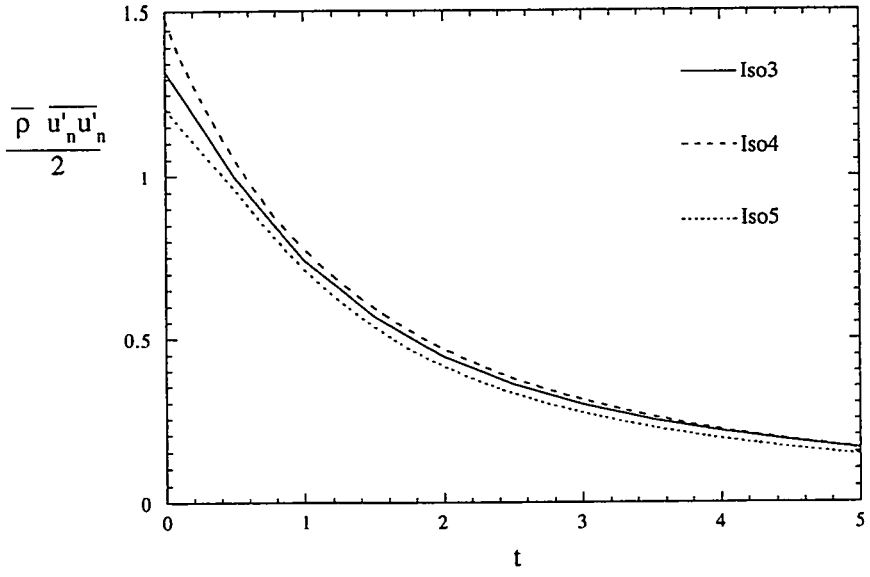

Figure 5.14: Evolution of $\overline{\rho}\ \overline{u'_n u'_n}$ for Runs Iso3 (nearly constant-density), Iso4 (light fluid moving fast) and Iso5 (heavy fluid moving fast)

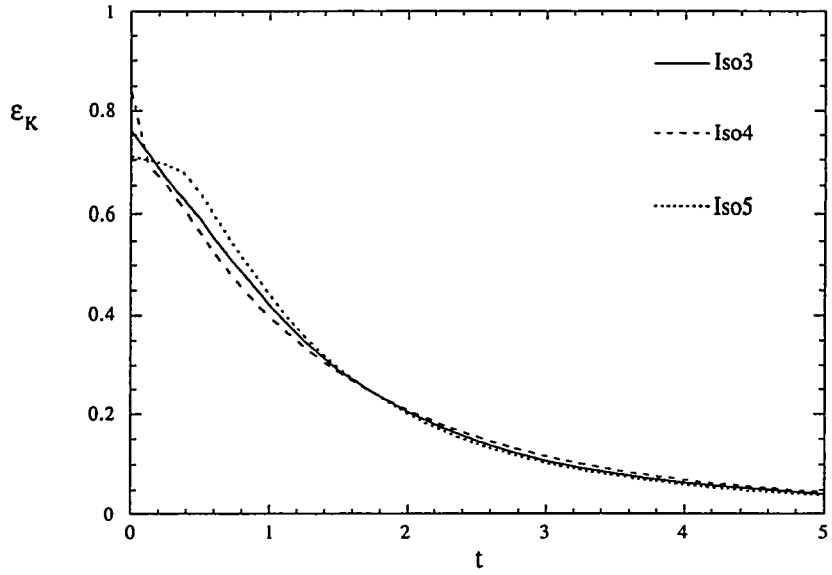

Figure 5.15: Total kinetic energy density dissipation rate for Runs Iso3 (nearly constant-density), Iso4 (light fluid moving fast) and Iso5 (heavy fluid moving fast)

due to the initial velocity field having the largest mean squared-velocity. Likewise, for Iso5, the dissipation rate is smallest due to the initial velocity field having the smallest mean squared-velocity. The dissipation rate for Iso4, however, quickly (for $t < 0.2$) becomes smaller than for the other two cases. As a result, the total kinetic energy density for this case decays slightly slower than for the other two cases (see Fig. 5.13). The dissipation rate for Iso5 quickly ($t < 0.2$) becomes largest. As a result, the total kinetic energy density for this case decays faster than for the other two cases (see Fig. 5.13). This can be seen more clearly in Fig. 5.16 which shows the time scale for the decay of the total kinetic energy density for these three cases. At times less than 0.2 the time scale is largest for Iso5 and smallest for Iso4. After this time and up to a time of about 2.4, the time scale of decay is largest for Iso4 and smallest for Iso5. After a time of 2.4 the nearly constant-density case, Iso3, has the largest time scale of decay.

Figure 5.17 shows the decay of $\overline{\rho' u_n' u_n'}/2$ as a function of time. In the nearly constant-density case, this triple correlation, $\overline{\rho' u_n' u_n'}/2$, is nearly zero due to the small density fluctuations. In the variable-density cases the triple correlation terms are initially nonzero, being positive for Iso5 and negative for Iso4. This triple correlation

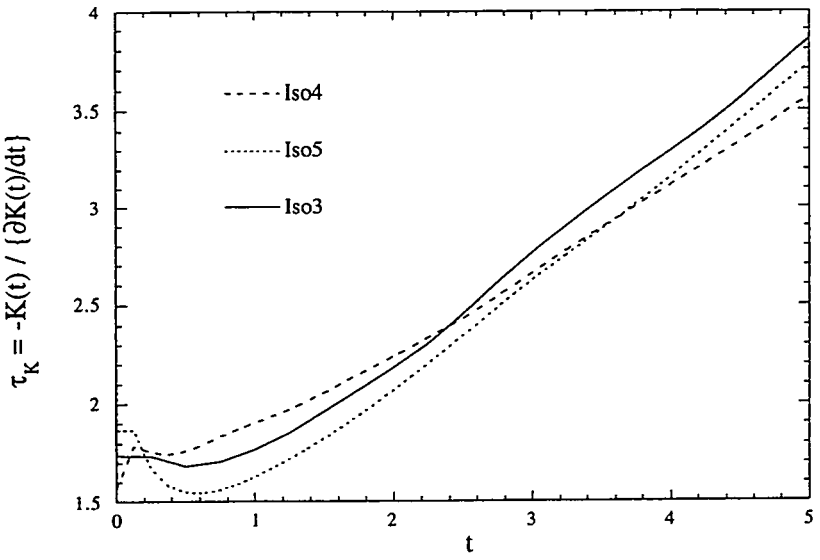

Figure 5.16: Total kinetic energy density time scale for decay for Runs Iso3 (nearly constant-density), Iso4 (light fluid moving fast) and Iso5 (heavy fluid moving fast)

decays faster for case Iso5 than for Iso4. When these triple correlations have decayed away, the mean squared-velocity term is equal to the total kinetic energy density [see eq. (4.2)].

Fast moving, light density case

In this section is discussed in more detail the energy decay for case Iso4. Equation (4.4) is the evolution equation for the total kinetic energy density, $\overline{\rho u_n' u_n'}/2$. Figure 5.18 contains plots of each term of this equation as a function of time for Run Iso4. This plot shows that the decay of total kinetic energy density is due to viscous dissipation, as dilatation effects are negligible.

To study the evolution behavior of the total kinetic energy in more detail, evolution equations can be written for each term of the total kinetic energy density, i.e., for each term on the right side of eq. (4.2). The evolution equation for $\overline{\rho}\ \overline{u_i' u_i'}/2$ is given as (for statistically homogeneous flow)

$$\underbrace{\frac{\partial}{\partial t}\left\{\frac{1}{2}\overline{\rho}\ \overline{u_n' u_n'}\right\}}_{A} = \underbrace{\frac{\overline{\rho}}{2}\ \overline{u_n' u_n' \frac{\partial u_j'}{\partial x_j}}}_{B} - \underbrace{\overline{\rho}\ \overline{\frac{u_n'}{\rho}\frac{\partial p}{\partial x_n}}}_{C} + \underbrace{\overline{\rho}\ \overline{\frac{u_n'}{\rho}\frac{\partial \tau_{nj}'}{\partial x_j}}}_{D}. \tag{5.1}$$

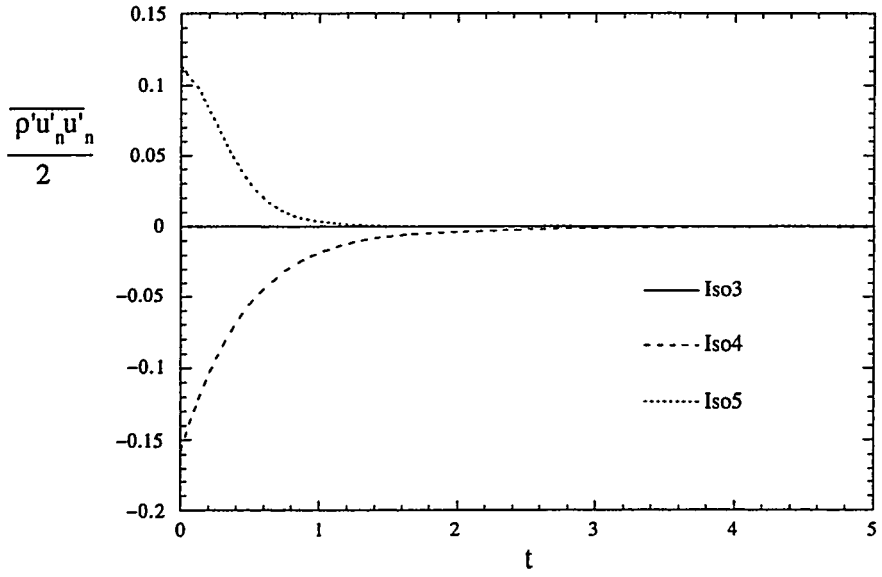

Figure 5.17: Evolution of $\overline{\rho' u_n' u_n'}$ for Runs Iso3 (nearly constant-density), Iso4 (light fluid moving fast) and Iso5 (heavy fluid moving fast)

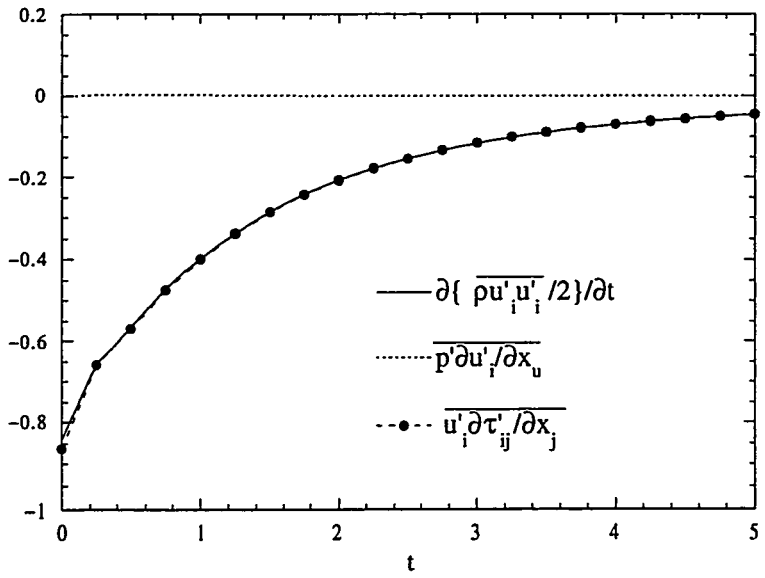

Figure 5.18: Terms in the evolution equation [eq. (4.4)] for total kinetic energy density for Run Iso4

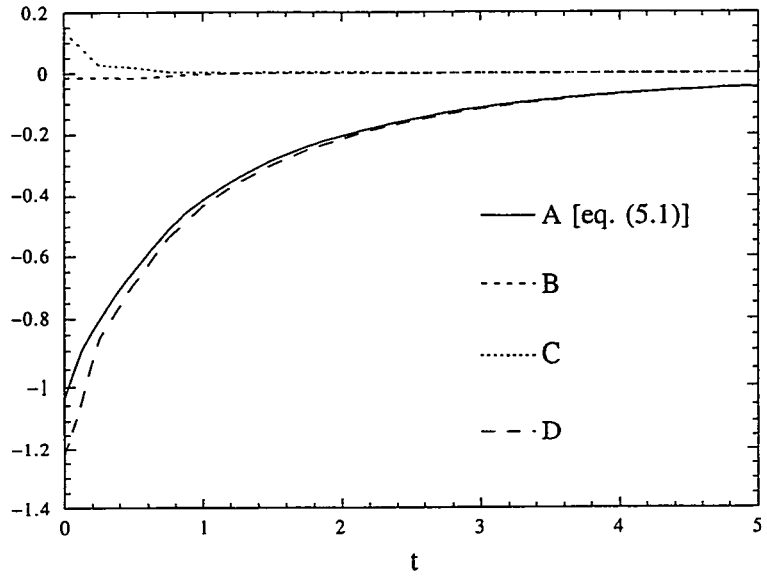

Figure 5.19: Contributing terms in the evolution equation for $\overline{\rho}\ \overline{u_i' u_i'}/2$ [eq. (5.1)] for Run Iso4

The first term on the right side, B, represents production/destruction of the mean-squared velocity due to dilatation/contraction effects and vanishes in an immiscible problem. The second term, C, is a modified pressure-work that acts against the turbulence. The third term, D, represents the destruction of turbulence due to viscous effects. Figure 5.19 plots each term of eq. (5.1) as a function of time. The decay of $\overline{\rho}\ \overline{u_i' u_i'}/2$ is mostly due to viscous dissipation. The modified pressure-work term slightly dampens the decay of $\overline{\rho}\ \overline{u_n' u_n'}/2$ and there is a small increase in the energy decay rate from term B.

The evolution equation for $\overline{\rho' u_n' u_n'}/2$ is

$$\underbrace{\frac{\partial}{\partial t}\left\{\frac{1}{2}\overline{\rho' u_n' u_n'}\right\}}_{A} = \underbrace{-\overline{\rho}\ \overline{u_n' u_n' \frac{\partial u_j'}{\partial x_j}}}_{B} \underbrace{- \overline{\frac{\rho' u_n'}{\rho}\frac{\partial P}{\partial x_n}}}_{C} + \underbrace{\overline{\frac{\rho' u_n'}{\rho}\frac{\partial \tau_{nj}'}{\partial x_j}}}_{D}. \tag{5.2}$$

Figure 5.20 plots each term of eq. (5.2) as a function of time. The decay of $\overline{\rho' u_n' u_n'}/2$ is, again, mostly due to viscous dissipation. The decay is dampened by the pressure-work term and there is an enhancement from dilatation effects.

Figure 5.21 shows a two dimensional slice of the x-y plane for run Iso4 at $t = 0.75$. The horizontal axis is the x-direction and the vertical axis is the y-direction. The

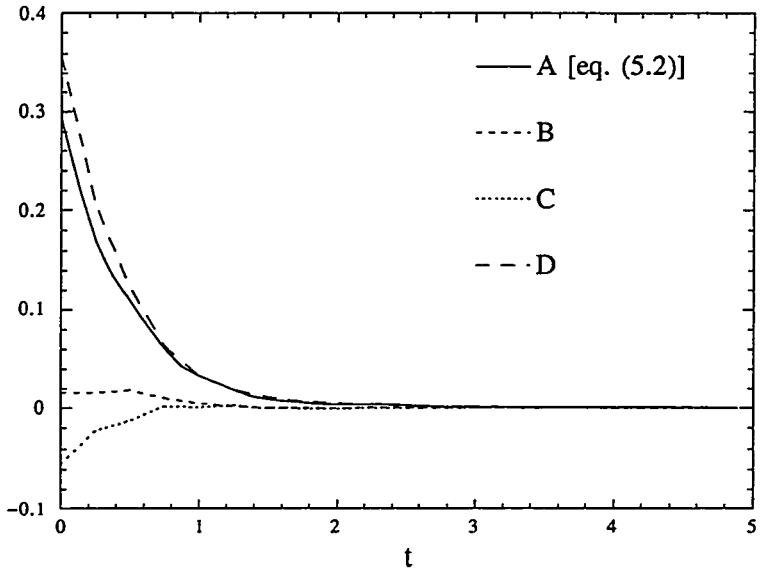

Figure 5.20: Contributing terms in the evolution equation for $\overline{\rho' u_i' u_i'}/2$ [eq. (5.2)] for Run Iso4

color field represents values of density with the orange being the heaviest and the purple being the lightest. The other colors represent a mixture of the two fluids with the green being the mean density. The contours are of the fluctuating pressure field with the solid lines representing positive fluctuations and the dashed lines representing negative fluctuations. The vectors give the magnitude and direction of the x-y velocity. The scale difference between the initial density field and the initial velocity field is evident, as it appears that the eddy size is somewhat larger than the density "blob" size. In this case, where the large velocity magnitudes are initially associated with the negative density fluctuations, the regions of higher velocities are to some extent associated with the low density regions and regions of the mixture of the two fluids (i.e., the interface between the heaviest and lightest fluids). Jetting occurs along the interface because the interface is being squeezed by motion of the heavy and light regions. The pressure field does not appear to be correlated with the density field, though there does appear to be regions of mixed fluid that are associated with smaller pressures. There are also regions between the heavy and light fluid where shearing and entrainment occurs. The length scales of the larger density "blobs" appear to be statistically similar to the length scales associated with the lower density "blobs".

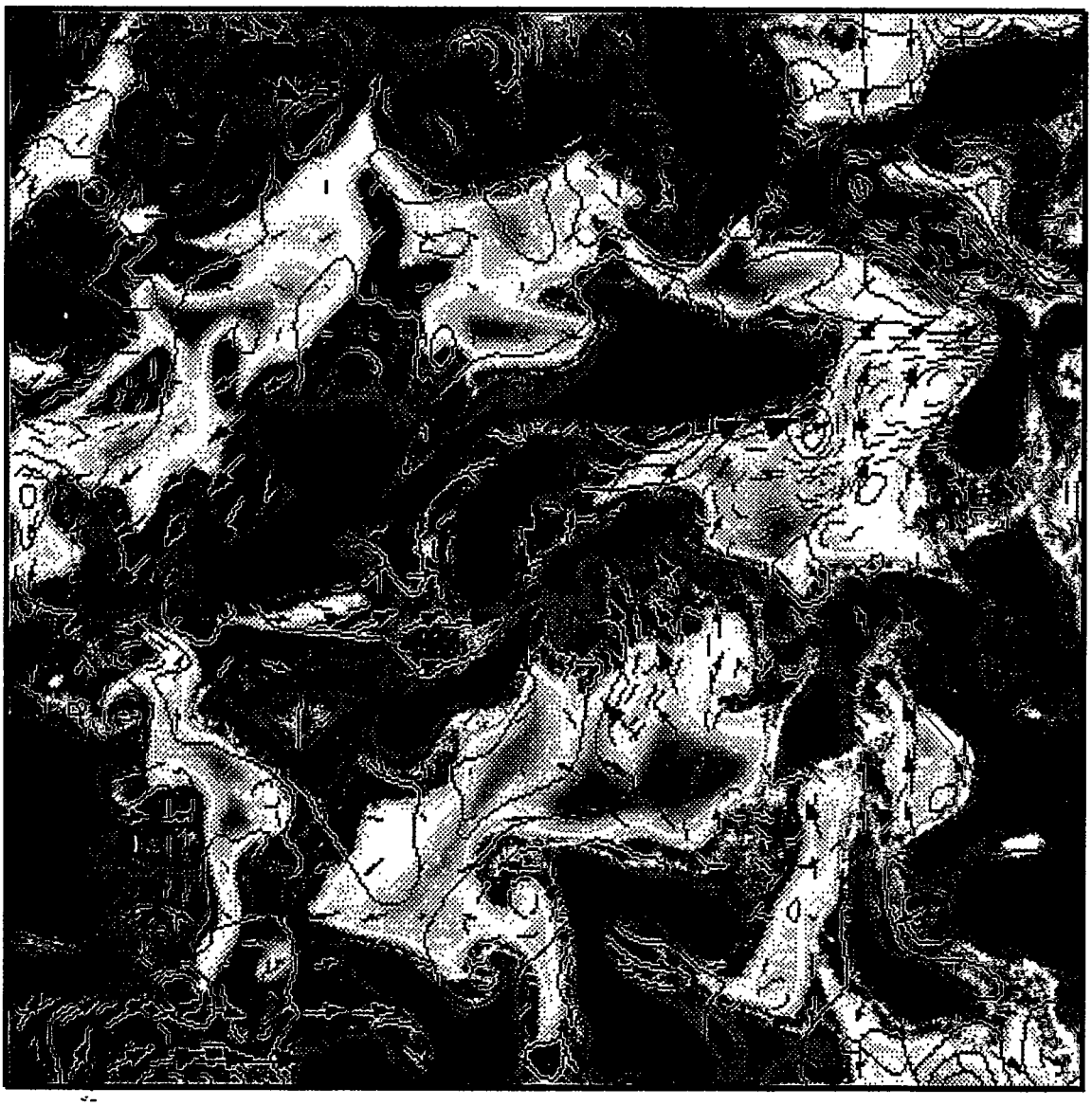

Figure 5.21: Two Dimensional slice of the x-y plane for Run Iso4

Fast moving, heavy density case

In this section is discussed in more detail the energy decay for case Iso5. Figure 5.22 contains plots of each term of the total kinetic energy density evolution equation [eq. (4.4)] as a function of time for this case. The decay of total energy is mostly due to viscous dissipation, although, the pressure-work term acts also as a small source for decay at early times.

Figure 5.23 contains plots of each term of the evolution equation for $\overline{\rho}\ \overline{u_n' u_n'}/2$ [eq. (5.1)] as a function of time. This shows that the decay of $\overline{\rho}\ \overline{u_n' u_n'}/2$ is also mainly due to viscous dissipation. The modified pressure-work term acts to dampen the decay at early times and there is a small source for decay due to dilatation/contraction effects from term B. For times greater than 1.5 all the decay is due to viscous dissipation.

Equation (5.2) describes the evolution of the triple correlation, $\overline{\rho' u_n' u_n'}/2$ and Fig. 5.24 contains plots of each term for this triple correlation as a function of time. This shows that, for times less than 0.25, the decay of this quantity is due to contributions from the modified pressure-work, viscous dissipation and dilatation/contraction effects, the modified pressure-work term being the largest contribution. The decay due to the modified pressure-work term occurs because there is a larger loss of energy due to the decay of the density field in this case (where the large velocity magnitudes are associated with the positive density fluctuations) than there is in the previous case (where the large velocity magnitudes are associated with the negative density fluctuations). More specifically, as the negative fluctuations decay, there is a dampening of total energy decay because the decay of negative fluctuations represents an increase in the density associated with that negative fluctuation.

Figure 5.25 shows a two dimensional slice of the x-y plane for run Iso5 at $t = 0.75$. The horizontal axis is the x-direction and the vertical axis is the y-direction. The color field represents the density with the orange being the heaviest and the purple being the lightest. The other colors represent a mixture of the two fluids with the green being the mean density. The contours are of the fluctuating pressure field, with the solid lines representing positive fluctuations and the dashed lines representing negative fluctuations. The vectors give the magnitude and direction of the x-y velocity. This case, where the larger velocity magnitudes are initially associated with positive density fluctuations, the configurations appear to be quite different than for the Iso4 case (see Fig. 5.21). The initial density fields for these two cases are the

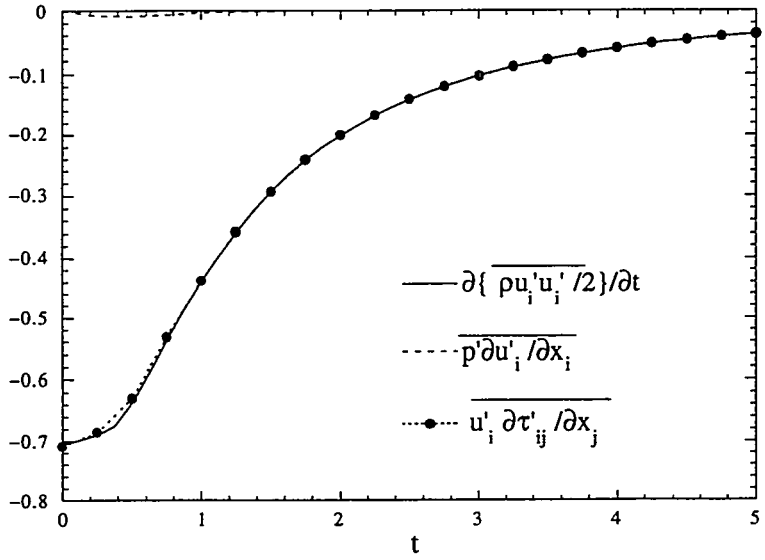

Figure 5.22: Terms in the evolution equation [eq. (4.4)] for total kinetic energy density for Run Iso5

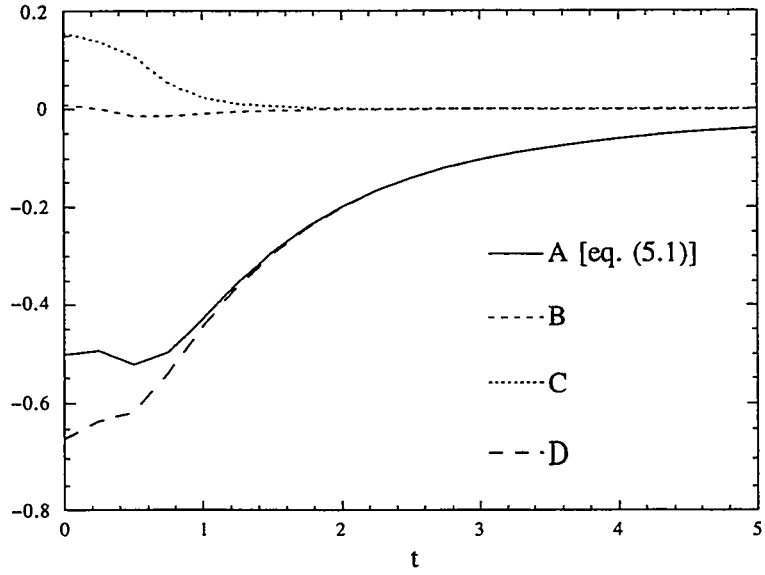

Figure 5.23: Contributing terms in the evolution equation for $\overline{\rho}\ \overline{u_i' u_i'}/2$ [eq. (5.1)] for Run Iso5

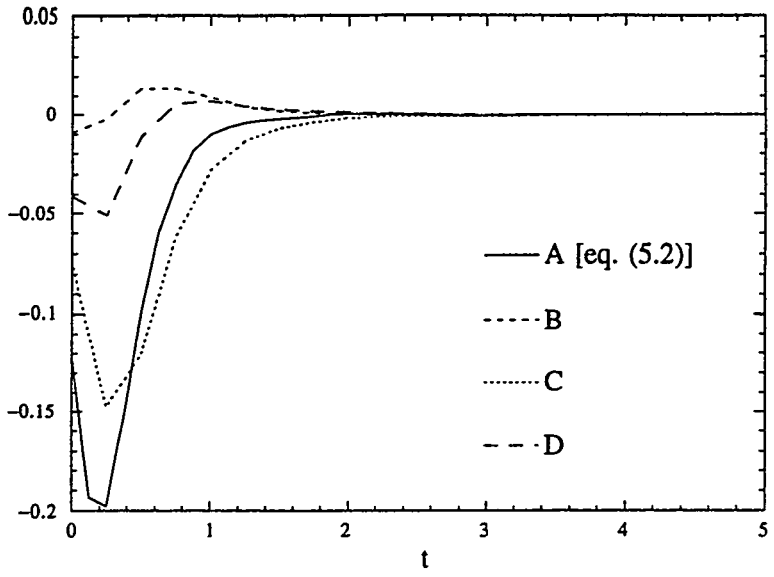

Figure 5.24: Contributing terms in the evolution equation for $\overline{\rho' u_i' u_i'}/2$ [eq. (5.2)] for Run Iso5

same so, in general, the structure is similar at this time for the two cases. For run Iso5, however, the length scales associated with the density field are smaller. Also, there are larger regions of mixed fluid. For this case (run Iso5), it appears that the lower pressure is predominantly associated with higher densities. Again, there are shear regions between the two fluids where entrainment appears to occur.

Figure 5.25: Two Dimensional slice of the x-y plane for Run Iso5

Decay of the density fields

It was shown that the decay of $b(t) = -\overline{\rho' v'}$ and of $B(t) = \overline{\rho'\rho'}/\overline{\rho}^2$ were approximately the same for the nearly constant-density case. For the cases where the density fluctuations are large, the decay of these two quantities are different. Figure 5.26 shows the decay of these quantities for case Iso4: here $b(t)$ is decaying faster then $B(t)$ at early times. At a time of $t = 1.5$ in the simulation, however, the two quantities are nearly the same, which is expected in the limit as the density fluctuations tend to zero. In case Iso5, the decay behavior of $b(t)$ and $B(t)$ is similar and is not presented here. Figure 5.27 compares the decay of $b(t)$ for both cases Iso4 and Iso5, showing that $b(t)$ decays slightly faster for case Iso4. This is because the dissipation for $b(t)$ is larger (at early times) for case Iso4, due to the larger initial mean square-velocity. Recall that the decay of $b(t)$ is driven by a correlation between the fluctuating specific volume and the velocity divergence [see eq. (4.17)]; therefore, as the initial velocities increase, so too does the initial dissipation rates of the density field. The decay of $B(t)$ for these two cases shows similar behavior and is not presented here. Figure 5.28 shows the evolution of the dissipation rate for $b(t)$ as a function of time for these two cases. At early times the dissipation rate for case Iso4 is larger, while at intermediate times the dissipation rate for case Iso5 is larger and at late times the dissipation rates are similar. For case Iso4, the dissipation rate peaks at an earlier time than case Iso5, indicating that molecular mixing occurs sooner in that case.

Figures 5.29 and 5.30 show the evolution of the pdf of the density field for cases Iso4 and Iso5. Comparing these two figures, the feature that immediately stands out is the skewed behavior of the pdf's as they evolve. For Run Iso4, the pdf is skewed to the negative side of the mean density of 1. For Run Iso5, the pdf is skewed to the positive side of the mean density of 1. The physical explanation for this behavior possibly lies in the entrainment rates of the heavy and light fluid into the mixing region. It has been observed (see, e.g., Dimotakis (1986) [28]) that, in spatially growing shear layers, an unequal amount of fluid is entrained from each of the freestreams, resulting in a mixed fluid that favors the high-speed fluid. The first experiments to show this were the incompressible, variable-density shear layer experiments of Brown and Roshko [15]. Brown showed [16] that the fluid associated with the higher velocities had higher entrainment rates into the mixing layer. If the low density fluid has higher velocity magnitudes (a case where $\overline{\rho' u_n' u_n'}$ is negative)

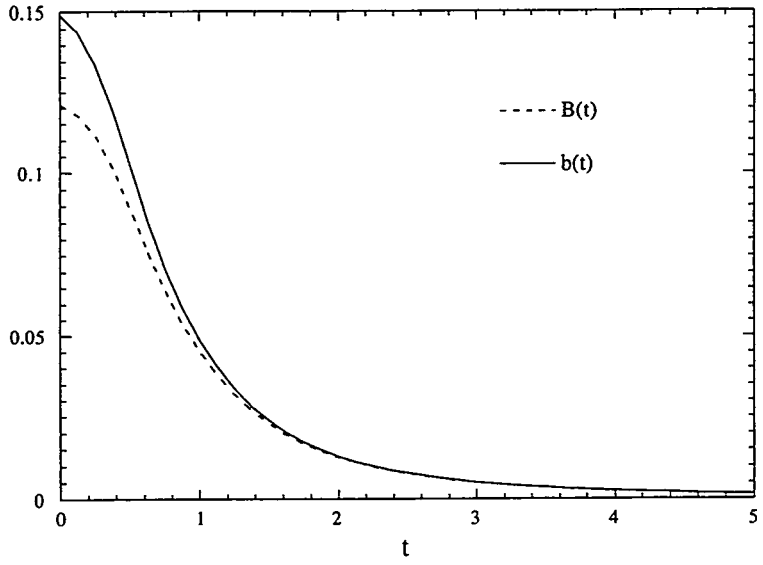

Figure 5.26: Evolution of $b(t) = -\overline{\rho' v'}$ and $B(t) = \overline{\rho' \rho'}/\overline{\rho}^2$ for Run Iso4

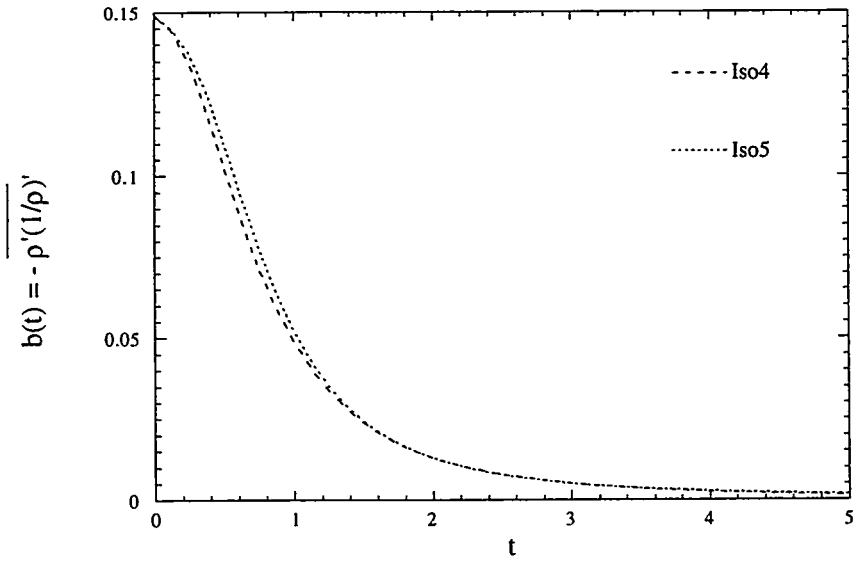

Figure 5.27: Evolution of $b(t) = -\overline{\rho' v'}$ for Runs Iso4 and Iso5

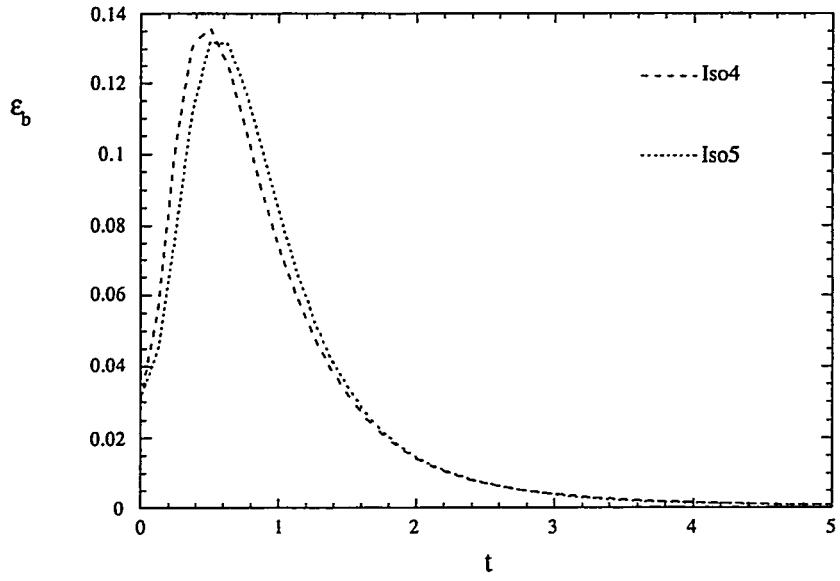

Figure 5.28: $b(t)$ dissipation rate evolution for Runs Iso4 and Iso5

then the low density fluid will entrain faster into the mixing region than the high density fluid. Likewise, if the high density fluid has higher velocity magnitudes (a case where $\overline{\rho' u_n' u_n'}$ is positive) then the high density fluid will entrain faster into the mixing region than the low density fluid. This behavior in variable-density shear layers can explain the behavior of the skewed pdf's of the density field shown here. In case Iso4, the low density fluid has relatively larger velocity magnitudes so that the triple correlation is negative and the entrainment rate of the low density fluid into the mixing region (the interface between the two fluids) is larger then that for the high density fluid. As a result the pdf of the density field evolves in a skewed manner with the skew to the negative of the mean density. Likewise, in case Iso5 the high density fluid has relatively larger velocity magnitudes so that the triple correlation is positive and the entrainment rate of the high density fluid into the mixing region is larger then for that of the low density fluid. As a result the pdf of the density field is evolving with a skew to the positive side of the mean density.

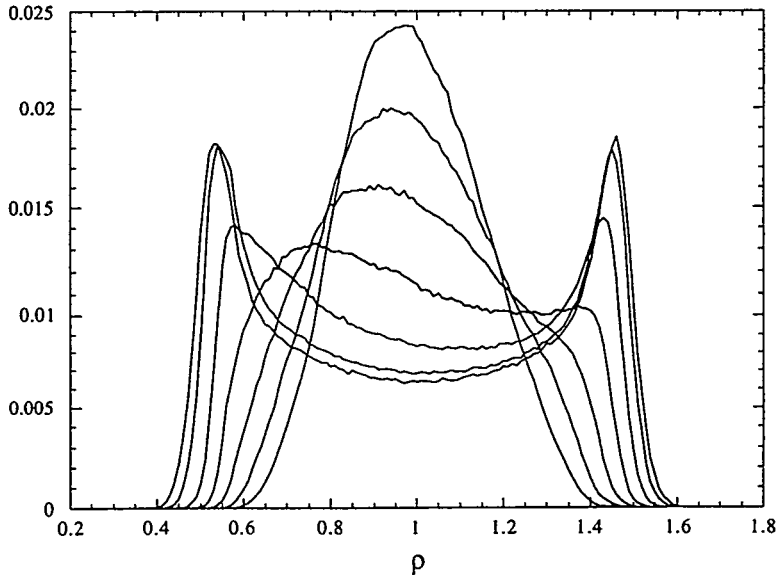

Figure 5.29: Density pdf evolution, $t = 0.0$ to 1.5 by 0.25, for Run Iso4

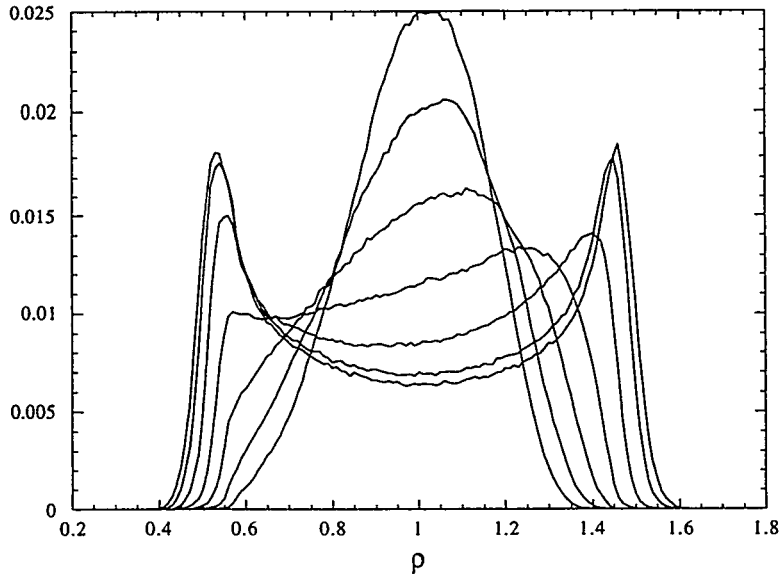

Figure 5.30: Density pdf evolution, $t = 0.0$ to 1.5 by 0.25, for Run Iso5

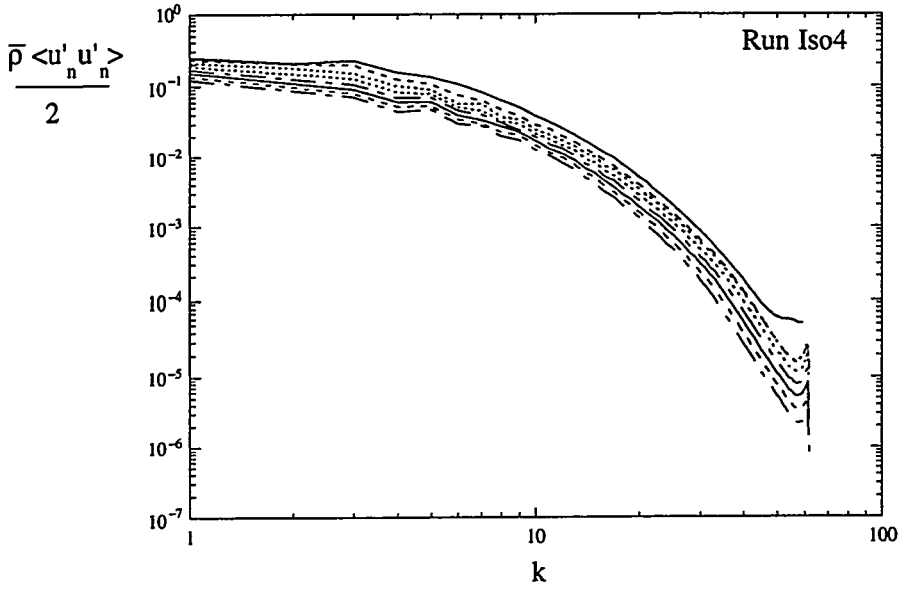

Figure 5.31: Spectral evolution of $\overline{\rho}u'_n u'_n/2$ for Run Iso4

Spectral evolution of the components of the kinetic energy density

The total turbulent kinetic energy density is given by eq. (4.2) as

$$\frac{1}{2}R_{ii}(t) = \frac{1}{2}\overline{\rho u'_i u'_i} = \frac{1}{2}\overline{\rho}\ \overline{u'_i u'_i} + \frac{1}{2}\overline{\rho' u'_i u'_i}$$

for decaying, isotropic variable-density turbulence. Given in this section is the spectral evolution of each term of this equation for runs Iso4 and Iso5. Figures 5.31 and 5.32 show the spectral evolution of $\overline{\rho}u'_n u'_n/2$ for these cases at a sequence of times from $t = 0$ to 3.5 in increments of 0.5. For run Iso4, the spectrum of $\overline{\rho}u'_n u'_n/2$ is decaying at all wavenumbers (i.e., full spectrum decay). For run Iso5, energy is building up the high wave numbers for times less than 1 before the spectrum reaches full spectrum decay.

Figures 5.33 and 5.34 show the spectral evolution of $\rho' u'_n u'_n/2$ for runs Iso4 and Iso5 for a sequence of times from $t = 0$ to 3.5 in increments of 0.5. For run Iso4, the spectrum of $\rho' u'_n u'_n/2$ is negative at all wavenumbers. As this spectrum evolves the values at each wavenumber decreases with time just as the spectrally integrated value of this spectrum, $\overline{\rho' u'_n u'_n}/2$, decays in time. For run Iso5, the spectrum of $\rho' u'_n u'_n/2$ is positive at all wavenumbers except at $k = 2$ where it is slightly negative. At the next time given, $t = 0.5$, the maximum of the spectrum has decreased and there has

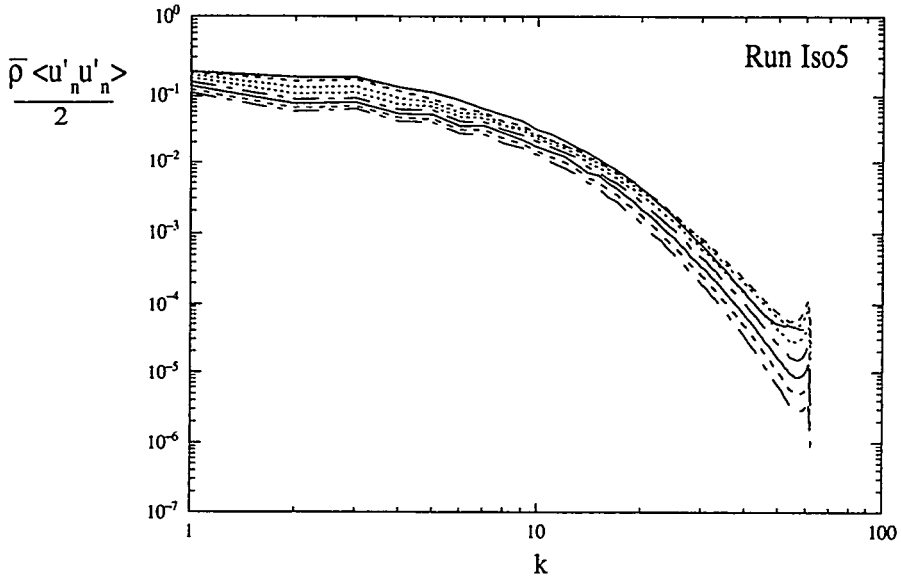

Figure 5.32: Spectral evolution of $\overline{\rho}u'_n u'_n/2$ for Run Iso5

been a slight increase at the high wavenumbers. Also, the minimum in the spectrum is at a larger negative value that at the initial time given. After this time the values of the spectrum are decaying to zero at all wavenumbers.

5.4.4 Case with a nearly constant density initially strongly dependent on the velocity field

In this section are described the results of two nearly constant-density cases with an initial density ratio of 1.02. The initial density fields for both cases are the same. The first case is Run Iso6. The initial velocity field used in this case is the same velocity field used in Run Iso4, so that the velocity is weighted such that the large velocities are associated with the negative density fluctuations and the statistical dependence is strong between the initial velocity and density fields. This is the same as initializing the velocity fields using Method A (see Section C.3 in the appendix) with $\vec{A}' = \vec{A}/(\overline{\rho} + 60\rho')$ where $\overline{\rho}$ is the mean density and ρ' are fluctuations about the mean. In the second case, Run Iso8, the initial velocity field is the same that is used in Run Iso5 and has a strong statistical dependence on the initial density field and weighted such that the large velocities are associated with positive fluctuations of the density. This is the same as using Method B (see Section C.3 in the appendix) with

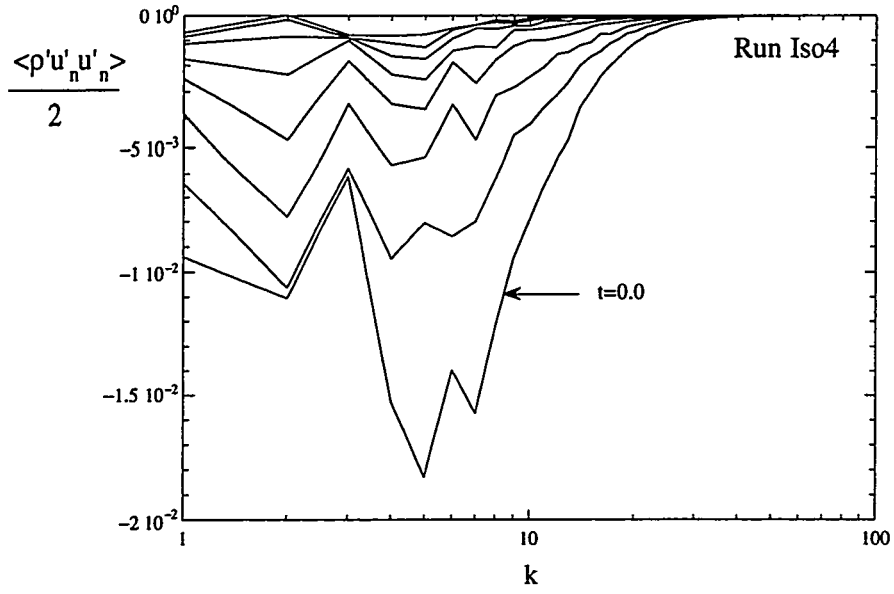

Figure 5.33: Spectral evolution of $\rho' u_n' u_n'/2$ for Run Iso4

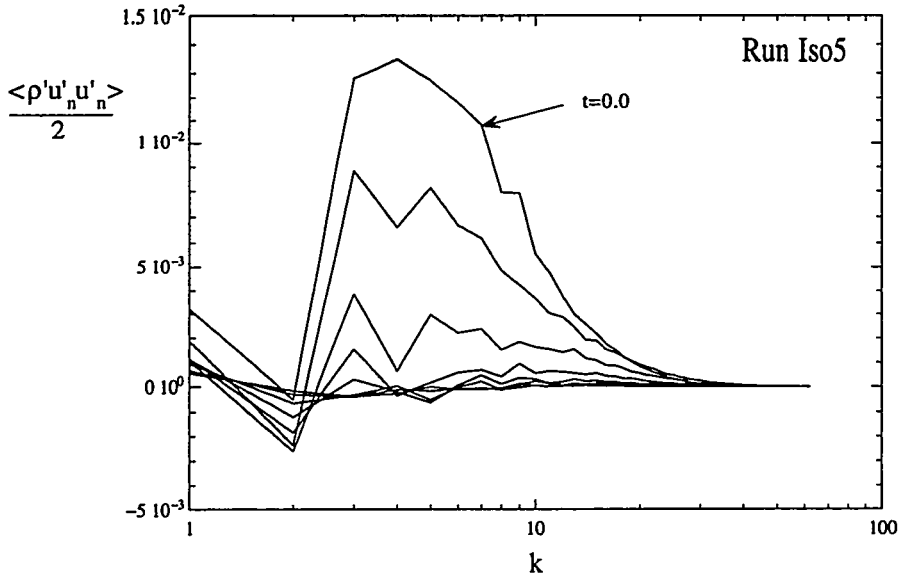

Figure 5.34: Spectral evolution of $\rho' u_n' u_n'/2$ for Run Iso5

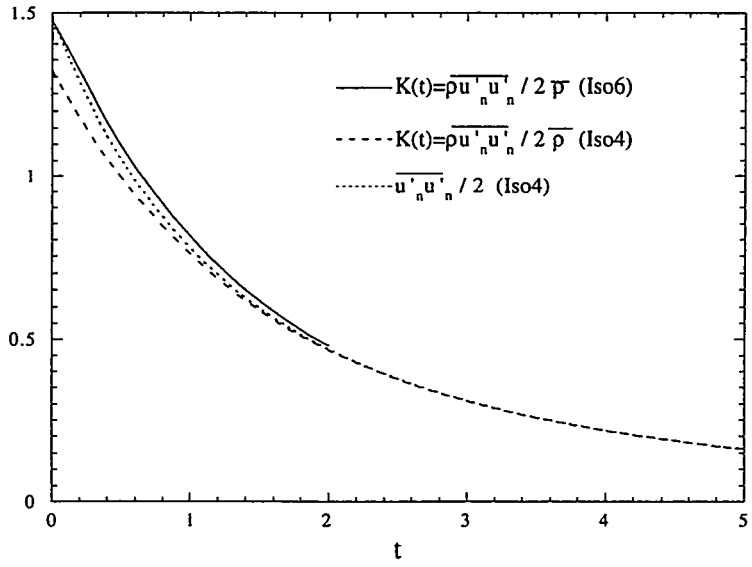

Figure 5.35: Total energy evolution for Runs Iso4 (large initial density fluctuations) and Iso6 (small initial density fluctuations). Both cases have strong initial statistical dependence such that the large velocities are associated with the negative density fluctuations

$\vec{A}' = (\overline{\rho} + 60\rho')\vec{A}$. The initial velocity field and density field statistics are given in Table 4.1. Comparisons of the total turbulent kinetic energy evolution will be made between runs Iso4 and Iso6 and runs Iso5 and Iso8. The evolution of the pdf's of the density field for runs Iso6 and Iso8 are also examined.

Because the density fluctuations are small in runs Iso6 and Iso8, the density field should behave as a passive scalar and not have strong effect on the energy decay processes of the flow. Figure 5.35 shows the evolution of the kinetic energy density, $K(t) = \overline{\rho u_n' u_n'}/2\overline{\rho}$, for runs Iso4 and Iso6 and the evolution of $\overline{u_n' u_n'}/2$ for run Iso4. $K(t)$ is not the same for both cases since the density fields are initially different. Also, $K(t)$ for case Iso6 and $\overline{u_n' u_n'}/2$ for case Iso4 are initially the same since the velocity fields are initially nearly the same and the density fluctuations are small for case Iso6. From this figure is seen that, as the flows evolve $K(t)$ for case Iso6 approaches that of case Iso4. This occurs at a time at which the large density fluctuations in run Iso4 have decayed appreciable (approximately $t \approx 2$).

Figure 5.8 shows the evolution of the pdf of the density field for run Iso3, which has an initially weak dependence between the velocity and density fields. In this

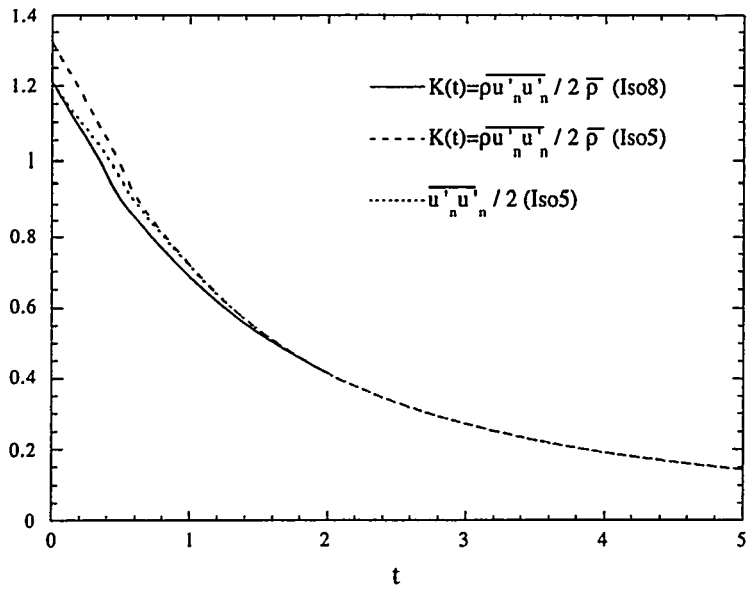

Figure 5.36: Total energy evolution for Runs Iso6 (large initial density fluctuations) and Iso8 (small initial density fluctuations). Both cases have strong initial statistical dependence such that the large velocities are associated with the positive density fluctuations

nearly constant-density case, where the initial velocity and density fields had only a small statistical dependence, the pdf evolves nearly symmetrically about the mean density. Figures 5.37 and 5.38 show the evolution of the pdf's of the density fields for runs Iso6 and Iso8, which initially has a strong dependence between the velocity and density field, though the initial fluctuations are small. These figures show that there is a significant effect on the evolution of the pdf due the the dependence of the velocity on the initial density field. The pdf for the case where the large velocity magnitudes are associated with the negative density fluctuations (Iso6) is strongly skewed negative of the mean value. For the case where the large velocity magnitudes are associated with the positive density fluctuations (Iso8), the pdf is strongly skewed positive of the mean value. The evolution of the pdf's of these density fields, which are essentially passive, looks remarkably similar to the analogous evolution for runs Iso4 (see Fig. 5.29) and Iso5 (see Fig. 5.30), which initially have large density variations. Since the density fluctuations are small in runs Iso6 and Iso8, the triple correlation terms, $\overline{\rho' u_n' u_n'}$, are also very small. The statistical dependence is such that, for run Iso6, the large velocity magnitudes are associated with the negative density

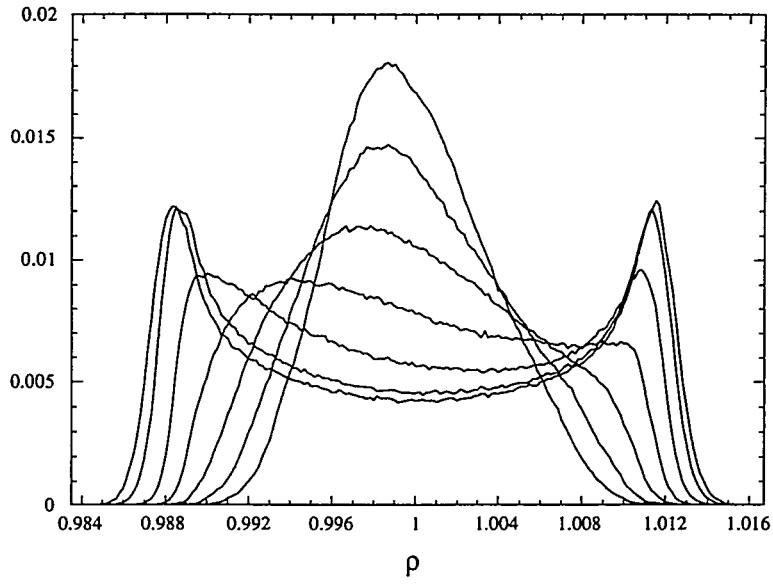

Figure 5.37: Density pdf evolution, $t = 0.0$ to 1.5 by 0.25, for Run Iso6

fluctuations (i.e., the low density field) so that the triple correlation term, $\overline{\rho' u_n' u_n'}$, is slightly negative (though very small). It has been argued in the previous sections that, for this situation, the skewness seen in the pdf is due to a higher entrainment rate for the low density fluid into the mixing region than for the high density fluid. Likewise, for run Iso8, the statistical dependence is such that the large velocities are associated with the positive density fluctuations (i.e., the high density fluid) so that the triple correlation term, $\overline{\rho' u_n' u_n'}$, is slightly positive (though also very small). It has also been argued that for this situation the skewness seen in the pdf is due to a higher entrainment rate for the high density fluid into the mixing region than for the low density fluid. This same explanation appears to hold, even though the density fields are basically passive. This is not surprising as the this entrainment behavior is seen in spatially evolving constant density mixing layers [16, 28].

5.5 Results for initial Gaussian pdf's

In this study, the effects of using initial density fields that have a Gaussian distribution (see Appendix D for initialization procedure) instead of a bimodal distribution are also addressed. The results of this work are not presented, however, because no new conclusions are contributed. The effects observed using the bimodal distribution are

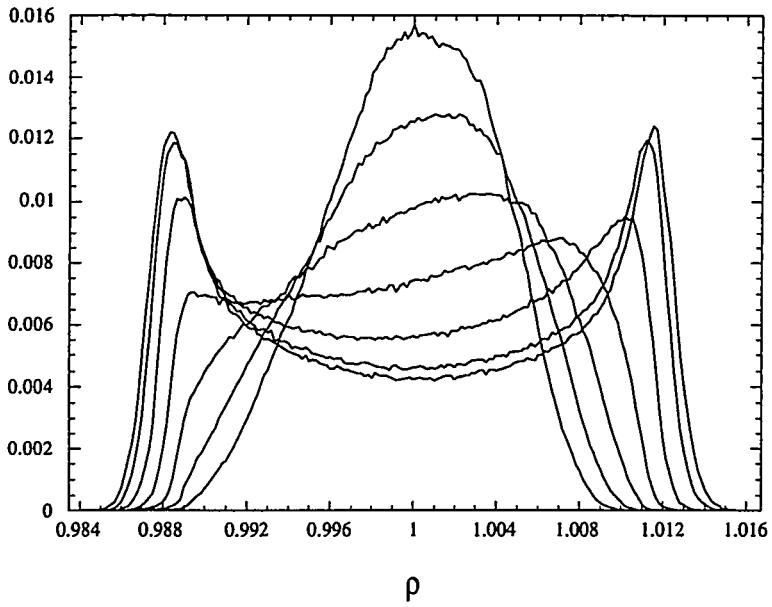

Figure 5.38: Density pdf evolution, $t = 0.0$ to 1.5 by 0.25, for Run Iso8

also present in the results using the Gaussian distribution. The effects of large density fluctuations seen in the results with the initial bimodal density pdf distribution are not as strong when the Gaussian distribution is used. When the density field has a Gaussian distribution, the most probable density is the mean density itself. The mean density in this study corresponds with a completely mixed fluid, and the density field is at a constant density. The bimodal distribution is different in that the most probable density is either a high density or a low density, or some value in between depending on the stage of the flow in the mixing process. At late times, the initial bimodal distribution evolves to a nearly Gaussian form, and it can be argued that a Gaussian distribution represents the late stages of the mixing of a bimodal scalar field.

5.6 Summary

The results presented in this chapter clearly identify the importance of the triple correlation term, $\overline{\rho' u_n' u_n'}$, on variable density flow. In Chapter 4, cases where the initial velocity and density fields were statistically independent were examined. It was shown that the triple correlation was initially nearly zero and did not grow to a large enough value to effect the statistical behavior of the decay. In this chapter, a

statistical dependence was initially imparted between the velocity and density fields and flow was examined. The triple correlation term is initially nonzero, its sign dependent on the type of statistical dependence. A positive sign indicates that the higher velocity magnitudes are associated with the larger density, while a negative sign indicates that the higher velocity magnitudes are associated with the smaller density.

Some conclusions can be drawn from this study of the isotropic decay of variable-density turbulence when compared with a decaying, isotropic constant-density turbulent flow. If, for both cases, the initial total turbulent kinetic energy densities are the same, the initial energy dissipation rates are different and depend on the statistical dependence between the velocity and density fields. If the triple correlation, $\overline{\rho' u_n' u_n'}$, is initially negative, the energy dissipation rate is the highest, while the case where the triple correlation is positive has the smallest energy dissipation rate.

It has also been seen that the pdf of the density field is *not* symmetric about the mean density and it is argued that this is due to different entrainment rates for the high and low density fluids into the mixing region (the mixed interface between the two fluids). This conclusion is based on analogy to numerous shear layer results (see e.g., Dimotakis (1986) [28]), the first of which are the results of Brown [16] in his study of the Brown and Roshko [15] variable-density mixing layer experiments. These shear layer studies showed that a spatially-growing shear layer entrains an unequal amount of fluid from each of the free streams, which results in a mixed fluid composition that favors the high-speed fluid. It has been seen in the results presented in this dissertation that the sign of the triple correlation, $\overline{\rho' u_n' u_n'}$, reflects this entrainment rate behavior.

Another important result has implications for passive scalar problems. If the velocity field is statistically dependent on density field but the density fluctuations are small so that the density field is passive, the pdf of the density field is not symmetric about its mean value. It is easily imagined that one could create a passive scalar experiment where there is a statistical dependence between the velocity and density fields.

Finally, it has been observed that, if the initial density field has a Gaussian distribution instead of a bimodal distribution, the same general effects as described in this chapter hold. However, for the cases studies, the Gaussian distribution results

observed are not as strong as in cases which have a bimodal distribution, even though the maximum density fluctuations were nearly equivalent in both cases. This has implications regarding the modeling of variable-density turbulence because inherent in most turbulence models is the assumption that the various quantities are Gaussianly distributed. It has also been seen that the pdf of the initially bimodal density field evolves towards a nearly Gaussian form (skewed and non-skewed depending on the statistical dependence on the velocity and density fields). So it could be argued that a Gaussian distribution for the density field occurs at late stages in the mixing of a bimodally distributed density field.

Chapter 6

BUOYANCY-GENERATED TURBULENCE

6.1 Introduction

The case of a variable-density fluid subjected to a constant (or gravitational) acceleration is also studied in this dissertation. The fluid is initially at rest, and, in the presence of the acceleration, the variations in density act as a source of potential energy for the flow. The potential energy is converted into kinetic energy as the fluid is set into motion. The velocity and density fields are directly correlated since it is the presence of the fluctuations in the density fields that create, through acceleration, motion of the fluid. This motion is resisted by drag and the variable-density field is smoothed by molecular diffusion. As the flow develops and mixing occurs, the source of potential energy diminishes as the density field tends toward a constant mean value. Through the action of viscosity, the kinetic energy is dissipated to heat and the flow eventually comes to rest.

In the case studied here, the gradient of the mean density is zero. Neglecting viscous and diffusion effects, since the extent of the fluid in the direction of the acceleration is unlimited, the acceleration would cause any fluid element to wander an unlimited distance in that direction. Thus, there is an infinite source of energy. In this problem, the potential energy is (1) eroded by diffusion and (2) converted into kinetic energy.

There are several parameters associated with the fluid and its flow that determine the subsequent motion caused by buoyancy forces. The potential energy is represented by statistical parameters that specify the initial random spatial distribution of the density field, e.g., the initial variance of the density. The molecular transport coefficients, the viscosity and diffusivity of the fluid, create sinks for the energy. Another parameter is the body force, i.e., the acceleration. From these parameters the initial state of the flow can be specified. In particular, a Reynolds number can be formulated (discussed below in Section 6.3.2) which characterizes the flow. Higher Reynolds number flows are of greatest interest because it is in these flows that the

motion of the fluid will be the most turbulent, as inertial forces dominate viscous and diffusive forces.

We are aware of only one other attempt to study a spatially homogeneous, buoyancy-driven flow. This is the work of Batchelor, Canuto and Chasnov [7] in which they assumed small density variations and invoked the Boussinesq approximation. Their work is discussed briefly in this chapter. A study of the variable-density problem, without the Boussinesq approximation, is also presented in this chapter. This problem has not previously been reported in the literature. In this dissertation the effects of different initial density ratios at a given Reynolds number are studied, as well as Reynolds number effects at a fixed initial density ratio. Departures from the Boussinesq limit are shown and discussed. For these cases, it is also demonstrated that the mean pressure gradient is not constant in time, and is dependent on the magnitude of the density difference and the Reynolds number.

6.2 List of Buoyancy-driven simulations

Specific conditions for the simulations are chosen in order to study (1) the effects of an increasing initial density ratio and (2) the effects of changing the initial "pseudo-Reynolds" number, R_o, (discussed in Section 6.3). The maximum initial density ratio used in this study is 4. At this density ratio, the numerical results are well resolved; however, for larger initial density ratios the numerical scheme becomes inaccurate at the maximum resolution utilized.

Table 6.1 lists all the simulations of buoyancy-driven turbulence reported in this dissertation. The runs with "Acc" in the run name are for the cases where the Boussinesq approximation (see section 6.4) has not been made. The run with "Bos" in the run name is a case where the Boussinesq approximation has been made (see section 6.3). For all the cases reported the Schmidt number, σ, is unity. For run Acc3c the grid size is 64^3, while for all other "Acc" simulations the grid size is 128^3. For the Boussinesq approximation case, run Bos9, the density field statistics are not given (i.e., ρ_{max}, ρ_{min}, ρ_{max}/ρ_{min} and θ_o) because the initial density distribution is created using the method given by Batchelor, et al. (discussed below in section 6.3) and these parameters are not relevant in that case. For the "Acc" cases the initial density field is created using the method of Eswaran and Pope, discussed in Chapter 4. This procedure creates an initial fluid with regions of high density, ρ_{max}, and low

Table 6.1: List of initial statistics for buoyancy-driven cases

Run No.	R_o	ν	σ	g	ρ_{max}	ρ_{min}	ρ_{max}/ρ_{min}	θ_o
Acc1a	256	7.800e-3	1.0	10.	1.05	0.95	1.105	0.0434
Acc1c	256	8.543e-3	1.0	1.0	1.60	0.40	4.000	0.5206
Acc2c	512	4.272e-3	1.0	1.0	1.60	0.40	4.000	0.5206
Acc3c	64	3.423e-2	1.0	1.0	1.60	0.40	4.000	0.5206
Acc4b	714	2.500e-3	1.0	1.0	1.40	0.60	2.333	0.3480
Bos9	64	1.562e-2	1.0	1.0				

density, ρ_{min}, typified by an integral length scale $l_\rho = 0.53$. The parameter θ_o, defined as $\theta_o = \overline{\rho'\rho'/\rho_o^2}^{\frac{1}{2}}|_{t=0}$, is a nondimensional measure of the initial density variations in the flow. As the initial density variations increase so too does θ_o, while as θ_o decreases the variable-density flow approaches the Boussinesq limit.

Runs Acc1a and Acc1c are made at a Reynolds number (defined below) of $R_o = 256$. Run Acc1c has moderately large initial density variations (such that the density ratio, ρ_{max}/ρ_{min}, equals 4) and in Run Acc1a the initial density variations are small (such that the density ratio equals 1.105) and, as will be shown below, is within the Boussinesq limit. These two simulations are made in order to study the effects of the initial density variation on the subsequent buoyancy-driven motion. Runs Acc1c, Acc2c and Acc3c all have the same initial density variations, a density ratio of 4, and the effects of different R_o are examined. Run Acc4b is made at a Reynolds number of $R_o = 714$ with an initial density ratio of 2.33. At this density ratio, $R_o = 714$ is near the largest Reynolds number that can be computed accurately. Run Bos9 is made to compare with the Boussinesq results of Batchelor, et al. [7].

6.3 Boussinesq Case

Batchelor, Canuto and Chasnov (1992) [7] presented the case of statistically homogeneous, buoyancy-driven turbulence. They assume small density fluctuations in the flow and, therefore, use the Boussinesq approximation in the equations of motion. A brief discussion of their results is presented in this section. We expect that, in the

limit as the density fluctuations tend to zero, the non-Boussinesq variable-density results approach the Boussinesq limit.

6.3.1 Navier-Stokes equations with the Boussinesq approximation

Following Batchelor, et al. [7], the equations of motion are derived for the Boussinesq approximation by first starting with the usual equations for the conservation of mass and momentum [eqs. (2.1) and (2.2)], written here as [7, 52]

$$\frac{\partial \rho}{\partial t} + \mathbf{u} \cdot \nabla \rho + \rho \nabla \cdot \mathbf{u} = 0, \tag{6.1}$$

$$\rho \left(\frac{\partial \mathbf{u}}{\partial t} + \mathbf{u} \cdot \nabla \mathbf{u} \right) = \rho \mathbf{g} - \nabla p + \mu \nabla^2 \mathbf{u}, \tag{6.2}$$

where ρ, p and $\mathbf{u}$ are the fluid density, pressure and velocity.

The Boussinesq approximation is valid [69] when the actual density and pressure fluctuations vary only slightly from their respective means, the vertical scale of motion is small compared with the scale height, and the Mach number is low. Separating the density and pressure into their mean and fluctuating parts gives

$$\rho = \rho_o + \rho' \tag{6.3}$$

and

$$p = p_h + p' \tag{6.4}$$

where $\rho_o = \overline{\rho}$ is the uniform and constant mean value of the density, ρ' is the variation about the mean density, p_h is the hydrostatic pressure corresponding to ρ_o and p' is the fluctuation about the hydrostatic pressure. Assuming low Mach number and small heat or mass transfer, eq. (6.1) becomes

$$\nabla \cdot \mathbf{u} = 0. \tag{6.5}$$

Thus, the velocity field is non-divergent.

Using the Boussinesq approximation, eq. (6.2) becomes

$$\frac{\partial \mathbf{u}}{\partial t} + \mathbf{u} \cdot \nabla \mathbf{u} = \frac{\rho' \mathbf{g}}{\rho_o} - \frac{\nabla (p - \rho_o \mathbf{g} \cdot \mathbf{x})}{\rho_o} + \nu \nabla^2 \mathbf{u}, \tag{6.6}$$

where $\nu = \mu/\rho_o$. The first term on the right side represents changes in the velocity due to the buoyancy force per unit volume. It is the primary source [34] for fluid motion in buoyancy-induced flows. The second term on the right side is the gradient of the pressure change that produces the fluid motion. The pressure difference, called the "motion" pressure [34], can be written as

$$p' = p - \rho_o \mathbf{g} \cdot \mathbf{x} = p - p_h,$$

where p is the actual pressure and p_h is hydrostatic pressure. Thus, the hydrostatic pressure has been removed from the problem in eq. 6.6. The hydrostatic balance can be demonstrated by considering the momentum equation [eq. (6.2)] for a fluid at rest the instant the acceleration is applied, which is

$$\rho \mathbf{g} - \nabla p = 0$$

or

$$\nabla p = \rho \mathbf{g}. \tag{6.7}$$

Thus, in the absence of velocity (at the instant the acceleration is applied), the gradient of the pressure is due to the buoyancy force.

A conservation equation is also needed to describe the evolution of the density variations. This equation is derived from a species concentration equation or the internal energy equation (see, e.g., Lesieur [52]), assuming low Mach number, to be

$$\frac{\partial \rho'}{\partial t} + \mathbf{u} \cdot \nabla \rho' = \mathcal{D} \nabla^2 \rho', \tag{6.8}$$

where $\mathcal{D}$ is the diffusivity of the density. Equations (6.5), (6.6) and (6.8) govern the motion of a buoyancy-driven flow within the Boussinesq limit.

6.3.2 Nondimensionalization

The equations of motion are here solved in nondimensional form. As previously discussed, there are several dimensional parameters associated with the fluid and its flow that determine the motion generated by buoyancy forces. These are the fluid viscosity, diffusivity and the acceleration. Also, a statistical measure of the initial

density variations is used; θ_o is a measure of the dimensionless density variations defined as

$$\theta_o = \left(\overline{\rho'\rho'/\rho_o^2}\right)^{\frac{1}{2}}_{T=0} = \rho^*/\rho_o, \tag{6.9}$$

where

$$\rho^* = \left(\overline{\rho'\rho'}\right)^{\frac{1}{2}}_{T=0} \tag{6.10}$$

is the rms value of the initial density fluctuations. A characteristic length scale is also needed. Here, we choose the length scale, l_o, which characterizes the wavelength at which the initial spatial spectrum of ρ' has its maximum. That is, $l_o = 2\pi/k_m$, where k_m is the wavenumber at which the density spectrum is a maximum. For the density fields studied here, $k_m = 3$ so that $l_o = 2\pi/3$.

It should be noted here that the nondimensionalization proposed in Chapter 2, which is suitable for the study of decaying, isotropic variable-density turbulence, is not suitable for the study of buoyancy-driven turbulence. For a buoyancy-driven problem, within the Boussinesq limit, a careful choice of dimensionless variables are defined in Batchelor, et al. [7], as

$$T = t\left(\frac{g\theta_o}{l_o}\right)^{\frac{1}{2}}, \tag{6.11}$$

$$\mathbf{X} = \frac{\mathbf{x}}{l_o}, \tag{6.12}$$

$$\mathbf{U} = \frac{\mathbf{u}}{(l_o g\theta_o)^{\frac{1}{2}}}, \tag{6.13}$$

$$P = \frac{p - \rho_o \mathbf{g}\cdot\mathbf{x}}{\rho_o l_o g\theta_o}, \tag{6.14}$$

and

$$\Theta' = \frac{\rho' g}{\rho_o g\theta_o} = \frac{\rho'}{\rho^*}. \tag{6.15}$$

Using this nondimensionalization, the equations of motion in the Boussinesq approximation can be rewritten as

$$\nabla \cdot \mathbf{U} = 0, \tag{6.16}$$

$$\frac{\partial \Theta'}{\partial T} + \mathbf{U} \cdot \nabla \Theta' = \frac{1}{\sigma R_o} \nabla^2 \Theta', \tag{6.17}$$

$$\frac{\partial \mathbf{U}}{\partial T} + \mathbf{U} \cdot \nabla \mathbf{U} = j\Theta' - \nabla P + \frac{1}{R_o} \nabla^2 \mathbf{U}, \tag{6.18}$$

where j is the unit vector in the direction of the acceleration. The so-called "pseudo-Reynolds number", R_o, is defined from the characteristic length and velocity scales as

$$R_o = \frac{\left(l_o{}^3 g\theta_o\right)^{\frac{1}{2}}}{\nu}, \tag{6.19}$$

and

$$\sigma = \frac{\nu}{\mathcal{D}}$$

is the Schmidt number. Equations (6.16), (6.17) and (6.18) are the nondimensional equations of motion in the Boussinesq approximation. In these equations the key independent, nondimensional parameters are R_o, θ_o and σ. In the Boussinesq approximation, θ_o does not arise as a separate nondimensional parameter as it does in the general problem (see Section 6.4), but only in the combination $g\theta_o$.

6.3.3 Comparison to Batchelor, et al.

Batchelor, Canuto and Chasnov [7] computed numerical solutions of eqs. (6.16), (6.17) and (6.18). Their results are presented here and a comparison is made using our numerical scheme in order to validate our numerical code. Also, an understanding of these Boussinesq results will help to identify non-Boussinesq effects which are studied in the following sections. In their study the initial velocity field is zero and the initial random density field is approximately statistically homogeneous and isotropic. This

initial density field is generated from the initial density spectrum $G(k,0) = \delta(k-2\pi)$ [7], where δ is the Dirac delta-function. This spectrum can be approximated [7] by

$$G(k,0) = \frac{A_n}{2\pi}\left(\frac{k}{2\pi}\right)^n \exp\left[-\frac{1}{2}n\left(\frac{k}{2\pi}\right)^2\right]$$

where $n = 64$ and A_n is given as

$$A_n = \left[\frac{2}{\pi}\right]^{\frac{1}{2}} \frac{n^{\frac{1}{2}(n+1)}}{1\cdot 3\cdot \ldots \cdot (n-1)}.$$

The normalization constant A_n is chosen so that the condition $\overline{\Theta'\Theta'}^{1/2}_{T=0} = 1$ [which arises from (6.10) and (6.15)] is satisfied. Batchelor et al. [7] presented dimensionless mean-square velocity in the direction of the acceleration and buoyancy histories as functions of R_o, for direct numerical simulations and large eddy simulations using 64^3 and 128^3 grid sizes.

Figure 6.1 shows the time history of the mean-square dimensionless velocity, in the direction of the acceleration, for various values of R_o with $\sigma = 1$. The Boussinesq results of Batchelor et al. are the solid lines and the results of our numerical scheme (run Bos9) solving the equations of motion with the Boussinesq approximation are given by the dots. From this figure we see that the velocity increases rapidly as the fluid is set into motion through acceleration. The mean-square velocity reaches a maximum and begins to decrease as the density field mixes and diffuses towards its constant mean value, and as viscous dissipation becomes appreciable. In this case, the velocity is directly correlated with the density field. The density field corresponds to a source of potential energy; when the acceleration is applied the fluid is set into motion and a conversion of potential energy to kinetic energy takes place. As the density field diffuses and mixes towards its mean value the source of potential energy decays and the remaining kinetic energy decays away through drag. The kinetic energy will eventually go to zero as the density field is uniformly mixed and there is no available potential energy. The results of our numerical scheme are computed using a mesh size of 128^3. Our Boussinesq numerical code produces results that agree with Batchelor, et al. It is seen from this figure that as R_o approaches infinity (a cases computed by Batchelor et al. as a large eddy simulation) the mean-square velocity approaches a limiting curve with a maximum at $T = 1.8$.

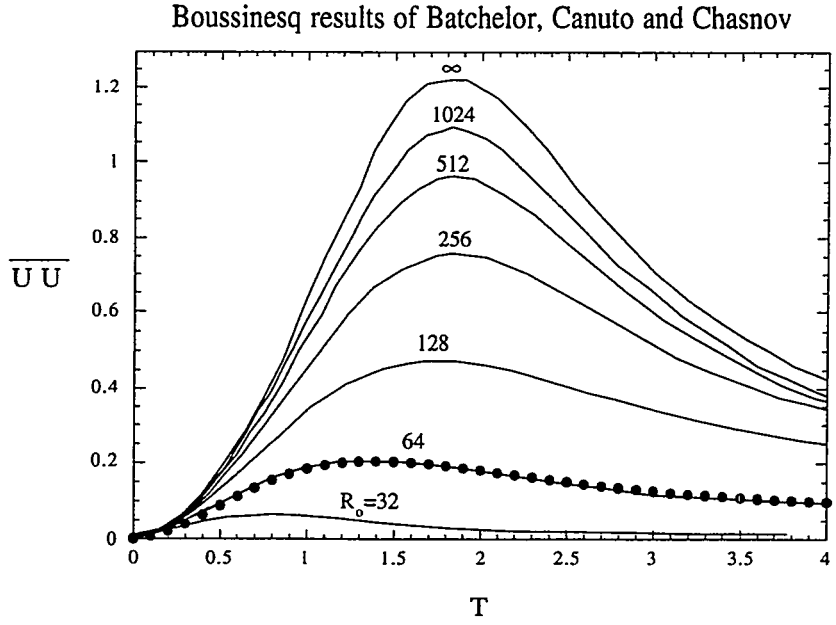

Figure 6.1: $\overline{U_i U_i}$ *vs.* T as a function of R_o. Dots are Boussinesq limit of variable-density case, solid curves are results of Batchelor, et al.

Figure 6.2 shows nondimensional mean-square of the density fluctuations as a function of the nondimensional time. For this quantity our numerical results again agree well with the results of Batchelor et al. The mean-square density also approaches a limiting curve as R_o approaches infinity. As pointed out in [7], at large values of R_o the mean-square buoyancy is conserved for small times, after which it cascades to smaller scales where it is diffused away.

6.4 Non-Boussinesq, variable-density nondimensionalization

Next we consider the case of a statistically homogeneous, buoyancy-driven turbulence with large density variations such that the Boussinesq approximation is not valid. Section 6.3.2 presents a nondimensionalization that is suitable for the buoyancy-driven problem. To discuss differences between the Boussinesq and non-Boussinesq cases we apply this nondimensionalization to the Navier-Stokes equations of motion which are non-Boussinesq. In addition to using the nondimensionalization (6.11), (6.12), and (6.13) we use the following for the pressure and total density

$$\tilde{P} = \frac{P}{\rho_o l_o g \theta_o}, \tag{6.20}$$

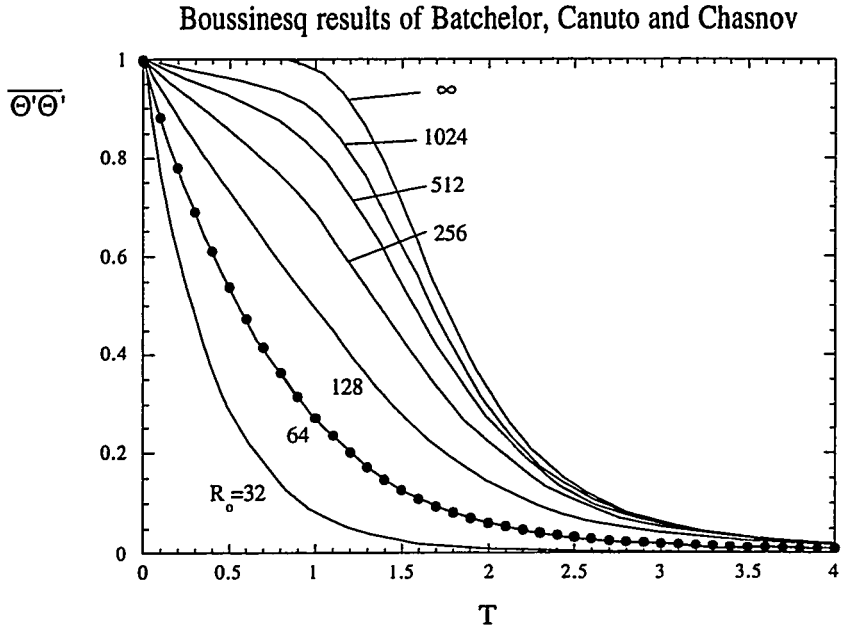

Figure 6.2: $\overline{\Theta'\Theta'}$ *vs.* T as a function of R_o. Dots are Boussinesq limit of variable-density case, solid curves are results of Batchelor, et al.

and

$$\Theta = \frac{\rho}{\rho_o}. \tag{6.21}$$

The nondimensionalization for the fluctuation density is

$$\Theta' = \frac{\rho'}{\rho^*}. \tag{6.22}$$

Applying this nondimensionalization, the divergent velocity condition given by eq. (2.11) becomes

$$\frac{\partial U_n}{\partial X_n} = -\frac{1}{\sigma R_o}\frac{\partial}{\partial X_n}\left\{\frac{1}{\Theta}\frac{\partial \Theta}{\partial X_n}\right\}, \tag{6.23}$$

the mass conservation equation [eq. (2.1)] becomes

$$\frac{\partial \Theta}{\partial T} + \frac{\partial \Theta U_n}{\partial X_n} = 0, \tag{6.24}$$

and the momentum equation [eq. (2.2)] becomes

$$\frac{\partial \Theta U_i}{\partial T} + \frac{\partial \Theta U_i U_j}{\partial X_j} = -\frac{\partial \tilde{P}}{\partial X_i} + \frac{1}{R_o}\frac{\partial \Upsilon_{ij}}{\partial X_j} + \frac{\Theta}{\theta_o}\frac{g_i}{g}. \tag{6.25}$$

where Υ_{ij} is the nondimensional viscous stress tensor. The term g_i/g is a unit vector that points in the direction of the acceleration. Eqs. (6.23), (6.24) and (6.25) are the nondimensional equations of motion without the Boussinesq approximation. From these equations it is clear that the adjustable parameters are R_o, σ and θ_o. Recall that θ_o is a nondimensional measure of the initial density variations and is defined by eq. (6.9). This measure did not appear as an independent nondimensional parameter in the Navier-Stokes equations with the Boussinesq approximation (it appears in conjunction with g) because its effects are absorbed into the nondimensionalization of the equations. However, in this non-Boussinesq case, nonlinearity does not allow its effects to be so simply scaled.

6.5 *Variable density effects for $R_o = 256$*

In this section is studied the results of two simulations, Accla and Acclc. Both simulations are made with the Navier-Stokes equations of motion where the Boussinesq approximation has not been made. Both are at a Reynolds number, R_o, of 256, a Schmidt number of $\sigma = 1$, and at a grid size of 128^3. The effects on the developing flow of increasingly larger initial density variations are examined. Both cases have an initial bimodal density distribution that is initialized using the method of Eswaran and Pope. The density ratio in the case with the initially small density fluctuations (Run Accla) is 1.105. As will be shown, at this ratio, the solution is within the Boussinesq limit (but solved with the non-Boussinesq equations of motion). Run Acclc has the same statistical distribution for the density field but the fluctuations are scaled such that the density ratio in this case is 4.0, which will be shown to be outside the Boussinesq limit. By comparing the results of these two simulations we can examine density effects on buoyancy-driven flows at this given Reynolds number.

For these buoyancy-driven cases the initial velocity field is set to zero, then slightly modified to account for the divergent velocity [eq. (2.11)] condition. Because the initial velocity field is nearly zero, density-velocity correlations are initially nearly zero; through the action of an acceleration, however, this correlation grows to a nonzero value. The acceleration is applied in the vertical (z-) direction and the developing flow is statistically axisymmetric about the vertical axis.

6.5.1 *Energy evolution*

We begin the study of variable-density effects at $R_o = 256$ by first examining at the time evolution of the total turbulent kinetic energy per unit mass as a function of time. Recall from Chapter 4 that the total turbulent kinetic energy per unit mass, which is half the trace of the generalized Reynolds stress tensor divided by the mean density [eq. (A.7)], is given as

$$K(t) = \frac{R_{nn}(t)}{2\overline{\rho}} = \frac{\overline{\rho u_n'' u_n''}}{2\overline{\rho}} = \frac{\overline{u_n' u_n'}}{2} + \frac{\overline{\rho' u_n' u_n'}}{2\overline{\rho}} - \frac{a_n a_n}{2}$$

where

$$a_i = -\frac{\overline{\rho u_i}}{\overline{\rho}} = -\frac{\overline{\rho' u_i'}}{\overline{\rho}}$$

is the negative of the turbulent mass flux per unit mass. Figure 6.3 shows the evolution of the total turbulent kinetic energy per unit mass evolution for the two cases (Run Accl c with an initial density ratio of 4 such that $\theta_o = 0.52$ and Accl a with an initial density ratio of 1.105 such that $\theta_o = 0.04$). This shows the effect of increasing initial density fluctuations. The results for run Accl a, given by the solid line curve, are within the Boussinesq approximation. That is to say, a flow within the Boussinesq approximation is on where the mean flow statistics match that of the Boussinesq approximation. The dashed curve shows the results of run Accl c. The total turbulent kinetic energy is initially nearly zero. At $T = 0$, the acceleration is initiated and the fluid is set into motion. The buoyancy force decays in time due to molecular diffusion. As a result the velocity reaches a maximum (at $T = 1.8$) and, through viscous effects, begins to decay. At $T = 4$ there is still a significant amount of kinetic energy in the flow. At later times, the total turbulent kinetic energy would eventually tend to zero as the thoroughly mixed fluid comes to rest due to the dissipation of kinetic energy into heat by viscous stresses. As the initial density fluctuations becomes larger, the growth rate of the nondimensional kinetic energy lowers. Likewise, the peak of the nondimensional turbulent kinetic energy is larger for the case with the smaller initial density fluctuations. As explained below, this result is due to the fact that the second and third terms on the right side of eq. (A.7) grow to larger values, which contribute to make the nondimensional total turbulent kinetic energy lower as R_o increases.

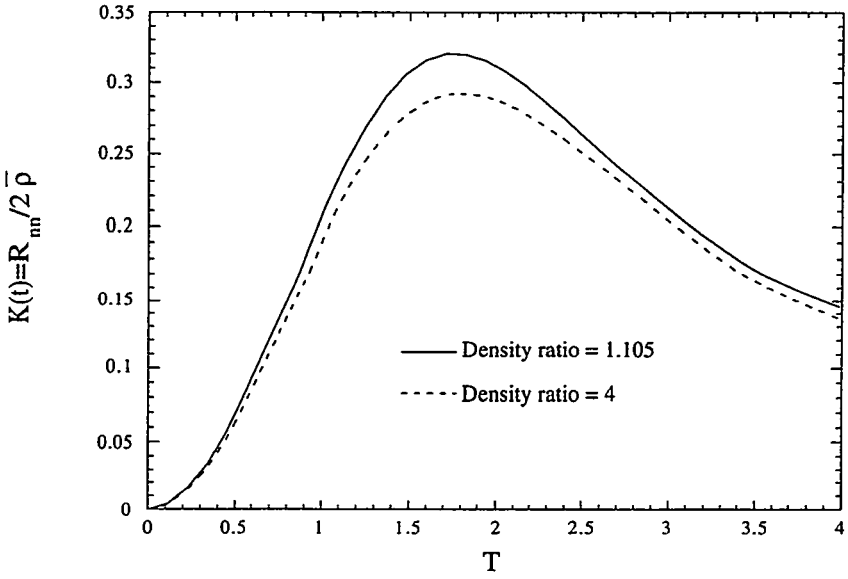

Figure 6.3: Total nondimensional turbulent kinetic energy per unit mass *vs.* T for $R_o = 256$ for the initial density ratio = 1.105 case (Run Acc1a) and the initial density ratio = 4 case (Run Acc1c)

Figure 6.4 shows the dimensionless mean-squared velocity as a function of dimensionless time. As the initial density fluctuations are increased the mean-squared velocity grows faster. For the initial density ratio of 1.105 case, the nondimensional mean-squared velocity reaches a peak at the same time as for the Boussinesq results [7], shown in Fig. 6.1. Figure 6.4 shows that, as the initial density fluctuations become larger, and the Boussinesq approximation is no longer valid, the nondimensional time at which the mean-squared velocity peaks decreases. In the limit as the initial density ratio becomes very large (much larger than 4), the time at which the mean-squared velocity reaches a maximum should approach a limiting value. This is because, as the initial density ratio increases, the time shift must be bounded but the $t = 0$ axis. This limit cannot be examined in this study due to resolution limitations of our numerical code.

Figure 6.5 shows the three components of the mean-squared velocity as functions of nondimensional time for both cases. This figure shows the axisymmetric nature of these buoyancy-generated flows, as the component in the direction of the acceleration (i.e., the vertical component, W) contains the largest amount of the kinetic energy,

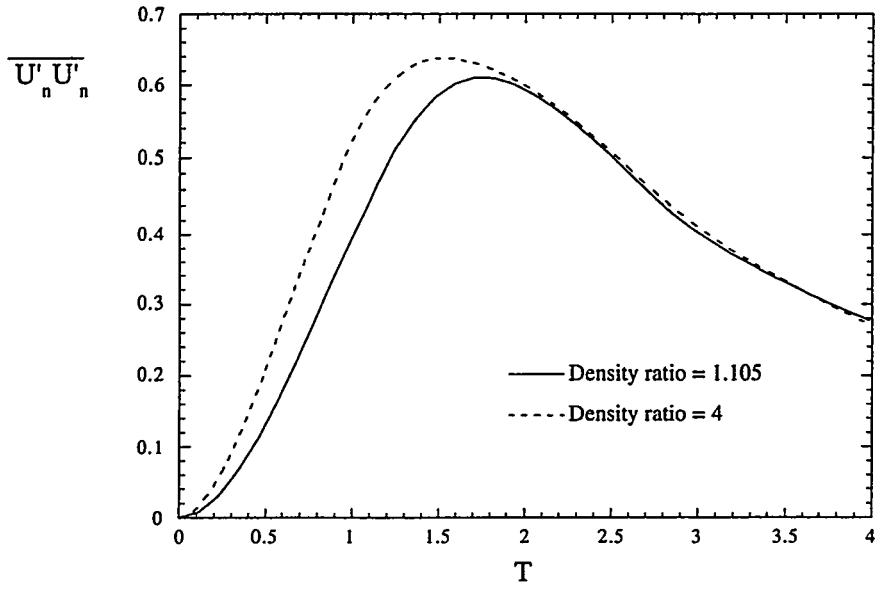

Figure 6.4: $\overline{U_i' U_i'}$ *vs.* T for $R_o = 256$ for the initial density ratio = 1.105 case (Run Acc1a) and the initial density ratio = 4 case (Run Acc1c)

whereas the two off-diagonal components are planar isotropic with each having nearly the same amount of energy. The difference between $\overline{U'U'}$ and $\overline{V'V'}$ can be attributed to statistical scatter in the simulations. Comparison with this figure and Fig. 6.4 shows that the vertical component, $\overline{W'W'}$, reaches a maximum at a time less than that for the total mean-squared velocity. Figure 6.6 shows the ratio

$$\gamma = \frac{2\,\overline{W'W'}}{\overline{U'U'} + \overline{V'V'}} \tag{6.26}$$

as a function of T. γ is a measure of the large-scale anisotropy [7] of the velocity field. For isotropic flow this quantity is unity. The discontinuous slope seen in the curve for the initial density ratio is 1.105 cases is due to the method of extracting the data from the numerical simulations and not physical. Predictions of the linearized equations with the Boussinesq approximation made by Batchelor et al. [7] give a value of γ at early times of eight. For the case where the initial density ratio is 1.105, the density fluctuations are small enough that the value of γ is the same as predicted by Batchelor et al. It is observed that as the initial density variations become larger, the anisotropy parameter, γ, decreases (at least for the early times). This measure of anisotropy at early times is a function of initial density ratio and becomes nearly

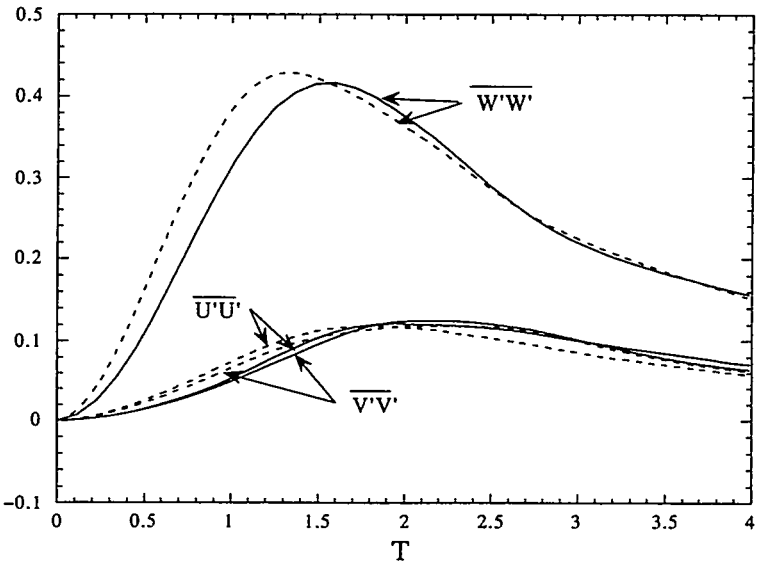

Figure 6.5: Nondimensional mean-squared velocity components for the initial density ratio = 1.105 case (solid lines) and the initial density ratio = 4 case (dashed lines)

the same constant value as the density fluctuations tend to zero. At the end of the simulations γ is approximately 2.5. The result for the case with the initial density ratio of 1.105 is a good indication that the initial density variations for that case allow the flow within the Boussinesq approximation limit, since the early time results agree well with the analytical predictions of Batchelor et al.

The total turbulent kinetic energy per unit mass, given by eq. (A.7), as a function of time for case with the initial density ratio of 1.105 is shown in Fig. 6.7. Initially each term in eq. (A.7) is nearly zero because the initial velocity is small. At this initial density ratio, the energy is made up almost completely from the mean-squared velocity since the triple correlation term, $\overline{\rho' u_n' u_n'}/2\overline{\rho}$, and the turbulent mass flux per unit mass, a_n, remain small.

An evolution equation for $\overline{\rho u_i' u_i'}/2$ is derived in Appendix B and written here as

$$\underbrace{\frac{d}{dt}\left\{\frac{1}{2}\overline{\rho u_i' u_i'}\right\}}_{A} = \underbrace{\overline{p\frac{\partial u_n'}{\partial x_n}}}_{B} + \underbrace{\overline{u_i'\frac{\partial \tau_{ij}'}{\partial x_j}}}_{C} + \underbrace{\overline{\rho' u_i' g_i}}_{D}. \tag{6.27}$$

The first term on the right side, term B, is a pressure-work term that represents a conversion of kinetic energy into internal energy. For the compressible case this

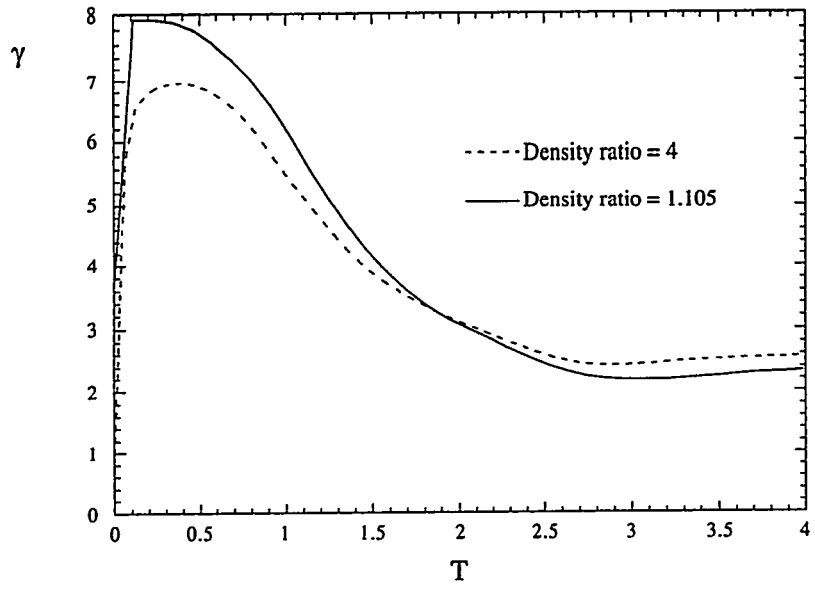

Figure 6.6: Measure of anisotropy of the mean-squared velocity for the initial density ratio = 1.105 case (solid lines) and the initial density ratio = 4 case (dashed lines)

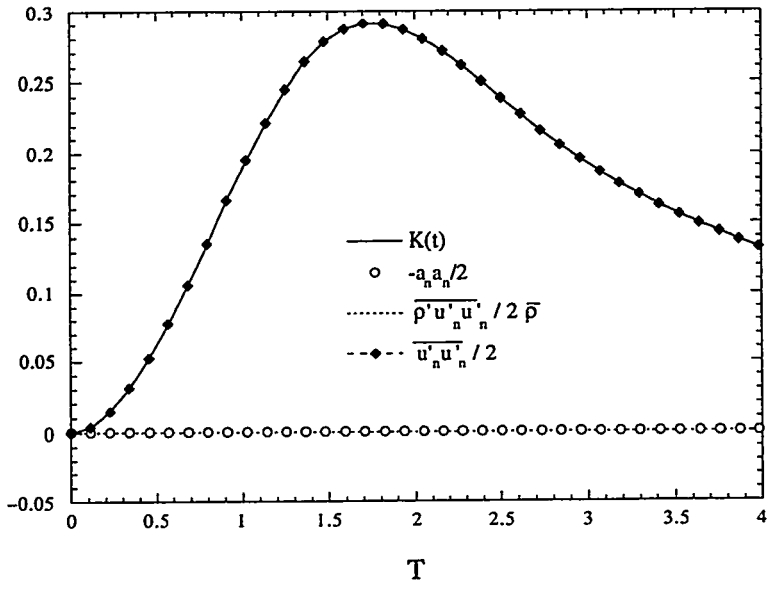

Figure 6.7: Terms of the total turbulent kinetic energy per unit mass for the initial density ratio = 1.105 case (Run Accla)

term is reversible; here it is not because the divergent velocity field is a result of the diffusion of mass. The second term, C, is the dissipation rate and the third term, D, is the buoyancy force term which represents a source of kinetic energy from the conversion of potential energy through the mass flux $\overline{\rho' u_i'}$. In the limiting case of vanishing molecular effects (i.e., zero viscosity and diffusivity) this equation reduces to

$$\frac{d}{dt}\left\{\frac{1}{2}\overline{\rho u_i' u_i'}\right\} = \overline{\rho' u_i'} g_i.$$

In this limit the only source of kinetic energy is from potential energy, and occurs through buoyancy effects. Figure 6.8 shows each term of this evolution equation [eq. (6.27)] as a function of time for the initial density ratio of 1.105 case. We see that the generation of kinetic energy is through the buoyancy term. The buoyancy term reaches a peak at a time of $T = 1$ and then decays away as the density field, which represents the source for potential energy, decays to a uniform density. The growth of the kinetic energy is impeded by viscous and drag effects. In the final stages of the flow, viscosity is the sink for which the kinetic energy is lost to heat and the flow reaches its final resting state. In this problem, where the initial density fluctuations are small with respect to its mean value, the pressure-work term does not affect the evolution of the kinetic energy.

To gain insight on the differences in the energy evolution between the case with the initial density ratio of 1.105 and that with the initial density ratio of 4, we show in Fig. 6.9 the total turbulent kinetic energy per unit mass and its components given by eq. (A.7) as a function of time for the case with the initial density ratio of 4. Comparison of this figure with Fig. 6.7 immediately highlights differences in the two cases. For the larger initial density ratio case, the triple correlation term, $\overline{\rho' u_n' u_n'}/2\overline{\rho}$, and the term associated with the mass flux, $a_n a_n/2$, which are initially nearly zero, grow to negative nonzero values with a minimum at approximately, $T = 1$, then decay to zero. In the smaller initial density ratio case these terms are small. The main contribution to the total turbulent kinetic energy is from the mean-squared velocity term, $\overline{u_n' u_n'}/2$, while the other two terms act to impede the growth of the total turbulent kinetic energy. By the time of approximately $T = 2.5$, the contributions from $\overline{\rho' u_n' u_n'}/2\overline{\rho}$ and $a_n a_n/2$ are small so that the total turbulent kinetic energy is just $\overline{u_n' u_n'}/2$.

Evolution equations for each term shown in Fig. 6.9 are derived in Appendix B.

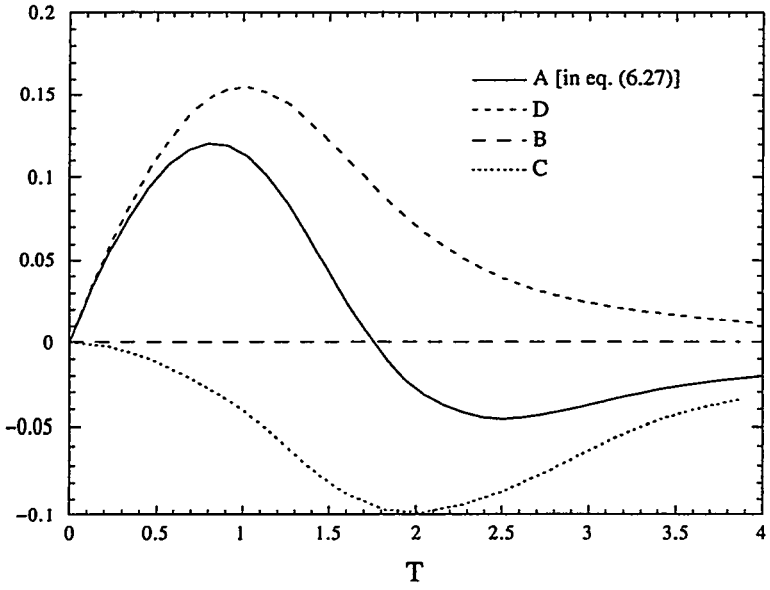

Figure 6.8: Terms in the evolution equation [eq. (6.27)] for $\overline{\rho u_i' u_i'}/2$ for initial density ratio of 1.105 case (Run Acc1a)

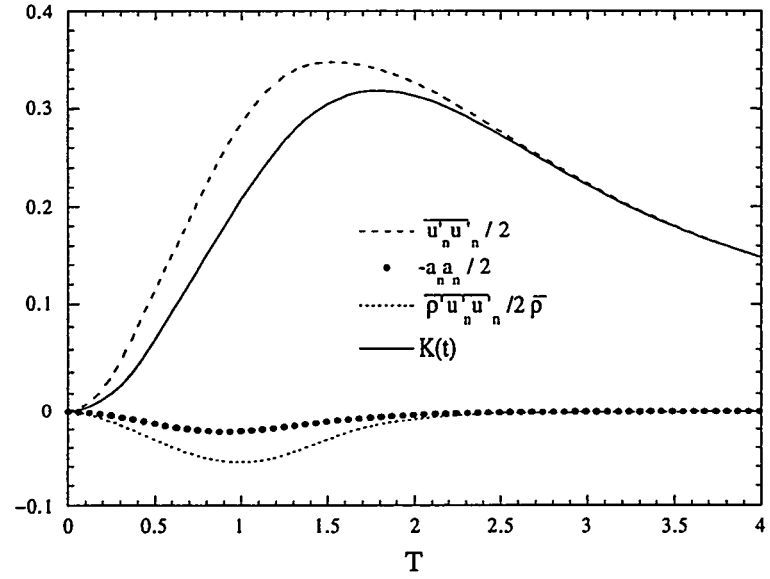

Figure 6.9: Terms of the total turbulent kinetic energy per unit mass for the initial density ratio = 4 case at $R_o = 256$ (Run Acc1c)

The evolution equation for $\overline{\rho}\ \overline{u_i'u_i'}$ is given by eq. (B.15), and written here as

$$\underbrace{\frac{d}{dt}\left\{\frac{1}{2}\overline{\rho}\ \overline{u_i'u_i'}\right\}}_{A} = \underbrace{\frac{\overline{\rho}}{2}\ \overline{u_i'u_i'\frac{\partial u_j'}{\partial x_j}}}_{B} - \underbrace{\overline{\rho}\ \overline{\frac{u_i'}{\rho}\frac{\partial p}{\partial x_i}}}_{C} + \underbrace{\overline{\rho}\ \overline{\frac{u_i'}{\rho}\frac{\partial \tau_{ij}'}{\partial x_j}}}_{D}. \tag{6.28}$$

The first term on the right side represents production/destruction due to dilatation effects. The second term on the right side, term C, can be rewritten as

$$\overline{\rho}\ \overline{\frac{u_i'}{\rho}\frac{\partial p}{\partial x_i}} = \underbrace{\overline{\rho}\ \overline{\left(\frac{u_i'}{\rho}\right)}\frac{\partial \overline{p}}{\partial x_i}}_{C_1} + \underbrace{\overline{\rho}\ \overline{\frac{u_i'}{\rho}\frac{\partial p'}{\partial x_i}}}_{C_2}, \tag{6.29}$$

where $\overline{p}$ is the hydrostatic pressure. A more complete discussion of the mean pressure gradient term is given below in section 6.5.4. The third term, D, is the viscous dissipation rate. Figure 6.10 shows the contribution of each term of eq. (6.28) as a function of nondimensional time. The growth of $\overline{\rho}\ \overline{u_i'u_i'}/2$ is due to the mean pressure gradient term, C_1. This term has incorporated into it the contribution from the buoyancy flux (see Section 3.1.3), which is the source for the kinetic energy. The viscous stress term, D, acts strongly to damp the growth of $\overline{\rho}\ \overline{u_i'u_i'}/2$ and is the main impedance to the growth of the mean-squared velocity. The dilatation term, B, and the fluctuating pressure (i.e., the motion pressure) gradient term, C_2, also act to slightly impede the growth of the mean-squared velocity. As the density fluctuations decay and the fluid mixes, the driving term for the growth (i.e., the mean pressure gradient) of $\overline{\rho}\ \overline{u_i'u_i'}/2$ reaches a maximum and tends to zero. The time rate-of-change of $\overline{\rho}\ \overline{u_i'u_i'}/2$ is positive up to a time of approximately $T = 1.5$. For times greater than 1.5, the contribution from the buoyancy flux is smaller than the effects due to viscosity and as a result the total turbulent kinetic energy is decaying as it is being converted into heat through viscous dissipation.

The evolution equation for the triple correlation term, $\overline{\rho' u_i'u_i'}/2$, is given by eq. (B.16), written here as

$$\underbrace{\frac{d}{dt}\left\{\frac{1}{2}\overline{\rho' u_i'u_i'}\right\}}_{A} = -\underbrace{\frac{\overline{\rho}}{2}\ \overline{u_i'u_i'\frac{\partial u_j'}{\partial x_j}}}_{B} - \underbrace{\overline{\frac{\rho' u_i'}{\rho}\frac{\partial p'}{\partial x_i}}}_{C_1} - \underbrace{\overline{\left(\frac{\rho' u_i'}{\rho}\right)}\frac{\partial \overline{p}}{\partial x_i}}_{C_2} + \underbrace{\overline{\frac{\rho' u_i'}{\rho}\frac{\partial \tau_{ij}'}{\partial x_j}}}_{D} + \underbrace{\overline{\rho' u_i' g_i}}_{E}. \tag{6.30}$$

Each term of this equation is plotted in Fig. 6.11 as a function of nondimensional time. The growth of $\overline{\rho' u_i'u_i'}/2$ is being driven by the mean pressure gradient. The buoyancy

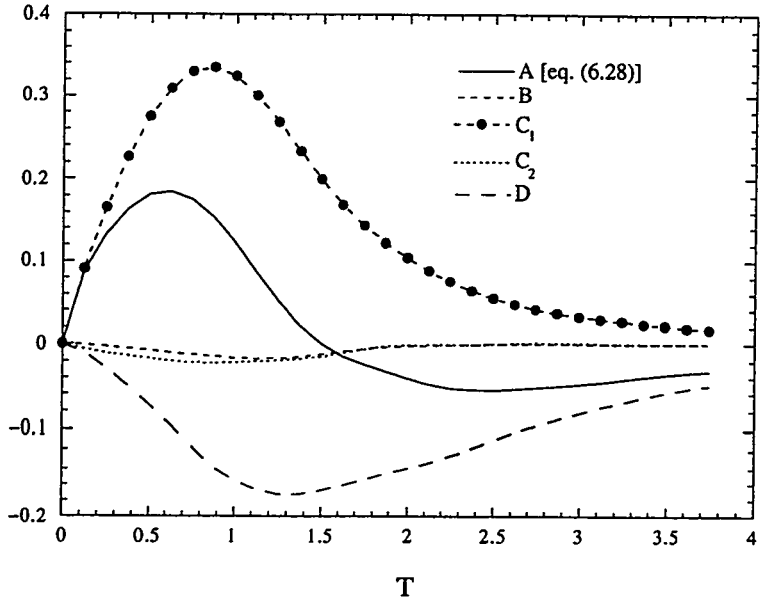

Figure 6.10: Terms of the evolution equation [eq. (6.28)] for $\overline{\rho}\,\overline{u_i'u_i'}/2$ for initial density ratio of 4 case (Run Acc1c)

flux term, term E, acts strongly to oppose the growth of this triple correlation term. Viscous effects also act to impede the growth of this triple correlation and ultimately are responsible for the dissipation of $\overline{\rho' u_i' u_i'}/2$ into heat. At late times, when the density variations are small, the mean pressure gradient and the buoyancy flux terms nearly balance and the time rate-of-change of this triple correlation is nearly zero.

6.5.2 Evolution of the mass flux

For the case of isotropic decay the fluctuating density-velocity correlation, $\overline{\rho' u_i'}$, is zero. For the buoyancy driven case this correlation is initially zero when the fluid is at rest and grows because the induced velocity is highly correlated with the density fluctuations. The evolution of the negative of the mass flux per unit mass, a_n, for both cases is given in nondimensional form, i.e., for

$$A_n = \frac{a_n}{(l_o g \theta_o)^{1/2} \theta_o},$$

in Fig. 6.12. For the case with the initial density ratio of 4, A_n grows to a larger value than for the other case even though this quantity is nondimensionalized. This

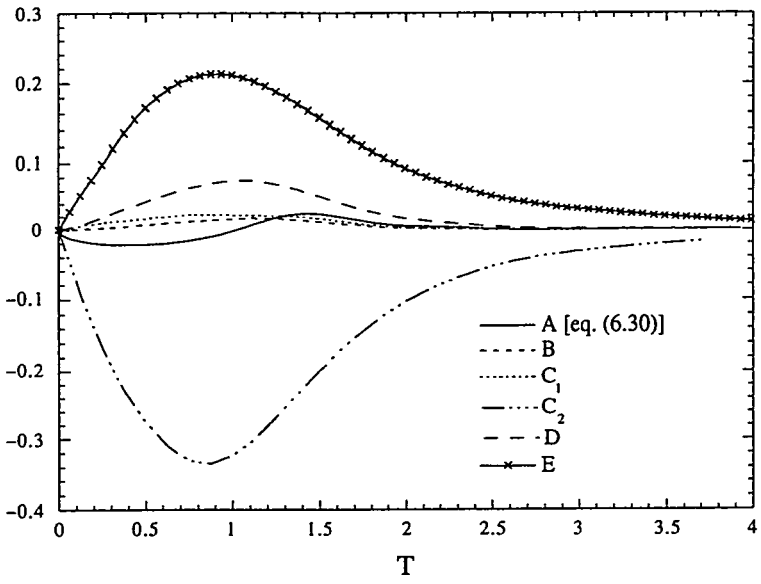

Figure 6.11: Terms of the evolution equation [eq. (6.30)] for $\overline{\rho' u_i' u_i'}/2$ for initial density ratio of 4 case (Run Acc1c)

is due to the available potential energy for the larger initial density ratio case being larger and, thus, having a larger buoyancy flux.

An evolution equation for a_i is derived in Appendix B, and written here, for homogeneous flow, as

$$\underbrace{\frac{da_i}{dt}}_{A} = \underbrace{\overline{u_i' \frac{\partial u_n'}{\partial x_n}}}_{B} - \underbrace{\left(\overline{v} - \frac{1}{\overline{\rho}}\right) \frac{\partial \overline{p}}{\partial x_n}}_{C} + \underbrace{\overline{v' \frac{\partial \sigma_{in}'}{\partial x_n}}}_{D}. \tag{6.31}$$

Figure 6.13 shows each term of this equation as a function of time for run Acc1c. The first term on the right side, term B represents production/destruction of the turbulent mass flux due to dilatation effects. The second term on the right side of this evolution equation is a contribution to the growth of the turbulent mass flux due to the mean pressure gradient multiplied by the factor $\overline{v} - 1/\overline{\rho} = b/\overline{\rho}$. It has been shown in the case of isotropic decaying turbulence (and also is shown below in the context of this buoyancy-driven problem) that b is a time dependent variable. Since the mean density, $\overline{\rho}$, is fixed in time, this equation shows that $\overline{v}$ is also a time dependent variable (An evolution equation for this quantity is derived in Appendix B). The mean pressure gradient term is responsible for the majority of the growth of

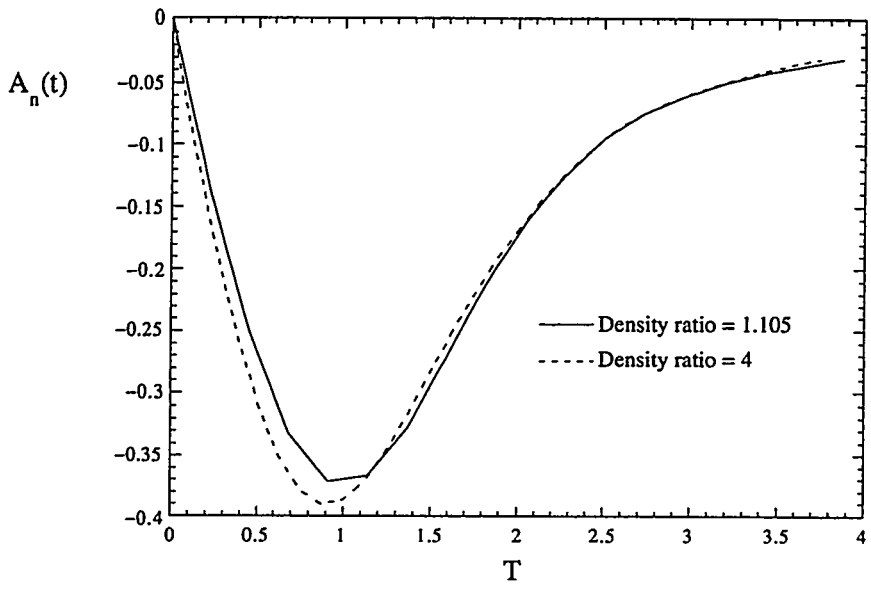

Figure 6.12: Turbulent mass flux for initial density ratio of 1.105 case (Run Acc1a) and the initial density ratio of 4 case (Run Acc1c)

the turbulence mass flux. The dilatation term, term B, also adds a small contribution to the growth of the turbulence mass flux. The third term on the right side of eq. (6.31), term D, represents a correlation between the fluctuating specific volume and fluctuating stress gradient. This term is discussed in more detail in the Section 6.5.4 in relation to the mean pressure gradient. At the instant an acceleration is applied, and prior to the onset of fluid motion, the evolution equation [eq. (6.31)] reduces to

$$\frac{da_i}{dt} = -\frac{b}{\overline{\rho}}\frac{\partial \overline{p}}{\partial x_n} - \overline{v'\frac{\partial p'}{\partial x_i}} = -\frac{1}{\overline{\rho}\,\overline{v}}\left\{bg_i + \overline{v'\frac{\partial p'}{\partial x_i}}\right\}.$$

The initial growth of the mass flux is therefore due to the acceleration. The second term on the right side is a correlation between the fluctuating specific volume and fluctuating pressure gradient. Initially this term is nonzero and it acts to impede the growth rate of the turbulence mass flux. This term is has similar effects in the flow as virtual mass. Just as virtual mass impedes the acceleration of a bubble rising in a liquid, $\overline{v'\frac{\partial p'}{\partial x_i}}$ impedes the acceleration of one fluid into the other.

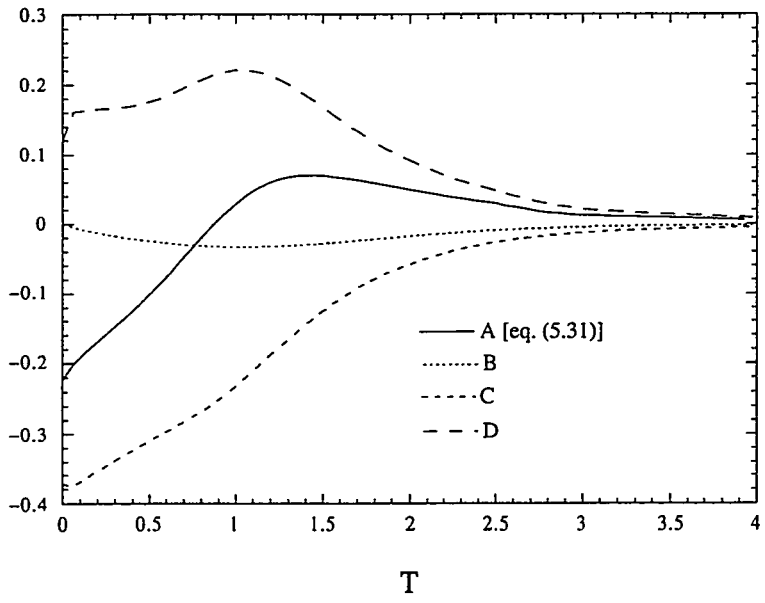

Figure 6.13: Terms of the turbulent mass flux evolution equation [eq. (6.31)] for initial density ratio of 4 case (Run Acc1c)

6.5.3 Velocity derivative skewness

The velocity derivative skewness is a measure of the strength of the nonlinear effects in the spectral transfer of energy and characterizes the rate at which enstrophy increases by vortex stretching [52]. The velocity derivative skewness is defined as [eq. (4.10)]

$$S_i(t) = -\frac{\overline{\left(\frac{\partial u_i}{\partial x_i}\right)^3}}{\overline{\left(\frac{\partial u_i}{\partial x_i}\right)^2}^{\frac{3}{2}}}\ , \text{ no summation on } i$$

where u_i is any component of the velocity ($i = 1, 2, 3$). Tavoularis et al. [86] report that for moderate Reynolds numbers $S_i(t) \approx 0.32 - 0.6$ for nearly-isotropic grid experiments. The larger the value of S_i the greater the effect of nonlinearity on the spectral energy transfer. Figures 6.14 and 6.15 show the velocity derivative skewness for the initial density ratio of 1.105 case (Run Acc1a), and the larger initial density ratio case (Run Acc1c), (both at $R_o = 256$), respectively. The subscripts $i = 1, 2$ represent the x- and y-directions (horizontal direction) and $i = 3$ is the z-direction (the direction of the acceleration). These two figures display that overall behavior that is similar for both cases. The initial values are different between the two cases

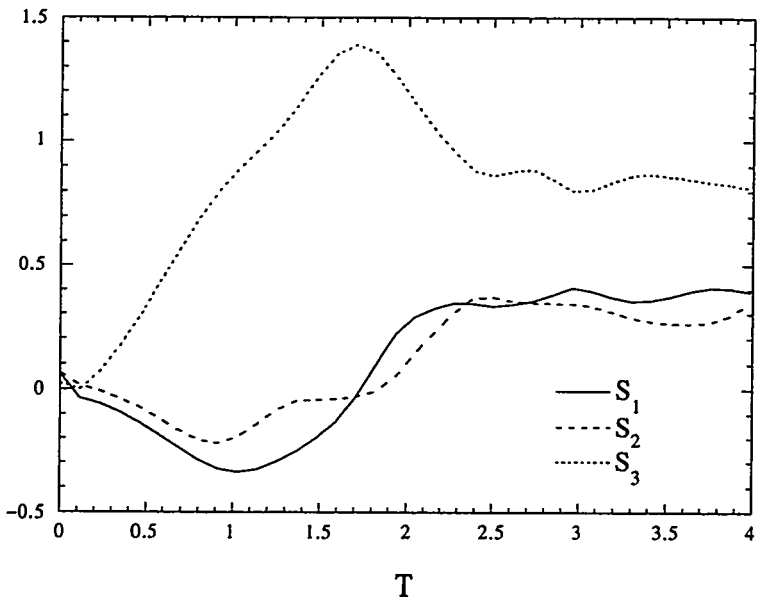

Figure 6.14: Velocity derivative skewness for each component for the initial density ratio of 1.104 case (Run Accla)

due to the differences in the initial conditions. Planar isotropy is seen in the horizontal components, as they have nearly the same value. In the horizontal direction the velocity derivative skewness is driven negative, and reaches a minimum value at a time that roughly corresponds with that for the maximum turbulent mass flux. As the mass flux decays it is observed that the velocity derivative skewness in the horizontal plane increases to a nearly constant value of 0.35 which is characteristic for laboratory experiments of isotropic turbulence. The vertical component grows to a large positive value and decreases to a nearly constant value that is roughly twice that for the horizontal components. This shows that nonlinear effects on the energy transfer are stronger in the the direction of the acceleration than in the horizontal direction. This also reflects that there is a strong growth of enstrophy in the direction of the acceleration due to vortex stretching (see Section 6.5.5). Figure 6.16 shows the average of the velocity derivative skewness over all three components for both cases. This shows that by a time of $T = 2$ the average velocity derivative skewness is a constant value of about 0.5 for both cases.

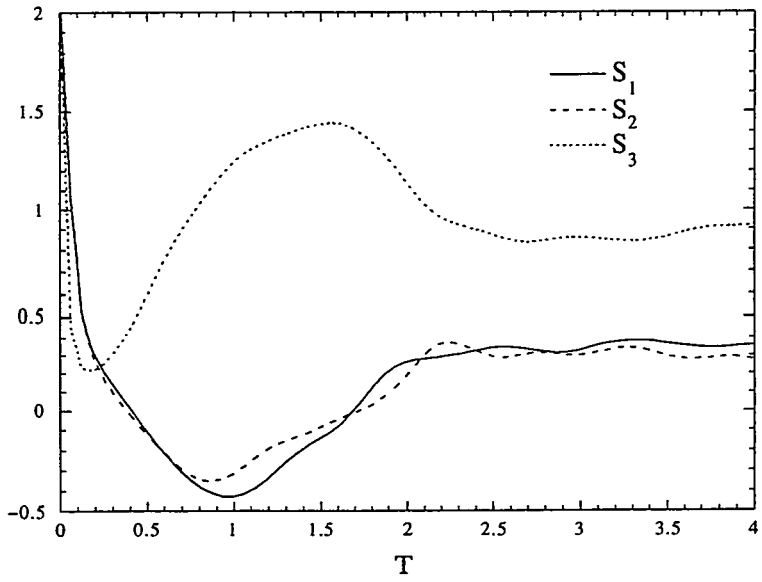

Figure 6.15: Velocity derivative skewness for each component for the initial density ratio of 1.104 case (Run Acc1a)

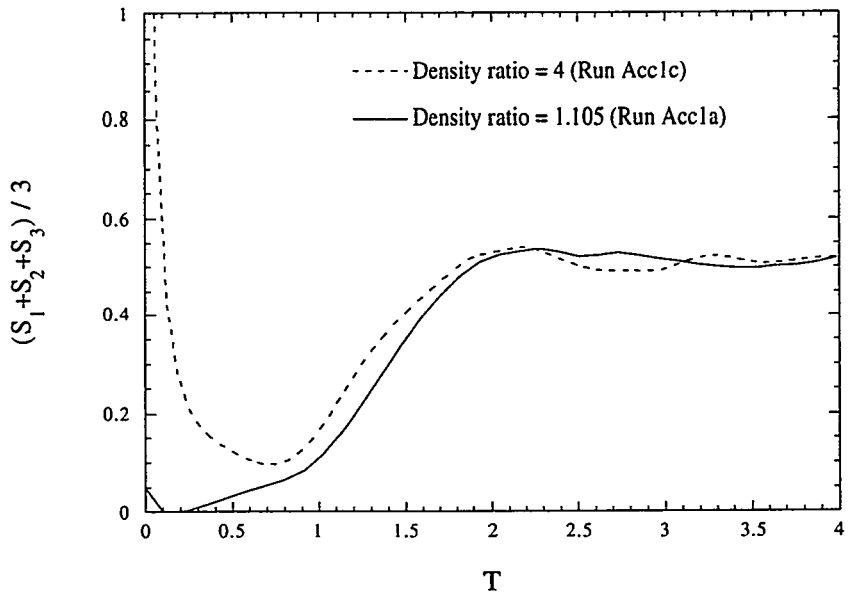

Figure 6.16: Average velocity derivative skewness for the initial density ratio of 1.104 case (Run Acc1a) and for the initial density ratio of 4 case (Run Acc1c)

6.5.4 *Mean pressure gradient evolution*

It has been shown that the mean pressure gradient drives the growth of the turbulence mass flux. Because of this important feature it will be studied in detail in this section. Our goal here is to investigate departures from the Boussinesq approximation in the mean pressure gradient. This will have much significance for the modeling of variable-density flows.

The equation for the gradient of the mean pressure is derived in Section 3.1.3 for the case where there is zero volumetric mean motion, $\overline{u}_i = 0$, and given by eq. (3.19), and repeated here

$$\underbrace{\frac{\partial \overline{p}}{\partial x_i}}_{A} = \underbrace{\frac{1}{\overline{v}}\, g_i}_{B} + \underbrace{\frac{1}{\overline{v}}\, \overline{v' \frac{\partial \tau'_{ni}}{\partial x_n}}}_{C_1} - \underbrace{\frac{1}{\overline{v}}\, \overline{v' \frac{\partial p'}{\partial x_i}}}_{C_2} + \underbrace{\frac{1}{\overline{v}}\, \overline{u'_i \frac{\partial u'_n}{\partial x_n}}}_{D}. \tag{6.32}$$

The first term on the right side is the contribution to the mean pressure gradient from the acceleration. The other three terms are due to fluctuating specific volume correlations with the fluctuating stress terms and a contribution from a correlation between the fluctuating velocity and the dilatation term. The last three terms on the right side represent a departure from the Boussinesq and hydrostatic limits. In the limit as the density variations tend to zero, these terms tend to zero and the mean pressure gradient becomes

$$\frac{\partial \overline{p}}{\partial x_i} = \overline{\rho} g_i,$$

which is the hydrostatic balance. In the absence of fluid motion (e.g., at time equal to zero) the mean pressure gradient is

$$\frac{\partial \overline{p}}{\partial x_i} = \frac{1}{\overline{v}} \left\{ g_i - \overline{v' \frac{\partial p'}{\partial x_i}} \right\}. \tag{6.33}$$

This shows that, in the absence of motion, the correlation between the fluctuation specific volume and fluctuating pressure gradient is a non-Boussinesq departure from the hydrostatic pressure gradient. As previously mentioned, this term has similar effects as virtual mass on a bubble. This correlation impedes turbulence mass growth rate just as virtual mass is attributed to impede the acceleration of a bubble rising in a liquid.

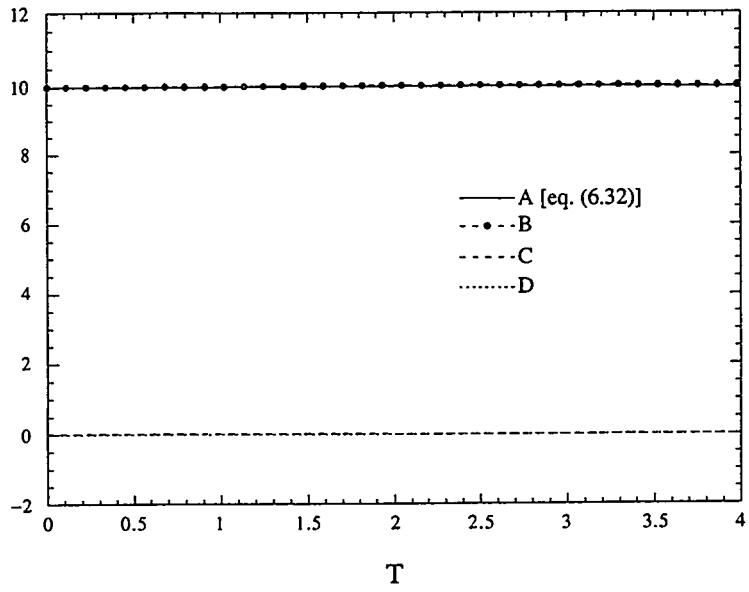

Figure 6.17: Evolution of terms in the mean pressure gradient [eq. (5.32)] for initial density ratio of 1.105 case at $R_o = 256$ (Run Accla)

Figure 6.17 shows each of the terms in the equation for mean pressure gradient for the case with the initial density ratio of 1.105 (Run Accla). In this case $g = 10$ and $\overline{\rho} = 1$ so that $\overline{\rho}g = 10$. For this case the mean pressure gradient is comprised mostly of the acceleration term $g/\overline{v}$, which is approximately equal to $\overline{\rho}g$. The second and third terms are initially nearly zero and remain small compared to $g/\overline{v}$. The fourth term, the correlation between the fluctuating specific volume and fluctuating pressure gradient starts out at a small nonzero value and represents less than one-percent of the contribution. This figure is consistent with the conjecture that the behavior of the buoyancy generated flow for this case is within the Boussinesq approximation limit, since the mean pressure gradient has the Boussinesq limiting value of $\overline{\rho}g$.

Figure 6.18 plots each of the terms in the equation for the mean pressure gradient for the case with the initial density ratio of 4 (Run Acclc). In this case $g = 1$ and $\overline{\rho} = 1$ so that, in the limit as the density variations tend to zero, the mean pressure gradient tends to the value $\overline{\rho}g = 1$. Initially, the mean pressure gradient is approximately 0.75 and the acceleration term, $g/\overline{v}$, is approximately 0.67. The correlation $\overline{v'(\partial p'/\partial x_i)}$ is approximately 0.08 and represents 11 percent of the initial mean pressure gradient. All other terms are initially nearly zero since the flow is nearly motionless. As the

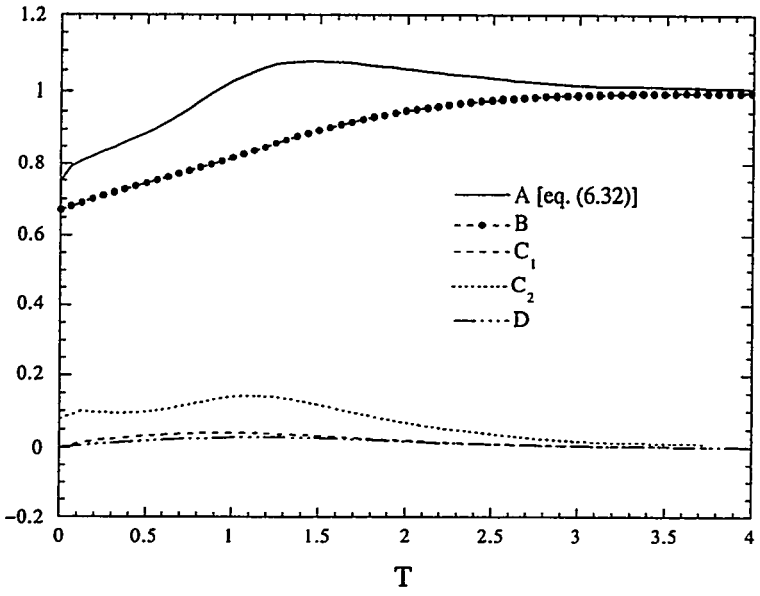

Figure 6.18: Evolution of terms in the mean pressure gradient [eq. (5.32)] for initial density ratio of 4 case at $R_o = 256$ (Run Acc1c)

flow develops the mean pressure gradient increases to a value slightly larger than 1.0 and at the last time shown has very nearly a constant value of 1.0. For this case the Boussinesq approximation implies the mean pressure gradient is constant in time with a value of 1.0. Therefore, the Boussinesq approximation is not valid in this case since the mean pressure gradient, which is partially responsible for the fluid motion, varies in time and differs significantly from the Boussinesq approximation limit. As the flow develops the second and third terms in the equation for the mean pressure gradient grow slightly from their nonzero values and contribute only a few percent to the total mean pressure gradient. The correlation $\overline{v'(\partial p'/\partial x_i)}$ remains a large contribution to the mean pressure gradient up to late times.

The departure from the Boussinesq limit shown here increases as the initial density fluctuations are increased. This is due to the fact that fluid of different density is accelerated differently as the density variations are increased. As a result, as the initial density fluctuations increase, so also does the magnitude of the correlation between the fluctuating specific volume and the fluctuating pressure gradient. Figure 6.19 shows the negative of this correlation as a function of nondimensional time (on a semi-log plot) for the cases with both large and small initial fluctuations. The magnitude of

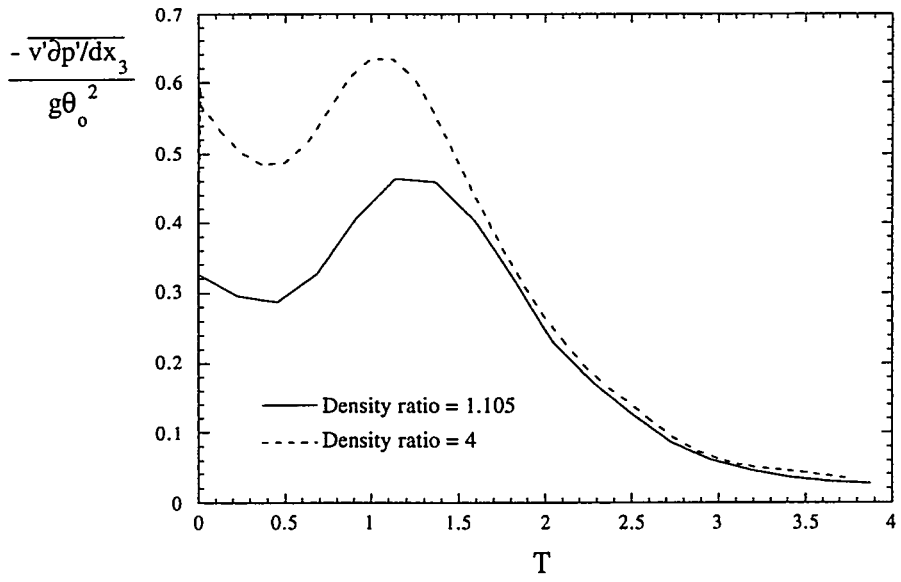

Figure 6.19: $-\overline{v' \, \partial p'/\partial x_3}$ evolution for initial density ratio of 1.105 and 4 cases

this correlation increases as the initial density fluctuations are increased. As a result, the mean pressure gradient deviates further from the Boussinesq approximation, and the mean pressure gradient becomes more non-uniform in time. This plot shows that this correlation has the same trends at this Reynolds number of 256 for large and small initial density fluctuations. The nonzero value at the initial time represents a "rapid" part of this correlation. The use of the term "rapid" implies that the correlation takes on a nonzero value the instant that the fluid feels an acceleration because it is an instant linear response of the mean pressure. As the flow develops this correlation increases due to the "slow" part which is a source of drag for the mass flux. At late times this correlation is decaying and represents a drag for the turbulent mass flux (see below in this section).

This correlation, $\overline{v'(\partial p'/\partial x_i)}$, is postulated by modelers (see, e.g., Besnard, et al., [10]) to behave as a "drag" term which impedes the growth of the turbulent mass flux. It has already been shown that the presence of this correlation indeed acts to impede the growth of the turbulent mass flux. These results, however, suggest that this correlation behaves as both a "drag" term and as a "rapid" term. The instant that the fluid is accelerated, this correlation immediately takes a nonzero value, even though the mass flux is zero. If this correlation behaved as only a "drag" on the

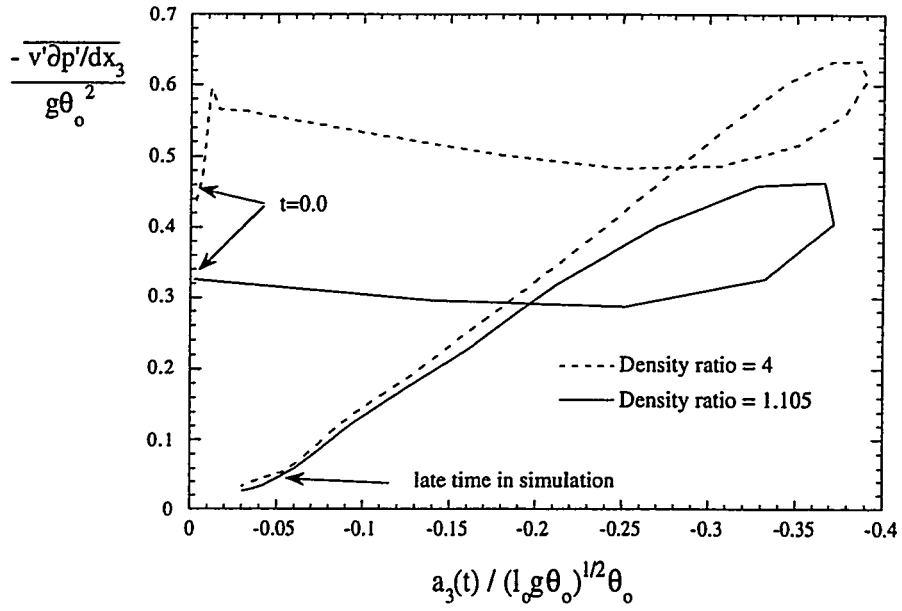

Figure 6.20: Nondimensional $-\overline{v'\,\partial p'/\partial x_3}$ vs. nondimensional a_3 for initial density ratio of 1.105 and 4 cases at $R_o = 256$

mass flux, it would grow with the mass flux. When the mass flux is zero so too would be this correlation. However, it has a nonzero value the instant the fluid is accelerated and thus is a "rapid" term. To understand how this correlation behaves as a function of the mass flux, it is plotted in nondimensional form as a function of the nondimensional mass flux in Fig. 6.20. This figure shows that indeed $\overline{v'(\partial p'/\partial x_i)}$ does not behave as drag term at early times. At the initial time, the negative of the nondimensional $\overline{v'(\partial p'/\partial x_i)}$ correlation is approximately 0.32 for the case with the initial density ratio of 1.105 and approximately 0.56 for the larger density ratio case. At $T = 0$, when the acceleration is applied, the dominant part of $\overline{v'(\partial p'/\partial x_i)}$ is the "rapid" part. As the flow evolves, the "rapid" part vanishes as the density fluctuations decay resulting in the decay of this correlation. Also as the flow evolves, the "drag" part increases causing an increase in $\overline{v'(\partial p'/\partial x_i)}$. Ultimately, at late times, the "drag" part is dominant as the "rapid" part has vanished so that $\overline{v'(\partial p'/\partial x_i)}$ decays nearly linearly with the mass flux. At late times in this buoyancy-driven turbulent flow this correlation represents a "drag" on turbulent mass flux.

Figure 6.21 shows a cross-section of the three-dimensional density field in the x-z plane for Run Acc4b. The horizontal axis corresponds to the x-direction and the

vertical axis is the z-direction. The color field represents the density with the orange being the heaviest fluid and the purple being the lightest. All other colors represent a mixture of the two fluids and the green corresponds to the mean density. The contours correspond to the fluctuating pressure field and the vectors indicate the direction and magnitude of the velocity. The acceleration is in the positive z-direction so that the heavy fluid is moving in the positive z-direction and the light fluid is moving in the opposite direction. This figure shows that the largest velocities are associated with the lighter fluid. The maximum pressures occur at the leading edges of the heavy fluid "blobs" and the smallest pressures are at the trailing edges (i.e., the wake region) of the heavy blobs. On the vertical interface between the heavy and light fluids are regions of high shear which create regions of large vorticity along the vertical interface. Gradients of pressure and gradients of density are perpendicular to each other along the vertical interface and, therefore, produce regions of large vorticity due to baroclinic torque. Also visible are regions where the light fluid is penetrating into regions of the heavy fluid and the breakdown of the large "blobs" into smaller ones occurs.

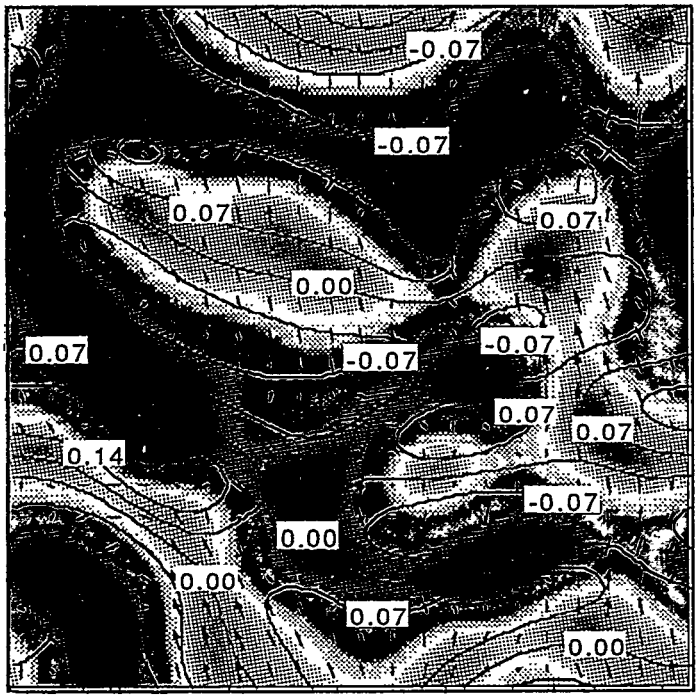

Figure 6.21: x-z cross section at the y midplane for an accelerated case at an early time

6.5.5 *Vorticity dynamics*

It is important to examine the vorticity dynamics in order to provide interpretations of the behavior of the developing flow. The vorticity equation is derived by taking the curl of the velocity equation

$$\frac{\partial u_i}{\partial t} + u_j \frac{\partial u_i}{\partial x_j} = -\frac{1}{\rho}\frac{\partial p}{\partial x_i} + \frac{1}{\rho}\frac{\partial \tau_{ij}}{\partial x_j} + g_i$$

to obtain (see, e.g., Lesieur (1990) [52])

$$\frac{\partial \omega_i}{\partial t} = \omega_j \frac{\partial u_i}{\partial x_j} - u_j \frac{\partial \omega_i}{\partial x_j} - \omega_i \frac{\partial u_j}{\partial x_j} + \frac{1}{\rho^2}\nabla\rho \times \nabla p + \nu \frac{\partial^2 \omega_i}{\partial x_j^2}, \tag{6.34}$$

where $\vec{\omega}$ is the vorticity. The first term on the right side represents the creation or destruction of vorticity through vortex distortion and rearrangement. The second term represents the advection of vorticity, while the third term represents production/destruction of vorticity due to dilatation. The fourth term is the baroclinic term and the last term accounts for the viscous dissipation of vorticity. The mean-squared vorticity equation is obtained by multiplying the vorticity equation [eq. (6.34)] by ω_i, rearranging and averaging, which gives

$$\underbrace{\frac{1}{2}\frac{d\overline{\omega_i\omega_i}}{dt}}_{A} = \underbrace{\overline{\omega_i\omega_j\frac{\partial u_i}{\partial x_j}}}_{B} \underbrace{-\overline{\frac{u_j}{2}\frac{\partial \omega_i\omega_i}{\partial x_j}}}_{C} \underbrace{-\overline{\omega_i\omega_i\frac{\partial u_j}{\partial x_j}}}_{D} + \underbrace{\overline{\frac{\omega_i}{\rho^2}\nabla\rho\times\nabla p}}_{E} + \underbrace{\nu\overline{\omega_i\frac{\partial^2\omega_i}{\partial x_j^2}}}_{F}. \tag{6.35}$$

The enstrophy is the variance of the vorticity [52]. Thus eq. (6.35) is an evolution equation of the enstrophy. The first term on the right side, term B, represents the stretching of the vorticity and is related to the velocity derivative skewness [52]. The last term on the right side, term F, can be written as

$$\nu\overline{\omega_i\frac{\partial^2\omega_i}{\partial x_j^2}} = \nu\frac{\partial^2}{\partial x_j^2}\left\{\frac{1}{2}\overline{\omega_i\omega_i}\right\} - \nu\overline{\frac{\partial\omega_i}{\partial x_j}\frac{\partial\omega_i}{\partial x_j}}. \tag{6.36}$$

The first term on the right side of (6.36) is the viscous transport of enstrophy and is zero in the present case because of statistical homogeneity. Thus,

$$\nu\overline{\omega_i\frac{\partial^2\omega_i}{\partial x_j^2}} = -\nu\overline{\frac{\partial\omega_i}{\partial x_j}\frac{\partial\omega_j}{\partial x_i}} = -2\nu\mathcal{P}.$$

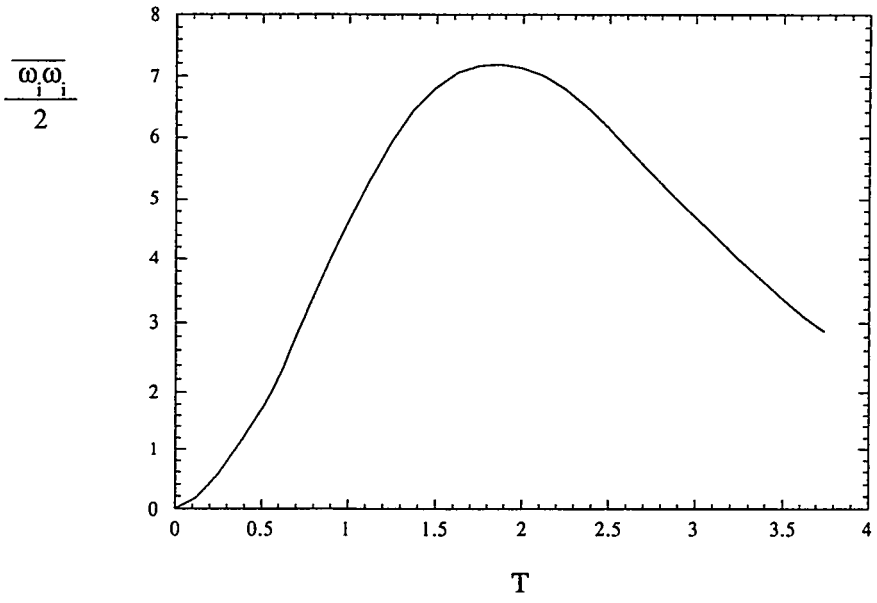

Figure 6.22: Enstrophy evolution for initial density ratio of 4 case (Run Acc1c)

The right side is the viscous dissipation of enstrophy and is related to the palinstrophy, $\mathcal{P}$, for homogeneous flow.

Figure 6.22 shows the enstrophy as a function of time for the case with the initial density ratio of 4 (Run Acc1c). The enstrophy, being initially small due to the fluid being initially nearly motionless, grows, reaches a maximum at approximately $T = 1.8$, and begins to decay through viscous effects. To understand the underlying physics each term in eq. (6.35) is plotted as a function of nondimensional time in Fig. 6.23. This shows that term E, the baroclinic term, is the one most responsible for the initial growth. The baroclinic term reaches a maximum and tends to zero as the density fluctuations decay towards zero. Term F, viscous dissipation, acts to damp the growth and eventually is responsible for the decay of the vorticity. After a time of approximately $T = 0.5$, nonlinear effects develop and the stretching of vorticity increases and acts to slow its decay. The other two terms which represent the advection of vorticity and the dilatation effects remain small in this case.

For further insight into the enstrophy development we look at the behavior of each component. Figure 6.24 shows these components as functions of time for the case with the initial density ratio of 4 (Run Acc1c). The axisymmetric aspect of this problem is seen in this figure as the components of vorticity in the horizontal (x and

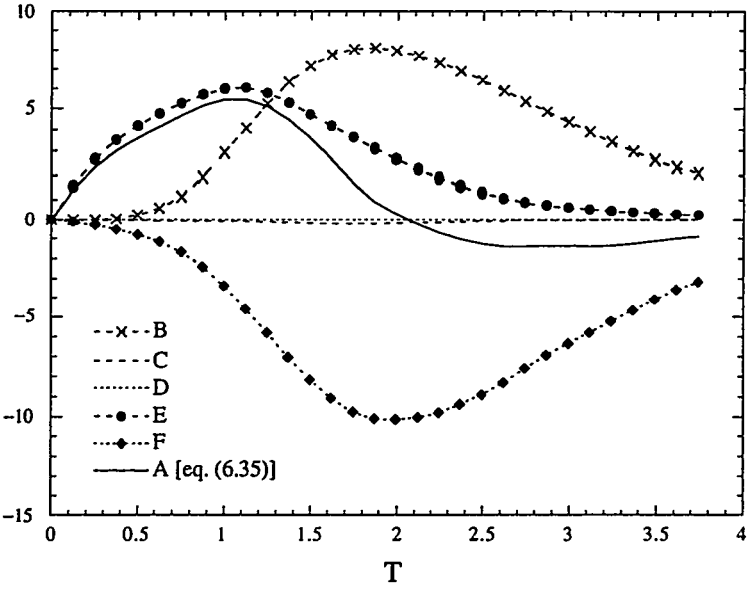

Figure 6.23: Terms of the enstrophy evolution equation [eq. (6.35)] for initial density ratio of 4 case (Run Acc1c)

y directions) are nearly the same and differ significantly from the vertical component. The difference between the two horizontal components can be attributed to the statistical scatter in the simulation. The main vorticity production is in the horizontal direction and is due to baroclinic generation of vorticity. The production of vorticity in the vertical direction is due to vortex turning and then stretching. The enstrophy reaches a maximum and begins to decay through viscous dissipation. Figure 6.25 shows each term of the enstrophy equation [eq. (6.35)] for the x-component. The behavior of the y-component contribution is similar to that for the x-component and is not shown here. Consistent with the interpretation of the overall enstrophy, this figure shows that the enstrophy production at early times for the horizontal components is due to baroclinic production. As the nonlinear effects of the flow develop the enstrophy is maintained by production through vortex stretching and it is surmised that it is decreased due to turning (into the vertical component). The viscous effect slows the growth of enstrophy and eventually is responsible for its decay. Figure 6.26 shows each term of the enstrophy equation [eq. (6.35)] for the z-component. This figure shows that, in the direction of the acceleration, the production of vorticity is due to vortex stretching and turning from the horizontal components. The baroclinic

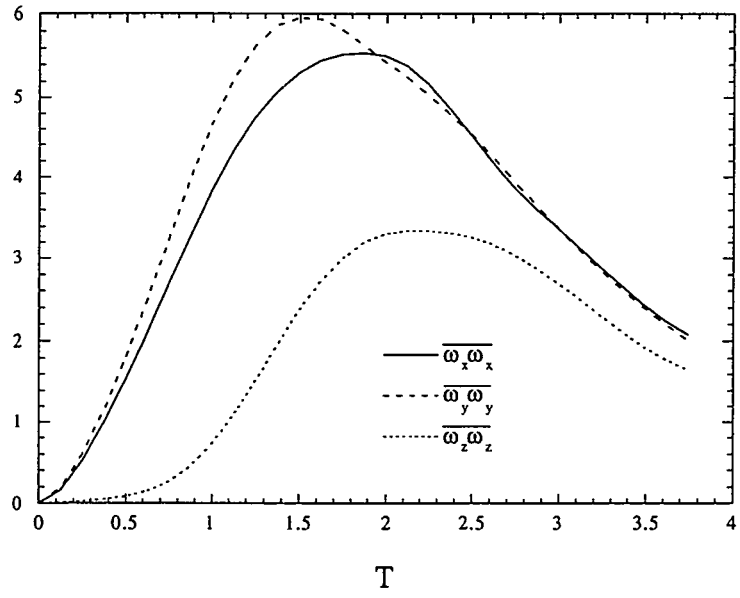

Figure 6.24: Contributions from each direction to the enstrophy for initial density ratio of 4 case (Run Acc1c)

production in this direction is small. Again, viscous effects act to slow the growth of vorticity and is responsible for its decay.

6.5.6 Evolution of the density field

In this section is discussed the evolution of the density field in these buoyancy-generated cases. The evolution of the variance of the density, of the quantity $b(t) = -\overline{\rho' v'}$, of the time scales of decay of $b(t)$, and of the pdf of the density field are examined.

Figure 6.27 contains plots of the variance of the nondimensional density for both initial density ratio cases. For this case at $R_o = 256$, the decay behavior of the nondimensional density is only slightly affected by the magnitude of the initial density fluctuations. The decay behavior is similar to that of the Boussinesq results of Batchelor, et al. for $R_o = 256$. The decay of the variance is slow and nearly linear for $T < 1$. For intermediate times, $1 < T < 2$, it is slightly more rapid and begins to slow again at $T \approx 2$. For the late times, the decay process is slower. At these times the density fluctuations are smaller than 5 percent of their initial value.

Figure 6.28 compares, for the case with initial density ratio of 1.105 (run Acc1a),

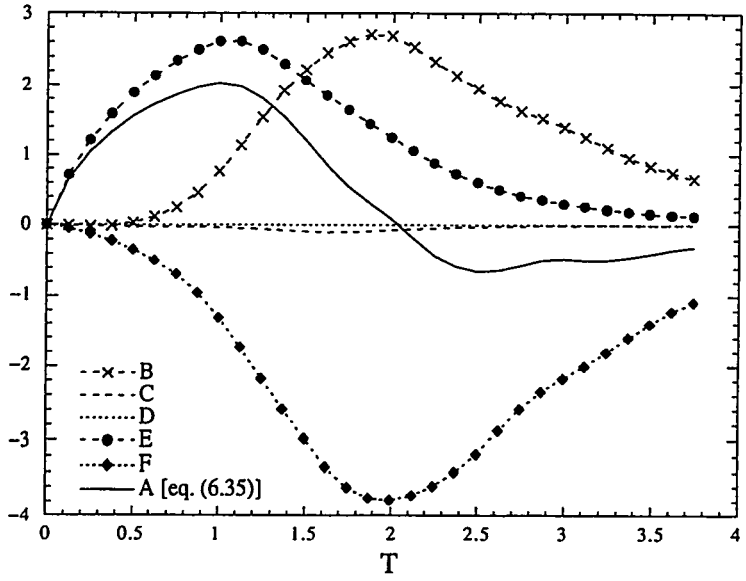

Figure 6.25: Terms of the x-direction contribution to the enstrophy evolution equation [eq. (6.35)] for initial density ratio of 4 case (Run Acc1c)

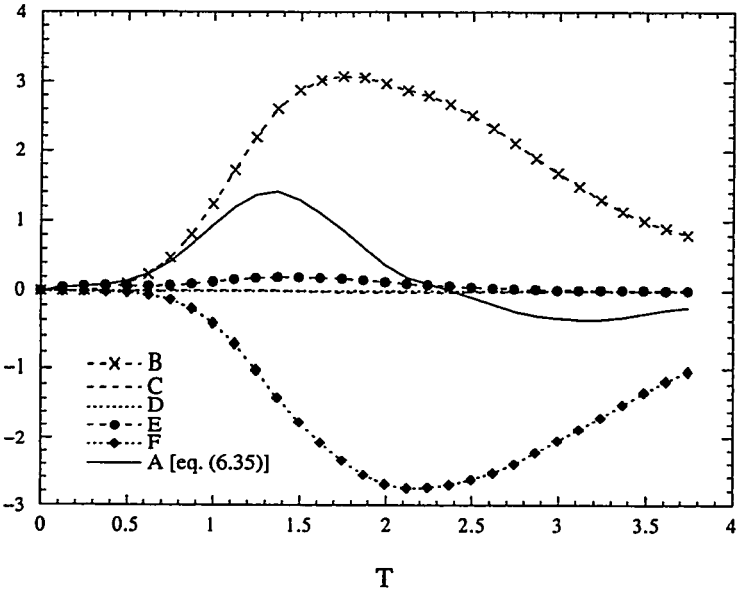

Figure 6.26: Terms of the z-direction contribution to the enstrophy evolution equation [eq. (6.35)] for initial density ratio of 4 case (Run Acc1c)

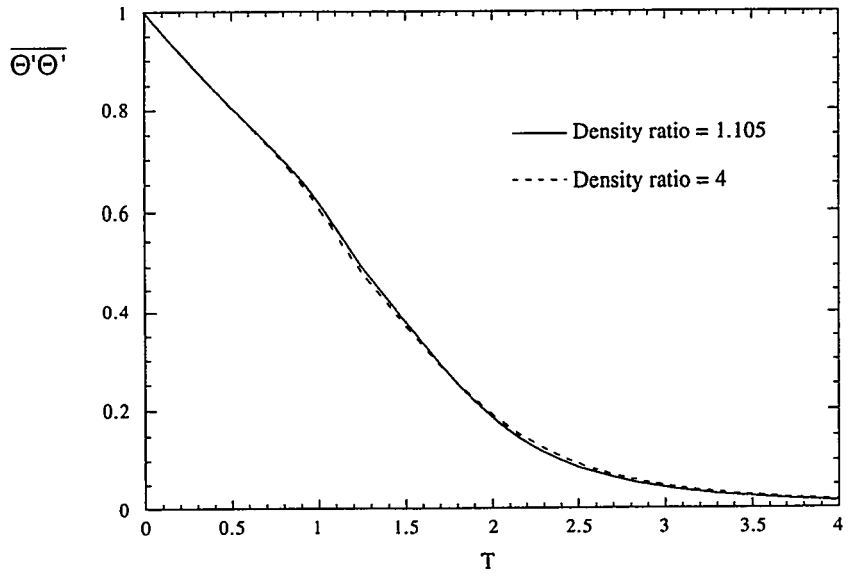

Figure 6.27: Variance of the nondimensional density at $R_o = 256$ for initial density ratio of 1.105 case (Run Acc1a) and 4 case (Run Acc1c)

the evolution of the quantity $B(t) = \overline{\rho'\rho'}/\overline{\rho}^2$ with the quantity $b(t) = -\overline{\rho'v'}$. In the limit as the density fluctuations tend to zero, $b(t) \approx B(t)$, and this figure shows that, at this small initial density ratio, $b(t)$ is nearly equal to $B(t)$.

Figure 6.29 shows the same quantities as plotted in Fig. 6.28 for the case with the initial density ratio of 4 (Run Acc1c). At this larger initial density ratio, $b(t)$ is not equal to $B(t)$. At early times, $b(t)$ is larger than $B(t)$ and is decaying faster. After a time of approximately $T = 2.75$, $b(t) \approx B(t)$. Also, it is seen in Fig. 6.18 that, after this time, the mean pressure gradient is very nearly $\overline{\rho}g$, which is the Boussinesq approximation limit for the mean pressure gradient. It has also been shown that after this time the total turbulent kinetic energy per unit mass is equal to $\overline{u_i'u_i'}/2$ as the terms $\overline{\rho'u_i'u_i'}$ and a_i are nearly zero. Therefore, these are good indications that the flow behavior is within the Boussinesq approximation limit of the flow. At a time of 2.75, the quantity $\left(\overline{\rho'\rho'}/\overline{\rho}^2\right)^{\frac{1}{2}} = 0.13$. Therefore, a possible rule of thumb for studying buoyancy-driven flows with an initial bimodal density distribution is that, if $\theta_o < 0.1$, then the flow is within the Boussinesq approximation limit, whereas, if $\theta_o > 0.1$ the flow is not within this limit. For the initial density ratio of 1.105 case (Run Acc1a), $\theta_o = 0.0434$ and all the results shown for that case are consistent with Boussinesq

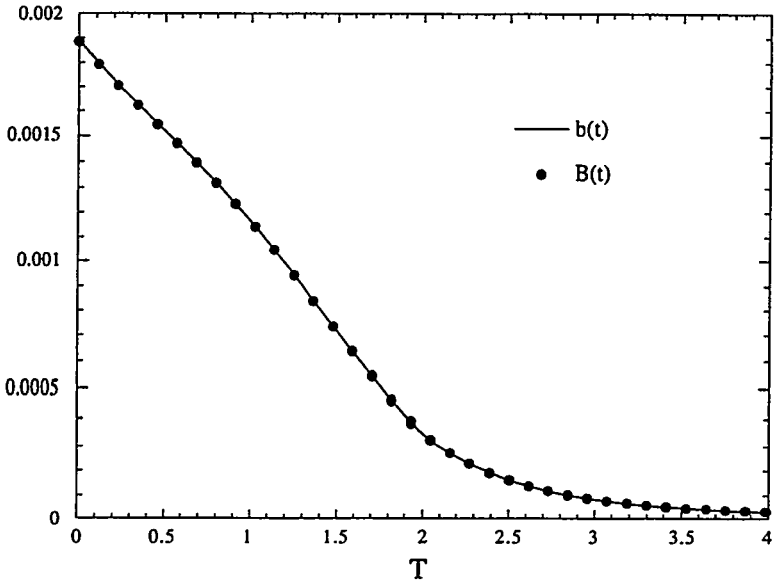

Figure 6.28: Comparison of $b(t)$ and $B(t)$ evolution for initial density ratio of 1.105 case at R_o=256 (Run Acc1a)

approximation limit expectations.

Figure 6.30 shows the time scale for the decay of $b(t)$, given by eq. (4.16), for both cases studied at $R_o = 256$. The decay time scales of the variance of the density field show the same trends and, therefore, are not presented here. Figure 6.30 shows that the time scale for decay for the case with the initial density ratio of 4 is much smaller for all times when $b(t)$ is larger than $B(t)$ (see Fig. 6.29). This means that $b(t)$ is decaying faster for the case with initially larger density fluctuations than for the case with small initial density fluctuations. The time scales grow slightly and then decrease to a value of 1.5, remain at the value for some time, then begin to increase indicating a change in the decay behavior. A linear increase in time scales correspond to a power-law decay, and a constant value for the time scale indicates an exponential decay. For the case with the initial density ratio of 4, from T of 1.5 to 2.75 the time scale of decay for $b(t)$ is nearly constant suggesting exponential decay.

Figure 6.31 show the evolution of the pdf of the density field for the case with the initial density ratio of 1.105 (Run Acc1a). At the initial time the pdf resembles a double-delta function with a "U"-shaped region in between, which represents regions of large and of small density separated by a thin interface in which there is a mixture

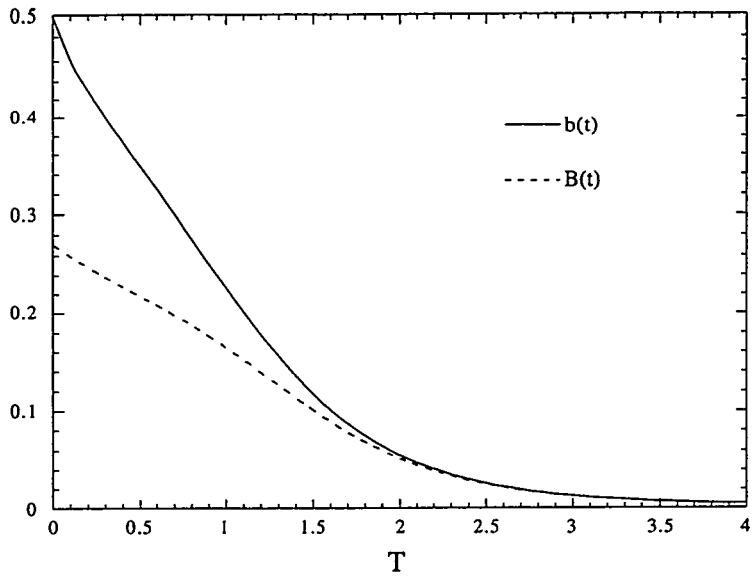

Figure 6.29: Comparison of $b(t)$ and $B(t)$ evolution for initial density ratio of 4 case at R_o=256 (Run Acc1c)

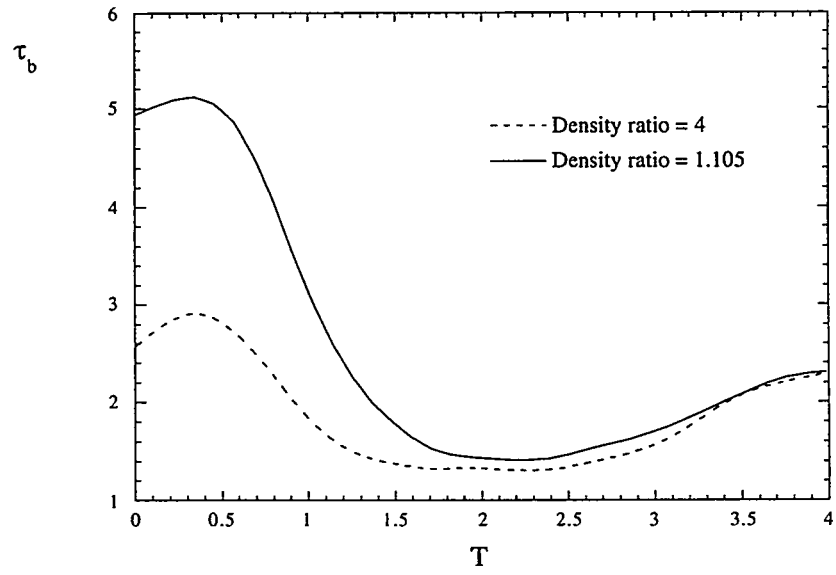

Figure 6.30: Comparison of the time scale of decay for $b(t)$ at $R_o = 256$ for initial density ratio of 1.105 case (Run Acc1a) and 4 case (Run Acc1c)

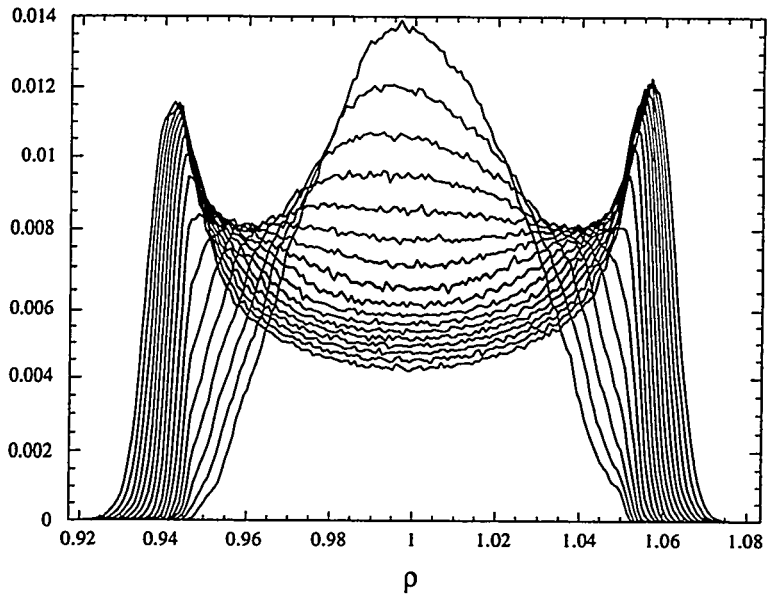

Figure 6.31: PDF evolution, for T=0.0 to 2.0 by 0.125, of the density field at $R_o = 256$ for initial density ratio of 1.105 case (Run Accla)

of the two fluids. As time evolves and the flow develops, the density field is mixing through convective and molecular effects, and the bimodal pdf evolves towards a nearly Gaussian function whose maximum is at the mean density of 1.0. For this case the pdf is slightly skewed to the lower side of the mean density. A Boussinesq approximation of this problem would give symmetric pdf because of the symmetry of the problem. The asymmetry seen in this non-Boussinesq case is similar to those presented in the results for isotropic decay where there was a statistical dependence of the velocity field on the density field (see Chapter 5). In buoyancy-driven flows the velocity field is inherently statistically dependent on the density field. The lower density fluid has the larger velocities associated with it so that the triple correlation, $\overline{\rho' u_i' u_i'}$, is negative. Therefore, the lower density fluid is entrained in the mixing region at a greater rate than the high density fluid, causing this slight skewness. As the initial density ratio increases (with R_o fixed) so too does the maximum value of $\overline{\rho' u_i' u_i'}$ and the skewness observed in the pdf of the density field also increases. Figure 6.32 shows the evolution of the pdf of the density field for the case with the initial density ratio of 4 (Run Acclc). As the initial density fluctuations increase so too does the skewed behavior seen in the pdf, as expected from the entrainment argument.

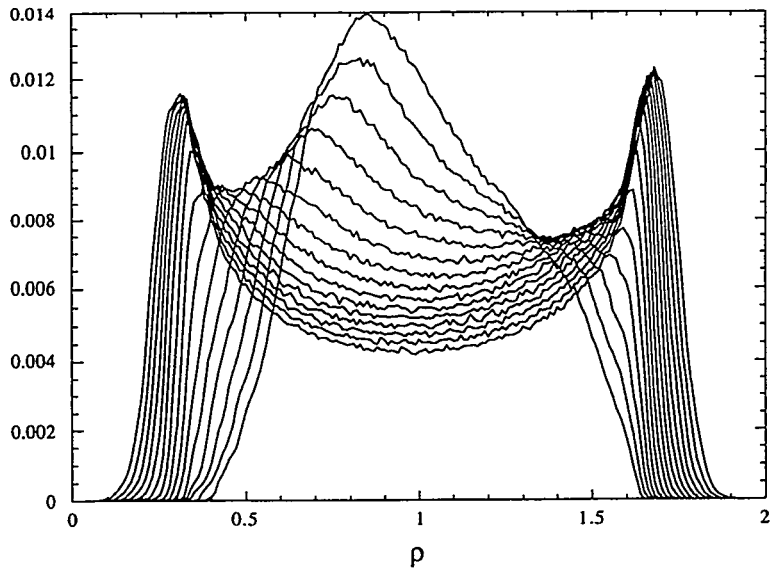

Figure 6.32: PDF evolution, for T=0.0 to 1.75 by 0.125, of the density field at $R_o = 256$ for initial density ratio of 4 case (Run Acc1c)

Two-dimensional cross-sections of the three dimensional density field are here presented for an accelerated case (Run Acc4b) at $T = 1$. Figure 6.33 shows the x-z cross-section at the y-midplane. The horizontal axis is the x-direction and the vertical axis is the z-direction. The orange color represents the heaviest fluid while the purple represents the lightest. All other colors are a mixture of the two fluids with the green representing the mean density. The acceleration is applied in the positive z-direction. Therefore, the heavy fluid is moving in the positive z-direction and the light fluid is moving in the opposite direction. At this time, the flow still exhibits some of the random nature of the initial conditions. However, there are several identifiable features that can be seen. The length scales of the density "blobs" are axisymmetric. At the leading edges of the heavy fluid, the interface between the heavy and the light fluids is very narrow. In the wake regions, at the trailing edges of the heavy fluid, the interface is more diffuse. There are narrow regions where the heavy fluid is jetting around the light fluid. Some of the smaller light fluid "blobs" are "U" shaped because drag between the heavy and light fluids is causing some of the light fluid particles to trail the main body of the light "blobs". Some of the light density fluid appears to have coalesced and formed an elongated "tube" in the direction of the

acceleration (seen near the horizontal center of the figure). Along the interface of this "tube" structure a Kelvin-Helmholtz-like shear layer has formed and entrainment regions are visible. Also visible are the "mushroom-like" features that are seen in Rayleigh-Taylor instabilities.

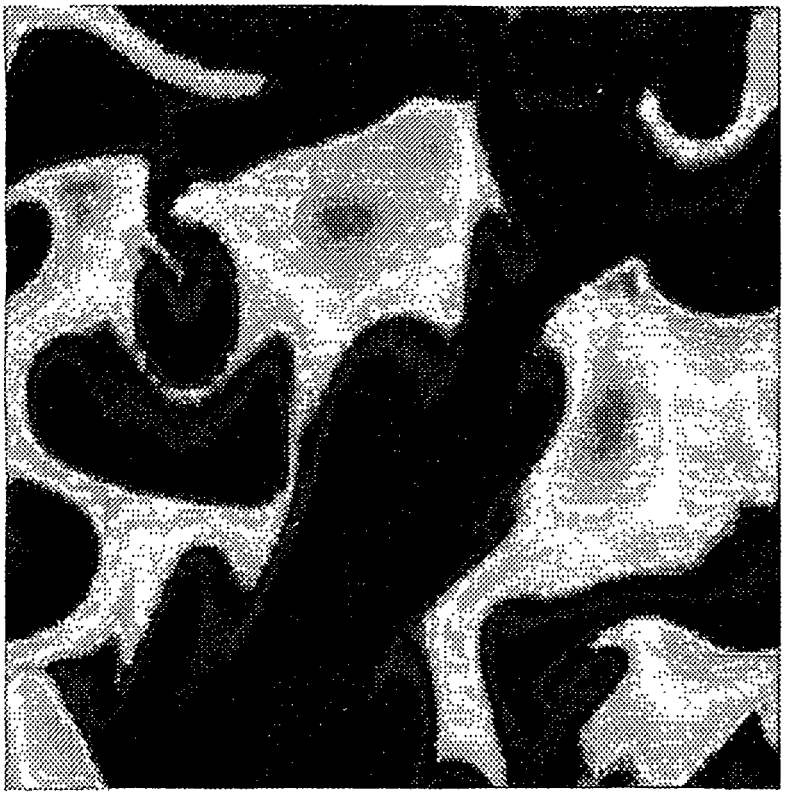

Figure 6.33: x-z cross-section of the density field near the y-midplane for an accelerated case at $T = 1$. Heaviest fluid is orange and the lightest is purple.

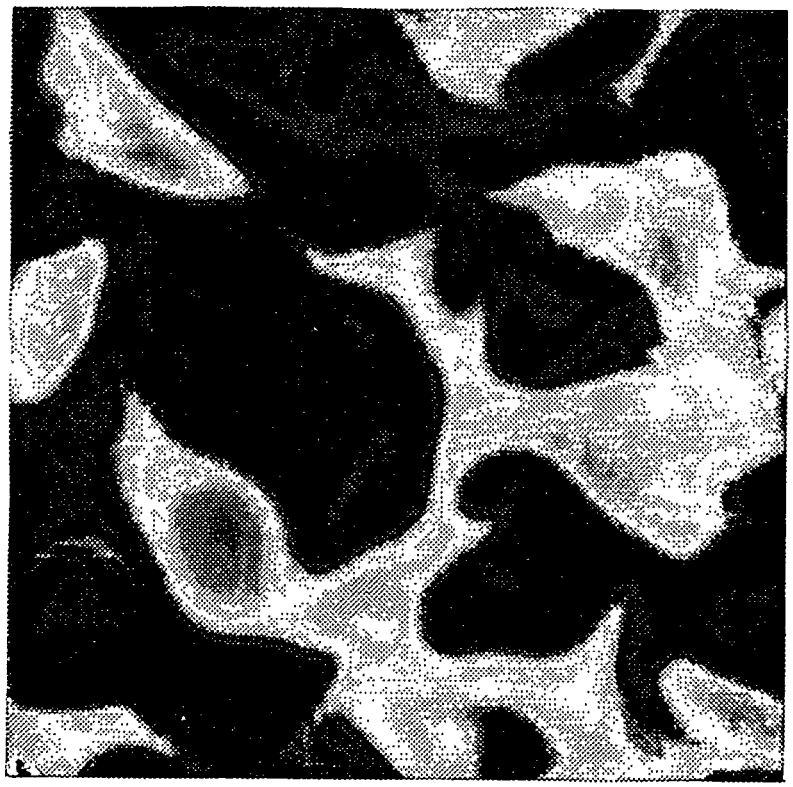

Figure 6.34: x-y cross-section at z=0.1 of the density field for an accelerated case at $T = 1$. Heaviest fluid is orange and the lightest is purple.

Figure 6.34 shows the x-y cross section at z=0.1. The horizontal axis is the x-direction and the vertical axis is the y-direction. This cross section is perpendicular the direction of acceleration (z-direction). The large nearly circular low density blob to the left of the center of the figure is a cross section of the elongated low-density "tube" discussed in the previous figure. The center of this tube contains low density fluid. This core is surrounded by a region of heavier fluid which in turn is surrounded by a region of light fluid. This show the entrainment behavior between the two fluids which is possibly due to a Kelvin-Helmholtz instability. This figure shows planar isotropy in the direction perpendicular to the acceleration and that the interface between the light and the heavy fluids is quite sharp. In regions where the heavy fluid is not well represented the interface is more diffuse.

Figure 6.35 shows the y-z cross section at x=0.25. The horizontal axis is the y-direction and the vertical axis is the z-direction. The low density "blob" at the bottom-center of the figure is a cross section of the elongated low density "tube" seen in Fig. 6.33. This figure shows similar features as seen in Fig. 6.33.

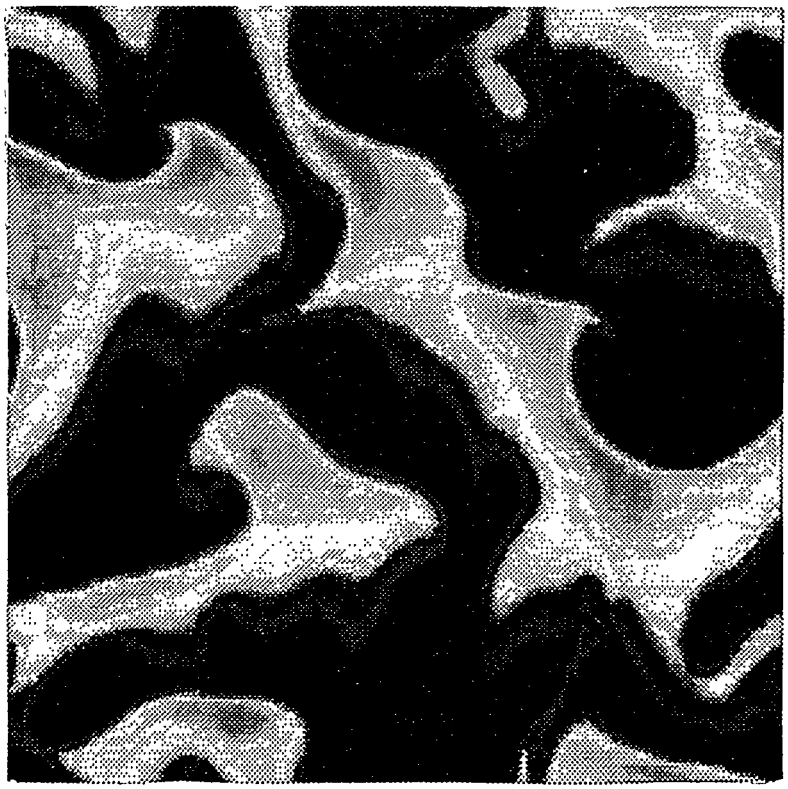

Figure 6.35: y-z cross-section at x=0.25 of the density field for an accelerated case at $T = 1$. Heaviest fluid is orange and the lightest is purple.

6.5.7 *Length scales*

In this section we examine the behavior of length scales. It is useful to discuss the anisotropy in terms of length scales, and hence to address the longitudinal and lateral microscales. The longitudinal microscale is defined as (see, e.g., Riley, et al. [72])

$$\lambda_{f_i}^2 = \frac{\overline{u_i' u_i'}}{\left(\frac{\partial u_i'}{\partial u_i}\right)^2} \; i = 1, 2, \; 3, \text{ no summation on } i \tag{6.37}$$

while the lateral microscale is defined as

$$\lambda_{g_{i,j}}^2 = \frac{\overline{u_i' u_i'}}{\left(\frac{\partial u_i'}{\partial u_j}\right)^2} \; i \neq j, \text{ no summation on } i \text{ or } j. \tag{6.38}$$

It can be shown that the various microscales are related to the slopes of the corresponding correlation functions [4, 57] (i.e., related to the second derivative of the correlation function at zero separation distance). For isotropic turbulence all three longitudinal microscales are equal, and all the lateral microscales are equal. Also, for isotropic turbulence the lateral and longitudinal microscales are related by $\lambda_{f_k} = \sqrt{2}\lambda_{g_{i,j}}$ [75].

Figure 6.36 is a plot of the longitudinal microscales for the two cases. The discontinuity in slope at the early times is due to an insufficient number of output times to obtain a continuous curve. The microscales in the vertical direction (i.e., the direction of the acceleration) are larger than the microscales in the horizontal direction. For these cases, the flows are highly nonisotropic. The effect of increasing initial density fluctuations is to decrease the microscales at early times. By a time of 2, when the density fluctuations have decayed to a small value, the microscales are nearly the same for both cases. The vertical microscales are larger than the horizontal partly because the vertical component of the kinetic energy is larger. This behavior is different from the case of stably stratified flow where the horizontal microscales are larger than the vertical microscales because the effect of stable stratification is to decrease the vertical component of the kinetic energy (see, e.g., Riley et al. [72]) and increase the scales in the horizontal.

Figure 6.37 is a plot of the lateral microscales for the two cases. Here, the horizontal microscales are averaged, assuming planar isotropy. The lateral microscales in the

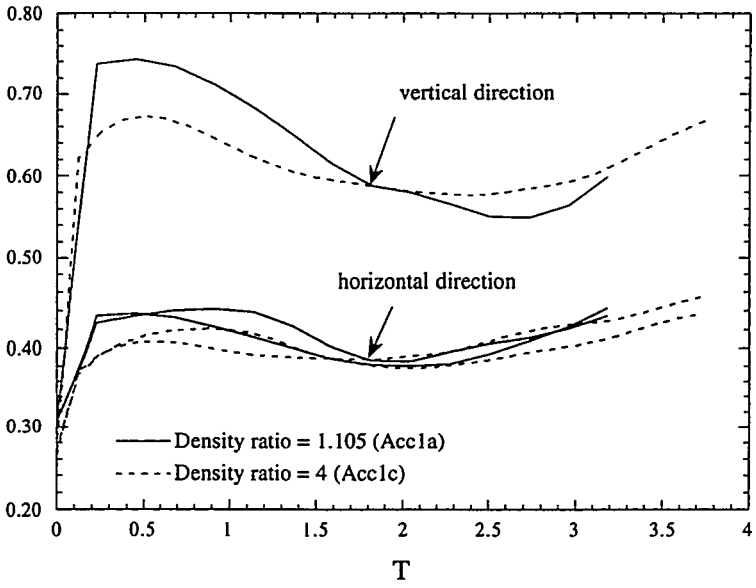

Figure 6.36: Longitudinal microscales for the initial density ratio of 1.104 case (Run Acc1a) and for the initial density ratio of 4 case (Run Acc1c)

vertical direction are smaller at early times than and the microscales in the horizontal direction. At later times, the microscales in the vertical direction are larger. Again, the effect on increasing initial density fluctuation is to decrease the microscales at early times. By a time of 2, when the density fluctuations have decayed to a small value, the microscales are nearly the same for both cases.

6.5.8 Spectral Evolution

One-dimensional spectra

In this section we present one-dimensional spectra for the fluctuating density and the three components of velocity. The one-dimensional spectra is extracted [72] as, (e.g., for the u-velocity component transformed in the x-direction),

$$E_{xu}(k) = \frac{1}{N_y N_z \Delta k} \sum_{i,j=1}^{N_y N_z} \hat{u}(k, y_i, z_j)\hat{u}^*(k, y_i, z_j),$$

where N_y and N_z are the number of grid points in the y and z directions, respectively.

Figure 6.38 shows the one-dimensional spectra for the u-velocity at $T = 0.5$ for all three directions for the case with the initial density ratio of 4. $E_{xu}(k)$ is the longitudi-

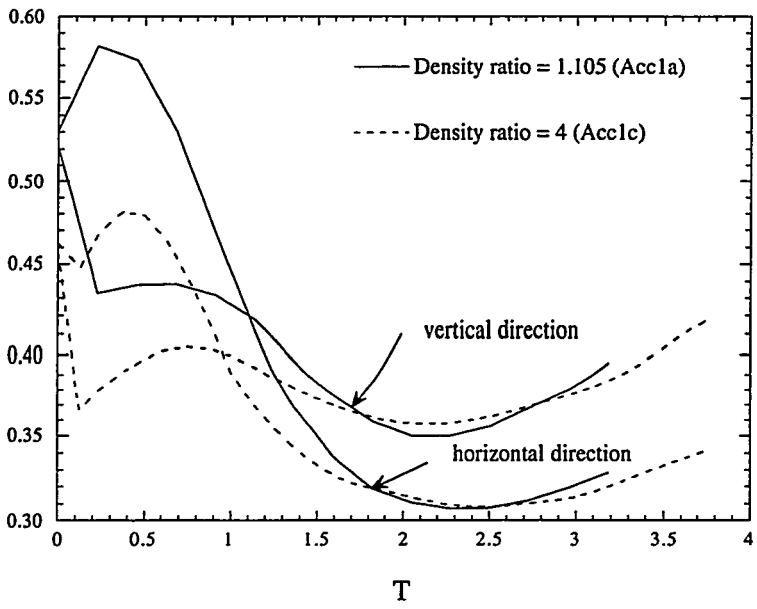

Figure 6.37: Lateral microscales for the initial density ratio of 1.104 case (Run Acc1a) and for the initial density ratio of 4 case (Run Acc1c)

nal spectrum of the u-velocity, $E_{yu}(k)$ is the lateral spectrum in the y-direction, and $E_{zu}(k)$ is the lateral spectrum in the z-direction. At this time, the length scales are larger in the horizontal direction, as indicated by the larger low wavenumber values for $E_{yu}(k)$ compared to $E_{zu}(k)$. This is consistent with the results seen in Fig. 6.37 which shows that, at early times, the lateral microscale is larger in the horizontal direction. It is observed (not plotted here) that $E_{xu}(k)$ and $E_{yv}(k)$ have the same shape and $E_{yu}(k)$ and $E_{xv}(k)$ have the same shape, which is due to the isotropy condition on the longitudinal and lateral correlation functions. Figure 6.39 shows the one-dimensional spectra for the u-velocity at $T = 2.0$ for all three directions for this case. At this time, the lateral microscale is larger in the vertical direction. This behavior is not as apparent in the spectra of these correlation functions.

Figure 6.40 shows the one-dimensional spectra for the fluctuating density field at $T = 0.0, 1.0$, and 3.0 for the case with an initial density ratio of 4. This shows that initially the fluctuating density field is isotropic. As time evolves, the density field becomes anisotropic. In the direction of the acceleration, the density field has more small scales associated with it, while, in the horizontal direction, the density field is planer isotropic. By a time of $T = 3.0$, when the density fluctuations have decayed

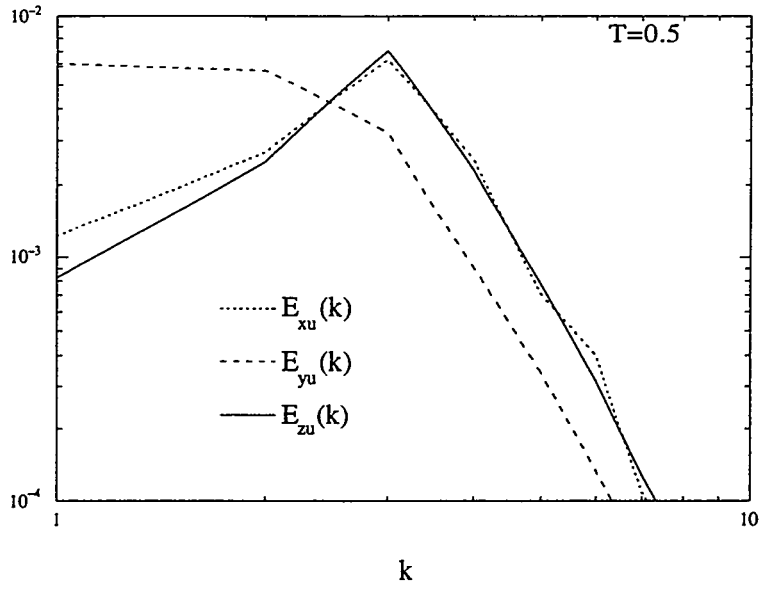

Figure 6.38: One-dimensional spectra for the u-velocity for the initial density ratio of 4 case (Run Acc1c) at T=0.5

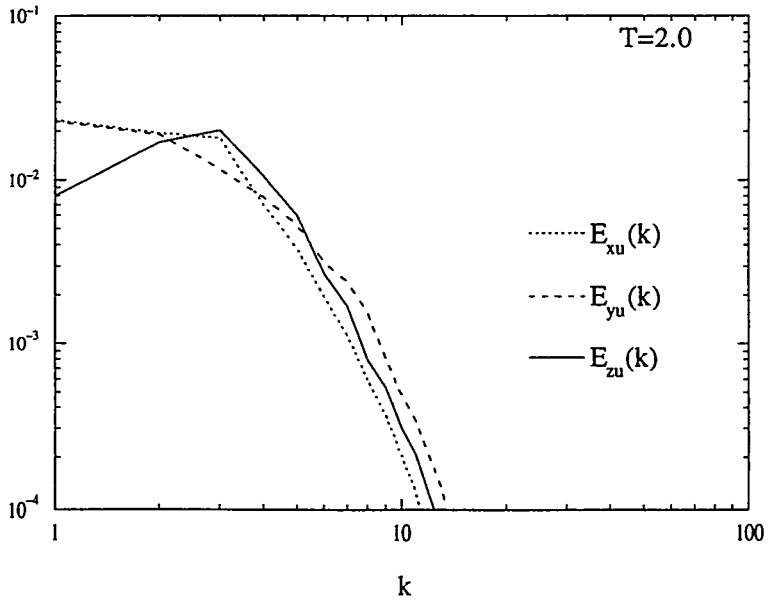

Figure 6.39: One-dimensional spectra for the u-velocity for the initial density ratio of 4 case (Run Acc1c) at T=2.0

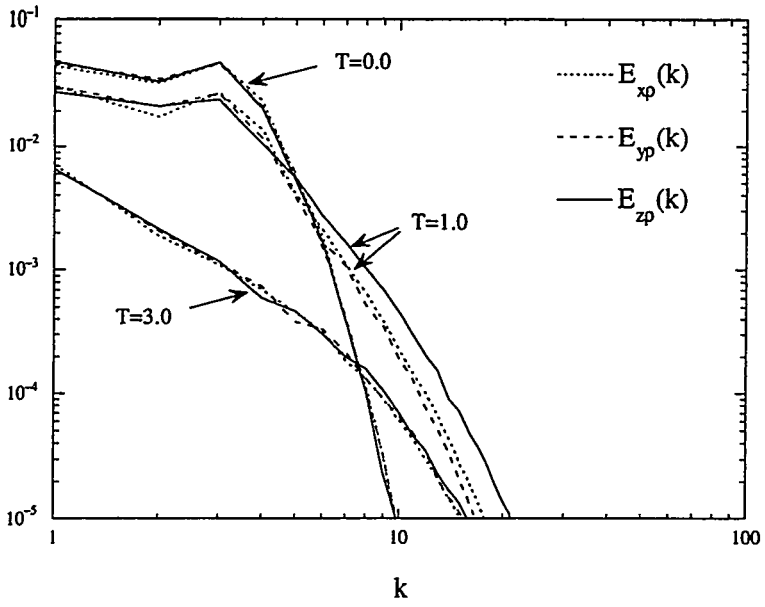

Figure 6.40: One-dimensional spectra for the fluctuating density field for all three directions for the initial density ratio of 4 case (Run Acc1c) at T=0.0, 1.0, and 3.0

to small quantities, the density field has returned to a nearly isotropic state.

Three-dimensional spectra

This section is presents the evolution of the spectra for various quantities for the case with the initial density ratio of 4 (Run Acc1c). The binning procedure for computing the spectra is discussed in Appendix E. The spectra for these simulations are computed for wavenumbers up to 64. We begin by examining the evolution of the spectrum of $\rho u_n' u_n'/2$ for run Acc1c. Figure 6.41 shows the evolution for a sequence of times from $T = 0$ to 3.75 by increments of 0.25. At $T = 0$ there very little energy because the initial velocity field is nearly zero. At early times, the spectrum increases at all wavenumbers shown, with a maximum at $k = 3$ which corresponds to the wavenumber at which the initial density field has a maximum spectral value. In this figure we see spectral values for the early times that do not range the entire wavenumber span in the simulation. The reason the spectra are plotted in this manner is because, at wavenumbers greater than those that are plotted, the spectrum has small negative values and, therefore, cannot be plotted on a log-log plot. It is observed that, as the flow develops, the cut-off for which the spectra become negative increases

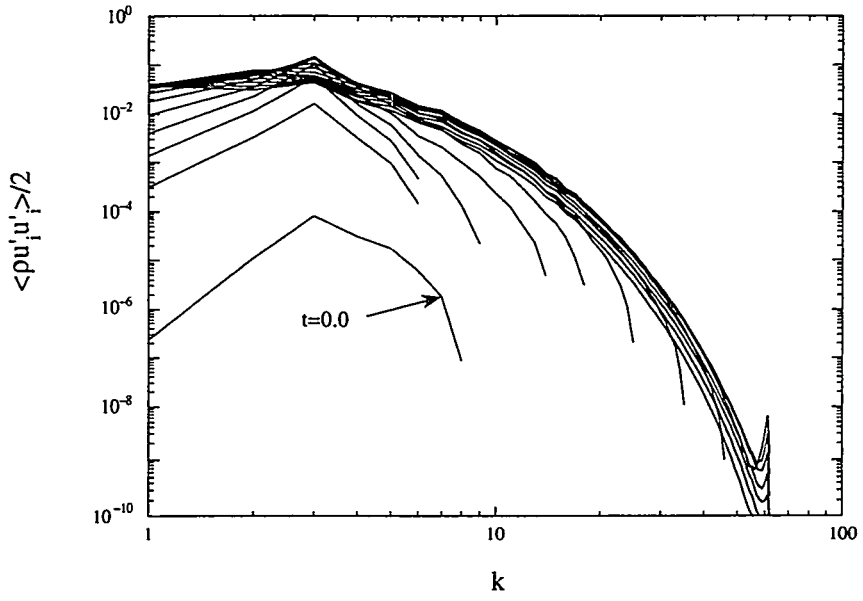

Figure 6.41: Spectral evolution of $\rho u_n' u_n'/2$ at $R_o = 256$ for initial density ratio of 4 case (Run Acc1c)

in wavenumber as energy is cascaded from low to high wavenumbers. After the spectrum has built up at the large wavenumbers, and cascade has been established, it begins to decay as the source of potential energy in this problem has been exhausted and viscous effects become dominant.

Figure 6.42 shows the evolution of the spectra for $\overline{\rho} u_n' u_n'/2$ for the same times given in Fig. 6.41. This shows that, during early times, the spectral energy for $\overline{\rho} u_n' u_n'/2$ is transferred to higher wavenumbers at a greater rate than the spectral energy for $\rho u_n' u_n'/2$. The maximum also occurs at $k = 3$. At late times the spectrum is decaying at all wavenumbers. The difference between the spectra of $\rho u_n' u_n'/2$ and $\overline{\rho} u_n' u_n'/2$ are due to the spectrum for $\rho' u_n' u_n'/2$. This is shown for early times in Fig. 6.43. At the initial time the spectra of $\rho' u_n' u_n'/2$ is nearly zero because the initial velocity field is nearly zero. As the flow develops, the magnitude grows to a maximum then decays away as the density fluctuations decay. The spectrum of $\rho' u_n' u_n'/2$ is negative since in this case the largest velocities are associated with the negative density fluctuations.

Figure 6.44 shows the evolution of the spectra of the density field for $T = 0.0$ to 3.75 by increments of 0.25. At early times, during convective mixing, the high wavenumber content increases rapidly. Once the density transfer has reached the

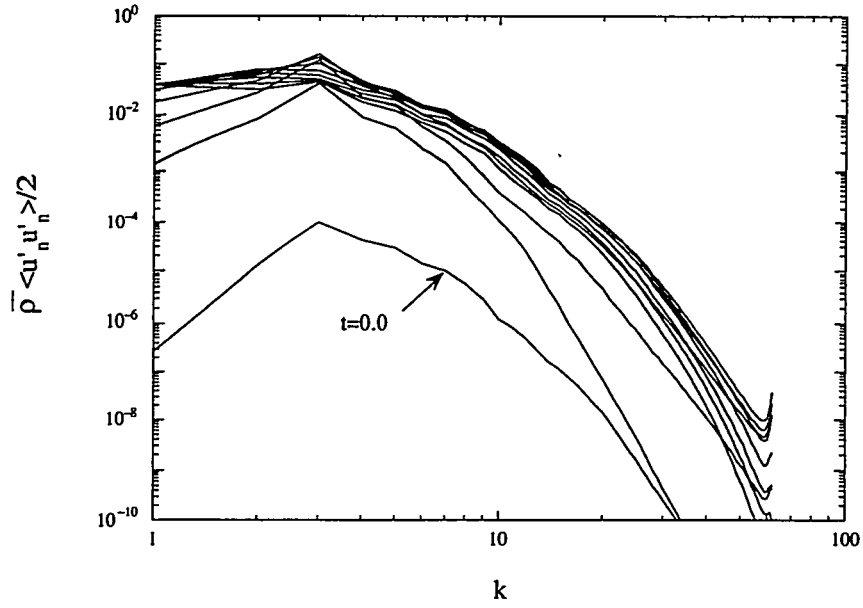

Figure 6.42: Spectral evolution of $\overline{\rho}u_n'u_n'/2$ at $R_o = 256$ for initial density ratio of 4 case (Run Acc1c)

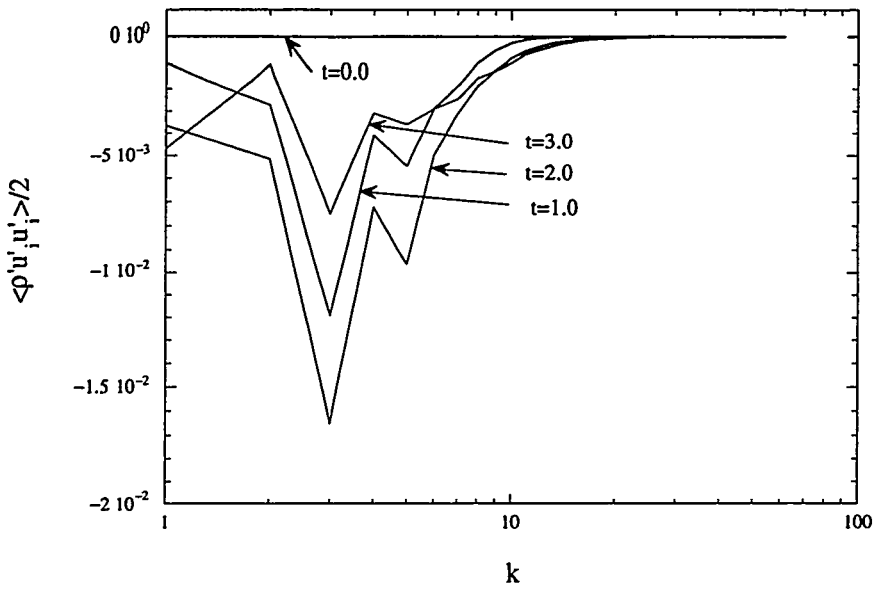

Figure 6.43: Spectral evolution of $\rho' u_n' u_n'/2$ at $R_o = 256$ for initial density ratio of 4 case (Run Acc1c)

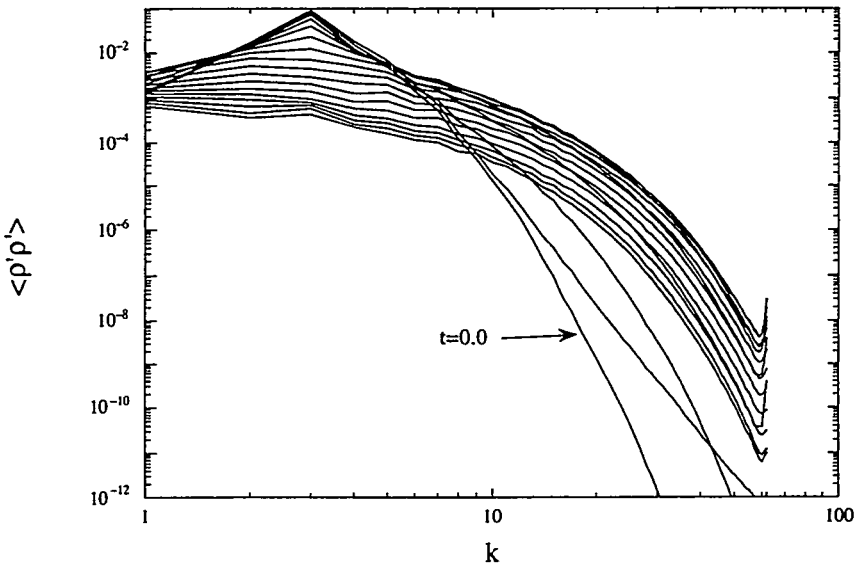

Figure 6.44: Spectral evolution of $\rho'\rho'$ at $R_o = 256$ for initial density ratio of 4 case (Run Acc1c)

dissipation scale then the density fluctuations decay due to molecular mixing. Figure 6.45 shows the spectral evolution of $(\partial u_n'/\partial x_n)$. This quantity is related to the density through condition (2.11). Therefore, at early times the maximum is at a wavenumber of 3. As the flow develops the maximum of this quantity shifts to a wavenumber of 14. The length scales associated with this wavenumber are the length scale where dilatation effects are most prominent. At late times as the velocities in the flow decay, so too does the spectrum of $(\partial u_n'/\partial x_n)$.

6.5.9 Summary of variable-density effects at $R_o = 256$

This section has discussed variable-density effects on the behavior of buoyancy-driven flow at $R_o = 256$. It has been shown that an important parameter that characterizes buoyancy driven flow is θ_o [eq. (6.9)], a measure of the intensity of the initial density fluctuations. A rule of thumb is suggested that, if θ_o is less than about 0.10, then the resulting buoyancy-driven flow is within the Boussinesq approximation. Likewise, if θ_o is larger than about 0.10 then the resulting flow is non-Boussinesq.

As the initial density fluctuations are increased, the flow behavior deviated increasingly away from the Boussinesq approximation limit. Also, the nondimensional

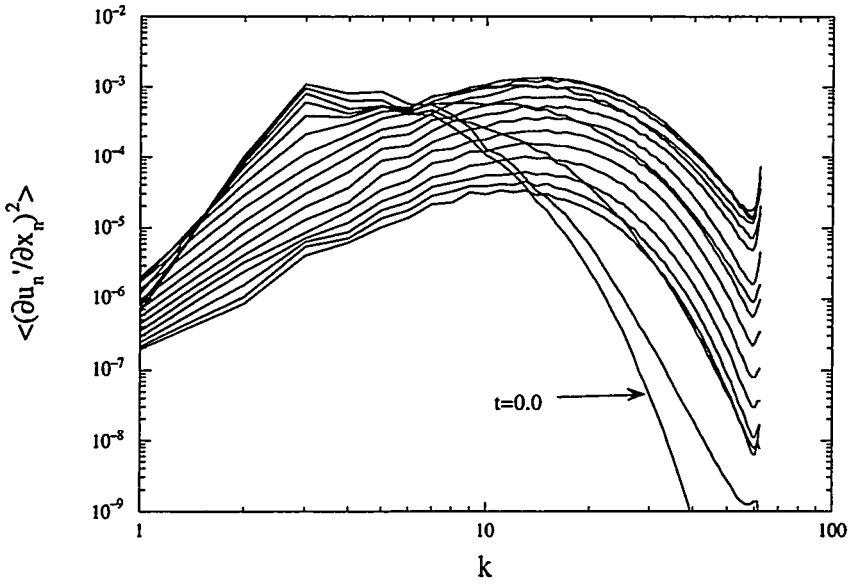

Figure 6.45: Spectral evolution of $(\partial u_n'/\partial x_n)$ at $R_o = 256$ for initial density ratio of 4 case (Run Acc1c)

mean-squared velocity increases, while the nondimensional kinetic energy decreases. The nondimensional time at which the mean-squared velocity reaches a maximum decreases as the initial density fluctuations increase. It is conjectured that, in the limit as the initial density ratio becomes very large (much larger than 4), the mean-square velocity history will approach a limiting curve since this quantity must remain bounded. This limiting case is not studied here due to resolution limitations in our numerical scheme.

There are three terms that contribute to the evolution of the total turbulent kinetic energy per unit mass, given by eq. (A.7):

$$K(t) = \frac{R_{nn}(t)}{2\overline{\rho}} = \frac{\overline{\rho u_n'' u_n''}}{2\overline{\rho}} = \frac{\overline{u_n' u_n'}}{2} + \frac{\overline{\rho' u_n' u_n'}}{2\overline{\rho}} - \frac{a_n a_n}{2}.$$

These three terms are the mean-squared velocity, $\overline{u_n' u_n'}/2$, a triple correlation term, $\overline{\rho' u_n' u_n'}/2\overline{\rho}$, and a mass flux term, $a_n a_n/2$. Within the Boussinesq limit, this triple correlation and the mass flux are very small compared to the first term. As the initial density fluctuations are increased, these two terms grow to large values and their effects become more important. These two terms are negative, resulting in a lower nondimensional kinetic energy per unit mass. Negative values for the triple

correlation term, $\overline{\rho' u_n' u_n'}/2\overline{\rho}$, correspond to larger velocity magnitude being associated with negative density fluctuations and is a result of the conservation of momentum.

A consequence of the Boussinesq approximation is that the mean pressure gradient (i.e., the gradient of the hydrostatic pressure) is uniform in time with the value $\overline{\rho} g_i$. This approximation is accurate in the limit of small density fluctuations but, as the initial density fluctuations increase, the mean pressure gradient becomes variable in time and its value is given by eq. (3.19) and written here as

$$\frac{\partial \overline{p}}{\partial x_i} = \frac{1}{\bar{v}} \left\{ g_i + \overline{v' \frac{\partial \tau_{ni}'}{\partial x_n}} + \overline{u_i' \frac{\partial u_n'}{\partial x_n}} - \overline{v' \frac{\partial p'}{\partial x_i}} \right\}.$$

In the limit as the density fluctuations tend to zero, eq. (3.19) gives the Boussinesq approximation for the mean pressure gradient. In the absence of fluid motion (e.g., at time equal to zero) the mean pressure gradient is

$$\frac{\partial \overline{p}}{\partial x_i} = \frac{1}{\bar{v}} \left\{ g_i - \overline{v' \frac{\partial p'}{\partial x_i}} \right\}.$$

Here, the correlation of the fluctuating specific volume-fluctuating pressure gradient is a non-Boussinesq departure from the hydrostatic pressure gradient. As the initial density fluctuations increase so also does this correlation. The presence of this correlation acts to impeded the growth of the turbulence mass flux. In the absence of an acceleration, this term is not present but immediately has a nonzero value the instant that an acceleration is applied.

The enstrophy is initially zero, grows to a maximum and then decays through viscous dissipation. The initial growth is due to a generation of vorticity in the plane perpendicular to the direction of the acceleration through baroclinic torque. The vorticity in this plane is much larger than the component in the direction of the acceleration, which receives vorticity through turning which is then enhanced by stretching. There is very little generation of this component due to baroclinic torque. The destruction of vorticity in all three directions is through viscous dissipation. It should be noted that, in the Boussinesq limit, the baroclinic torque only act in the planes perpendicular to the acceleration.

It has been also shown that, for consistency with the Boussinesq approximation, the quantity $b(t) = -\overline{\rho' v'}$ should be equal to $B(t) = \overline{\rho' \rho'}/\overline{\rho}^2$. Also, as the initial density fluctuations increase, the pdf of the density field has an increasingly larger

skew (to the negative side of the mean density) associated with it. It is argued that this skewness is attributed to larger entrainment rates of the lighter fluid than the heavier fluid into the mixing region.

6.6 Reynolds number effects

This section describes the results of three simulations that differ only in the "pseudo-Reynolds" number of buoyancy-driven flows, with values $R_o = 256$ (Acc1c), $R_o = 512$ (Acc2c) and $R_o = 64$ (Acc3c). The effect of different Reynolds numbers is studied using an initially bimodal density field with an initial density ratio, ρ_{max}/ρ_{min}, of 4 for each case. The case with $R_o = 512$ is near the limit at which a density ratio of 4 can be computed accurately without losing numerical resolution. Higher Reynolds numbers can be achieved by using subgrid modeling (i.e., large eddy simulations) to resolve the small scales (as was done for the Boussinesq results of Batchelor et al. [7]). As established in the previous section, at this initial density ratio, the flow is outside the limits of validity of the Boussinesq approximation. Therefore, these simulations were computed with the Navier-Stokes equations of motion without the Boussinesq approximation. In these simulations $g = 1$ and $\sigma = 1$. The grid size is 128^3 in runs Acc1c and Acc2c and 64^3 in run Acc3c. A courser mesh size is used for the case at $R_o = 64$ case because at this mesh size the flow is well resolved.

The initial velocity field is set to zero then slightly modified to account for the required divergence of the velocity field [eq. (2.11)] . An acceleration is be applied in the vertical direction and the developing flow is statistically axisymmetric in the horizontal planes.

6.6.1 Energy evolution

Consider the energetics of the flow. A quantity of interest is the time history of the mean-squared velocity for different R_o. Figure 6.46 shows the mean-squared velocity as a function of time. Some of the trends that are seen in the Boussinesq results of Batchelor et al., (see Fig. 6.1) are also observed in these non-Boussinesq cases. As the Reynolds number is increased, the mean-squared velocity appears to be approaching a limiting curve. As was discussed in Section 6.5.1, the mean-square velocity reaches a maximum at $T = 1.5$, which is an earlier time than in the Boussinesq approximation

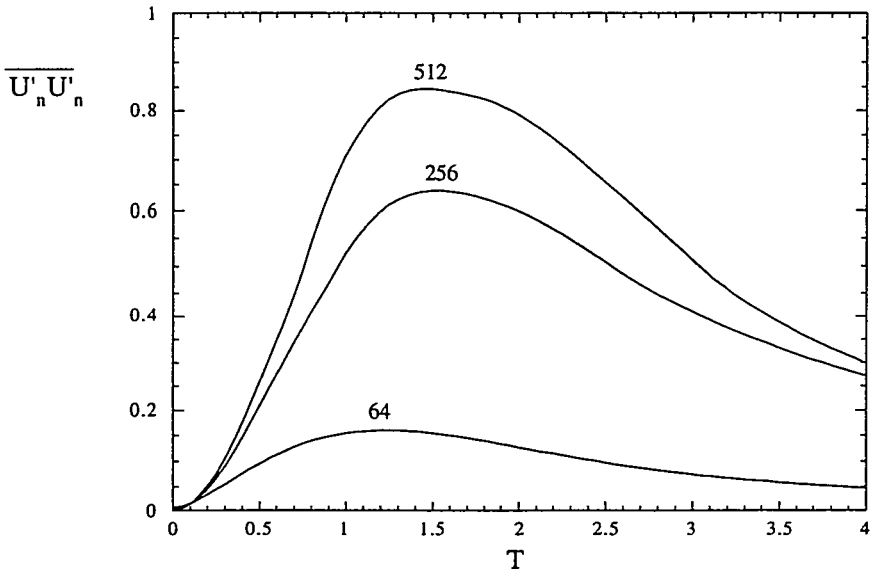

Figure 6.46: $\overline{U'U'}$ *vs.* T for non-Boussinesq cases with an initial density ratio of 4 at various R_o

limit. And for the case with $R_o = 512$, the shape of this curve differs somewhat from the corresponding curve in the Boussinesq approximation limit [Batchelor et al. [7]]. The progression of the limiting behavior would be more clear if the gap that exists between the cases with $R_o = 64$ and $R_o = 256$ were filled with results from a case with $R_o = 128$.

A measure of large-scale anisotropy, γ, [7] of the flow is given by eq. (6.26). Figure 6.47 contains plots of γ for these three cases of different R_o. As the Reynolds number is increased the flow becomes more anisotropic at very early time and then becomes less anisotropic at later times. This figure also shows that the degree of anisotropy appears to asymptote to a constant value that is Reynolds number dependent. This is not so surprising as the velocity field (from which the measure of anisotropy is derived) evolution is dependent on R_o. Note that the flow is initially very nonisotropic. However, as the flows develop, they become more isotropic, as spectral energy transfer occurs, especially at high wavenumbers. The higher R_o cases allow more energy at higher wave numbers and hence are more isotropic.

Figure 6.9 shows each term in the equation for the total energy per unit mass [eq. (A.7)] for the initial density ratio of 4 case at $R_o = 256$. Figures 6.48 and 6.49 show

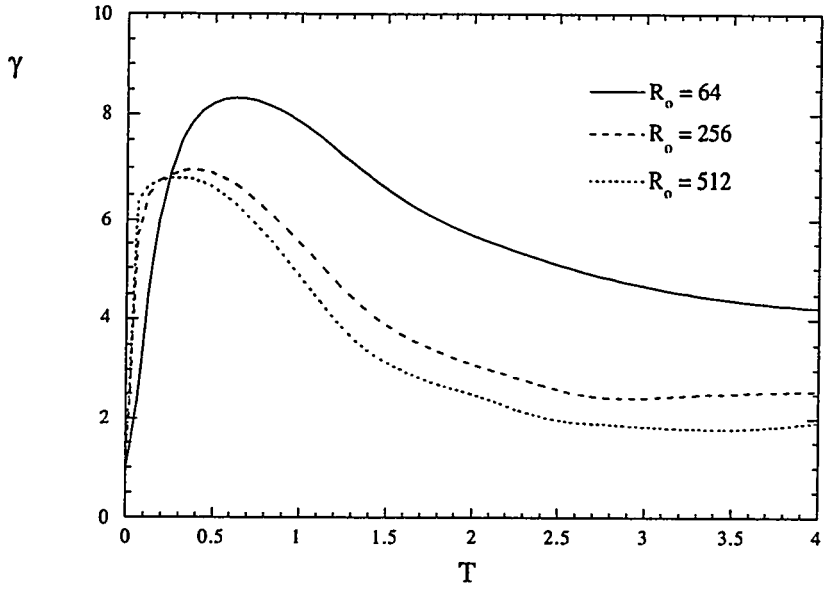

Figure 6.47: Measure of anisotropy of the mean-squared velocity for the initial density ratio of 4 cases for various R_o

the corresponding information for the cases with $R_o = 64$ and 512. Comparisons of these three figures show several features that vary with the Reynolds number. As the Reynolds number is increased, each term in the total turbulent kinetic energy equation increases in value. This is due to an increase in the velocities that are generated through buoyancy effects. The increases in the initial Reynolds number are achieved by lowering the viscosity of the problem. With $\sigma = 1$ held fixed for these cases, $\mathcal{D}$ also changes. Thus, as R_o increases, both viscosity (which slows the flow down) and diffusion (which reduces the forcing) are weaker, so larger velocities are obtained. The magnitude of triple correlation term, $\overline{\rho' u_n' u_n'}$ and the term associated with the mass flux, $\overline{\rho} a_n a_n$, are initially nearly zero, grow to maxima and then decay to zero. These terms are decaying at times when the total turbulent kinetic energy is increasing (thus the velocities are increasing) because the density fluctuations are decaying. Also, it appears that, just as the mean-squared velocity is approaching a limiting curve as the Reynolds number is increasing, $\overline{\rho' u_n' u_n'}$ and $\overline{\rho} a_n a_n$ are approaching limiting curves. Figure 6.50 shows the evolution of $\overline{\rho' u_n' u_n'}$ for these three cases. As the Reynolds number increases so also does the magnitude of this triple correlation term. As R_o increases, the magnitude reaches a peak value at a time of $T = 1$. For the case

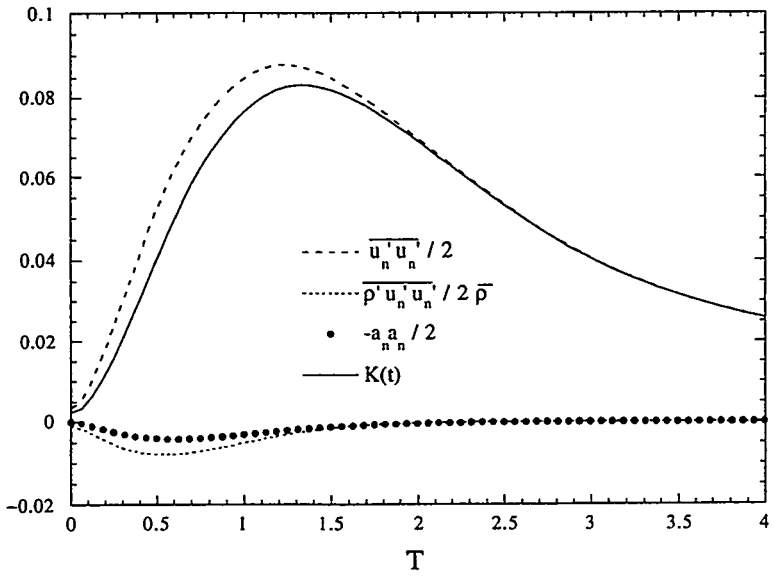

Figure 6.48: Terms of the total turbulent kinetic energy per unit mass for the initial density ratio of 4 cases at $R_o = 64$ (Run Acc3c)

with $R_o = 512$ this quantity decays to a slightly positive nonzero value at late times. Since $\overline{\rho}$ is constant in these problems, the behavior of $\overline{\rho} a_n a_n$ can be understood by examining the behavior of a_n.

The nondimensional turbulent mass flux per unit mass, A_n (see section 6.5.2), is plotted as a function of time for these three cases in Fig. 6.51. As R_o increases, the growth of the mass flux increases and appears to be approaching a limiting curve with a maximum at about $T = 0.9$.

6.6.2 Velocity derivative skewness

Figure 6.52 shows the evolution of the velocity derivative skewness averaged over all three components for the three variable-density cases with an initial density ratio of 4. The early time behavior is a result of the initialization procedure. As R_o increases, the viscosity and diffusivity decrease (since the Schmidt number is fixed) resulting in a smaller velocity divergence and smaller initial velocities. At late times the velocity derivative skewnesses for the higher R_o cases are nearly the same at a constant value of 0.5, whereas, for the case with $R_o = 64$, the velocity derivative skewness has a nearly constant value of 0.2. Thus, the spectral energy transfer (and vortex stretching) is

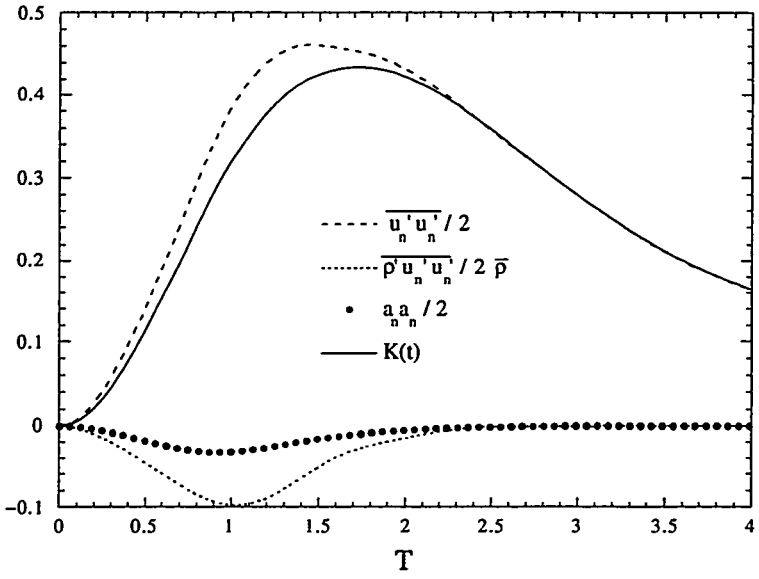

Figure 6.49: Terms of the total turbulent kinetic energy per unit mass for the initial density ratio of 4 cases at $R_o = 512$ (Run Acc2c)

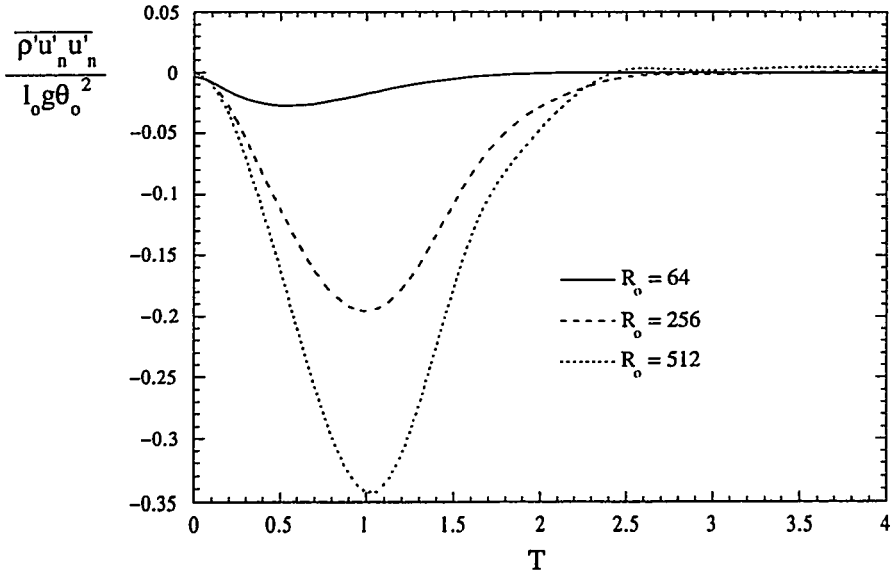

Figure 6.50: Evolution of $\overline{\rho' u_n' u_n'}/(l_o g \theta_o^2)$ for the density ratio of 4 cases at various R_o

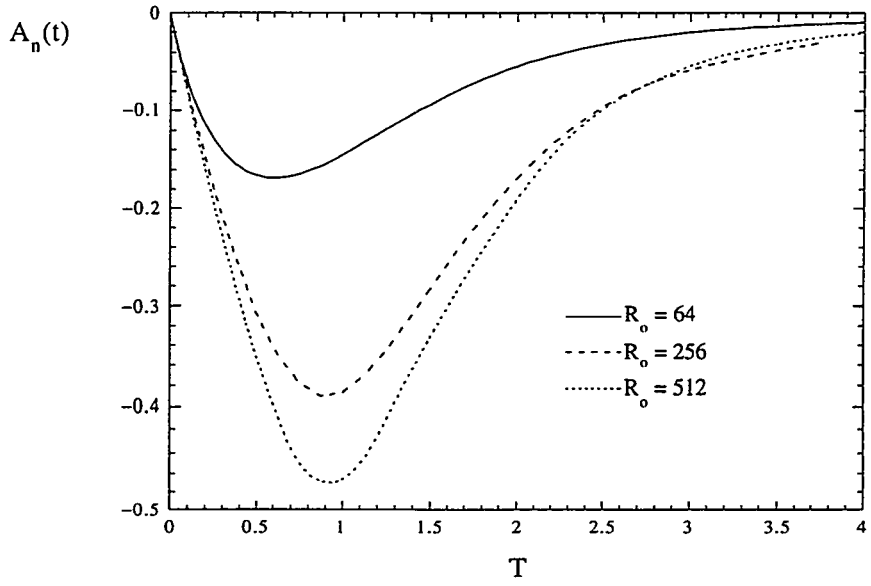

Figure 6.51: Turbulent mass flux for initial density ratio of 4 cases at various R_o

larger in the higher R_o cases. The case with $R_o = 64$ is not very turbulent because the vortex stretching is small. The difference in the velocity derivative skewness for the case with $R_o = 64$ and the higher Reynolds number cases is understood by observing the evolution of the isotropic Taylor Reynolds number, $R_\lambda = \lambda \mathcal{U}/\nu$, (i.e., the Reynolds number based on the isotropic Taylor scale) for these three cases shown in Fig. 6.53. It has been shown that these problems are highly anisotropic; however, the isotropic Taylor Reynolds number is used for the following discussions. For the case with $R_o = 64$, the Taylor Reynolds number increases to a maximum no larger than $R_\lambda \leq 5.0$. For the other two cases, R_λ grows to values larger than 20. It has been seen that, in numerical simulations of decaying, isotropic turbulence [66, 37, 60], values of the velocity derivative skewness decrease as R_λ decreases for $R_\lambda \leq 20$. In grid turbulence experiments [86] it is found that the velocity derivative skewness also decreases for decreasing R_λ if $R_\lambda \leq 5$. The velocity derivative skewness in these accelerated cases exhibits this same dependence on R_λ.

6.6.3 Evolution of the mean-pressure-gradient

The mean-pressure-gradient is given by eq. (3.19). Figure 6.18 shows each term of this equation as a function of nondimensional time for the case in which the initial

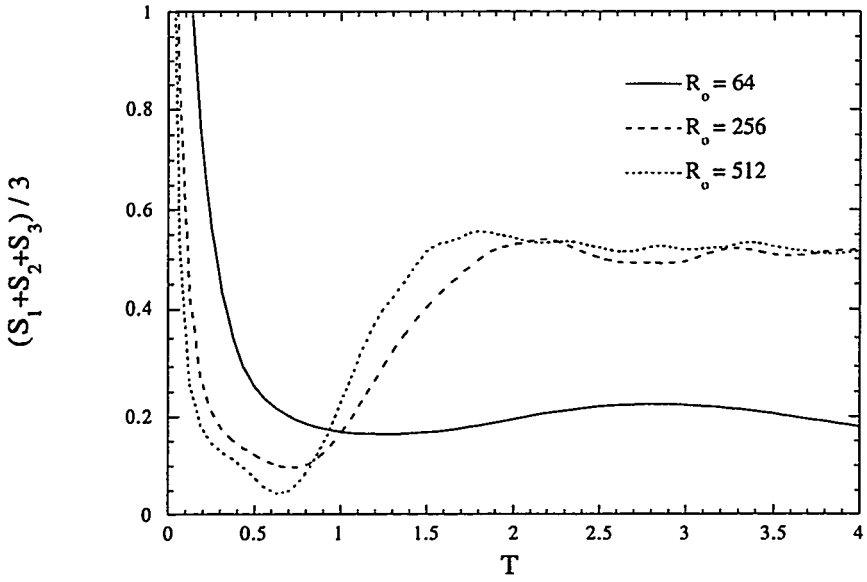

Figure 6.52: Average velocity derivative skewness for the density ratio of 4 cases at various R_o

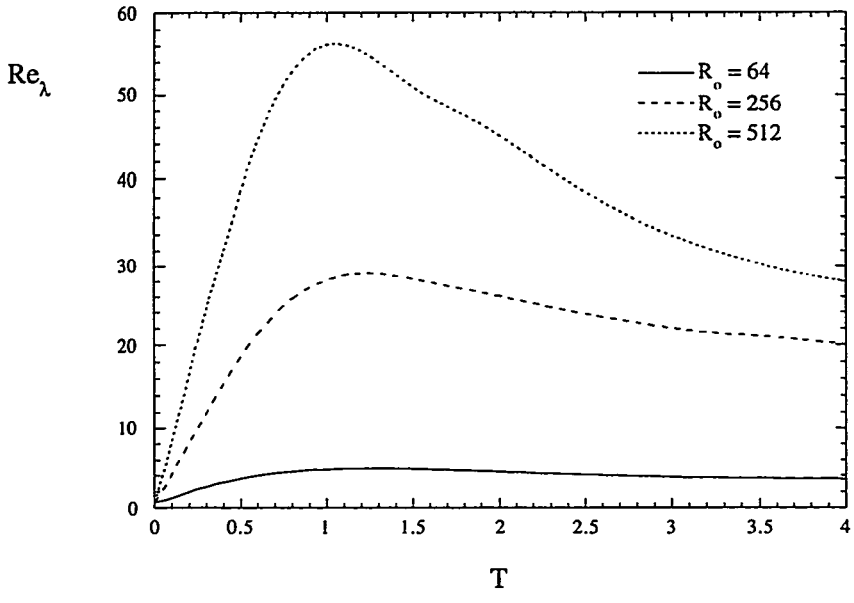

Figure 6.53: Taylor Reynolds number evolution for the density ratio of 4 cases at various R_o

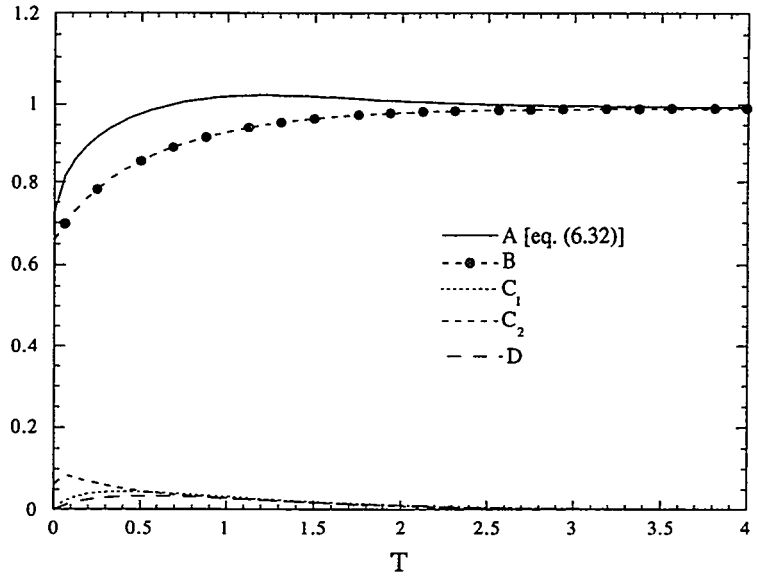

Figure 6.54: Evolution of terms in the mean-pressure-gradient equation [eq. (6.32)] for initial density ratio of 4 case at $R_o = 64$ (Run Acc1c)

density ratio is 4 and $R_o = 256$. To understand Reynolds number effects on the mean-pressure-gradient we also plot each term in the mean-pressure-gradient equation as a function of time for the cases at $R_o = 64$ and 512. These are shown in Figs. 6.54 and 6.55 respectively. Comparisons between these two figures and fig. 6.18 show that the main contribution to the mean-pressure-gradient is through the acceleration term, $g/\overline{v}$. As R_o increases, the contribution from $\overline{v' \frac{\partial p'}{\partial x_i}}$ increases. The contributions from the viscous and the dilatation terms are small in all three cases. This comparison also shows that as R_o increases the mean-pressure-gradient becomes more variable in time which is due to the behavior of $\overline{v' \frac{\partial p'}{\partial x_i}}$. This increasing nonuniformity is seen more clearly in Fig. 6.56 which shows the time histories of the mean-pressure-gradients for these three cases. As R_o increases, the early time growth of the mean-pressure-gradient is reduced due to the buoyancy flux, and the maximum mean pressure that is obtained (near a time of 1.4) increases. For the case with $R_o = 64$ the mean-pressure-gradient becomes nearly constant near the value of 1 (as given by the Boussinesq approximation) at an earlier time than for the other two cases. For the higher R_o cases the mean-pressure-gradient has larger variations in time and, for times greater than 3, decays quite slowly.

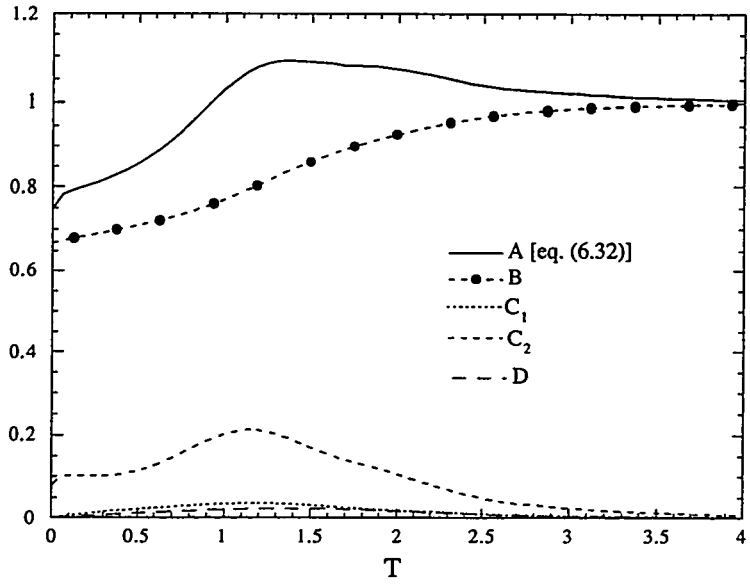

Figure 6.55: Evolution of terms in the mean-pressure-gradient equation [eq. (6.32)] for initial density ratio of 4 case at $R_o = 512$ (Run Acc1c)

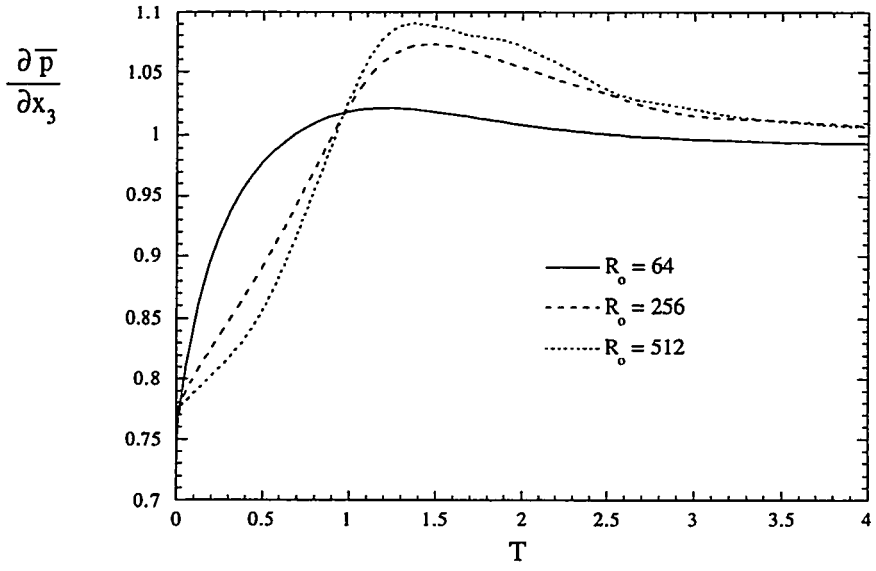

Figure 6.56: Mean-pressure-gradient evolution for initial density ratio of 4 cases at various R_o

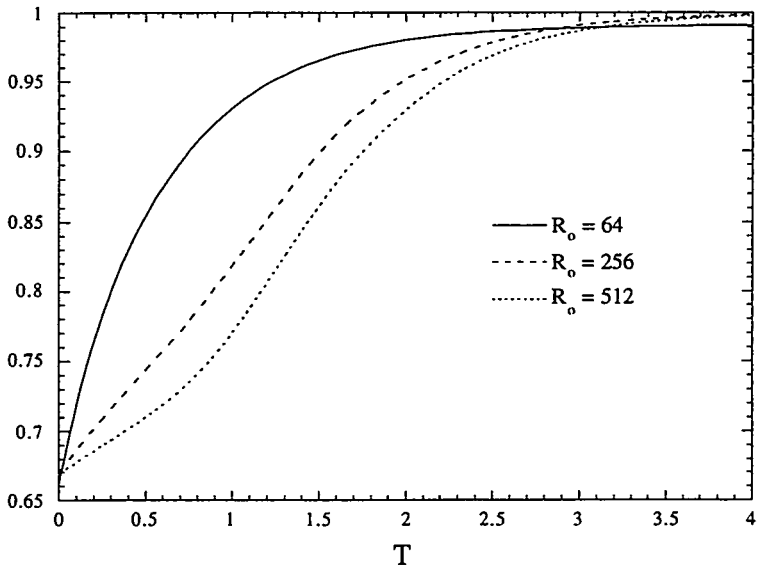

Figure 6.57: Evolution of $g/\overline{v}$ for initial density ratio of 4 cases at various R_o

The main terms contributing to this variability are the acceleration term, $g/\overline{v}$, and the $\overline{v' \frac{\partial p'}{\partial x_i}}$ correlation. Figure 6.57 shows the time history of the acceleration term, $g/\overline{v}$. As R_o increases, the growth of $g/\overline{v}$ is slowed. This is due to the fact that the mean specific volume, $\overline{v}$, follows the evolution of $b = -\overline{\rho' v'} = \overline{\rho}\,\overline{v} - 1$ because $\overline{\rho}$ is a constant. Figure 6.58 shows the evolution of the mean specific volume for the various Reynolds number cases. As the density fluctuations decay away, the quantity b is tending to zero so that the mean specific volume is tending to a constant value of 1. As R_o increases the rate-of-decay of the mean specific volume decreases, which in turn causes a slower growth of $g/\overline{v}$. It will be shown below in the discussion of the density fields that the variance of the density fluctuations and $b(t)$ approach limiting curves as the Reynolds number increases. Since the evolution of the mean specific volume follows the evolution of $b(t)$, it also approaches a limiting curve as the Reynolds number increases. Likewise, so also does $g/\overline{v}$ since g is constant in time for these problems.

The next largest term contributing to the mean pressure gradient in the direction of the acceleration is the correlation between the fluctuating specific volume and the fluctuating pressure gradient, i.e., $-\overline{v' \, \partial p'/\partial x_3}$. Figure 6.59 shows the evolution of this term for these three cases with an initial density ratio of 4. For these cases,

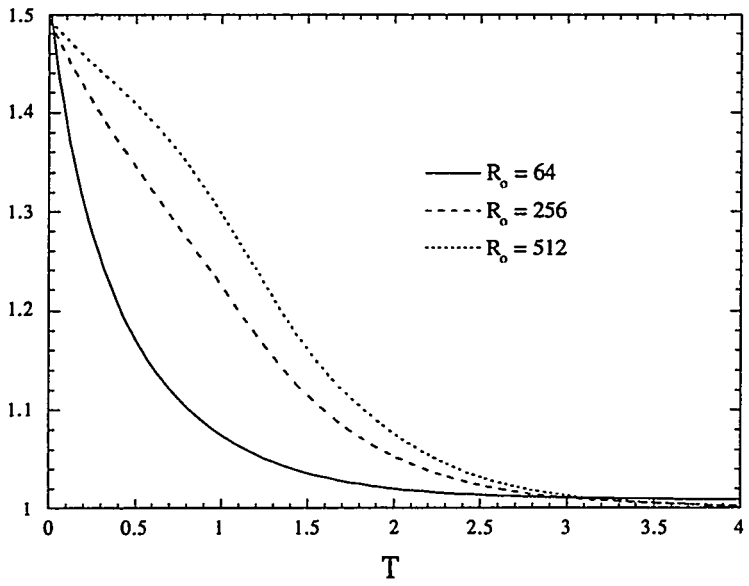

Figure 6.58: Evolution of the mean specific volume, $\overline{v}$, for initial density ratio of 4 cases at various R_o

the correlation between the fluctuating specific volume and the fluctuating pressure gradient has a value initially nearly 0.56. This correlation is nonzero the instant that the density field feels an acceleration. At this instant, it is a "rapid" part that impedes the growth of the turbulent mass flux. The term "rapid" is used because it is an instantaneous response of the mean pressure. For the case with $R_o = 64$ the starting value of this correlation is slightly lower than for the other two cases, due to the fact that the initial density field for that case is statistically similar but not identical to the other two cases. The reason for this is because the the case with $R_o = 64$ is computed on a 64^3 grid and the other two cases (which have identical initial density fields) are computed on a 128^3 grid. As R_o increases this correlation grows and peaks at a time of approximately $T = 1.1$. The growth of this term is due to the "slow" part, which behaves like a drag on the growth of the mass flux. The decay behavior of this correlation after a time of 1.1 describes mostly the "slow" part of this correlation. To see this behavior more clearly this correlation is plotted in nondimensional form as a function of the nondimensional mass flux, shown in Fig. 6.60. At early times this correlation is not proportional to the mass flux. The early time behavior is what has been referred to above as the "rapid" part. As

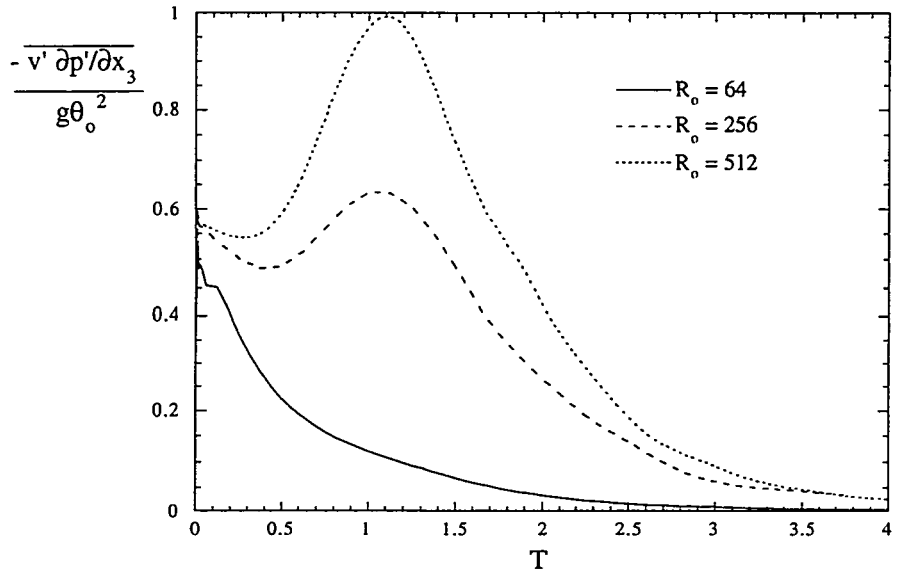

Figure 6.59: Evolution of $-\overline{v'\partial p'/\partial x_3}$ for initial density ratio of 4 cases at various R_o

the flow develops, this correlation becomes proportional to the mass flux, behavior which is termed the "slow" part. At late times in all three cases this correlation is nearly linearly proportional to the mass flux as the "rapid" part has decayed and the behavior is due mostly to the "slow" part.

6.6.4 Evolution of the Density field

This section discusses the evolution of the density fields as functions of R_o for these buoyancy-driven cases with an initial density ratio of 4. It has been seen that, in the Boussinesq approximation results of Batchelor et al., the variance of the density fluctuations approaches a limiting curve as the Reynolds number is increased. It has also been shown, in the Boussinesq results, that the variance decays more slowly at early times as R_o is increased. Figure 6.61 shows the evolution of the variance of the density fluctuations as a function of R_o for the cases with the initial density ratio of 4. For these cases with large initial density fluctuations this plot shows behavior similar to that reported by Batchelor et al. [7] . The decay of the density fluctuations is slower at early times as R_o increases, and it appears that the variance is approaching a limiting curve as the Reynolds number goes to infinity.

The trend for the variance to decay slower, at early times, as R_o increases, is due

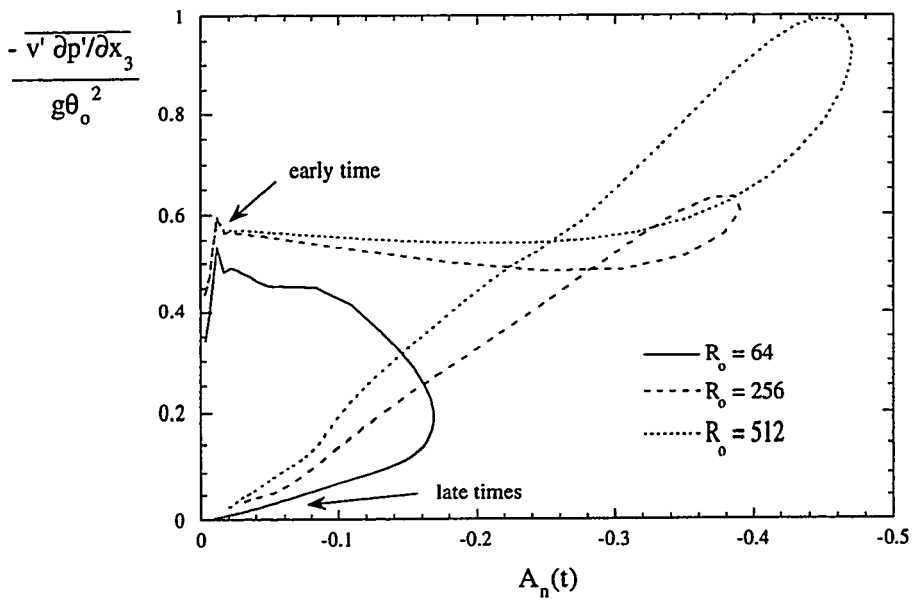

Figure 6.60: Nondimensional $-\overline{v'\partial p'/\partial x_3}$ as a function of nondimensional $a_3(t)$ for initial density ratio of 4 cases at various R_o

to the fact that the dissipation scales for the density decrease as R_o increases. Figure 6.62 shows the dissipation rate histories for the density fluctuations for these three cases. The dissipation rate for the case with $R_o = 64$ has a maximum at $T = 0$ and then decreases with time. As R_o increases, the initial dissipation rate decreases. For these three cases the Schmidt number is a fixed value of 1. R_o is varied by changing the viscosity and thus the diffusivity also changes, resulting in changes of the initial dissipation rate. For the higher R_o cases, the dissipation rate slowly increases, as the density is cascading to smaller scales through convective effects, and reaches a maximum when the density has cascaded to the dissipation scale. After this time the density is decaying through diffusion. In the limit as R_o goes to infinity it is conjectured that the mean-squared density is conserved for a small period of time when dissipation effects are negligible (consistent with the results of Batchelor et al.). During this short period of time the spectra of the density has increasing values at higher wave numbers (smaller scales). After this short period of time the spectrum of the density has reached the dissipation scales and dissipation effects become important. This behavior is analogous to the enstrophy blow-up phenomenon discussed by Lesieur [52] (Chapter 6, section 7.3).

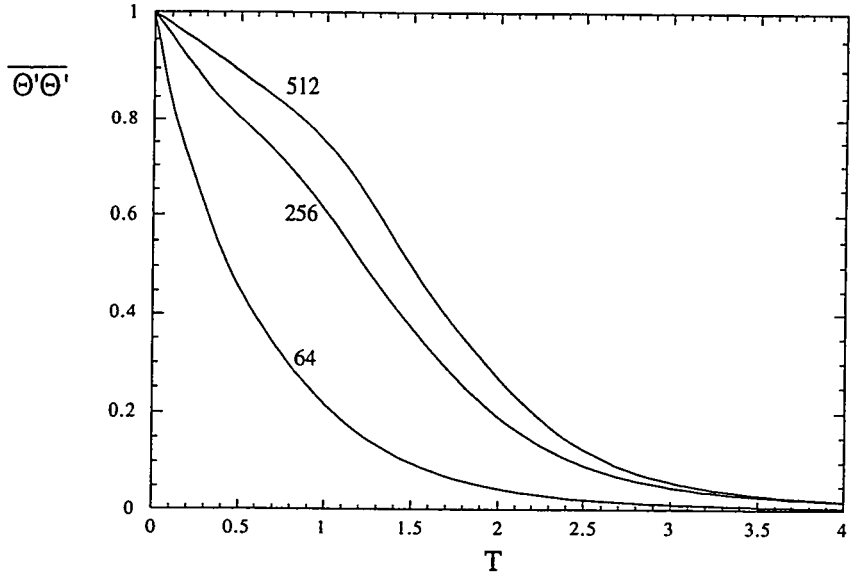

Figure 6.61: $\overline{\Theta'\Theta'}$ *vs.* T as a function of R_o for non-Boussinesq cases with an initial density ratio of 4

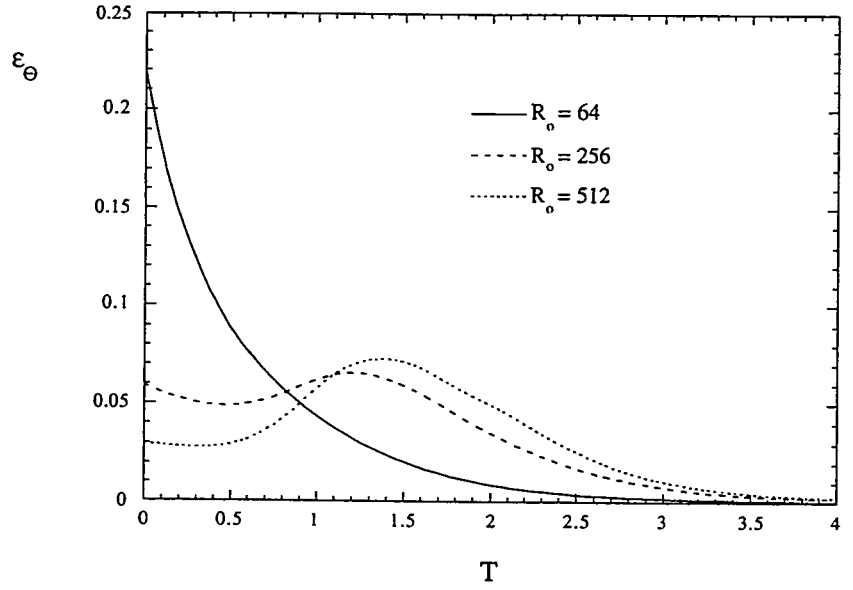

Figure 6.62: Dissipation rate evolution of the fluctuating density field for initial density ratio of 4 case at various R_o

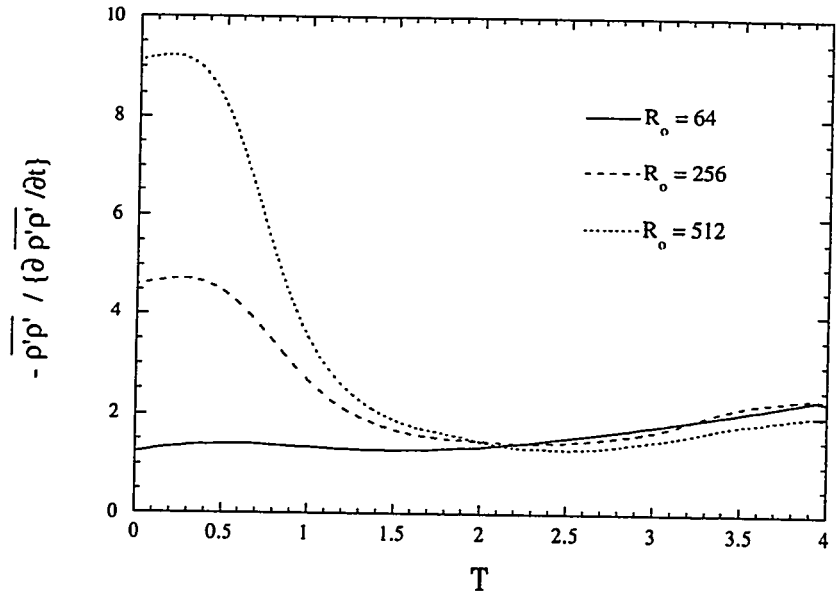

Figure 6.63: Evolution of the time scale of decay of the variance of the fluctuating density field for initial density ratio of 4 case at various R_o

Figure 6.63 shows the time scale of decay for the quantity, $\overline{\rho'\rho'}$, as a function of time for the three values of R_o. These plots show that the decay times are larger for increased R_o at early times, consistent with the slower decay behavior of the density fluctuations. After a time of 1.5 the time scales for all three cases are nearly the same and slowly growing linearly. This suggests, perhaps, that the variance of the density fluctuations is decaying as a power-law at the late times.

Figure 6.64 shows the evolution of the quantities $b(t) = -\overline{\rho'v'}$ and $B(t) = \overline{\rho'\rho'}/\overline{\rho}^2$ as functions of time for the three cases. Comparison of the behavior in this plot with that seen in Fig. 6.50 (which shows the evolution of $\overline{\rho' u_n' u_n'}$) suggest that, in the limit where $b(t) \approx B(t)$, $\overline{\rho' u_n' u_n'}$ is approximately zero. Thus, when $b(t) \approx B(t)$ the flow is nearly "Boussinesq".

Figure 6.32 shows the early time evolution of the pdf of the density field for the case with an initial density ratio of 4 at $R_o = 256$. Figures 6.65 and 6.66 show the same kind of plot for the cases with $R_o = 64$ and 512, respectively. This comparison shows that the skewness seen in the pdf is stronger as the Reynolds number increases. This behavior is expected since the velocity differences between the high and low density fluids increase as the Reynolds number increases. Thus the entrainment rates of the

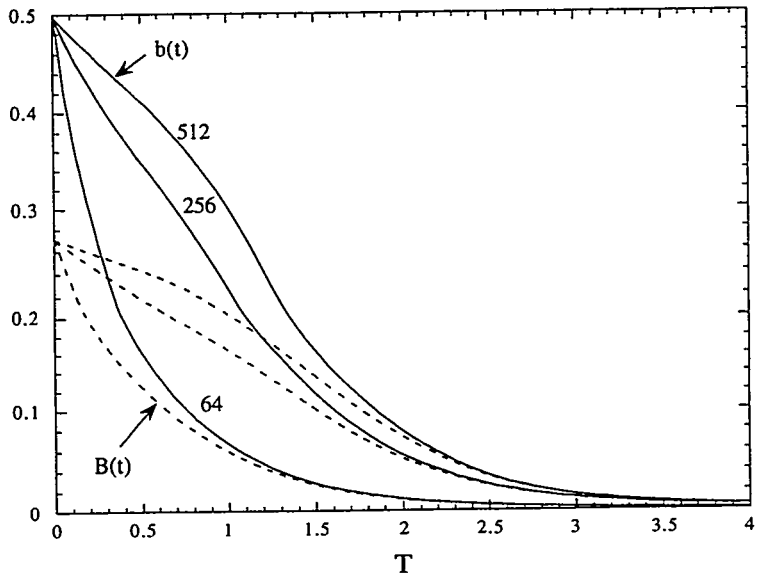

Figure 6.64: Comparison of $b(t)$ and $B(t)$ evolution for initial density ratio of 4 case at various R_o

low density fluid also increase as the Reynolds number increases. The reason the velocity ratio increases with increasing R_o is two-fold. As R_o increases there is less reduction in forcing, due to less diffusion of the density and there is less dissipation of kinetic energy, which acts to slow the flow down. This, in turn, allows the energy to grow to larger values causing a larger velocity ratio between the high and low density. The high velocities are associated with the negative density fluctuations, which is a result of momentum conservation.

6.6.5 Effects of R_o on spectral quantities

This section shows the spectra of the energy per unit mass, of the fluctuating density and of the velocity divergence for different R_o at $T = 1.0$. Figure 6.67 shows the spectrum of the energy per unit mass, computed as

$$E_{nn}(k,t) = \frac{< u_n' u_n' >}{2} = \frac{1}{\Delta k N_i} \sum \hat{u}_n' \hat{u}_n'^*.$$

As R_o increases, so also does the energy at high wavenumber values. Thus, the energy has smaller scales associated with it. The low wavenumber content is also larger, indicating that the flow is more energetic.

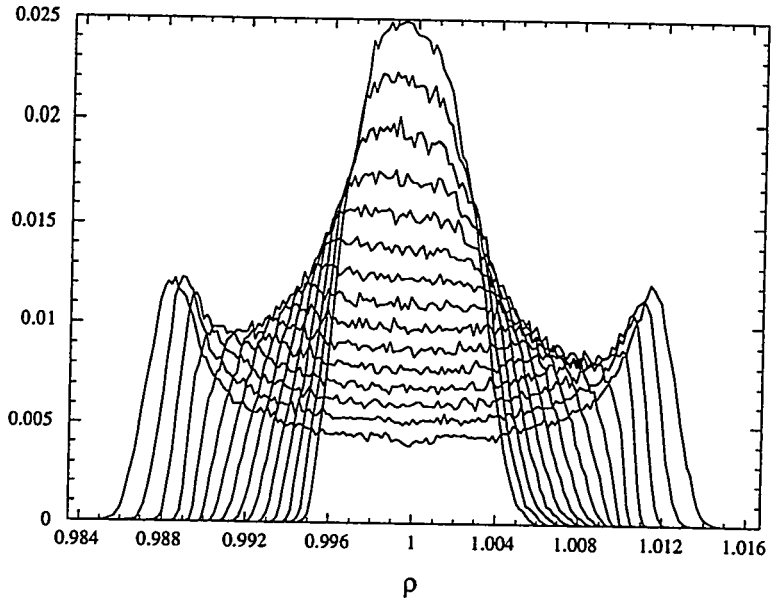

Figure 6.65: PDF evolution, for T=0.0 to 1.75 by 0.125, of the density field at $R_o = 64$ for initial density ratio of 4 case (Run Acc3c)

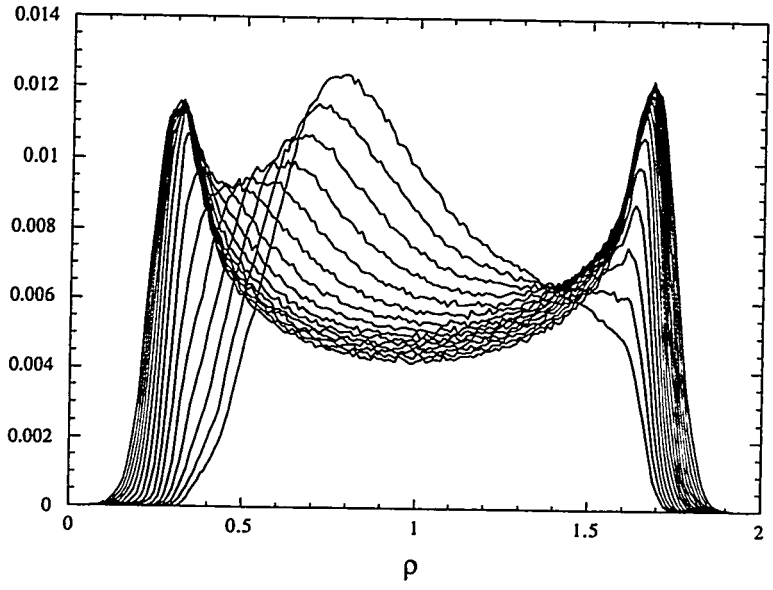

Figure 6.66: PDF evolution, for T=0.0 to 1.75 by 0.125, of the density field at $R_o = 512$ for initial density ratio of 4 case (Run Acc2c)

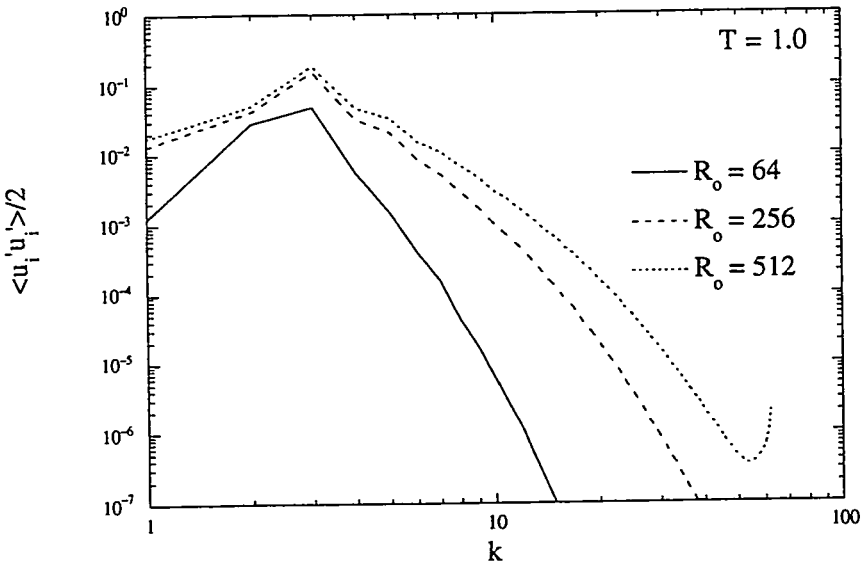

Figure 6.67: Spectra of $u_n' u_n'$ at $R_o = 256$ at $T = 1.0$ for different R_o

Figure 6.68 shows the spectra of the density fluctuations at the same time for various R_o. As R_o is increased, the density field has smaller scales. The dissipation scales for the fluctuating density decreases with R_o. Thus, the decay of the fluctuating density is slower at early time (see Fig. 6.62) and the low wavenumber content is larger for the higher R_o cases.

Figure 6.69 shows the spectra of the velocity divergence. As R_o is increased, the scales at which the velocity divergence is more energetic are smaller as the spectral peak shifts to higher wavenumbers. For the case with $R_o = 512$, the peak is at a wavenumber of 23 and there is a "tail-up" at the higher wavenumbers. These spectra show that, as R_o is increased, the velocity divergence becomes more difficult to resolve.

6.6.6 Summary of R_o effects

This section has described the results of three simulations, Acc1c, Acc2c and Acc3c, of a buoyancy-generated turbulent flow. These simulations initially have the same statistical density distributions with an initial density ratio of 4. The method of Eswaran and Pope is employed to obtain an initial bimodal density distribution. The effects of varying Reynolds number, R_o, are examined.

It appears that the effects of variable density increase with θ_o and R_o. These

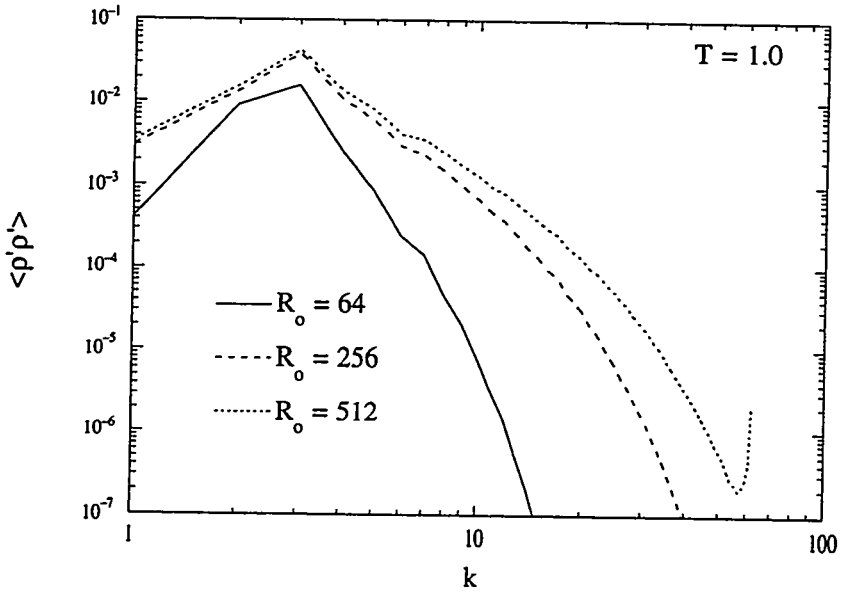

Figure 6.68: Spectra of $\rho'\rho'$ at $R_o = 256$ at $T = 1.0$ for different R_o

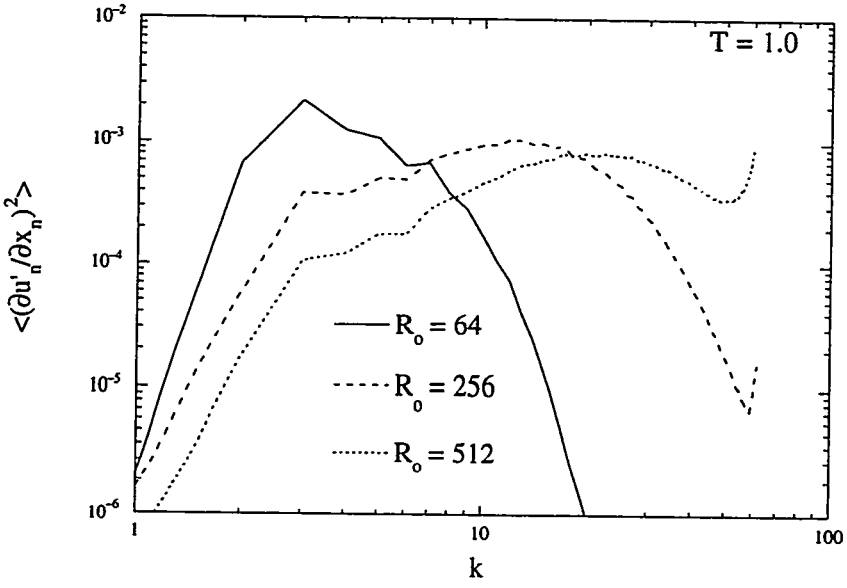

Figure 6.69: Spectra of $(\partial u'_n/\partial x_n)$ at $T = 1.0$ for different R_o

effects increase with R_o since the Schmidt number is held fixed both the viscosity and diffusivity decrease. This results in less reduction in forcing, due to less diffusion of density fluctuations and there is less dissipation of kinetic energy, which acts to slow the flow down. weaker, and thus have more of an effect on the flow.

It is seen that, for these cases, the time histories of the mean-squared velocity exhibit Reynolds number behavior similar to the results of Batchelor et al. [7] employing the Boussinesq approximation. As R_o is increased, the mean-squared velocity appears to approach a limiting curve. The peak value of the mean-squared velocity occurs at a time of $T = 1.5$, which is less than the value of 1.8 obtained with the Boussinesq approximation. This difference is due to differences in the intensity of the initial density fluctuations. As the initial density fluctuations are increased, the time at which the mean-squared velocity reaches a peak decreases. It is conjectured that this time shift will reach a limiting value as the initial density fluctuations are increased since this behavior must be bounded. This limiting behavior has not been examined in this work because of the resolution limitations of our numerical scheme prevent us from studying the effects of larger initial density fluctuations. The limiting curve, towards which the mean-squared velocities are approaching, for the non-Boussinesq case is different than that for the Boussinesq case. Not only is the time different at which the maximum occurs is, but also so is the shape of the curve. Figure 6.46 shows the mean-squared velocity histories for different R_o for the cases with the initial density ratio of 4. At $R_o = 256$ the decay of the mean-square velocity, just after the peak, is slower up to $T = 2$ than it is thereafter. This behavior is not present in the Boussinesq case (see Fig. 6.1).

It is shown that the total turbulent kinetic energy and the terms that make up this energy increase as R_o is increased. The total turbulent kinetic energy per unit mass is given as

$$K(t) = \frac{R_{ii}(t)}{2\overline{\rho}} = \frac{\overline{u_i' u_i'}}{2} + \frac{\overline{\rho' u_i' u_i'}}{2\overline{\rho}} - \frac{a_i a_i}{2}$$

The first term on the right side is the contribution from the mean-squared velocity. The second term is due to correlations between the fluctuating density and squared fluctuating velocity. The third term is due to the turbulent mass flux, $a_i = -\overline{\rho' u_i'}/\overline{\rho}$. As R_o is increased each of these terms increases and also appears to be approaching a limiting curve. The second term is negative, thus that term and the third act to

decrease the total turbulent kinetic energy.

The mean pressure gradient becomes more variable in time as R_o is increased. The main contributions to the mean pressure gradient are from the acceleration term, $g/\overline{v}$, and $-\overline{v'(\partial p'/\partial x_i)}$. As R_o is increased, larger variations in $g/\overline{v}$ occur due to the mean specific volume, $\overline{v}$, changing with time. The mean specific volume follows the behavior of $b = -\overline{\rho' v'}$ through the relation $b = \overline{\rho}\,\overline{v} - 1$. It is seen that $-\overline{v'\partial p'/\partial x_i}$ is nonzero the instant that the fluid feels an acceleration and its initial value is dependent on the strength of the acceleration, g, and the initial density fluctuations. The initial value is not Reynolds number dependent. At early times $-\overline{v'\partial p'/\partial x_i}$ represents a "rapid" part (i.e., an instantaneous response that is proportional to the mean pressure) in the evolution of the turbulent mass flux, a_i, and at later times behaves as a "slow" or "drag-like" part (i.e., is proportional to the mass flux). This correlation thus impedes the growth of the mass flux.

The variance of the fluctuating density appears to approach a limiting curve just as for the Boussinesq results of Batchelor et el. [7]. It is seen that, when $b(t) \approx B(t) = \overline{\rho'\rho'}/\overline{\rho}^2$, the flow is "Boussinesq" since $\overline{\rho' u_i' u_i'}$ and a_i are nearly zero and the mean pressure gradient is approximately

$$\frac{\partial \overline{p}}{\partial x_i} = \overline{\rho} g_i.$$

Also, as R_o increases, the skewness in the pdf of the density field also increases. It is argued that this is due to a larger velocity ratio between the high and low density fluid, which causes a larger entrainment rate for the low density fluid into the mixing region than for the high density fluid. Thus, the low density fluid is entrained into the mixing region at greater rates than is the high density fluid.

Chapter 7

MODEL COMPARISONS

In this chapter results of numerical simulations are compared to predictions of two variable-density turbulence models. The first section discusses the objective of this aspect of the study. The following section describes the models as applied to a statistically homogeneous, variable-density fluid subjected to an acceleration. In the last two sections the results and conclusions of this aspect of the study are discussed.

7.1 Object of Study

In the study we present in this chapter, we desire to isolate variable-density effects from other fluid dynamical effects to as great a degree as possible. There are many unanswered questions regarding constant-density turbulence which also apply in the variable-density case. In this study it is desirable, however, to separate the variable density effects from those of constant-density turbulence, which are more appropriately studied using constant-density simulations. The objective of the work discussed in this chapter is to investigate the effectiveness and suitability of the structure and hierarchy of the modeled equations discussed below in Section 7.2. The DNS results for accelerated turbulence are ideal for studying many of the major issues in modeling variable-density turbulence.

We will attempt to elucidate, through DNS, modeling issues that are analytically difficult or even intractable, such as the nature of the pressure correlations. Specifically, we address (i) the effects of the $\overline{v'(\partial p'/\partial x_n)}$ term in the equation for a_n; (ii) the form of the "drag" term in this equation; and (iii) the efficacy of the extensions of traditional k-ϵ modeling ansatz to variable-density turbulence, e.g., using a single ϵ-equation.

7.2 Models

7.2.1 BHR Model

The Besnard, Harlow and Rauenzahn model (BHR) [10] is an extension of one-point k-ϵ closures to variable-density turbulence. The intent of this model is to obtain a tractable closure to solve practical engineering problems. The model is derived from the usual equations of motion [eqs. (2.1) and (2.2)] and includes an energy and species equation. These equations are Favre averaged and, for the incompressible case, equations for the one-point Reynolds stress tensor, the turbulent energy dissipation rate, species concentrations, and correlations for the density-velocity and specific volume-density fluctuations are derived. The higher-order unknowns in these equations are closed using typical constant density assumptions (e.g., Launder, Reece and Rodi [49]) which are extended to account for a variety of variable-density effects. The details of the closure development can be found in Besnard et al. (1992) [10].

The BHR model equations, given as eqs. (48)-(54) in [10], are derived for general inhomogeneous, anisotropic flows in the limit of high Reynolds number. They are rewritten here for the specific case of a statistically homogeneous, variable-density fluid subjected to an acceleration. The evolution equation for the correlation between the specific volume and the density fluctuations, i.e., $b = -\overline{\rho' v'}$, [eq. (50) in [10]] reduces to

$$\frac{\partial b}{\partial t} = -c_{1b}\left(\frac{2\overline{\rho}\epsilon}{R_{nn}}\right) b. \tag{7.1}$$

The right side is a dissipation term due to a turbulent "cascade" analogous to the cascade of energy, which is assumed to be independent of the diffusivity. The turbulent mass flux model equation [eq. (49) in [10]] reduces to

$$\frac{\partial a_n}{\partial t} = \frac{b}{\overline{\rho}}\frac{\partial \overline{P}}{\partial x_n} - c_{1a}\left(\frac{2\overline{\rho}\epsilon}{R_{nn}}\right) a_n. \tag{7.2}$$

Note that, for consistency with the definitions used in this study, the sign of a_i is the negative of that given by Besnard et al. [10]. The second term on the right side is a model of the correlation between the fluctuating specific volume and fluctuating pressure gradient, which is modeled as a "slow-part" of this correlation, causing a drag or "decay" of a_n. Again this term is assumed to be independent of viscosity and

diffusivity. Besnard et al. suggested that this could be modeled as a "rapid" term or a combination of "rapid" and "slow" parts, but chose to incorporate only the "slow" part. The kinetic energy equation [eq. (48)] reduces to

$$\frac{\partial R_{nn}}{\partial t} = 2a_n \frac{\partial \overline{P}}{\partial x_n} - 2\overline{\rho}\epsilon. \tag{7.3}$$

The last term on the right side is the energy dissipation term and is again modeled independent of viscosity. At this point it is appropriate to note that the time scales for dissipation of a_n and b are "constructed" from a time scale associated with the energy cascade, $\tau \sim R_{nn}/(\rho\epsilon)$. This assumption is based on (1) turbulence characterized by a "large" inertial range where the dissipation rate is independent of viscosity (or diffusivity) and (2) that this cascade also dominates the dissipation of "a_n" and "b". While this assumption may be suitable for well-developed, high Reynolds number turbulence, it is clearly questionable for the case of accelerated turbulence. Thus our DNS provides a stern test of the single-point model. Finally, the energy dissipation equation [eq. (51)] becomes

$$\frac{\partial \epsilon}{\partial t} = c_{3\epsilon}\left(\frac{2\overline{\rho}\epsilon}{R_{nn}}\right) a_n \frac{\partial \overline{P}}{\partial x_n} - c_{2\epsilon}\left(\frac{2\overline{\rho}\epsilon}{R_{nn}}\right)\epsilon. \tag{7.4}$$

The hierarchy of the generation of fluid motion is as follows: through the action of an acceleration a pressure gradient is established. The presence of fluctuations in the density, "b", coupled to the pressure gradient generates a mass flux, "a_i". This mass flux, coupled to the pressure gradient, produces the Reynolds stress, "R_{ij}". Finally, the kinetic energy, "R_{nn}", is dissipated into heat.

7.2.2 CS Model

The Clark and Spitz model (CS) [23] is a two-point (spectral) phenomenological model. The advantage of a two-point (spectral) formulation is that it eliminates the need for length-scale/dissipation equations and corollary assumptions which are employed in one-point modeling. The usual constant-density issues arise in the closure as well as additional difficulties from variable-density effects. For example, the spectral transfers occur not just as triadic interactions of velocity, but also as a quartic interactions of velocity and density. Also, no simple "Poisson" equation for the pressure can be found. There are also many more correlations and hence more closure

assumptions to address. The CS model is not intended as a rigorous solution to these problems, but as an attempt to relieve some of the limitations inherent in the one-point k-ϵ, or R_{ij}-ϵ, formalism. It is not intended as a practical engineering closure, but rather as a tool to study turbulence and turbulence closures. Issues of self-similarity, length-scale, time-scale equilibrium and space-time scaling during rapid accelerations can be addressed.

The model derivation is based on two-point correlation equations for variable-density, incompressible turbulence, represented in mass-averaged ("Favre"-averaged) variables. These equations are Fourier transformed with respect to the separation distance between the two points. The equations are closed in a manner analogous to the constant-density model of Besnard, Harlow, Rauenzahn and Zemach (BHRZ model) [9]. That is, a modified "Leith diffusion" [51] closure is employed for the k-space transfers and time scales. This variable-density model reduces to a modified BHRZ model in the limit of constant-density, isotropic turbulence. The model is derived specifically for homogeneous, accelerated turbulence and it reduces to a model for a passive scalar in isotropic turbulence for vanishing density variations. The details of the closure can be found in Clark and Spitz (1995) [23].

The derivation of the model gives a similar hierarchical structure (see Section 7.2.1) as the BHR model for the case of a statistically homogeneous turbulence subjected to an acceleration. The model equations (used in this study) [23], are

$$\frac{\partial b(k,t)}{\partial t} = -\frac{\partial}{\partial k}\left\{\left(\frac{C_{bR1}}{\theta_R(k)} + \frac{C_{ba1}}{\theta_a(k)} - \frac{C_{bA1}}{\theta_A(k)}\right) k b(k,t)\right\}$$

$$+\frac{\partial}{\partial k}\left\{\left(\frac{C_{bR2}}{\theta_R(k)} + \frac{C_{ba2}}{\theta_a(k)} + \frac{C_{bA2}}{\theta_A(k)}\right) k^2 \frac{\partial b(k,t)}{\partial k}\right\} - 2\overline{D}k^2 b(k,t), \qquad (7.5)$$

$$\frac{\partial a_n(k,t)}{\partial t} = -\frac{\partial}{\partial k}\left\{\left(\frac{C_{aR1}}{\theta_R(k)} + \frac{C_{aa1}}{\theta_a(k)} - \frac{C_{aA1}}{\theta_A(k)}\right) k a_n(k,t)\right\}$$

$$+\frac{\partial}{\partial k}\left\{\left(\frac{C_{aR2}}{\theta_R(k)} + \frac{C_{aa2}}{\theta_a(k)} + \frac{C_{aA2}}{\theta_A(k)}\right) k^2 \frac{\partial a_n(k,t)}{\partial k}\right\}$$

$$-\left\{\frac{C_{RP1}\beta_{RP1}}{\theta_a(k)} + \frac{C_{RP2}\beta_{RP2}}{\theta_R(k)}\right\} a_n(k,t) - \frac{b(k,t)}{\overline{\rho}}\frac{\partial \overline{P}}{\partial x_n} - \left[\frac{\overline{\mu}}{\overline{\rho}} + \overline{D}\right] k^2 a_n(k,t), \qquad (7.6)$$

and

$$\frac{\partial R_{nn}(k,t)}{\partial t} = -\frac{\partial}{\partial k}\left\{\left(\frac{C_{R1}}{\theta_R(k)}\right) kR_{nn}(k,t)\right\} + \frac{\partial}{\partial k}\left\{\left(\frac{C_{R2}}{\theta_R(k)}\right) k^2 \frac{\partial R_{nn}(k,t)}{\partial k}\right\}$$

$$-2a_n(k,t)\frac{\partial \overline{P}}{\partial x_n} - 2\frac{\overline{\mu}}{\overline{\rho}}k^2 R_{nn}(k,t) \tag{7.7}$$

where

$$\theta_R(k) = \left[\frac{1}{\overline{\rho}}\int_0^k q^2 R_{nn}(q)dq\right]^{-1/2},$$

$$\theta_a(k) = \left[k^2\sqrt{a_n(k,t)a_n(k,t)}\right]^{-1},$$

$$\theta_A(k) = \left[k\sqrt{a_n(t)a_n(t)}\right]^{-1},$$

where β_{RP1} and β_{RP2} are chosen to be $1/b(t)$, and

$$b(\mathbf{x},\mathbf{k}) = -\int_0^\infty \overline{\rho'(\mathbf{x}_1)v'(\mathbf{x}_2)}e^{-i\mathbf{k}\cdot\mathbf{r}}d\mathbf{r}, \tag{7.8}$$

$$a_i(\mathbf{x},\mathbf{k}) = \int_0^\infty \overline{u_i''(\mathbf{x}_1)\rho(\mathbf{x}_1)v'(\mathbf{x}_2)}e^{-i\mathbf{k}\cdot\mathbf{r}}d\mathbf{r},, \tag{7.9}$$

$$R_{ij}(\mathbf{x},\mathbf{k}) = \int_0^\infty \frac{1}{2}\overline{[\rho(\mathbf{x}_1)+\rho(\mathbf{x}_2)]\,u_i''(\mathbf{x}_1)u_j''(\mathbf{x}_2)}e^{-i\mathbf{k}\cdot\mathbf{r}}d\mathbf{r}. \tag{7.10}$$

The center coordinate, $\mathbf{x}$, and a relative coordinate, $\mathbf{r}$, are defined as

$$\mathbf{x} = \frac{1}{2}\left[\mathbf{x}_1 + \mathbf{x}_2\right], \tag{7.11}$$

$$\mathbf{r} = \mathbf{x}_1 - \mathbf{x}_2, \tag{7.12}$$

so that

$$\mathbf{x}_1 = \mathbf{x} + \frac{1}{2}\mathbf{r}, \tag{7.13}$$

$$\mathbf{x}_2 = \mathbf{x} - \frac{1}{2}\mathbf{r}. \tag{7.14}$$

With homogeneity, $R_{ij}(\mathbf{x},\mathbf{k}) = R_{ij}(\mathbf{k})$, $a_i(\mathbf{x},\mathbf{k}) = a_i(\mathbf{k})$ and $b(\mathbf{x},\mathbf{k}) = b(\mathbf{k})$. In the single-point limit, $a_i(\mathbf{x},\mathbf{x}) = \overline{u_i''}(\mathbf{x})$.

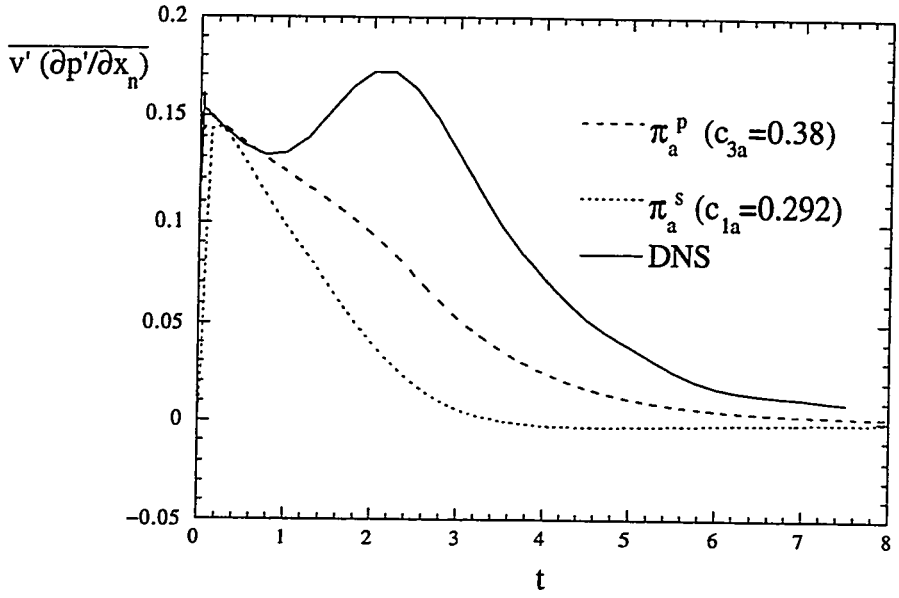

Figure 7.1: $\overline{v'(\partial p'/\partial x_n)}$ term and models for Run Acc1c

7.3 *Results*

7.3.1 *BHR model comparisons*

We begin our investigation of the BHR model by first examining the closure of the $\overline{v'(\partial p'/\partial x_n)}$ term in the a_n equation. This term in the BHR model represents the dissipation of a_n and is modeled as a "slow" (drag) term in eq. (30) in [10], i.e.,

$$\pi_a^s = c_{1a}\left(\frac{2\overline{\rho}\epsilon}{R_{nn}}\right)a_n. \tag{7.15}$$

It is postulated by Besnard et al. [10] that the model for this term may also include a "rapid" term, i.e., eq. (32) in [10],

$$\pi_a^p = -c_{3a}\frac{b}{\overline{\rho}}\frac{\partial \overline{p}}{\partial x_n}. \tag{7.16}$$

Both these models are plotted as a function of time for the DNS case Acc1c in Fig. 7.1. This shows that the "rapid" model [eq. (7.16)] give better early time agreement with the DNS data than the "slow" model [eq. (7.15)].

It is also observed that, in the limit as b goes to zero, the equation for a_n might not drive a_n to zero. Physically, there should not be any mass flux when the density fluctuations are zero. To enforce this behavior, a possible modification to the

dissipation term [eq. (7.15)] in eq. (7.2) might have the form

$$\pi_a^s = c_{1a}\left(\frac{2\overline{\rho}\epsilon}{R_{nn}}\right)\frac{a_n}{b^m}, \tag{7.17}$$

rather than that given by eq. (7.15). This is a "one-point" analogy to a closure assumption of Clark and Spitz [23] and ensures that, when the density fluctuations tend to zero (b tends to zero), a_n also tends to zero.

With these model changes, it is proposed that a modified BHR model for the turbulence mass flux equation [eq. (7.2)] is

$$\frac{\partial a_n}{\partial t} = (1-c_{3a})\frac{b}{\overline{\rho}}\frac{\partial \overline{P}}{\partial x_n} - c_{1a}\left(\frac{2\overline{\rho}\epsilon}{R_{nn}}\right)\frac{a_n}{b^m} - c_{1aa}\frac{\sqrt{a_n a_n}}{K^{3/2}}\frac{a_n}{b^m}. \tag{7.18}$$

This modified a_n equation reduces to eq. (7.2) if $c_{3a} = c_{1aa} = m = 0$.

Comparisons are made between the DNS data for run Acc1c, the BHR model [eqs. (7.1)-(7.4)], and the modified BHR model [eq. (7.2) replaced by (7.18)]. For this investigation the follow model coefficients are used in both the BHR model and the modified BHR model: $c_{1b} = 1.0$, $c_{2\epsilon} = 1.92$, and $c_{3\epsilon} = 1.61$. Equation (7.18) is used for the BHR model calculation with $c_{3a} = c_{1aa} = c_{ab2} = 0.0$, $c_{1a} = 2.2$ and $c_{ab1} = 1.0$. For the modified BHR calculation, eq. (7.18) is also used with $c_{1a} = 0.0$, and $c_{1aa} = 1.5$. For both calculations the initial values are: $R_{nn}(t=0) = 3.006e^{-4}$, $b(t=0) = 0.5$, $a(t=0) = 0.0$ and $\epsilon(t=0) = 8.7979e^{-7}$. The value for $\epsilon(t=0)$ is chosen in order to give the correct length scale of b which in turn gives the correct early time trajectory of a_n.

Figure 7.2 shows the evolution of b for the DNS and the model results. The BHR model and the modified model for the decay of b give the same results and are somewhat different then the DNS result. The initial value for ϵ is artificially small, leading to an inadequate dissipation of b at the early times. This is a deficiency in the methodology of one-point closures. In these closures, an equation for either the energy dissipation, a length scale or a time scale is derived. In the BHR closure an energy dissipation equation is chosen. There is an insufficient number of parameters to define proper length and time scales for the various quantities. Thus, we can choose ϵ to give either the correct energy dissipation or the correct length scale of b, but not both. We chose ϵ to match the initial scale of b and not the initial energy dissipation because the scale of b is the only identifiable length scale at the initial time. This

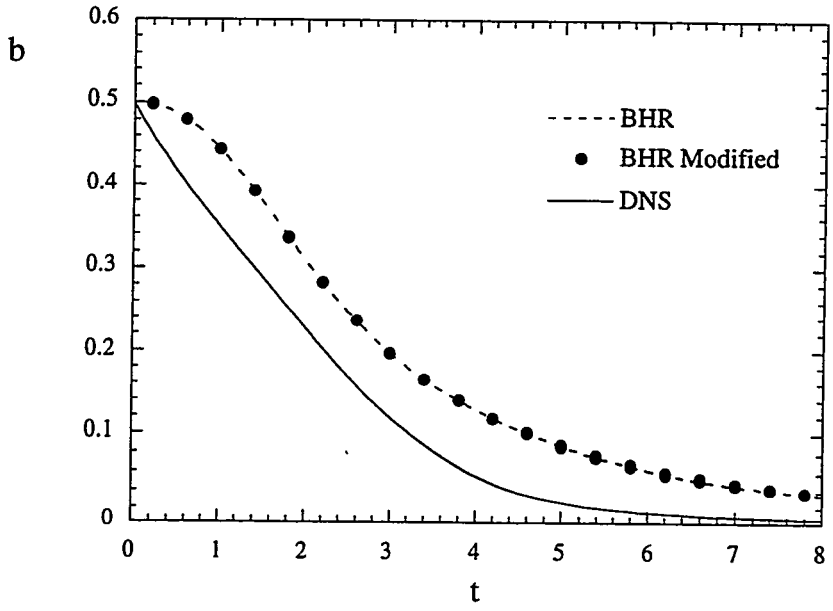

Figure 7.2: Evolution of b for Run Acc1c DNS and BHR models

gives a correct length scale for b but is a poor estimation of the time scale. Therefore, b does not dissipate fast enough and, as a result, the subsequent behavior is incorrect. Also, inherent in these types of models is the assumption of self-similarity in the flow (i.e., there is a well defined inertial range in the limit of high Reynolds numbers). In this buoyancy-generated problem, there is no identifiable inertial range at the early times because the Reynolds number is low. The flows studied in the DNS simulations are dominated by viscous diffusion, and is not accounted for in the BHR model. It was seen that the behavior given by the BHR model is extremely sensitive to the choice for $\epsilon(t = 0)$.

Figure 7.3 shows the evolution of a_n for the DNS and the model results. The correct length scale for b is chosen, thus giving an early time match between the models and the DNS. The late time behavior is not correct because of the over predictions of b at late times. The modified BHR model matches the DNS only slightly better than the original BHR model.

Figure 7.4 shows the evolution of R_{nn} for the DNS and the model results. Again the early time behavior of the models and the DNS agree well. This is due to the agreement seen in the evolution of a_n. The DNS results decay much more rapidly

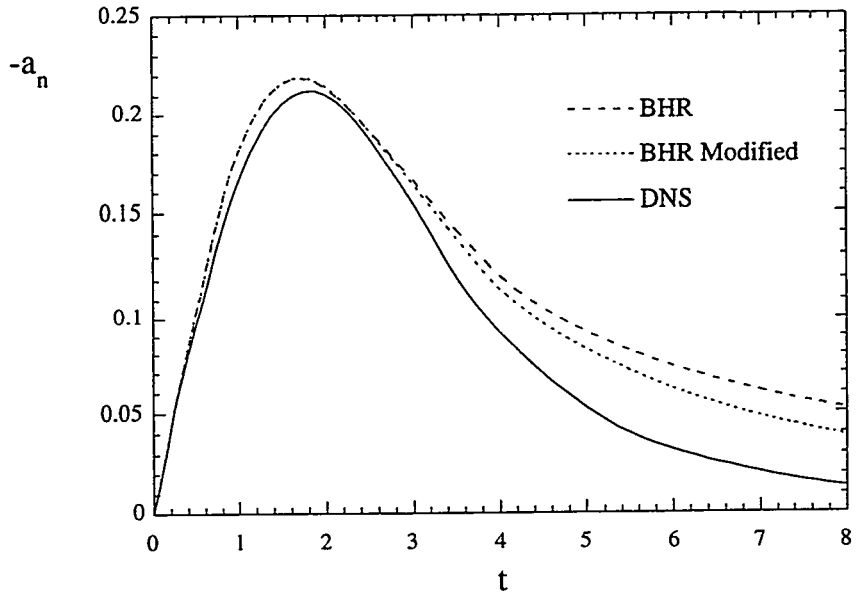

Figure 7.3: Evolution of a_n for Run Acc1c DNS and BHR models

after a time of 4 than do the model predictions. This can, perhaps, be attributed to the fact that the models are for high Reynolds number flows while the DNS results are at a low Reynolds number. One the other hand, the difference could be due to the error in the prediction of b. Again, the modified BHR model gives slightly better agreement with the DNS.

Figure 7.5 shows the evolution of $\partial\overline{p}/\partial x_n$ for the DNS and the model results. The model comparisons show relatively good agreement with the DNS. Again, the modified BHR result appears to have slightly better agreement. The early time behavior is quite different and the time at which the mean pressure gradient reaches a maximum is different for the models and the DNS.

7.3.2 CS model comparisons

We begin our comparison with the CS model and the DNS data by first modifying the model. From the data comparison with the BHR model it was seen that a correction to the b-coupling to the pressure term was needed to account for the "rapid" part of $\overline{v'(\partial p'/\partial x_n)}$ in order to properly model the early time behavior of a_n. This correction in the BHR model is given by eq. (7.16) and will also be made in the CS model. It

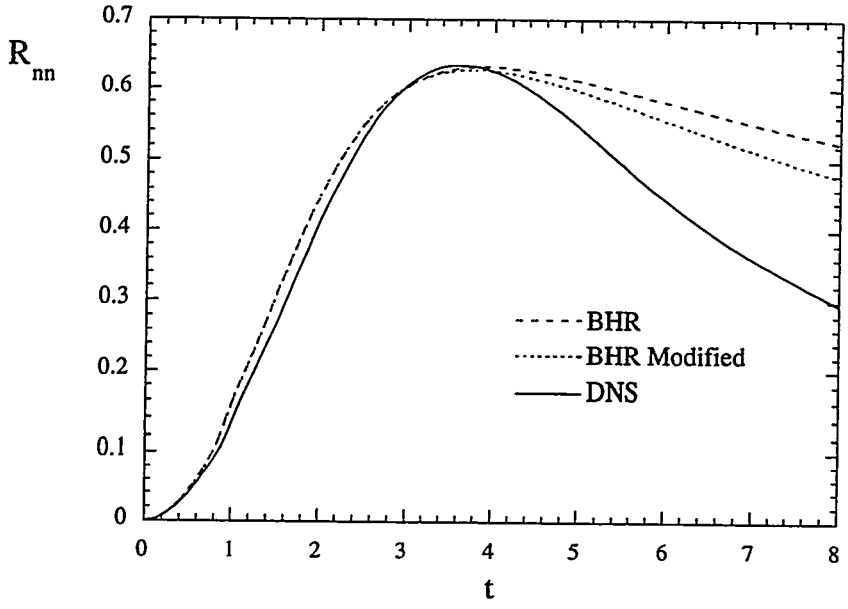

Figure 7.4: Evolution of R_{nn} for Run Acc1c DNS and BHR models

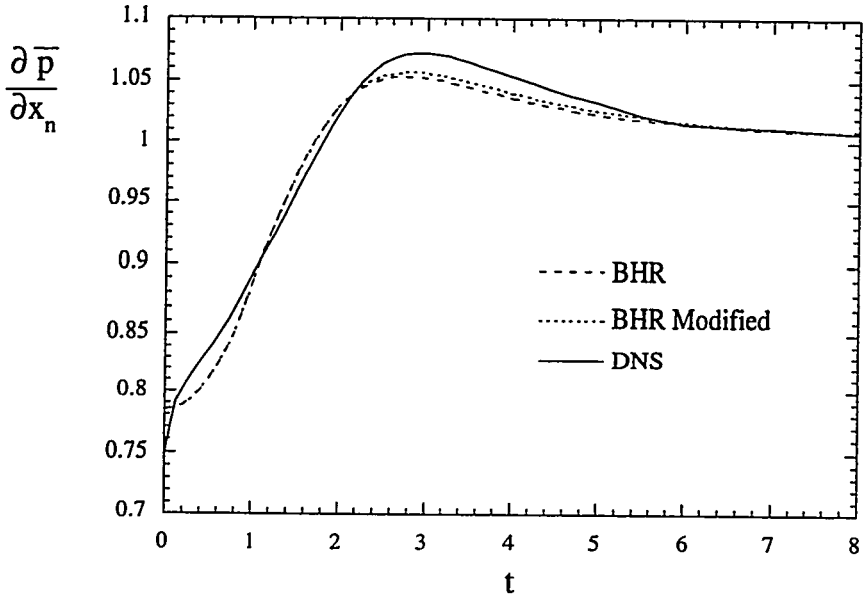

Figure 7.5: Evolution of $\overline{v'(\partial p'/\partial x_n)}$ for Run Acc1c DNS and BHR models

seem reasonable that a spectral model would have the form

$$\overline{v'\frac{\partial p'}{\partial x_n}} = f[b(k)]\frac{\partial \overline{p}}{\partial x_n}. \tag{7.19}$$

There are infinite possibilities for the form of $f[b(k)]$; for simplicity we choose

$$\overline{v'\frac{\partial p'}{\partial x_n}} = C_{vdp}b(k)\frac{\partial \overline{p}}{\partial x_n}. \tag{7.20}$$

Thus, the modified a_n equation in the CS model becomes

$$\frac{\partial a_n(k,t)}{\partial t} = -(1-C_{vdp})\frac{b(k,t)}{\overline{\rho}}\frac{\partial \overline{P}}{\partial x_n} \tag{7.21}$$

$$-\frac{\partial}{\partial k}\left\{\left(\frac{C_{aR1}}{\theta_R(k)}+\frac{C_{aa1}}{\theta_a(k)}-\frac{C_{aA1}}{\theta_A(k)}\right)ka_n(k,t)\right\}$$

$$+\frac{\partial}{\partial k}\left\{\left(\frac{C_{aR2}}{\theta_R(k)}+\frac{C_{aa2}}{\theta_a(k)}+\frac{C_{aA2}}{\theta_A(k)}\right)k^2\frac{\partial a_n(k,t)}{\partial k}\right\}$$

$$-\left\{\frac{C_{RP1}\beta_{RP1}}{\theta_a(k)}+\frac{C_{RP2}\beta_{RP2}}{\theta_R(k)}\right\}a_n(k,t)-\left[\frac{\overline{\mu}}{\overline{\rho}}+\overline{D}\right]k^2a_n(k,t), \tag{7.22}$$

Using this modified a_n equation we now compare the model predictions with the DNS results for run Acc1c. For this investigation the following model coefficients are used: $C_{RP1}=0.125$, $C_{vdp}=0.35$, $C_{aa1}=C_{aA1}=-.2424$, $C_{R1}=C_{aR1}=C_{bR1}=\sqrt{6}C_k^{-3/2}/11$, $C_{R2}=C_{aR2}=C_{bR2}=2\sqrt{6}C_k^{-3/2}/11$; all other coefficients being set to zero. C_k is the Kolmogorov constant, chosen to be 1/2. The initial spectra for $b(k)$ and $R_{nn}(k)$ taken from the DNS are used for initial conditions in the CS model; in addition $\overline{\rho}=1$ and $\overline{\mu}=\overline{D}=8.543e^{-3}$. The comparison between the CS model and the DNS is made by examining one-point statistics.

Figure 7.6 shows the evolution of b for the DNS (run Acc1c) and the CS model. The model prediction of the early time behavior is slightly incorrect. However, the late time behavior from the model agrees well with the DNS. This comparison is significantly better than that of the BHR model, illustrating that the added length

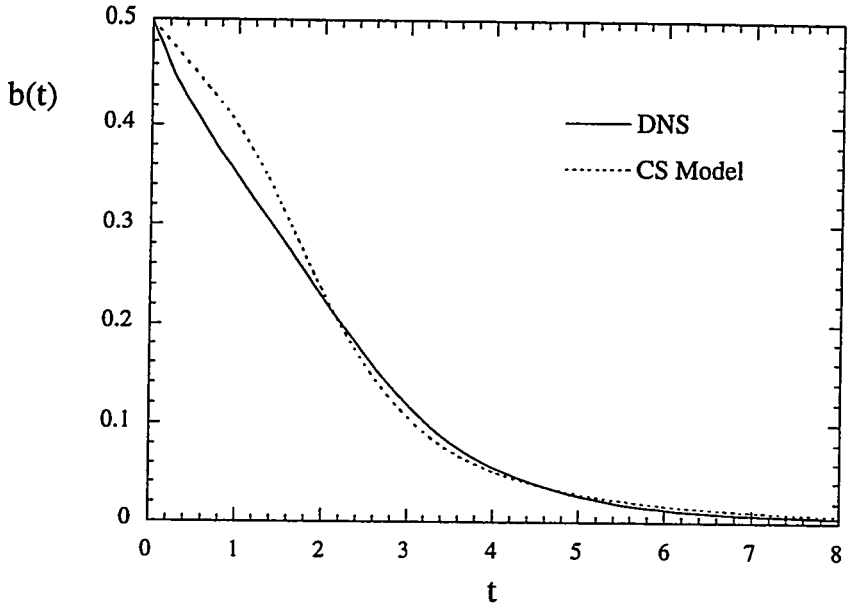

Figure 7.6: Evolution of b for Run Acc1c DNS and the CS model

scale information for b in the CS model allows for the behavior of b to be predicted more accurately.

Figure 7.7 shows the evolution of a_n for this comparison. Again, there is reasonable agreement between the DNS and the CS model. The late time behavior is captured more accurately using the CS model than the BHR model, because the late time behavior for b is more accurately predicted.

Figure 7.8 shows the evolution of R_{nn} and Fig. 7.9 the evolution of $\partial\overline{p}/\partial x_n$ for this comparison, both demonstrating good agreement at all times.

These results show that the closure given by (7.20) provides a good representation of the one-point statistics. This closure assumes that the spectrum of $\overline{v'(\partial p'/\partial x_n)}$ can be modeled from the spectrum of b. Figure 7.10 shows the spectrum of b from the model and $\overline{v'(\partial p'/\partial x_n)}$ from the DNS at an early time ($t = 0.1$). Using the spectrum of b to model that of $\overline{v'(\partial p'/\partial x_n)}$ is clearly inaccurate. The spectrum of $\overline{v'(\partial p'/\partial x_n)}$ is much broader and has a peak value at higher k than the spectrum for b. Given that the CS model uses only assumptions of "local" transfer in k-space, it is difficult to see how this spectrum can be produced from the CS methodology. These results, however, indicate that the errors in the spectral representation, in the CS model do not seem to irreparably harm the one-point statistics. The reason for this might be

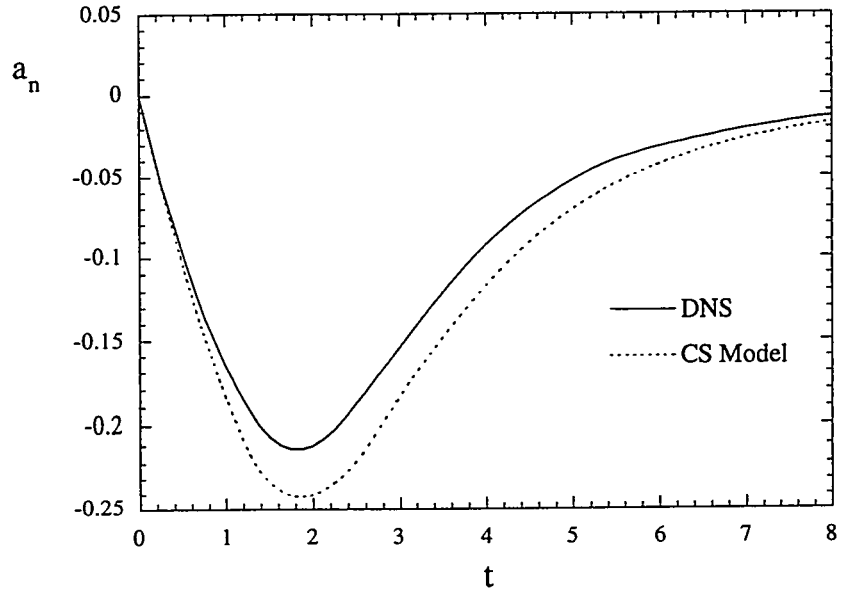

Figure 7.7: Evolution of a_n for Run Acc1c DNS and the CS model

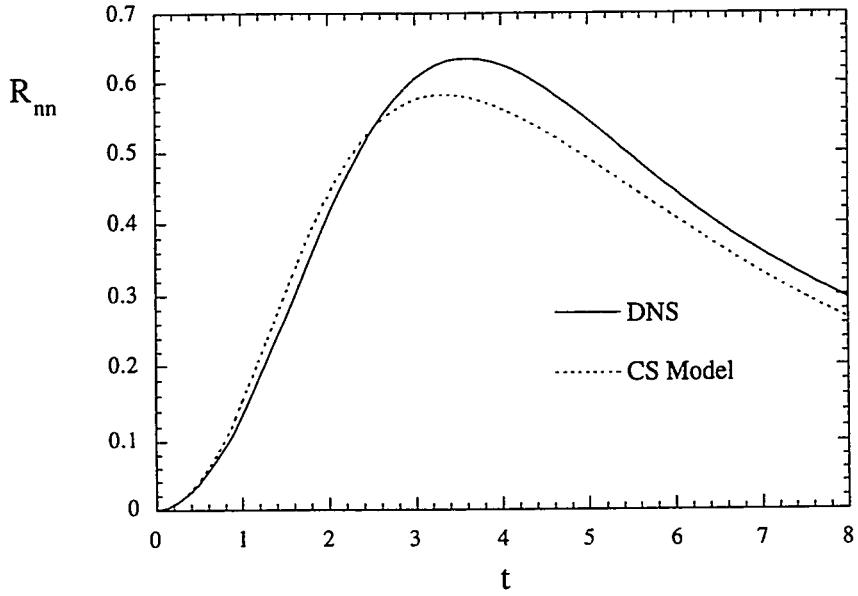

Figure 7.8: Evolution of R_{nn} for Run Acc1c DNS and the CS model

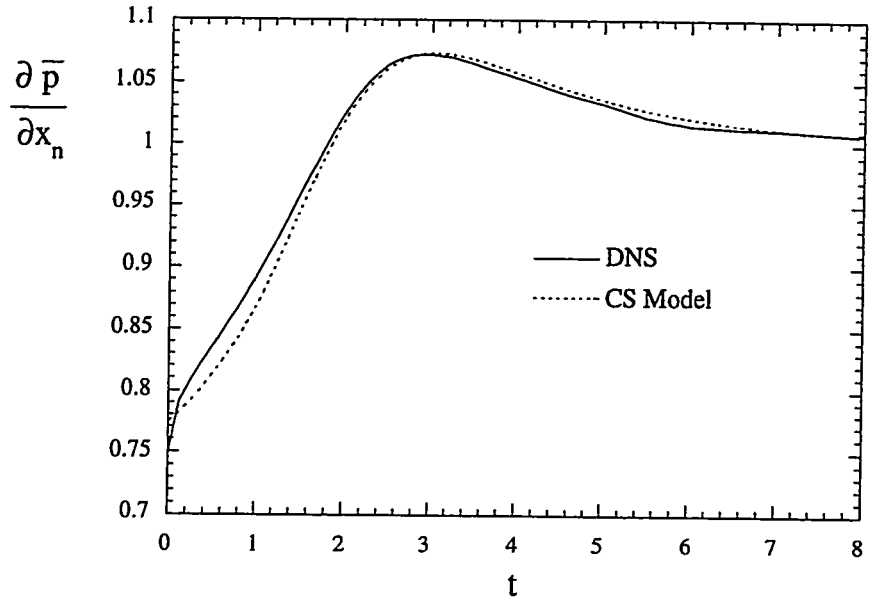

Figure 7.9: Evolution of $\overline{v'(\partial p'/\partial x_n}$ for Run Acc1c DNS and the CS model

that the dominant effects in the flow studied may be at lower wavenumbers at this low Reynolds number.

It is also noted here that the value of the drag coefficient used in the CS model is $C_{RP1} = 0.125$. This value is considerably smaller than drag coefficients used in other variable-density models and two-phase models. The reason for this is two-fold. First, the drag terms of the CS model, the parameters β_{RP1} and β_{RP2}, are chosen to be proportional to $1/b(t)$, which forces the drag to increase as $b(t)$ vanishes. Second, the length scale of b (i.e., determined from $b(k)$) is "independent" of the energy-containing scales, thus permitting a large drag, even with small dissipation of energy. Thus, if $b = 0$ (so that there are no density fluctuations) the mass flux is forced to be zero. The question then arises: is $\beta_{RP1} = \beta_{RP2} = 1/b(t)$ the correct form for these drag terms? Given the complexity of the exact equation (see Clark and Spitz [23]) and the simplicity of model assumptions, it is not possible to provide a definite answer. An effect such as $\beta = F[1/b(k)]$ is probably necessary, but there is an infinite number of possible forms. The form chosen ($\beta = 1/b$) for this comparison seems to indicate that the decays at late times for b, a_n and R_{nn} are reasonably modeled. Further study is needed, perhaps including cases of an acceleration followed by free decay, and acceleration reversal, in order to see if this form is correct.

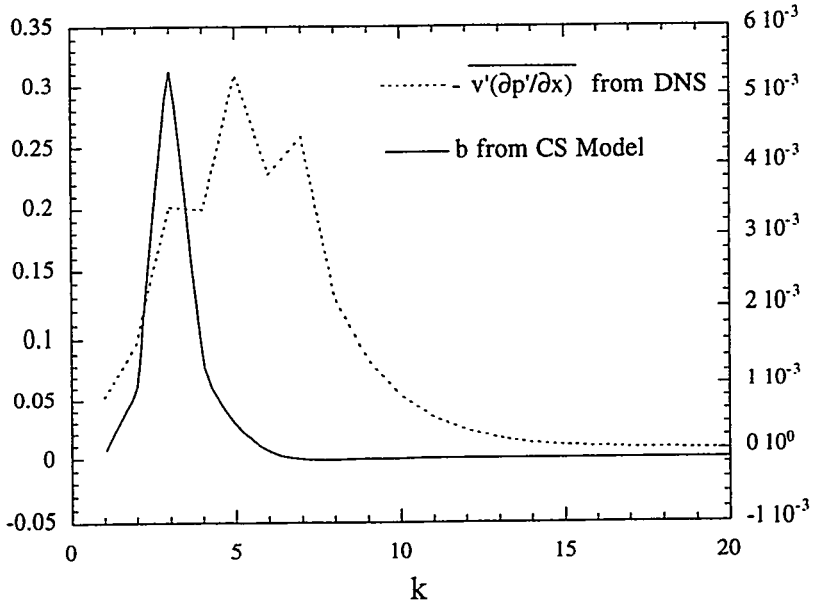

Figure 7.10: Spectra of $\overline{v'(\partial p'/\partial x_n)}$ for Run Acc1c DNS and of b for the CS model at $t = 0.1$

7.4 Conclusions

It is essential in the equation for a_n in both the BHR model and the CS model that the correction to the b-coupling to the mean pressure gradient term be modified to account for the effects due to $\overline{v'(\partial p'/\partial x_n)}$. Thus, the mean pressure gradient term should have the form

$$(1-c)\frac{b}{\overline{\rho}}\frac{\partial \overline{P}}{\partial x_n}.$$

The drag term in the equation for a_n in the CS model, using $\beta_{rp1} = \beta_{rp2} = 1/b(t)$, gives reasonable agreement between the one-point statistics and the DNS results. It has also been seen that the inclusion of this effect in the BHR model slightly improves the comparison between the BHR and the DNS results at late times.

The spectra of $\overline{v'(\partial p'/\partial x_n)}$ shows some effects that are not accounted for in current closures (e.g., broadening of the spectrum and a peak value at higher k than for the $b(k)$ spectra) . More detailed studies are needed to determine the effects and proper modeling for them. Thus, further DNS study would be desirable to examine the effects in the limit of small but finite (not infinitesimal) diffusivity to determine the importance of dilatational effects. The spectral effects seen in this comparison are

probably not capturable in a genuine manner in a one-point closure (where everything is lumped into simple scalings). These effects, however, may be capturable in an "augmented" spectral closure where the diffusive effects of density are accounted for in an energy equation for the dilatational part of the velocity field.

Chapter 8

CONCLUSIONS AND FUTURE WORK

Direct numerical simulations of incompressible, variable-density turbulence have been carried out. We resort to numerical techniques to study variable-density flow because of our desire to obtain a complete description of the flow field, so that detailed information including detailed statistical information of interest can be obtained. Also, the parameters of the problem can be easily varied. The numerical algorithm used in this study is based on the algorithm first proposed by McMurtry [58] but with three modifications:

(1) In the study of McMurtry, the velocity field is divergent due to heat release and mass diffusion. In this study, the velocity field is divergent due only to the diffusion of mass.

(2) A modification of the projection step is made which allows the treatment of larger density fluctuations.

(3) A modification is made to the mean pressure gradient to account for large density variations in the presence of gravity (or flow acceleration).

Two problems have been studied. The first is the decay of isotropic, variable-density turbulence, and the second is statistically homogeneous buoyancy-generated turbulence. In the latter case the density fluctuations are large enough that the Boussinesq approximation is not always valid. The effects of large density fluctuations were studied for both these problems.

8.1 Isotropic Decay of statistically independent initial fields

For the case where the initial velocity and density fields are statistically independent, comparisons between a nearly constant-density case and a variable-density case are reported. This comparison shows that the presence of variations of density has little effect on the overall statistical decay of the flow. For example, the decay of the total turbulent kinetic energy density closely follows the decay of the mean-square velocity. This is due to the fact that $\overline{\rho' u_i' u_i'}$ is initially zero and remains small so that it has

little effect on the decay processes.

For these cases, the pdf's of the density field, which are initially bimodal, evolve to a nearly Gaussian form and are symmetric about the mean density.

8.2 Isotropic Decay of statistically dependent initial fields

Next, statistical dependence was initially imparted between the velocity and density fields and the subsequent flow was examined. Two types of statistical dependence were studied, one such that the larger velocity magnitudes are initially associated with the positive density fluctuations, and the other such that the larger velocity magnitudes are initially associated with the negative density fluctuations. The triple correlation term, $\overline{\rho' u_i' u_i'}$, is initially nonzero, its sign dependent on the type of statistical dependence. A positive sign indicates that the higher velocity magnitudes are associated with larger densities, while a negative sign indicates that higher velocity magnitudes are associated with the smaller densities.

Some conclusions can be drawn from this study of isotropic decay of variable-density turbulence when compared with a decaying, isotropic constant-density turbulent flow. If, for both cases, the initial total turbulent kinetic energy densities are the same, the initial energy dissipation rates are different and depend on the statistical dependence between the velocity and density fields. If the triple correlation, $\overline{\rho' u_n' u_n'}$, is initially negative, the energy dissipation rate is the highest, while the case where the triple correlation is positive has the smallest energy dissipation rate.

The pdf of the density field becomes asymmetrical about the mean density, and it is argued that this is due to different entrainment rates of the high and low density fluids into the mixing region (the mixed interface between the two fluids). This conclusion is based on analogy to numerous shear layer results (see e.g., Dimotakis (1986) [28]), the first of which are the results of Brown [16] in his study of the Brown and Roshko [15] variable-density mixing layer experiments. These shear layer studies showed that a spatially-growing shear layer entrains an unequal amount of fluid from the two free streams, which results in a mixed fluid composition that favors the high-speed fluid. It has been seen in the results presented in this dissertation that the sign of the triple correlation, $\overline{\rho' u_n' u_n'}$, reflects this entrainment rate behavior.

Another important result has implications for passive scalar problems. If the velocity field is statistically dependent on density field, but the density fluctuations

are small so that the density field is passive, the pdf of the density field still becomes asymmetric.

8.3 Buoyancy-generated turbulence

Two types of studies were made for the buoyancy-generated turbulence case. First, the effects of increasing the initial density fluctuations are studied at a fixed initial Reynolds number, $R_o = 256$. And second, the effects of increasing R_o are studied at an initial density ratio of 4.

8.3.1 Variable-density effects at $R_o = 256$

An important parameter that characterizes buoyancy driven flow is θ_o. This parameter is given by eq. (6.9) and is a statistical measure of the magnitude of the initial density fluctuations of the fluid. If θ_o is less than approximately 0.1 then the resulting buoyancy-driven flow is within the Boussinesq approximation. Likewise, if θ_o is larger that 0.1 then the resulting flow is non-Boussinesq.

As the initial density fluctuations increase the flow behavior deviates more from the Boussinesq limit and the nondimensional mean-squared velocity grows at a greater rate. This is related to the fact that the buoyancy flux increases with increasing initial density fluctuations. The nondimensional time at which the mean-squared velocity reaches a maximum decreases as the initial density fluctuations increase. The maximum peak value of the mean-squared velocity occurs at a nondimensional time of $T = 1.5$ for the case with the initial density ratio of 4. This time is earlier than that of the Boussinesq results, where the peak occurs at $T = 1.8$. It is anticipated that, in the limit as the initial density ratio becomes very large (much larger than 4), the mean-square velocity history will approach a limiting curve because its evolution must be bounded. This is not studied here due to resolution limitations in the numerical scheme, which limits the maximum initial density ratio to be around 4.

The total turbulent kinetic energy per unit mass consists of three terms given by eq. (A.7):

$$K(t) = \frac{R_{nn}(t)}{2\overline{\rho}} = \frac{\overline{\rho u_n'' u_n''}}{2\overline{\rho}} = \frac{\overline{u_n' u_n'}}{2} + \frac{\overline{\rho' u_n' u_n'}}{2\overline{\rho}} - \frac{a_n a_n}{2}. \tag{8.1}$$

These three terms are the mean-squared velocity, $\overline{u_n' u_n'}/2$, a triple correlation term, $\overline{\rho' u_n' u_n'}/2\overline{\rho}$, and a mass flux product term, $a_n a_n/2$. Within the Boussinesq limit, this triple correlation and mass flux are relatively small. As the initial density fluctuations are increased, these terms increase, and their effects become a significant part of the evolution of the total turbulent kinetic energy. The summation of these three terms gives a nondimensional total turbulent kinetic energy that grows to a lower value as the initial density fluctuations are increased. The triple correlation term, $\overline{\rho' u_n' u_n'}/2\overline{\rho}$, becomes negative as a result of the conservation of momentum.

A consequence of the Boussinesq approximation is that the mean pressure gradient is uniform in time and its value is $\overline{\rho} g_i$, i.e., the hydrostatic pressure gradient. This approximation is good in the limit of small density fluctuations but, as the initial density fluctuations increase, the mean pressure gradient becomes variable in time and its value is given by eq. (3.19), written here as

$$\frac{\partial \overline{p}}{\partial x_i} = \frac{\overline{\rho}}{b+1} \left\{ g_i + \overline{v' \frac{\partial \tau_{ni}'}{\partial x_n}} + \overline{u_i' \frac{\partial u_n'}{\partial x_n}} - \overline{v' \frac{\partial p'}{\partial x_i}} \right\}.$$

In the limit as the density fluctuations tend to zero, eq. (3.19) gives the Boussinesq approximation for the mean pressure gradient, i.e., the hydrostatic balance. In the absence of fluid motion (e.g., at time equal to zero) the mean pressure gradient is

$$\frac{\partial \overline{p}}{\partial x_i} = \frac{\overline{\rho}}{b+1} \left\{ g_i - \overline{v' \frac{\partial p'}{\partial x_i}} \right\}.$$

Here, the correlation between the fluctuation specific volume and the fluctuating pressure gradient is a non-Boussinesq departure from the hydrostatic pressure gradient. This correlation increases with increasing initial density fluctuations. The presence of this correlation acts to impeded the growth of the turbulence mass flux. In the absence of an acceleration, this term is zero but immediately has a nonzero value the instant that an acceleration is applied.

The mean-squared vorticity is initially zero, grows to a maximum and then decays through viscous dissipation. The initial growth of the mean-squared vorticity is due to a generation of vorticity, through baroclinic torque, in the plane perpendicular to the direction of the acceleration. As a result, the vorticity in this plane is much larger than in the direction of the acceleration. In the direction of the acceleration

there is a generation of vorticity through vortex rearrangement, but there is very little generation due to baroclinic torque.

A measure of the validity of the Boussinesq approximation is found by comparing the two terms $b(t) = -\overline{\rho' v'}$ and $B(t) = \overline{\rho'\rho'}/\overline{\rho}^2$. If the quantity $b(t)$ is approximately equal to the quantity $B(t)$ then the mean flow is adequately described by the Boussinesq approximation. Also, as the initial density fluctuations increase, the pdf of the density field develops a larger skewness (to the negative side of the mean density). It is argued that this skewness is attributed to larger entrainment rates of the light fluid into the mixing region than the heavier fluid. For these accelerated cases, the triple correlation term, $\overline{\rho' u_n' u_n'}/2\overline{\rho}$, becomes negative, indicating that the largest velocites in the flow are associated with the negative density fluctuations. As a result, the pdf of the density field is skewed to the negative of the mean density. This behavior is also seen in the isotropic decay results for the case which has the initial velocity and density fields statistically dependent such that the large velocities are associated with the negative density flucutations.

8.3.2 Effects of varying R_o

The time histories of the mean-squared velocity exhibit the same Reynolds number behavior as the results of Batchelor et al. [7], which assumed the Boussinesq approximation. As R_o increases, the nondimensional mean-squared velocity approaches a limiting curve. However, the limiting curve is different from that for the Boussinesq case. Not only is the time where the maximum occurs different, but also the shape of the curve. Figure 6.46 shows the histories of the mean-squared velocity as functions of R_o for the cases with the density ratio of 4. At $R_o = 256$ the decay of the mean-square velocity, just after the peak, is slower up to $T = 2$ than it is thereafter. This behavior is not present in the Boussinesq case (see Fig. 6.1).

The total turbulent kinetic energy and the terms that make up this energy [see eq. (8.1)] increase with increasing R_o. As R_o increases each of the terms in this equation appear to be approaching limiting curves.

The mean pressure gradient becomes more variable in time as R_o increases. The main contributions to the mean pressure gradient are from the acceleration term, $g/\overline{v}$, and the negative of the correlation between the fluctuating specific volume and gradient of the fluctuation pressure, $-\overline{v'\partial p'/\partial x_i}$. As R_o is increased, larger variations

in $g/\overline{v}$ occur. The correlation $-\overline{v'\partial p'/\partial x_i}$ is nonzero the instant that the fluid feels an acceleration, and its initial value is dependent on the strength of the acceleration and the magnitude of the initial density fluctuations. The initial value is not Reynolds number dependent. At early times $-\overline{v'\partial p'/\partial x_i}$ represents a "rapid" part (i.e., not proportional to the mass flux) in the evolution of the turbulent mass flux, a_i, and at later times behaves as a "slow" drag-like part (i.e., is proportional to the mass flux). The presence of this correlation impedes the growth of the mass flux.

The variance of the fluctuating density appears to approach a limiting curve. When $b(t) \approx B(t)$ the flow is within the Boussinesq limit since $\overline{\rho' u_i' u_i'}$ and a_i are nearly zero and the mean pressure gradient is approximately

$$\frac{\partial \overline{p}}{\partial x_i} = \overline{\rho} g_i.$$

Also, as R_o increases, the skewness in the pdf of the density field increases.

8.4 Model comparisons

It has been shown that, in the equation for a_n in both the BHR and the CS models, it is essential that the b coupling to the mean pressure gradient be modified to account for the effects due to $\overline{v'(\partial p'/\partial x_n)}$. Thus, the mean pressure gradient term should have the form

$$(1-c)\frac{b}{\overline{\rho}}\frac{\partial \overline{P}}{\partial x_n},$$

where the coefficient c is approximately 0.4. The drag term in the equation for a_n for the CS model, using $\beta_{rp1} = \beta_{rp2} = 1/b(t)$, gives reasonable agreement with the one-point statistics of the DNS results. It has also been seen that the inclusion of this effect in the BHR model only slightly improves the comparison between the BHR and the DNS results at late times. Overall, late time behavior of the BHR results do not agree well with the DNS data. The are several reasons for this. First, the simple time and length scales used in the one-point model are such that the density field and the energy field have the same scales. As a result, the evolution of b is not correct, causing late time differences in the evolution of a_n and R_{nn} between the BHR model predictions and the DNS results. Secondly, the BHR model assumes spectral equilibrium (i.e., a high Reynolds number flow). Clearly, the DNS results are not in

spectral equilibrium because the Reynolds number is small. There is good qualitative agreement between the DNS and the CS model. The late time behavior is captured more accurately using the CS model than the BHR model, because the late time behavior for b is more accurately predicted.

The spectra of $\overline{v'(\partial p'/\partial x_n)}$ shows some effects (broadening of the spectrum, dilation effect, and a shift in k where the spectrum of $\overline{v'(\partial p'/\partial x_n)}$ is a maximum) that are not accounted for in current closures. More detailed studies are needed to determine these effects and their proper modeling. The dilatation effects are analogous to "low-Reynolds" number effects: as the diffusivity becomes small, these effects also become small. Thus, further DNS study would be desirable in order to examine dilatational effects in the limit of finite (not infinitesimal) diffusivity. These spectral effects seen in this comparison are probably not capturable in a genuine manner in a one-point closure (where everything is lumped into simple scalings). These effects, however, may be capturable in an "augmented" spectral closure where the diffusive effects of density are accounted for in an energy equation for the diffusive part of the velocity field.

8.5 Future Work

Based on the results of this dissertation, the following two directions of research are recommended: (1) the continued use of numerical methods to gain further fundamental understanding of such flows and (2) bridging the gap between the theoretical understanding and engineering applications of variable-density flows by comparison of simulation results to model predictions. These issues are addressed below:

(1) A continued use of numerical simulations is essential to help advance the fundamental understanding of these flows. Two physical problems, in addition to those addressed in this dissertation, can be addressed. The first is the case of the "return-to-isotropy" in a variable-density turbulent fluid (case a). To address this problem a variation of the acceleration case can be used. An acceleration can act to convert the initially motionless fluid to a statistically axisymmetric, nonisotropic flow. Once the flow is in motion, the acceleration can then be "turned-off" in the numerical simulation and the nonisotropic flow will then return to isotropy. It has been seen in constant-density flows that the evolution of the various components of the anisotropy tensor and the Reynolds tensor are governed by the action of the triple correlation of

the fluctuating velocities. Also, the decay rate of the anisotropy is strongly dependent on the spectral locations of the anisotropy. In the variable-density case, the question is: does the triple correlation of the fluctuating density and velocities contribute to the evolution of the anisotropy tensor, and does the variable-density fluid affect the spectral locations of the anisotropy? The second additional flow of interest that should be addressed is the case of a variable-density flow subjected to a de-acceleration (case b). Again, a variation of the acceleration case will be used. Here, after the flow is developed, the de-acceleration of the flow is achieved by "changing the direction of acceleration". The flow will then de-accelerate and reverse direction. Changes in the rate of mixing due to these physical processes could be studied.

(2) To bridge the gap between the theoretical understanding of such flows and their engineering applications, the numerical data of problems (a), (b), and the results of this dissertation should be compared to a variety of one-point ("engineering") and two-point ("spectral") models of variable-density turbulent flow. These comparisons will help to validate and identify deficiencies in these models and, wherever possible, improvements to these models could be made. In particular, the spectral character of these flows can be studied and compared with an existing two-point, "spectral" model (e.g., the CS model). Once the model has been compared with numerical data, and some degree of confidence in the model has been achieved, it could then be spectrally integrated to obtain a one-point engineering model. This integrated model could be compared to other existing one-point models (e.g., the BHR model). This comparison will be valuable in understanding and improving one-point engineering models.

BIBLIOGRAPHY

[1] Andronov, V. A., Bakhrakh, S. M., Meshkov, E. E., Mokhov, V. N., Nikiforov, V. V., Pevnitskii, A. V. and Tolshmyakhov, A. I. *Sov. Phys. Dolk.*, **27**, 393 (1982)

[2] Barrett, T. K. and Van Atta, C, W., "Experiments on the inhibition of mixing in stably stratified decaying turbulence using laser Doppler anemometry and laser-induced fluorescence", *Phys. Fluids A*, **3**, (5), (1991)

[3] Batchelor, G. K., "The theory of axisymmetric turbulence", *Proc. Roy. Soc. London A*, **186**, (1946)

[4] Batchelor, G. K., The theory of homogeneous turbulence, Cambridge University press, 1953

[5] Batchelor, G. K. and Townsend, A. A., "Decay of Isotropic turbulence in the initial period", *Proc. Roy. Soc. London A*, **193**, (1948)

[6] Batchelor, G. K. and Townsend, A. A., "Decay of turbulence in the final period", *Proc. Roy. Soc. London A*, **194**, (1948)

[7] Batchelor, G. K., Canuto, V. M. and Chasnov, J. R., "Homogeneous buoyancy-driven turbulence", *J. Fluid Mech*, **235**, *pp.* 349-378 (1992)

[8] Besnard, D., Bonnet, M., Gauthier, S., Hass, J. F. and Spitz, P., in *Proceedings of the 16th ISSWST*, Aachen, Federal Republic of Germany, 1987, edited by H. Groning (VCH, New York, 1988).

[9] Besnard, D., Harlow, F. H., Rauenzahn, R. M. and Zemach, A. C., "Spectral Transport Model of Turbulence", Los Alamos National Laboratory Report LA-11821-MS (1990)

[10] Besnard, D., Harlow, F. H., Rauenzahn, R. M. and Zemach, A. C., "Turbulence Transport Equations for Variable-Density Turbulence and Their Relationship to Two-Field Models", Los Alamos National Laboratory Report LA-12303-MS (1992)

[11] Birkhoff, G., "Taylor Instability and Laminar Mixing", Los Alamos Scientific Laboratory Report LA-1862 (1954)

[12] Bird, R. B., Stewart, W. E. and Lightfoot, E. N., Transport Phenomena, John Wiley & Sons, 1960

[13] Bracewell, R. N., The Fourier Transform and Its Applications, McGraw-Hill, 1986

[14] Broadwell, J. E. and Breidenthal, R. E., "A simple model of mixing and chemical reaction in a turbulent shear layer", *J. Fluid Mech.*, **125**, *pp.* 397-410 (1982)

[15] Brown, G. L. and Roshko, A., "On density effects and large structure in turbulent mixing layers", *J. Fluid Mech.*, **64**, *pp.* 775-816 (1974)

[16] Brown, G. L., "The Entrainment and Large Structure in Turbulent Mixing Layers", *Fifth Australasian Conference on Hydraulics and Fluid Mechanics*, at University of Canterbury, New Zealand (1974)

[17] Canuto, C., Hussaini, M. Y., Quarteroni, A. and Zang, T. A., Spectral Methods in Fluid Mechanics, Springer-Verlag, 1988

[18] Chandrasekhar, S., "The theory of axisymmetric turbulence", *Phi. Trans. Roy. Soc.*, **242**, (1950)

[19] Chasnov, J., Canuto, V. M. and Rogallo, R, S., "Turbulence spectrum of a passive temperature field: Results of a numerical simulation", *Phys. Fluids*, **31**, (8), (1988)

[20] Chen, S. Y., (private communication)

[21] Chen, C., Riley, J. J. and McMurtry, P. A., "A Study of Favre Averaging in Turbulent Flows with Chemical Reaction", *Combustion and Flame*, **87**, *pp.* 257-277 (1991)

[22] Clark, T. T., PH.D thesis, University of New Mexico, 1992

[23] Clark, T. T. and Spitz, P., "A Spectral Model for Variable-Density Turbulence", Los Alamos National Laboratory Report LA-12671-MS (1994)

[24] Clark, T. T. and Zemach, C., "A Spectral Model Applied to Homogeneous Turbulence", *Phys. Fluids*, **7**, (7) (July 1995)

[25] Comte-Bellot, G and Corrsin, S., "Simple Eulerian time correlation of full and narrow-band velocity signals in grid-generated, 'isotropic' turbulence", *J. Fluid Mech*, **48**, *pp.* 273-337 (1971)

[26] Cooley, J. W., Lewis, P. A. W. and Welch, P. D., "The Fast Fourier Transform Algorithm: Programming Considerations in the Calculation of Sine, Cosine and Laplace Transforms", *J. Sound Vib.*, **12**, (3), *pp.* 315-337 (1970)

[27] Cranfill, C., "A New Multifluid Turbulent-Mix Model", Los Alamos National Laboratory document LA–UR-92-2484 (1992)

[28] Dimotakis, P. E., "Two-Dimensional Shear-layer Entrainment", *AIAA Journal*, **24**, 11, *pp.* 1791-1796 (1986)

[29] Dobran, Flavio, "Theory of Structured Multiphase Mixtures", in Lecture Notes in Physics, edited by W. Beiglb'ock, Springer Verlag **372**, (1991)

[30] Eswaran, V. and Pope, S. B., "Direct numerical simulations of the turbulent mixing of a passive scalar", *Phys. Fluids*, **31**, 3 (March 1988)

[31] Favre, A., in *Problems of Hydrodynamics and Continuum Mechanics.*, SIAM, (1969)

[32] Feiereisen, W. J., Reynolds, W. J. and Ferziger, J. H., "Numerical Simulation of Compressible, Homogeneous Turbulent Shear Flow", Dep. of Mechanical Engineering Report, Stanford Univ., Rep TF-13 (1981)

[33] Gauthier, S. and Bonnet, M., "A $k-\epsilon$ model for turbulent mixing in shock-tube flows induced by Rayleigh-Taylor instability", *Phys. Fluids A*, **2**, (9) (September 1990)

[34] Gebhart, B., Jaluria, Y., Mahajan, R. and Sammakia, B, Buoyancy-Induced Flows and Transport, Hemisphere Publishing Corporation, 1988

[35] Glimm, J., Li, X. L., Menikoff, R., Sharp, D. H., and Zhang, Q., "A numerical study of bubble interactions in Rayleigh-Taylor instability for compressible fluids", *Phys. Fluids A*, **2**, 11 *pp.* 2046-54 (Nov 1990)

[36] Harlow, F. H., (unpublished notes)

[37] Herring, J. R. and Kerr, R. M., "Comparison of direct numerical simulations with predictions of two-point closures for isotropic turbulence convecting a passive scalar", *J. Fluid Mech*, **118**, *pp.* 205-219 (1982)

[38] Hinze, J. O., Turbulence, McGraw-Hill, 1975

[39] Hopfinger, E. J., "Turbulence in Stratified Flows: A Review", *Phys. Fluids A*, 4, (10), *pp.* 5287-5303 (1992)

[40] Itsweire, E. C., Helland, K. N. and Van Atta, C. W., "The evolution of grid-generated turbulence in a stably stratified fluid" *J. Fluid Mech*, **162**, *pp.* 299-338 (1986)

[41] Ishii, M., Thermo-fluid Dynamic Theory of Two-phase Flow, Eyrolles, Paris 1975

[42] Jayesh, and Warhaft, Z., "Probability Distribution of a Passive Scalar in Grid-Generated Turbulence", *J. Geophy. Res.*, **92**, c5, *pp.* 3503-3506 (1987)

[43] Jayesh, and Warhaft, Z., "Probability distribution, conditional dissipation, and transport of passive temperatures in grid-generated turbulence", *Phys. Fluids A*, **4**, (10), *pp.* 2292-2307 (1992)

[44] Jayesh, Tong, C. and Warhaft, Z., "On temperature spectra in grid turbulence", *Phys. Fluids*, **6**, (1), *pp.* 306-312 (1994)

[45] Joseph, D. D., "Fluid Dynamics of two miscible liquids with diffusion and gradient stresses", *Eur. J. Mech., B/Fluids*, **9**, 6, *pp.* 565-596 (1990)

[46] Kataoka, I., "Local Instant Formulation of Two-Phase Flow", *Int. J. Multiphase Flow*, **12**, 5 *pp.* 745-758 (1986)

[47] Kataoka, I., and Serizawa, A., "Basic Equations of Turbulence in Gas-Liquid Two-Phase Flow", *Int. J. Multiphase Flow*, **15**, 5 *pp.* 843-855 (1989)

[48] Kolmogorov, A. N., "On degeneration of isotropic turbulence in an incompressible viscous fluid", *Dolk. Akad. Nauk. SSSR*, **31**, *pp.* 538-541 (1941)

[49] Launder, B. E., Reece, G. J., and Rodi, W., "Progress in the development of a Reynolds-stress turbulence closure", *J. Fluid Mech*, **68**, *pp.* 537-566 (1975)

[50] Landahl, M. T., and Mollo-Christensen, E. Turbulence and Random Processes in Fluid Mechanics, Cambridge University Press, 1994

[51] Leith, C. E., "Diffusion Approximation to Inertial Energy Transfer in Isotropic Turbulence", *Phys. Fluids* **10**(7), *pp.* 1409-1416 (1967)

[52] Lesieur, M., Turbulence in Fluids, Kluwer-Academic Press, 1990

[53] Lesieur, M. and Rogallo, R. S., "Large-eddy simulation of passive scalar diffusion in isotropic turbulence", *Phys. Fluids A*, **1**, (4) (March 1989)

[54] Lienhard, J. H. and Van Atta, C. W., "Decay of turbulence in thermally stratified flow" *J. Fluid Mech*, **210**, *pp.* 57-112 (1988)

[55] Linden, P. F. and Redondo, J, M., "Molecular mixing in Rayleigh-Taylor instability. Part I: Global Mixing", *Phys. Fluids A*, **3**, (5), (1991)

[56] Lumley, J. L., Stochastic Tools in Turbulence, Academic Press, 1970

[57] McComb, W. D., The Physics of Fluid Turbulence, Oxford Science Publications, 1990

[58] McMurtry, P. A., PH.D thesis, University of Washington, 1987

[59] Mell, W. E., (private communication)

[60] Mell, W. E., PH.D thesis, University of Washington, 1994

[61] Métais, O. and Lesieur, M., "Spectral large-eddy simulation of isotropic and stably stratified turbulence", *J. Fluid Mech*, **239**, *pp.* 157-194 (1992)

[62] Mohamed, M. S. and LaRue, J. C., "The decay of turbulent structure in a uniform shear flow", *J. Fluid Mech*, **68**, *pp.* 577-590 (1990)

[63] Najm, Habib N., "A Predictor-Corrector Method for Modeling Low Mach Number Reacting Flow" Submitted to *J. Comp. Phys.* (1995)

[64] Orszag, S. A., "Numerical Methods for the Simulation of Turbulence", *Phys. Fl. Suppl. II*, **12**, 250 (1969)

[65] Orszag, S. A. and Patterson Jr., G. S., "Numerical Simulation of Three Dimensional Homogenous Isotropic Turbulence", *Phys. Fl. Rev. Let.*, **28**, 76-79 (1972)

[66] Orszag, S. A. and Patterson Jr., G. S., "Numerical Simulations of Turbulence", in Statistical models and turbulence, edited by M Rosenblatt and C. Van Atta, Springer Verlag **12**, 127-147 (1972)

[67] Panton, R. L., Incompressible Flow, John Wiley & Sons, 1984

[68] Peyret, R. and Taylor, T. D., Computation Methods for Fluid Flow, Springer-Verlag, 1983

[69] Phillips, O. M., The Dynamics of the Upper Ocean, Cambridge University Press, 1977

[70] Press, W. H., Flannery, P. B., Teukolsky, S. A. and Vetterling, W. T., Numerical Recipes in C, Cambridge University Press, 1988

[71] Pumir, A. "A numerical study of the mixing of a passive scalar in three dimensions in the presence of a mean pressure gradient", *Phys. Fluids*, **6**, (6) (June 1994)

[72] Riley, J. J., Metcalfe, R, W. and Weissman, M. A., "Direct Numerical Simulations of Homogeneous Turbulence in Density-Stratified Fluids", in *Nonlinear Properties of Internal Waves*, AIP Conference Proceedings No. 76, ed. by B. J. West *pp.* 79-112 (1981)

[73] Robey, H. F., "Spectrum of a Passive Scalar in the Inertial-Convective Subrange of and Anisotropic Turbulent Flow", *Phys. Rev. Let.*, **65**, 11, *pp.* 1360-1363 (1990)

[74] Rogallo, R. S., "Numerical experiments in Homogeneous Turbulent Shear Flow", Stanford University Report No. TF-25 (1986)

[75] Rogers, M. M., Moin, P., and Reynolds, W. C., "The Structure and Modeling of the Hydrodynamic and Passive Scalar Fields in Homogeneous Turbulent Shear Flow", NASA TM 81315 (1981)

[76] Ruetsch, G. R. and Maxey, M, R., "Small-scale features of vorticity and passive scalar fields in homogeneous isotropic turbulence", *Phys. Fluids A*, **3**, (5), (1991)

[77] Saffman, P. G., "The large-scale structure of homogeneous turbulence", *J. Fluid Mech*, **27**, *pp.* 581-593 (1967)

[78] Sharp, D. H., "An overview of Rayleigh-Taylor Instability" em Physica bf 12D, *pp.* 3-18 (1984)

[79] She, Z. S., Chen, S., Doolen, G. Kraichnan, R. H. and Orszag, S. A., "Reynolds number dependence of isotropic Navier-Stokes turbulence", *Phys. Rev. Let.*, **70**, 21, *pp.* 3251-4 (1993)

[80] Shy, S. S. and Briedenthal, R, E., "Turbulent stratified interfaces", *Phys. Fluids A*, **3**, (5), (1991)

[81] Smeeton, V. S. and Youngs, D. L., "Experimental Investigation of Turbulent Mixing by Rayleigh-Taylor Instability", AWE REPORT No. O 35/87 (1987)

[82] Sreenivasan, K. R., Tavoularis, S., Henry, R. and Corrsin, S., "Temperature fluctuations and scales in grid-generated turbulence", *J. Fluid Mech*, **100**, *pp.* 597-621 (1980)

[83] Stewart, H. B. and Wendroff, B., "Two-Phase Flows: Models and Methods", *J. Comp. Phys.*, **56**, *pp.* 363-409 (1984)

[84] Sturtevant, B., "Rayleigh-Taylor instability in compressible flows," *Shock Waves and Shock Tubes*, Proceedings of the 16th Int'l. Symp. on Shock Waves and Shock Tubes, H. Grönig, Ed., RWTH, Aachen, VCH Physik Verlag, *p.* 89 (1987)

[85] Synge, J. L. and Griffith, B. A., Principles of Mechanics, McGraw-Hill, 1942 *p.* 41.

[86] Tavoularis, S., Bennett, J. C. and Corrsin, S., "Velocity-derivative skewness in small Reynolds number, nearly isotropic turbulence", *J. Fluid Mech.*, **88**, *pp.* 63-69 (1978)

[87] Tennekes, H. and Lumley, J. L., A First Course in Turbulence, The MIT Press, 1972

[88] Warhaft, Z. and Lumley, J. L., "An experimental study of the decay of temperature fluctuations in grid-generated turbulence", *J. Fluid Mech*, **88**, pt. 4, *pp.* 659-684 (1978)

[89] Werner, J. A. Dahm, Southerland, K. B. and Buch, K. A., "Direct, high resolution, four-dimensional measurements of the fine scale structure of Sc$\ll$1 molecular mixing in turbulent flow", *Phys. Fluids A*, **3**, (5), (1991)

[90] Yoon, K. and Warhaft, Z., "The evolution of grid turbulence under conditions of stable thermal stratification" *J. Fluid Mech*, **215**, *pp.* 601-638 (1990)

[91] Youngs, D. L., "Three-dimensional numerical simulation of turbulent mixing by Rayleigh-Taylor instability", *Phys. Fluids A*, **3**, (5), (1991)

[92] Zang, T. A., "On the rotation and skew-symmetric forms for incompressible flow simulations", *Applied Numerical Mathematics*, 7 (1991)

[93] Zemach, A. C., (private communication)

Appendix A

AVERAGING

The most common approach in the study of turbulence involves the use of the Reynolds-averaged equations [38]. These equations are used to model the effects of turbulence in various applications. The Reynolds-averaged equations are derived from the conservation equations of motion by, first, separating the dependent variables into mean and fluctuating components, and then averaging the equations. There are two types of decompositions of the dependent variables, a Reynolds decomposition and a Favre decomposition [21, 31].

A.1 Reynolds averaging

For the study of constant-density turbulence a Reynolds decomposition is typically used. A Reynolds decomposition of the dependent variable is

$$f = \bar{f} + f' \tag{A.1}$$

where $\bar{f}$ is the average of f and f' is the fluctuation about the average. There are three types of averages used in studying turbulent flows. Time averages are appropriate for statistically stationary turbulence. Space averages appropriate for statistically homogeneous turbulence. And ensemble averages, taken over a number of identical realizations of the flow, are utilized if neither space nor time averages are appropriate. The average of the fluctuation is zero by definition,

$$\overline{f'} = 0,$$

whereas the product of two fluctuating quantities is, in general, nonzero,

$$\overline{f'f'} \neq 0.$$

The average of two dependent variables reduces to

$$\overline{fg} = \bar{f}\bar{g} + \overline{f'g'}.$$

If f and g are the two components of velocity then,

$$\overline{u_i u_j} = \overline{u}_i \overline{u}_j + \overline{u_i' u_j'}.$$

In constant-density turbulence, $\overline{u_i' u_j'}$ is often modeled in the Reynolds-averaged Navier-Stokes equations.

A.2 Favre averaging

For the study of variable-density flows it is common to use mass-weighted averaging due to Favre [31]. The Favre decomposition of the velocity is

$$u_i = \tilde{u}_i + u_i''$$

where the mass-weighted average velocity, $\tilde{u}_i$, is defined as

$$\tilde{u}_i = \frac{\overline{\rho u_i}}{\bar{\rho}}.$$

Here ρ is the density of the fluid. In this case the average of the fluctuation is not equal to zero. It can be shown that this average is

$$a_i \equiv \overline{u_i''} = -\frac{\overline{\rho' u_i'}}{\bar{\rho}}, \tag{A.2}$$

where a_i is the negative of the turbulent mass flux divided by the mean density. However, the density-weighted average of u_i'' is zero, i.e.,

$$\overline{\rho u_i''} = \bar{\rho} \tilde{u}_i'' = 0. \tag{A.3}$$

The mass-weighted averaged velocity is

$$\tilde{u}_i = \frac{\overline{\rho u_i}}{\bar{\rho}} = \bar{u}_i - a_i.$$

In variable-density flow, the density-velocity-velocity correlation is

$$\overline{\rho u_i u_j} = \overline{\rho(\tilde{u}_i + u_i'')(\tilde{u}_i + u_i'')} = \bar{\rho} \tilde{u}_i \tilde{u}_j + \tilde{u}_i \overline{\rho u_j''} + \tilde{u}_j \overline{\rho u_i''} + \overline{\rho u_i'' u_j''}.$$

Using condition (A.3) this becomes

$$\overline{\rho u_i u_j} = \overline{\rho}\tilde{u}_i\tilde{u}_j + \overline{\rho u_i'' u_j''}. \tag{A.4}$$

Here, $\overline{\rho u_i'' u_j''}$ is the generalized Reynolds stress tensor for variable-density turbulence:

$$R_{ij}(t) = \overline{\rho u_i'' u_i''}.$$

Using eq. (A.4) this can be written as

$$R_{ij}(t) = \overline{\rho u_i'' u_j''} = \overline{\rho u_i u_j} - \overline{\rho}\tilde{u}_i\tilde{u}_j. \tag{A.5}$$

Recall that

$$u_i = \overline{u}_i + u_i' = \tilde{u}_i + u_i''.$$

Density-weighted averaging of this leads to

$$\tilde{u}_i = \overline{u}_i - \overline{u''}_i = \overline{u}_i - a_i.$$

Substituting this for $\tilde{u}_i$ and $u_i = \overline{u}_i + u_i'$ into (A.5) leads to

$$R_{ij}(t) = \overline{\rho u_i'' u_j''} = \overline{\rho}\ \overline{u_i' u_j'} + \overline{\rho' u_i' u_j'} - \bar{\rho} a_i a_j. \tag{A.6}$$

This is another form of the generalized Reynolds stress tensor for variable-density turbulent flow. The density-weighted turbulent kinetic energy per unit mass is

$$K(t) = \frac{R_{nn}}{2\overline{\rho}} = \frac{1}{2\overline{\rho}}\left\{\overline{\rho}\ \overline{u_n' u_n'} + \overline{\rho' u_n' u_n'} - \bar{\rho} a_n a_n\right\}. \tag{A.7}$$

Finally, the total fluid kinetic energy is half the trace of eq. (A.4), or

$$KE(t) = \frac{1}{2}\overline{\rho u_n u_n} = \frac{1}{2}\overline{\rho}\tilde{u}_n\tilde{u}_n + \frac{1}{2}\overline{\rho u_n'' u_n''}. \tag{A.8}$$

Appendix B

EVOLUTION EQUATIONS

In this appendix, the averaging procedures discussed in Appendix A are used to derive evolution equations for the variance of the density, the fluctuating density-fluctuating specific volume correlation, the density-weighted average kinetic energy and the components of this energy. The assumption of statistical homogeneity will be made as well as the assumption that spatial gradients of mean quantities, except pressure, are zero, i.e.,

$$\frac{\partial \overline{()}}{\partial x_i} \equiv 0. \tag{B.1}$$

Statistical homogeneity applies to all quantities except pressure whose gradient is assumed homogeneous (see section 3.1.3). In this study the mean density has a constant value (i.e., it does not vary in time) of unity,

$$\overline{\rho} = 1, \tag{B.2}$$

and the flow will have zero mean velocity,

$$\overline{u_i} = 0. \tag{B.3}$$

The $\overline{()}$ is a volume average over the entire flow field (computational domain).

B.1 Density variance equation

The variance of the density field is $\overline{\rho'\rho'}$. The derivation of its evolution equation starts with the equation for the conservation of mass, eq. (2.1),

$$\frac{\partial \rho}{\partial t} + \frac{\partial \rho u_i}{\partial x_i} = 0,$$

which can be rewritten as

$$\frac{\partial \rho}{\partial t} + u_i \frac{\partial \rho}{\partial x_i} + \rho \frac{\partial u_i}{\partial x_i} = 0.$$

Substituting the Reynolds decomposition for the velocity and density into this equation and using conditions (B.2) and (B.3) leads to

$$\frac{\partial \rho'}{\partial t} + u_i' \frac{\partial \rho'}{\partial x_i} + \overline{\rho} \frac{\partial u_i'}{\partial x_i} + \rho' \frac{\partial u_i'}{\partial x_i} = 0.$$

Multiply this by $2\rho'$ to get

$$\frac{\partial \rho' \rho'}{\partial t} + \frac{\partial u_i' \rho' \rho'}{\partial x_i} + (2\overline{\rho}\rho' + \rho'\rho') \frac{\partial u_i'}{\partial x_i} = 0.$$

Finally, volume averaging this equation and using condition (B.1) gives, with rearrangement

$$\frac{\partial \overline{\rho' \rho'}}{\partial t} = -2\overline{\rho}\, \overline{\rho' \frac{\partial u_i'}{\partial x_i}} - \overline{\rho' \rho' \frac{\partial u_i'}{\partial x_i}}. \tag{B.4}$$

This is the evolution equation for the variance of the fluctuating density.

B.2 Equation for $b = -\overline{\rho'(1/\rho)'}$

The quantity, b, is the negative of the correlation between the fluctuating density and the fluctuating specific volume:

$$b(t) = -\overline{\rho' \left(\frac{1}{\rho}\right)'}.$$

Because $\rho = \overline{\rho} + \rho'$, this can be written as

$$b(t) = \overline{\rho}\overline{(1/\rho)} - 1 = \overline{\rho}\,\overline{v} - 1 \tag{B.5}$$

where $v = 1/\rho$ is the specific volume, or as [10]

$$b(t) = -\overline{\rho' \left(\frac{1}{\overline{\rho} + \rho'} - \frac{1}{\overline{\rho}}\right)} = \overline{\left(\frac{\rho'\rho'}{\rho\overline{\rho}}\right)}.$$

Clearly, $b(t)$ is nonnegative and in the limit as the density fluctuations tend to zero $b(t) \approx \overline{\rho'\rho'}/\overline{\rho}^2 - \overline{\rho'\rho'\rho'}/\overline{\rho}^3 + \ldots$. The derivation of the evolution equation for $b(t)$ starts

with the equation for the conservation of mass, eq. (2.1). Substituting for the specific volume, $v = 1/\rho$, into this equation gives

$$\frac{\partial(1/v)}{\partial t} + \frac{1}{v}\frac{\partial u_i}{\partial x_i} + u_i\frac{\partial(1/v)}{\partial x_i} = 0.$$

Rewriting this as

$$-\frac{1}{v^2}\frac{\partial v}{\partial t} + \frac{1}{v}\frac{\partial u_i}{\partial x_i} - \frac{u_i}{v^2}\frac{\partial v}{\partial x_i} = 0,$$

multiplying by $-v^2$, adding

$$2v\frac{\partial u_i}{\partial x_i}$$

to each side of the equation, and rearranging leads to

$$\frac{\partial v}{\partial t} + \frac{\partial v u_i}{\partial x_i} = 2v\frac{\partial u_i}{\partial x_i}. \tag{B.6}$$

This is the evolution equation for the specific volume. Substituting the Reynolds decomposition for the velocity and specific volume into this equation and using condition (B.3) leads to

$$\frac{\partial \overline{v}}{\partial t} + \frac{\partial v'}{\partial t} + \frac{\partial \overline{v}\,u_i'}{\partial x_i} + \frac{\partial v' u_i'}{\partial x_i} = 2\overline{v}\frac{\partial u_i'}{\partial x_i} + 2v'\frac{\partial u_i'}{\partial x_i}.$$

Volume averaging this equation and using condition (B.1) gives

$$\frac{\partial \overline{v}}{\partial t} = 2\overline{v'\frac{\partial u_i'}{\partial x_i}}. \tag{B.7}$$

This is the evolution equation for the mean specific volume. Multiply eq. (B.7) by $\overline{\rho}$, and noting that,

$$\overline{\rho}\frac{\partial \overline{v}}{\partial t} = \frac{\partial \overline{\rho}\;\overline{v}}{\partial t} = \frac{\partial(\overline{\rho}\;\overline{v} - 1)}{\partial t} = \frac{\partial b}{\partial t}$$

and

$$\frac{\partial \overline{\rho}}{\partial t} = 0$$

gives

$$\frac{\partial b}{\partial t} = 2\overline{\rho}\;\overline{v'\frac{\partial u_i'}{\partial x_i}}. \tag{B.8}$$

This is the evolution equation for $b(t)$.

B.3 Equation for the Total Kinetic Energy Density

The total kinetic energy density is given by eq. (A.8), written here for a case with zero mean flow, $\overline{u}_i = 0$, as

$$KE(t) = \frac{1}{2}\overline{\rho u_n u_n} = \frac{1}{2}\overline{\rho u_n' u_n'} = \frac{1}{2}\overline{\rho}\ \overline{u_n' u_n'} + \frac{1}{2}\overline{\rho' u_n' u_n'}. \tag{B.9}$$

Note that for the case of isotropic decay, where $a_i = 0$, the total kinetic energy density divided by the mean density is the same as the total turbulent kinetic energy per unit mass (see eq. (A.7)). An evolution equation for (B.9) is now derived. The starting point is the momentum equation, eq. (2.2),

$$\frac{\partial \rho u_i}{\partial t} + \frac{\partial \rho u_i u_j}{\partial x_j} = -\frac{\partial p}{\partial x_i} + \frac{\partial \tau_{ij}}{\partial x_j} + \rho g_i$$

with the viscous stress tensor defined by

$$\tau_{ij} = \mu \left\{ \frac{\partial u_i}{\partial x_j} + \frac{\partial u_j}{\partial x_i} - \frac{2}{3}\delta_{ij}\frac{\partial u_n}{\partial x_n} \right\}.$$

Multiplying the momentum equation by u_i gives

$$u_i \frac{\partial}{\partial t}\{\rho u_i\} + u_i \frac{\partial}{\partial x_j}\{\rho u_i u_j\} = -u_i \frac{\partial p}{\partial x_i} + u_i \frac{\partial \tau_{ij}}{\partial x_j} + \rho u_i g_i \tag{B.10}$$

The momentum equation can be rewritten as

$$\frac{\partial u_i}{\partial t} + u_j \frac{\partial u_i}{\partial x_j} = -\frac{1}{\rho}\frac{\partial p}{\partial x_i} + \frac{1}{\rho}\frac{\partial \tau_{ij}}{\partial x_j} + g_i. \tag{B.11}$$

Multiplying this by ρu_i gives

$$\rho u_i \frac{\partial u_i}{\partial t} + \rho u_i u_j \frac{\partial u_i}{\partial x_j} = -u_i \frac{\partial p}{\partial x_i} + u_i \frac{\partial \tau_{ij}}{\partial x_j} + \rho u_i g_i. \tag{B.12}$$

Adding eqs. (B.10) and (B.12) together

$$\frac{\partial}{\partial t}\{\rho u_i u_i\} + \frac{\partial}{\partial x_j}\{\rho u_j u_i u_i\} = -2u_i \frac{\partial p}{\partial x_i} + 2u_i \frac{\partial \tau_{ij}}{\partial x_j} + 2\rho u_i g_i.$$

Substituting $u_i = u_i'$ (using condition (B.3)) and $\rho = \overline{\rho} + \rho'$ (in the acceleration term), then averaging and dividing by 2 leads to

$$\frac{\partial}{\partial t}\left\{\frac{1}{2}\overline{\rho u_i' u_i'}\right\} + \frac{\partial}{\partial x_j}\left\{\frac{1}{2}\overline{\rho u_j' u_i' u_i'}\right\} = -\overline{u_i'\frac{\partial p}{\partial x_i}} + \overline{u_i'\frac{\partial \tau_{ij}'}{\partial x_j}} + \overline{\rho' u_i'} g_i.$$

This is the evolution equation for the total kinetic energy density. Assuming statistical homogeneity and applying condition (B.1) gives

$$\frac{\partial}{\partial t}\left\{\frac{1}{2}\overline{\rho u_i' u_i'}\right\} = \overline{p\frac{\partial u_i'}{\partial x_i}} + \overline{u_i'\frac{\partial \tau_{ij}'}{\partial x_j}} + \overline{\rho' u_i'} g_i. \tag{B.13}$$

This is the evolution equation for the total kinetic energy density for a statistically homogeneous flow. The first term on the right side is the pressure work term and represents changes in the total kinetic energy due to dilatation effects. The second term is viscous dissipation and the third term is work due to gravitational acceleration. For isotropic decay, this equation reduces to

$$\frac{\partial}{\partial t}\left\{\frac{1}{2}\overline{\rho u_i' u_i'}\right\} = \overline{p\frac{\partial u_i'}{\partial x_i}} + \overline{u_i'\frac{\partial \tau_{ij}'}{\partial x_j}}. \tag{B.14}$$

For isotropic decay, the evolution of the total kinetic energy density (which is the same as the turbulent kinetic energy density) is due only to pressure work and viscous dissipation.

B.4 The equation for $\overline{\rho}\ \overline{u_i' u_i'}$.

We will now write equations for the two terms that make up the total kinetic energy density, given in eq. (B.9). The evolution equation for $\overline{\rho}\ \overline{u_i' u_i'}$ is derived in this section. The starting point for this derivation is the equation for the momentum per unit mass, eq. (B.11). Multiplying this equation by u_i one obtains

$$\frac{\partial}{\partial t}\left\{\frac{1}{2}u_i u_i\right\} + u_i u_j \frac{\partial u_i}{\partial x_j} = -\frac{u_i}{\rho}\frac{\partial p}{\partial x_i} + \frac{u_i}{\rho}\frac{\partial \tau_{ij}}{\partial x_j} + u_i g_i.$$

Then multiplying by $\overline{\rho}$ and substituting $u_i = u_i'$ gives

$$\frac{\partial}{\partial t}\left\{\frac{1}{2}\overline{\rho}\ u_i' u_i'\right\} + \overline{\rho}\ u_i' u_j' \frac{\partial u_i'}{\partial x_j} = -\overline{\rho}\ \frac{u_i'}{\rho}\frac{\partial p}{\partial x_i} + \overline{\rho}\ \frac{u_i'}{\rho}\frac{\partial(\overline{\tau}_{ij} + \tau_{ij}')}{\partial x_j} + \overline{\rho}\ u_i' g_i.$$

Finally, averaging and rearranging leads to

$$\frac{\partial}{\partial t}\left\{\frac{1}{2}\overline{\rho}\,\overline{u_i'u_i'}\right\} = \frac{\overline{\rho}}{2}\,\overline{u_i'u_i'\frac{\partial u_j'}{\partial x_j}} - \overline{\rho}\,\overline{\frac{u_i'}{\rho}\frac{\partial P}{\partial x_i}} + \overline{\rho}\,\overline{\frac{u_i'}{\rho}\frac{\partial \tau_{ij}'}{\partial x_j}}, \tag{B.15}$$

This is the evolution equation for $\overline{\rho}\,\overline{u_i'u_i'}$. This is the mean squared velocity contribution to the total kinetic energy density (for isotropic decay, the turbulent kinetic energy density). The first term on the right side is due to dilatation effects. The second term is a modified pressure work term and the third term is the loss of energy due to viscous dissipation. The pressure gradient is discussed in more detail in section 3.1.3.

B.5 The equation for $\overline{\rho' u_i' u_i'}$

In this section is derived an equation for the second term of the evolution of the total kinetic energy density, eq. (B.9). Note that

$$\frac{1}{2}\overline{\rho' u_i' u_i'} = \frac{1}{2}\overline{\rho u_i' u_i'} - \frac{1}{2}\overline{\rho}\,\overline{u_i' u_i'}.$$

With this relationship, it is clear that an evolution equation for $\overline{\rho' u_i' u_i'}$ can be found by subtracting eq. (B.15) from eq. (B.13) to give

$$\frac{\partial}{\partial t}\left\{\frac{1}{2}\overline{\rho' u_i' u_i'}\right\} = -\frac{\overline{\rho}}{2}\,\overline{u_i' u_i'\frac{\partial u_j'}{\partial x_j}} - \overline{\frac{\rho' u_i'}{\rho}\frac{\partial p}{\partial x_i}} + \overline{\frac{\rho' u_i'}{\rho}\frac{\partial \tau_{ij}'}{\partial x_j}} + \overline{\rho' u_i'} g_i. \tag{B.16}$$

The first term on the right side represents changes due to dilatational effects. The second term is a modified pressure work term and the third term is the loss of energy due to viscous dissipation. The pressure gradient is discussed in more detail in section 3.1.3.

For isotropic decay, eq. (B.16) can be simplified to

$$\frac{\partial}{\partial t}\left\{\frac{1}{2}\overline{\rho' u_i' u_i'}\right\} = -\frac{\overline{\rho}}{2}\,\overline{u_i' u_i'\frac{\partial u_j'}{\partial x_j}} - \overline{\frac{\rho' u_i'}{\rho}\frac{\partial p'}{\partial x_i}} + \overline{\frac{\rho' u_i'}{\rho}\frac{\partial \tau_{ij}'}{\partial x_j}}. \tag{B.17}$$

B.6 Equation for $a_n = -\overline{\rho' u_n'}/\bar{\rho}$

The turbulent kinetic energy per unit mass can be written as [eq. (A.7)]

$$K(t) = \frac{1}{2\overline{\rho}}\left\{\overline{\rho}\,\overline{u_n' u_n'} + \overline{\rho' u_n' u_n'} - \bar{\rho} a_n a_n\right\}.$$

The third term on the right side is a contribution due to the turbulent mass flux, a_n. The definition of a_n is given by eq, (A.2) and shown here as

$$a_n = -\frac{\overline{\rho' u_n'}}{\bar{\rho}}.$$

For decaying isotropic turbulence a_n is zero and, if $\overline{u}_i = 0$, then the total fluid kinetic energy per unit mass is equal to the total turbulent kinetic energy per unit mass. However, for the case with a gravitational acceleration the turbulent mass flux is not zero. An equation for the evolution of this turbulence mass flux is derived in this section. The starting point is the momentum equation, eq. (2.2). Substituting the Favre decomposition for the velocity into this equation gives

$$\frac{\partial \rho \tilde{u}_i}{\partial t} + \frac{\partial \rho u_i''}{\partial t} + \frac{\partial}{\partial x_n}\left\{\rho \tilde{u}_i \tilde{u}_n + \rho \tilde{u}_i u_n'' + \rho \tilde{u}_n u_i'' + \rho u_i'' u_n''\right\} = \frac{\partial \sigma_{in}}{\partial x_n} + \rho g_i. \qquad \text{(B.18)}$$

Averaging and recalling that $\overline{\rho u_i''} = 0$ gives

$$\frac{\partial \overline{\rho} \tilde{u}_i}{\partial t} + \frac{\partial}{\partial x_n}\left\{\overline{\rho} \tilde{u}_i \tilde{u}_n\right\} + \frac{\partial}{\partial x_n}\left\{\overline{\rho u_i'' u_n''}\right\} = \frac{\partial \overline{\sigma_{in}}}{\partial x_n} + \overline{\rho} g_i, \qquad \text{(B.19)}$$

the equation for the Favre-averaged mean velocity. Starting with the conservation of mass [eq, (2.1)], substituting the Favre decomposition for the velocity and the Reynolds decomposition for the density, and averaging gives

$$\frac{\partial \overline{\rho}}{\partial t} + \frac{\partial \rho \tilde{u}_n}{\partial x_n} = 0.$$

Using this form of the conservation of mass, the Favre averaged mean flow equation can be rewritten as

$$\overline{\rho}\frac{\partial \tilde{u}_i}{\partial t} + \overline{\rho} \tilde{u}_n \frac{\partial}{\partial x_n}\left\{\tilde{u}_i\right\} = \frac{\partial}{\partial x_n}\left\{\overline{\sigma}_{in} - R_{in}\right\} + \overline{\rho} g_i. \qquad \text{(B.20)}$$

where, $R_{in} = \overline{\rho u_i'' u_n''}$ is the generalized Reynolds stress tensor. Substituting the Favre decomposition for the velocity into the equation for the momentum per unit mass [eq. (B.11)] and multiplying by $\overline{\rho}$ leads to

$$\overline{\rho}\frac{\partial \tilde{u}_i}{\partial t} + \overline{\rho}\frac{\partial u_i''}{\partial t} + \overline{\rho} \tilde{u}_n \frac{\partial \tilde{u}_i}{\partial x_n} + \overline{\rho} \tilde{u}_n \frac{\partial u_i''}{\partial x_n} + \overline{\rho} u_n'' \frac{\partial \tilde{u}_i}{\partial x_n} + \overline{\rho} u_n'' \frac{\partial u_i''}{\partial x_n} = \frac{\overline{\rho}}{\rho}\frac{\partial \sigma_{in}}{\partial x_n} + \overline{\rho} g_i. \qquad \text{(B.21)}$$

Subtracting eq. (B.20) from eq. (B.21) and rearranging the result gives

$$\frac{\partial u_i''}{\partial t} + u_n'' \frac{\partial}{\partial x_n}\{\tilde{u}_i + u_i''\} + \tilde{u}_n \frac{\partial u_i''}{\partial x_n} = \left(\overline{v} - \frac{1}{\overline{\rho}}\right)\frac{\partial \overline{\sigma}_{in}}{\partial x_n} + v'\frac{\partial \overline{\sigma}_{in}}{\partial x_n} + v\frac{\partial \sigma_{in}'}{\partial x_n} + \frac{1}{\rho}\frac{\partial R_{in}}{\partial x_n}.$$

Finally, averaging and recalling that $a_i = \overline{u_i''}$, gives

$$\frac{\partial a_i}{\partial t} + a_n \frac{\partial \tilde{u}_i}{\partial x_n} + \overline{u_n''\frac{\partial u_i''}{\partial x_n}} + \tilde{u}_n \frac{\partial a_i}{\partial x_n} = \left(\overline{v} - \frac{1}{\overline{\rho}}\right)\frac{\partial \overline{\sigma}_{in}}{\partial x_n} + \overline{v\frac{\partial \sigma_{in}'}{\partial x_n}} + \frac{1}{\rho}\frac{\partial R_{in}}{\partial x_n}. \qquad \text{(B.22)}$$

This is the evolution equation for the turbulent mass flux. Assuming statistical homogeneity, this equation reduces to

$$\frac{\partial a_i}{\partial t} + \overline{u_n''\frac{\partial u_i''}{\partial x_n}} = -\frac{b}{\overline{\rho}}\frac{\partial \overline{p}}{\partial x_i} + +\overline{v'\frac{\partial \sigma_{in}'}{\partial x_n}},$$

where

$$\frac{b}{\overline{\rho}} = \left(\overline{v} - \frac{1}{\overline{\rho}}\right),$$

and $b = \overline{\rho}\,\overline{v} - 1$. For the case of zero mean velocity, $u_i'' = u_i' - \tilde{u}_i$. Substituting u_i'' into this equation and exploiting homogeneity gives

$$\frac{\partial a_i}{\partial t} = \overline{u_i'\frac{\partial u_n'}{\partial x_n}} - \frac{b}{\overline{\rho}}\frac{\partial \overline{p}}{\partial x_i} + \overline{v'\frac{\partial \sigma_{in}'}{\partial x_n}}. \qquad \text{(B.23)}$$

This is the evolution equation for the turbulence mass flux for a statistically homogeneous, variable-density flow with zero mean velocity. The first term on the right side represents changes in the mass flux due to dilatation effects. The second term represents changes due to the mean pressure gradient. In this term is the buoyancy flux. The third term represents changes due to a correlation between the fluctuating specific volume and the gradient of the fluctuating stress.

Appendix C

VELOCITY INITIALIZATION PROCEDURE

There are two types of velocity fields used in this study. The first is the velocity field used by Mell [60], which has an initial Taylor Reynolds number of 55. This velocity field is initially in full spectrum decay, i.e., the velocity field is decaying at all wavenumbers (at all scales) in the spectrum, and is used in the study where the initial velocity and density fields are statistically independent. The initialization for these fields is a two step process described in section C.2. The second initial velocity field uses the same initial energy spectrum that is obtained from Mell's initial velocity field. A random velocity field is initialized using this energy spectrum, and it is not in full spectrum decay. This is used in the case where the initial velocity and density fields are statistically dependent.

The first section in this appendix describes how an initial velocity is computed from a given energy spectrum. The following sections then describe the initializations for the statistically independent and the statistically dependent velocity fields.

C.1 Computing the velocity field from a predefined initial energy spectrum

In the study of isotropic turbulence using direct numerical simulations, the mean velocity, $\bar{u}_i$ is constant in space and time and therefore it is common to use a Galilean transformation to choose a coordinate system such that the mean velocity $\overline{u}_i = 0$. The fluctuating velocity field is initialized using the method of Orszag and Patterson [65] suitably modified to account for the non-solenoidal aspect of the velocity [eq. (2.11)].

We define the initial velocity as the curl of a random vector potential (see below), $\vec{\phi}$, and the gradient of a scalar, ψ, that is

$$\vec{u} = \nabla \times \vec{\phi} + \nabla\psi. \tag{C.1}$$

Taking the divergence of the velocity leads to

$$\nabla \cdot \vec{u} = \nabla^2 \psi$$

since $\nabla \cdot \nabla \times \vec{\phi} \equiv 0$. If we define $\psi = -\mathcal{D} \ln \rho$ such that

$$\nabla \cdot \vec{u} = -\mathcal{D} \nabla^2 \ln \rho, \tag{C.2}$$

then the condition given by eq. (2.11) is satisfied, assuming the molecular diffusivity $\mathcal{D}$ is constant. Equation (C.2) is obtained from the initial density field.

The components of the random vector potential $\vec{\phi}$ are computed using the method of Box and Muller [70] to create a pair of random deviates from the same normal distribution, starting from a pair of uniformly distributed random numbers. Using this method, the Fourier amplitude of the random vector potential is written as

$$\hat{A}(\vec{k}) = x_1 + \imath x_2 \ for \ i = 1, 2, 3 \tag{C.3}$$

where x_1 and x_2 is (from Box and Muller)

$$x_1 = a(-2 \log_e U_1)^{\frac{1}{2}} \cos 2\pi U_2$$

$$x_2 = a(-2 \log_e U_1)^{\frac{1}{2}} \sin 2\pi U_2.$$

U_1 and U_2 are independent random variables which are uniformly distributed on the interval (0,1), and a is the rms of the velocity potential field that arises from using the energy spectrum $E(k)$. Assuming ergodicity, the total (volume averaged) kinetic energy per unit mass is related to the energy spectrum in isotropic turbulence [52] as

$$\frac{1}{2}\overline{u_n' u_n'} = \int_o^\infty E(k) dk \tag{C.4}$$

In this spectrum we define the shell between wavenumbers k_B and $k_B + \Delta k$ as shell B. The energy in shell B is approximated as:

$$\int_B E(k) dk = \sum_{k \in B} \mid \hat{u}(k) \mid^2 \cong N_B \mid \hat{u}(k) \mid^2$$

where N_B is the number of discrete modes in shell B, and the approximate equality used here is based on the assumption that the shell is thin enough that the values of $\mid \hat{u}(k) \mid$ for every mode in the shell are, on average, the same. Thus the mean square of the Fourier amplitudes defined in the shell is

$$\mid \hat{u}(k) \mid = \left[\frac{1}{N_B}\int_B E(k)dk\right]^{\frac{1}{2}}. \tag{C.5}$$

Defining the incompressibility part of the velocity as $\vec{u} = \nabla \times \vec{A}$ (where $\vec{A} = \vec{\phi}$, the random vector potential) and transforming to Fourier space gives $\hat{\vec{u}} = \imath\vec{k} \times \hat{\vec{A}}$. From this, using isotropy of the velocity field, the mean of the square of the velocity amplitudes becomes

$$\overline{\mid \hat{u} \mid^2} = 2a^2 \mid k \mid^2 .$$

Solving for a gives

$$a = \frac{\overline{\mid \hat{u} \mid^2}^{1/2}}{\sqrt{2} \mid k \mid}.$$

Substituting eq. (C.5) into this gives

$$a = \frac{\left[\frac{1}{2N_B}\int_B E(k)dk\right]^{\frac{1}{2}}}{\mid k \mid},$$

using in the definitions for x_1 and x_2 above. Substituting x_1 and x_2 into eq. (C.3), then $\vec{u} = \nabla \times \vec{A}$ is known. Adding the affect due to the divergent velocity condition, the total initial velocity is then

$$\vec{u} = \nabla \times \vec{A} - \mathcal{D}\nabla \ln \rho. \tag{C.6}$$

For the studies presented here we also enforce the condition that the mass flux, $\overline{\rho' u_i'}$, be initially zero. In the case of isotropic decay this correlation between the velocity field and the density field should always remain zero. In the case of an accelerated field the correlation, which is initially zero, will quickly become non-zero as the high density part of the field is set in motion in the direction of the acceleration and the low-density fluid is set in motion in the opposite direction. Thus a strong correlation develops between density and velocity fields in the accelerated case.

C.2 Statistically independent initial velocity field

This section describes the initialization procedure developed by Mell [60] to create an initial velocity field that is in full spectrum decay with the maximum initial Taylor Reynolds number that can be obtained with the given mesh resolution. At the start of a simulation the velocity field and density field are statistically independent. Following Mell [60], the two stages for this procedure are:

(I) An initial energy spectrum function, $E(k,0)$, is defined using an analytical function that is expressed by an exponential. In this case that function is, from Orszag and Patterson [65]

$$E(k,0) = \alpha(k/c)^4 e^{-\frac{n}{2}(k/c)^2}, \tag{C.7}$$

which is the energy spectrum from Batchelor's final stage of turbulence decay [5, 6]. Here (from Mell [60]) the shape parameter is

$$c = \frac{(2\pi)^{1/2}\Delta k}{A}$$

and that scale parameter is

$$\alpha = \frac{64}{15}\left(\frac{2}{\pi}\right)^{1/2}\frac{\nu^2}{c^3}\left(\frac{k_c}{B}\right)^4.$$

The energy spectrum in this stage (and in stage(II)) must be such that the following constraints [30] imposed by the numerical implementation are satisfied: (a) the smallest scales are well resolved, i.e., $\eta_k k_{max} = B > 1$, and (b) the integral length scale is sufficiently small compared the periodic mesh, $l\Delta k = A \leq O(1)$. From these constraints A and B are known. The only unknown is then ν which is imposed by choosing an initial Taylor Reynolds number. This value is set by choosing $Re_\lambda = (u_{rms}\lambda)/\nu \approx 50$, which for the simulations here gives $\nu = 0.005$.

The initial velocity is computed from $E(k,0)$ using the method described in section C.1. The simulation with this initial velocity field ran until $E(k,t)$ has developed to the point of self-similar decay.

(II) In the second stage of the initialization the self-similar spectrum obtained from stage (I) is rescaled to obtain a new spectrum that has higher initial Taylor

Reynolds numbers associated with it. Once the velocity field in stage (I) has reached self-similar decay, i.e.,

$$E(k,t) = \frac{u^2 l}{2} F(kl,t),$$

a new scaled energy spectrum can be defined as

$$E'(k,t) = \alpha' F(kl',t) = \alpha' F(kl[l'/l],t) = \frac{2\alpha'}{u^2 l} E(k[l'/l],t). \tag{C.8}$$

The integral length scale, l', and Kolmogorov scale, η'_k are

$$l' = l,$$

and

$$\eta'_k = \left\{ \left(\frac{l'}{l}\right)^3 \frac{\alpha'}{\alpha} \right\}^{1/4} \eta_k.$$

In this stage, $\alpha = u^2 l/2 = \overline{u_i u_i}\, l/2$. Again A and B are chosen to satisfy the constraints (a) and (b) above. Using eq. (C.8) the scaled energy spectrum is found (with some curve fitting) by choosing α'. With $E'(k,0)$ found the new velocity field is obtained using the method described in section C.1. This new scaled velocity field will reach full spectrum decay more rapidly than that from stage (I) and will have a large Taylor Reynolds number when it reaches full spectrum decay.

C.3 Statistically dependent initial velocity field

This section describes an initialization scheme that is based on that given in section C.1 but is modified so that the initial velocity field is statistically dependent on the initial density field. From section C.1 the initial velocity field is given in eq. (C.1). The Fourier transform of this initial velocity field gives

$$\hat{\vec{u}} = \imath \vec{k} \times \widehat{\vec{A}}' - \imath \mathcal{D} \vec{k} \hat{\psi}.$$

In this scheme $\vec{A}'$ (in real space) is defined such that

$$\vec{A}' = f(\rho)\vec{A}$$

where $\vec{A}$ is the random vector potential computed from the method described in section C.1 and $f(\rho)$ is some function of density. There are two functions used in this study.

A. Large density corresponds to low velocity magnitude

In this case the function $f(\rho)$ is defined such that the density and velocity magnitude are inversely correlated. Therefore, where the density has a negative fluctuation about its mean (low density) the velocity magnitude is high. This is achieved by defining $f(\rho)$ as

$$f(\rho) = \frac{1}{\rho}$$

so that

$$\vec{A}' = \frac{\vec{A}}{\rho}.$$

With this definition, the initial random vector potential, $\hat{A}_i$, corresponds to an initial random momentum field. Clearly, where the density is large the velocity magnitude will be small.

B. Large density corresponds to high velocity magnitude

In this case the function $f(\rho)$ is defined such that the density and velocity are positively correlated. Therefore, where the density has a positive fluctuation about its mean (high density) the velocity magnitude is high. This is achieved by defining $f(\rho)$ as

$$f(\rho) = \rho$$

so that

$$\vec{A}' = \rho\vec{A}.$$

With this definition, the initial random vector potential, $\vec{A}$, corresponds to (something like) an initial random velocity per unit mass field. Clearly, where the density is large the velocity magnitude will be large also.

Once $\hat{A}_i'$ has been determined the energy spectrum, $E_{A'}(k)$, associated with it is computed. Then the initial velocity potential, $\hat{A}_i'$, is properly scaled so that this potential corresponds with the desired initial energy spectrum, $E(k)$. The scaling used is

$$\hat{A}_i' = \frac{E(k)}{E_{A'}(k)} \hat{A}_i'.$$

With this scaling, the initial velocity field has the initial desired spectral shape. It is also desired that the total initial kinetic energy, $R_{nn} = \overline{\rho u_n' u_n'}/2$, for a variable-density case using either velocity initialization (A) or (B) is the same as that for a nearly constant-density case. In order to achieve this the initial velocity field must be rescaled (similar to the spectral scaling). The scaling parameter is the initial R_{nn} for a nearly constant-density case divided by the initial R_{nn} for the variable-density case.

Appendix D

DENSITY INITIALIZATION PROCEDURE

The majority of the results presented in this dissertation used the bimodal probability density for the initial density field. This is the method of Eswaran and Pope [30] (see also Mell [60]). Some of the results discussed in this dissertation also used an initial density field with a Gaussian probability density. The initialization procedure for this Gaussian distribution of the initial density field is a method analogous to that described in section C.1 for the initial velocity field. Two different Gaussian spectra were used for the initializations of the density field. In the study of isotropic decay of variable-density fluid the initial spectral function was Batchelor's final stage of decay spectrum, eq. (C.7). For the buoyancy driven case which was used to compare with the results of Batchelor et al., the initial spectral distribution could be approximated by a delta function. This chapter described these two methods.

D.1 Method of Eswaran and Pope

In this method the density field was set up similar to that of Eswaran and Pope [30]. The initial density field conforms approximately to a double-delta-function pdf which has peaks at ρ_{max} and ρ_{min}. In order for the field to be well resolved the density field is smoothed to avoid sharp gradients. This produces a pdf that has a nonzero value between the peaks. This method is set up in three stages.

(a) In this first stage a discrete density energy spectrum is defined as

$$E_\rho(nk_o) = \sum_{K_n} \hat{\phi}(\vec{k})\hat{\phi}^*(\vec{k}), \tag{D.1}$$

where K_n is the set of all wavenumbers that satisfy $(n-\frac{1}{2})k_o \leq k \leq (n+\frac{1}{2})k_o$. Here

$$\hat{\phi}(\vec{k}) = \left\{\frac{f_{\hat{\phi}}(k)}{4\pi k^2}\right\}^{1/2} \exp(2\pi\imath\theta(\vec{k})). \tag{D.2}$$

The function $f_{\hat{\phi}}(k)$ is defined to be the "top-hat" function

$$f_{\hat{\phi}}(k) = \begin{cases} 1 & \text{if } k_s - k_o/2 \leq k \leq k_s + k_o/2 \\ 0 & \text{otherwise} \end{cases} . \tag{D.3}$$

Here $\theta(\vec{k})$ are uniformly distributed random numbers between 0 and 1 and k is the magnitude of $\vec{k}$. The initial integral length scale of the density field is determined by the value of k_s.

Using eq. (D.2) the Fourier phases of the initial density field are randomly chosen. The Fourier amplitudes of the density field are assigned random values such that the resulting density-energy spectrum is equal to the specified function $f_{\hat{\phi}}(k)$.

(b) The second stage in this initialization procedure is the inverse-Fourier transform of $\hat{\phi}(\vec{k})$ to physical space. In real space, the density value at each grid point is reset to ρ_{max} if the value at that grid point is positive, and to ρ_{min} if it is negative. This procedure gives approximately a "double-delta" pdf for $\phi(\vec{x})$.

(c) The final stage removes the steep spatial gradients in the density field that were set up in stage (b) and also sets the mean value for the density field to $\overline{\rho}$. To accomplish these, $\phi(\vec{x})$ is Fourier transformed to Fourier space and the high wavenumber components are filter out using the following filter:

$$\hat{\phi}(\vec{k}) = F(\vec{k})\hat{\phi}(\vec{k}) \tag{D.4}$$

where

$$F_{\hat{\phi}}(k) = \begin{cases} 1 & if\ k \leq k_c \\ (k/k_c)^{-2} & if\ k \geq k_c \end{cases} . \tag{D.5}$$

The mean density value is fixed by setting the $\hat{\phi}(\vec{k} = 0)$ component to $\overline{\rho}$. The mean density in the simulations used in this study, $\overline{\rho} = (\rho_{max} + \rho_{min})/2 = 1.0$. Also for this study, $k_s = 2.89$, $k_o = 4$ and $k_c = 5.6$. These parameters produce large "blobs" of density in the field.

D.2 Initial density field from an prescribed initial spectral function

The method described in this section is used to set up an initial density field that has an initial Gaussian pdf. This method is analogous to that for setting up an initial

velocity field. In Fourier space the initial density field is defined as

$$\hat{\rho}(\vec{k}) = x_1 + ix_2 \tag{D.6}$$

where x_1 and x_2 is (from Box and Muller)

$$x_1 = a_\rho(-2\log_e U_1)^{\frac{1}{2}} \cos 2\pi U_2$$

$$x_2 = a_\rho(-2\log_e U_1)^{\frac{1}{2}} \sin 2\pi U_2.$$

U_1 and U_2 are independent random variables which are uniformly distributed on the interval (0,1) and a_ρ is the rms of the random field that arises from using initially defined density energy spectrum, $E_\rho(k)$. From section C.1, a_ρ is solved to be

$$a_\rho = \frac{\left[\frac{1}{2N_B}\int_B E_\rho(k)dk\right]^{\frac{1}{2}}}{\mid k \mid}.$$

There two types of initial density spectral functions used in this study. For the case of isotropic decaying, variable-density turbulence, Batchelor's final stage of decay energy spectrum was chosen:

$$E_\rho(k,0) = \alpha(k/c)^4 e^{-\frac{n}{2}(k/c)^2}.$$

For the buoyancy driven case used for comparison with the Boussinesq results of Batchelor et al., the initial random density field is generated from the initial density spectrum $E_\rho(k,0) = \delta(k-2\pi)$ [7], where δ is the Dirac delta-function. This spectrum can be approximated by

$$E_\rho(k,0) = \frac{A_n}{2\pi}\left(\frac{k}{2\pi}\right)^n \exp\left[-\frac{1}{2}n\left(\frac{k}{2\pi}\right)^2\right] \tag{D.7}$$

where $n = 64$ and A_n is given as

$$A_n = \left[\frac{2}{\pi}\right]^{\frac{1}{2}} \frac{n^{\frac{1}{2}(n+1)}}{1\cdot 3\cdot \ldots \cdot (n-1)}. \tag{D.8}$$

Here, A_n is a normalization such that the $E_\rho(k,0)$ properly approximates the Dirac function. The mean density value is set by setting the $\hat{\rho}(\vec{k}=0)$ component to $\overline{\rho}$.

Appendix E

SPECTRA COMPUTATION

In this appendix is described the method of computing spectra in this dissertation (see, e.g., Riley et al. [72]). For isotropic flows it is useful to compute a three dimensional spectrum. This is defined by splitting up the Fourier space into a series of concentric shells such that

$$k_i - \frac{\Delta k}{2} \leq |\vec{k}| \leq k_i + \frac{\Delta k}{2}$$

where k_i is the center of the *ith* shell and Δk is the width of the shell. In our study here $\Delta k = 1$. The spectrum of $\hat{\phi}$, the three-dimensional Fourier transform of ϕ, is defined as

$$E_\phi(k_i)\ \Delta k = \frac{1}{N_i} \sum \hat{\phi}(\vec{k}) \hat{\phi}^*(\vec{k}), \tag{E.1}$$

where N_i is the number of points in the *ith* shell, and $\hat{\phi}^*$ is the complex conjugate of $\hat{\phi}$. With this definition, the energy spectrum discussed in Chapter 4 is defined as

$$E_{nn}(k,t) = \frac{< u_n' u_n' >}{2} = \frac{1}{\Delta k N_i} \sum \hat{u}_n' \hat{u}_n'^*.$$

Likewise, the density spectra is defined as

$$E_\rho(k,t) = \frac{< \rho' \rho_n' >}{2} = \frac{1}{\Delta k N_i} \sum \hat{\rho}' \hat{\rho}_n'^*.$$

The velocity divergence spectra is defined using eq. (E.1), where $\phi \equiv \partial u_n'/\partial x_n$.

For the spectra of other quantities, such as $(\rho' v')$, $(\rho u_n' u_n')$ and $(\rho' u_n' u_n')$ it is useful to define the spectrum as

$$E_{\phi\psi}(k_i)\ \Delta k = \frac{1}{N_i} \sum \left[\hat{\phi}(\vec{k}) \hat{\psi}^*(\vec{k}) + \hat{\phi}^*(\vec{k}) \hat{\psi}(\vec{k}) \right], \tag{E.2}$$

where, for the quantity $(\rho' v')$, $\phi = \rho'$ and $\psi = v'$; for $(\rho u_n' u_n')$, $\phi = \rho u_n'$ and $\psi = u_n'$ and for $(\rho' u_n' u_n')$, $\phi = \rho' u_n'$ and $\psi = u_n'$.

For anisotropic flows it is useful to compute a one-dimensional spectrum (e.g., in the z-direction),

$$E_{z\phi}(k)\ \Delta k = \frac{1}{N_x N_y} \sum_{i,j=1}^{N_x N_y} \hat{\phi}(x_i, y_j, k)\hat{\phi}^*(x_i, y_j, k), \tag{E.3}$$

where $\hat{\phi}$ is the one-dimensional Fourier transform of ϕ in the z-direction, and N_x and N_y are the number of grid points in the x and y directions, respectively.